UNIVERSITY OF SOUTHAMPTON

FACULTY OF ENGINEERING, SCIENCE AND MATHEMATICS

SCHOOL OF ELECTRONICS AND COMPUTER SCIENCE

Particle Swarm Optimization Aided MIMO Transceiver Design

by

Wang Yao

A thesis submitted in partial fulfilment of the
requirements for the award of Doctor of Philosophy
at the University of Southampton

January 2011

SUPERVISORs:
Professor Lajos Hanzo
and
Professor Sheng Chen

This report is dedicated to:
My family.

UNIVERSITY OF SOUTHAMPTON

ABSTRACT

Faculty of Engineering, Science and Mathematics
School of Electronics and Computer Science

A thesis submitted in partial fulfilment of the requirements for the award of Doctor of Philosophy

Particle Swarm Optimization aided MIMO transceiver design

by Wang YAO

In this treatise, we design Particle Swarm Optimization (PSO) aided MIMO transceivers. The employment of multiple antennas leads to the concept of multiple-input multiple-output (MIMO) systems, which constitute an effective way of achieving an increased capacity. When multiple antennas are employed at the Base Station (BS), it is possible to employ Multiuser Detection (MUD) in the uplink. However, in the downlink (DL), due to the size as well as power consumption constraints of mobile devices, so-called Multiuser Transmission (MUT) techniques may be employed at the BS for suppressing the multiuser interference before transmissions, provided that the DL channel to be encountered may be accurately predicted.

The MUT scheme using the classic MMSE criterion is popular owing to its simplicity. However, since the BER is the ultimate system performance indicator, in this treatise we are more interested in the Minimum BER MUT (MBER-MUT) design. Unlike the MBER-MUD, the MBER-MUT design encounters a constrained nonlinear optimization problem due to the associated total transmit power constraint. Sequential Quadratic Programming (SQP) algorithms may be used to obtain the precoder's coefficients. However, the computational complexity of the SQP based MBER-MUT solution may be excessive for high-rate systems. Hence, as an attractive design alternative, continuous-valued PSO was invoked to find the MBER-MUT's precoder matrix in order to reduce its computational complexity.

Two PSO aided MBER-MUTs were designed and explained. The first one may be referred to as a symbol-specific MBER-MUT, while the other one may be termed as the average MBER-MUT. Our simulation results showed that both of our designs achieve an improvement in comparison to conventional linear MUT schemes, while providing a reduced complexity compared to the state-of-art SQP based MBER-MUT.

Later, we introduced discrete multi-valued PSO into the context of MMSE Vector Precoding (MMSE-VP) to find the optimal perturbation vector. As a nonlinear MUT scheme, the VP provides an attractive BER performance. However, the computational complexity imposed during the search for optimal perturbation vector may be deemed excessive, hence it becomes necessary to find reduced-complexity algorithms while maintaining a reasonable BER performance. Lattice-Reduction-aied (LRA) VP is the most popular approach to reduce the complexity imposed. However, the LRA VP is only capable of achieving a suboptimum BER performance, although its complexity is reduced. Another drawback of LRA VP is that its complexity is fixed, which is beneficial for real-time implenebtations, but it is unable to strike a trade-off between the target BER and its required complexity. Therefore, we developed a discrete multi-valued PSO aided MMSE-VP design, which has a flexible complexity and it is capable of iteratively improving the achievable.

In Chapter 5, our contributions in the field of Minimum Bit Error Rate Vector Precoding (MBER-VP) are unveiled. Zero-Forcing Vector Precoding (ZF-VP) and MMSE Vector Precoding (MMSE-VP) had already been proposed in the literature. However, to the best of our knowledge, no VP algorithm was proposed to date based on the direct minimisation of the BER. Our improved MMSE-VP design based on the MBER criterion first invokes a regularised channel inversion technique and then superimposes a discrete-valued perturbation vector for minimising the BER of the system. To further improve the system's BER performance, an MBER-based generalised continuous-valued VP algorithm was also proposed. Assuming the knowledge of the information symbol vector and the CIR matrix, we consider the generation of the effective symbol vector to be transmitted by directly minimising the BER of the system. Our simulation results show the advantage of these two VP schemes based on the MBER criterion, especially for rank-deficient systems, where the number of BS transmit antennas is lower than the number of MSs supported. The robustness of these two designs to the CIR estimation error are also investigated. Finally, the computational complexity imposed is also quantified in this chapter.

With the understanding of the BER criterion of VP schemes, we then considered a new transceiver design by combing uniform channel decomposition and MBER vector precoding, which leads to a joint transmitter and receiver design referred as the UCD-MBER-VP scheme. In our proposed UCD-MBER-VP scheme, the precoding and equalisation matrices are calculated by the UCD method, while the perturbation vector is directly chosen based on the MBER criterion. We demonstrated that the proposed algorithm outperforms the existing benchmark schemes, especially for rank-deficient systems, where the number of users supported is more than the number of transmit antennas employed. Moreover, our proposed joint design approach imposes a similar computational complexity as the existing benchmark schemes.

Acknowledgements

I would like to express my gratitude to my supervisors Professor Lajos Hanzo and Professor Sheng Chen for their outstanding supervision and support throughout the past time in my PhD research. They have offered me constant encouragement and advice throughout the process.

Many thanks to my colleagues in the Communications Group for their support, help and discussions throughout my research so far.

The financial support of the ECS is also gratefully acknowledged.

I would also like to express my appreciation to my parents, Qin Yao and Qin Li. Special thanks also to my relatives in China for their love to me.

List of Publications

1. **W. Yao S. Chen and L. Hanzo**, “A Transceiver Design Based On Uniform Channel Decomposition and MBER Vector Perturbation”, IEEE Transactions on Vehicular Technology, Volume 59, Issue 6, July 2010, pp. 3153 - 3159.

2. **S. Chen, W. Yao and L. Hanzo**, “Semi-blind adaptive spatial equalisation for MIMO systems with high-order QAM signalling”, IEEE Transactions on Wireless Communications, Volume 7, Issue 11, Part 2, November 2008, pp. 4486-4491.

3. **W. Yao S. Chen S. Tan and L. Hanzo**, “Minimum Bit Error Rate Multiuser Transmission Designs Using Particle Swarm Optimisation”, IEEE Transcations on Wireless Communications, Volume 8, Issue 10, October 2009, pp. 5012-5017.

4. **S. Chen, W. Yao and L. Hanzo**, “Semi-Blind Adaptive Beamforming for High-Throughput Quadrature Amplitude Modulation Systems”, International Journal of Automation and Computing (IJAC), Volume 7, Issue 4, pp. 565-570.

5. **S. Chen, W. Yao, H. R. Palally and L. Hanzo**, “Particle Swarm Optimisation Aided MIMO Transceiver Designs”, “Computational Intelligence in Expensive Optimization Problems”, USA: Springer-Verlag, pp. 487-511.

6. **S. Chen, L. Hanzo and W. Yao**, “Semi-Blind Spatial Equalisation for MIMO Channels with Quadrature Amplitude Modulation”, Proceedings of IEEE International Conference on Communications (ICC), Beijing, China, May 2008, pp. 599 - 603.

7. **S. Chen, W. Yao and L. Hanzo**, “CMA and soft decision-directed scheme for semi-blind beamforming of QAM systems”, Proceedings of IEEE Vehicular Technology Conference (VTC) Fall, Calgary, Canada, September 2008, pp. 1-5.

8. **W. Yao S. Chen and L. Hanzo**, “Improved MMSE vector precoding based on the MBER criterion”, Proceedings of IEEE VTC Spring, Barcelona, Spain, April 2009, pp. 1-5.

9. **W. Yao S. Chen and L. Hanzo**, “Particle Swarm Optimisation Aided Minimum Bit Error Rate Multiuser Transmission”, Proceedings of IEEE ICC, Dresden, Germany, June 2009, pp. 1-5.

10. **H. R. Palally, S. Chen, W. Yao and L. Hanzo**, “Particle Swarm Optimisation Aided Semi-blind Joint Maximum likelihood Channel Estimation and Data Detection for MIMO Systems”, IEEE Workshop on Statistical Signal Processing 2009, Cardiff, Wales, UK, Aug.31-Sept.3 2009, pp. 309-312.

11. **W. Yao S. Chen and L. Hanzo**, “Particle swarm optimisation aided multiuser transmission schemes for MIMO communication”, Proceedings of 3rd International Conference of Bio-Inspired Systems and Signal Processing, Valencia, Spain, Jan. 20-23, pp. 53-60.

12. **W. Yao S. Chen and L. Hanzo**, “Generalised Vector Precoding Design Based on the MBER Criterion for Multiuser Transmission”, Proceedings of IEEE Vehicular Technology Conference (VTC) Fall, Ottawa, Canada, Sep. 6-9, 2010, pp. 1-5.

13. **W. Yao S. Chen and L. Hanzo**, “Minimum Bit Error Rate Based Generalised Vector Precoding Design for Multiuser Transmission”, *accepted in* IEEE Transactions on Vehicular Technology.

Contents

List of Symbols

General notation

- $E[\cdot]$ Expectation
- $(\cdot)^{-1}$ Matrix or variable inversion
- $(\cdot)^{*}$ Complex conjugate
- $(\cdot)^{T}$ Transpose
- $(\cdot)^{H}$ Hermitian (conjugate transpose)
- $|\cdot|$ Absolute value
- $\|\cdot\|$ Norm
- $\Re[\cdot]$ Real part of a variable
- $\Im[\cdot]$ Imaginary part of a variable
- $tr(\cdot)$ Trace of a matrix
- $Q(\cdot)$ Area under the tail of the standardized Gaussian distribution
- $sgn(\cdot)$ Signum function
- $L(\cdot)$ Lagrange function
- $mod(\cdot)$ Modulo operation
- $\bigtriangledown(\cdot)$ Gradient

Symbols

- N Number of transmit antennas

- K Number of users at the receiver side
- $\mathbf{x}$ Information symbol vector
- $\mathbf{H}$ Channel matrix
- $\mathbf{P}$ MUT precoding matrix
- $\mathbf{R}$ Covariance matrix
- $\mathbf{I}$ Identity matrix
- α Power scaling factor
- λ Lagrange multiplier
- $\mathrm{E_T}$ Total transmit power
- $\mathbf{z}$ Transmitted signal vector in MUT
- $\mathbf{n}$ AWGN
- σ_n^2 Noise variance
- $\hat{\mathbf{y}}$ Received signal vector before the modulo operation
- $\mathbf{y}$ Received signal vector after the modulo operation
- $\boldsymbol{\omega}$ Perturbation vector in VP
- $\mathbf{u}$ Perturbed symbol vector in VP
- S Population size of the swarm in PSO
- $\check{\mathbf{P}}$ The position of a particle
- $F(\check{\mathbf{P}})$ Fitess value of a particle
- $\mathbf{P}b$ The individual's best visited position so far
- $\mathbf{G}b$ The entire swarm's best visited position so far
- $\mathbf{V}$ The velocity of a particle
- c_1, c_2 The acceleration coefficients in PSO
- w Inertia weight in PSO
- S The legitimate search space in PSO

Chapter 1

Introduction

Compared to conventional Single-Input-Single-Output (SISO) systems employing a single transmit and a single receiver antenna, Multiple-Input-Multiple-Output (MIMO) systems [1] are capable of achieving a higher spectral efficiency. Since their conception, MIMOs have found numerous applications [2–5], and since the characteristics of MIMO channels are pivotal in their study, in the next section we provide a rudimentary introduction to the subject.

1.1 MIMO Channels

The family of MIMO channels may be grouped into three types, namely point-to-point, multipoint-to-single-point and point-to-multipoint channels, as detailed below.

1. Point-to-point.

   The classic point-to-point MIMO system is represented by a transmitter and receiver pair, where both the transmitter and the receiver use several antennas, each associated with a separate modulator and demodulator. Naturally, the antennas potentially interfere with each other, hence interference cancelation techniques have been proposed for the mitigation of the inter-antenna-interference (IAI) [6–8]. Fig. 1.1 shows a typical point-to-point MIMO scenario.

2. Multipoint-to-singlepoint.

   The classic multipoint-to-singlepoint MIMO system is represented by decentralised uplink transmitters and a single central receiver. The uplink of multiuser mobile communication systems constitutes an example of MIMO systems of this type, therefore, it is also often referred to as a multiple access channel. The joint receiver at the base station has to recover the individual users' signals from its received signal, and since a number of users transmit at the same time in the same band, this received signal is the superposition of all the active users' signals. This leads to the so-called multiuser detection (MUD) problem, which has attracted substantial research interests [9–12], hence it is not

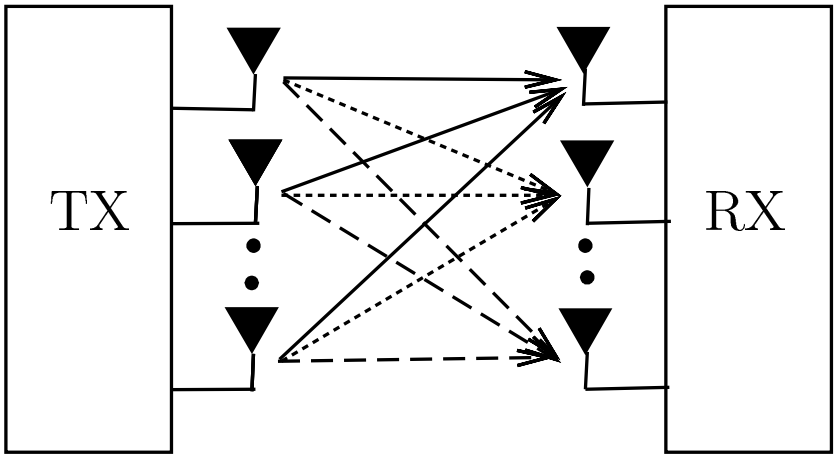

Figure 1.1: MIMO system associated with a point-to-point MIMO channel. 'TX' stands for transmitter, while 'RX' means receiver.

concerned in this treatise. The block diagram of the MIMO multiple access channel is shown in Fig. 1.2.

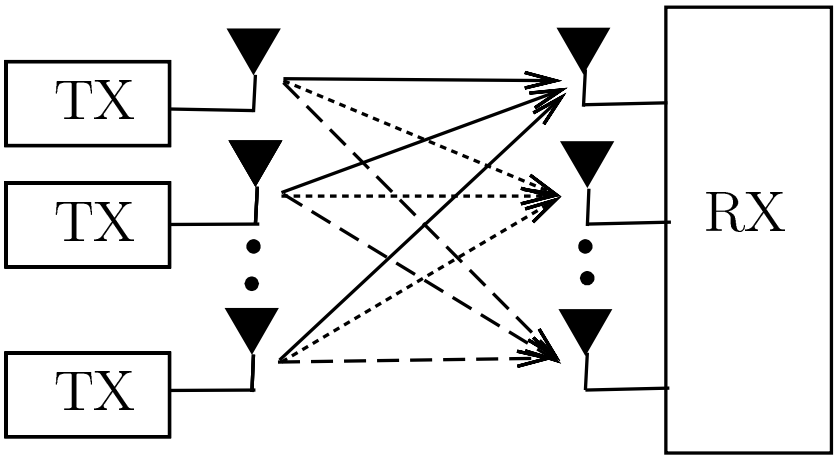

Figure 1.2: MIMO system with decentralised MS transmitters and central BS receiver (MIMO multiple access channel). 'TX' stands for transmitter, while 'RX' means receiver.

3. Point-to-multipoint.

   The classic point-to-multipoint MIMO system is represented by a central transmitter and decentralised receivers. An example of this MIMO system is constituted by the downlink of multiuser mobile communication systems, which is also often termed as a MIMO aided broadcast system. It is characterized by the fact that the end-points of the channels over which the transmission takes place are not co-located but distributed. Hence the employment of MUD at the MSs is not feasible. As a design alternative, the signal to be transmitted to all the users has to be pre-processed, hence this technique is referred to as multiuser transmission (MUT). In this thesis, we will focus our attention on the family of MIMO broadcast systems and discuss several schemes designed for MUT. The block diagram of the MIMO broadcast channel is depicted in Fig. 1.3.

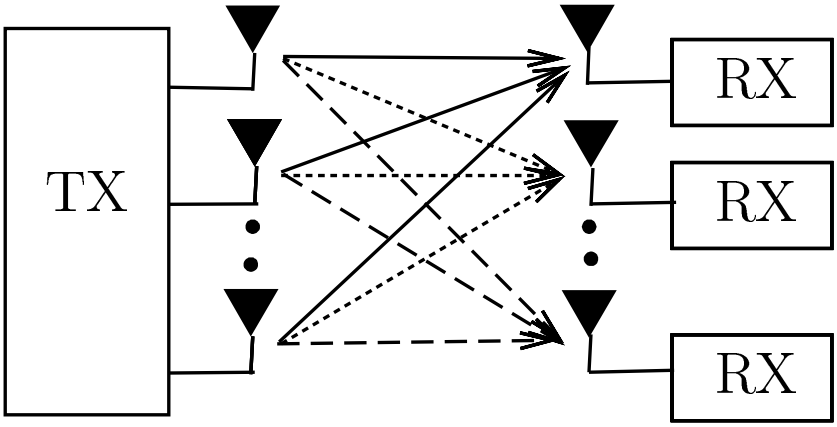

Figure 1.3: MIMO system with central BS transmitter and decentralised MS receivers (MIMO broadcast channel). 'TX' stands for transmitter, while 'RX' means receiver.

1.2 Motivation and Novel Contributions

As stated above, numerous designs have been proposed for multiuser MIMO point-to-point communications [6–8], and for multiuser MIMO multi-point to single-point communications [13–17]. One of the methodologies that all these designs share in common is that they would all try to eliminate the multiuser interference (MUI) at the receiver side. However, this is not particularly practical for multiuser downlink (DL) MIMO single-point to multi-point communications. Considering a multiuser mobile broadcast system, where there is naturally no cooperation between the MSs at the DL receiver, the multiuser interference encountered at the MSs cannot be readily mitigated. Hence, the performance of the system is limited due to the desired signal contamination imposed by the multiuser interference. Therefore we need other techniques of improving the attainable system performance in this scenario. This motivates the research of MUT schemes that are capable of mitigating the MUI at the DL transmitter, namely at the Base Station (BS), so that the signals received at the MS are only noise-contaminated, but free from MUI. Another related advantage of DL-MUT techniques is that they allow us to use low-complexity MSs, which require low-power-consumption single-user-detectors to detect the received signals. This is important, because in the wireless Internet a large proportion of the data transmission would happen in the downlink. Hence, even if cooperation was allowed among MSs at the receiver side, the employment of high-complexity MUDs at the MSs would still remain unattractive for the operator companies, because the charge that can be stored in the MS's battery is limited. Hence the MS's battery would have to be recharged frequently, if high-complexity detection devices are embedded in the MS. Although one may argue that systems employing MUT techniques impose an increased power consumption at the BS, which may increase the expenses of the operator company, the company's profit might still be increased, since it may benefit from a higher increase in its revenue than in its expense, owing to supporting more users. Moreover, in the context of co-operative mobile communications, MSs may act as relay stations and the employment of MUT techniques may reduce the power consumed at the MS's detector. The third advantage of MUT is that it reduces the signal latency at the MS caused by high-complexity detection at the cost of a modest signal latency at the BS, which is imposed by transmit pre-processing required.

Based on the above-mentioned arguments, the advantages and importance of employing MUT techniques in a DL broadcast system have been made plausible. Fig.1.4 shows the family tree of MUT schemes, which may be grouped into linear and nonlinear classes. Linear MUT schemes include classic zero-focing Multiuser Transmission (ZF-MUT) [18], Minimum Mean Square Error Multiuser Transmission (MMSE-MUT) [18] and Minimum Bit Error Rate Multiuser Transmission (MBER-MUT) [5, 19–21]. The MBER-MUT class may be further divided into symbol-specific MBER-MUTs [19–21] and average MBER-MUTs [5]. Both of these MBER-MUT algorithms will be detailed in Chapter 3. In terms of nonlinear MUTs, two popular schemes are constituted by the Tomlison-Harashima precoders (THP) [22] and by Vector Precoding techniques (VP) [23]. Similar to linear MUDs, linear MUTs tend to impose a low computational complexity, but exhibit a modest BER performance, while nonlinear approaches achieve an attractive BER performance, but tend to suffer from a high computational complexity [24].

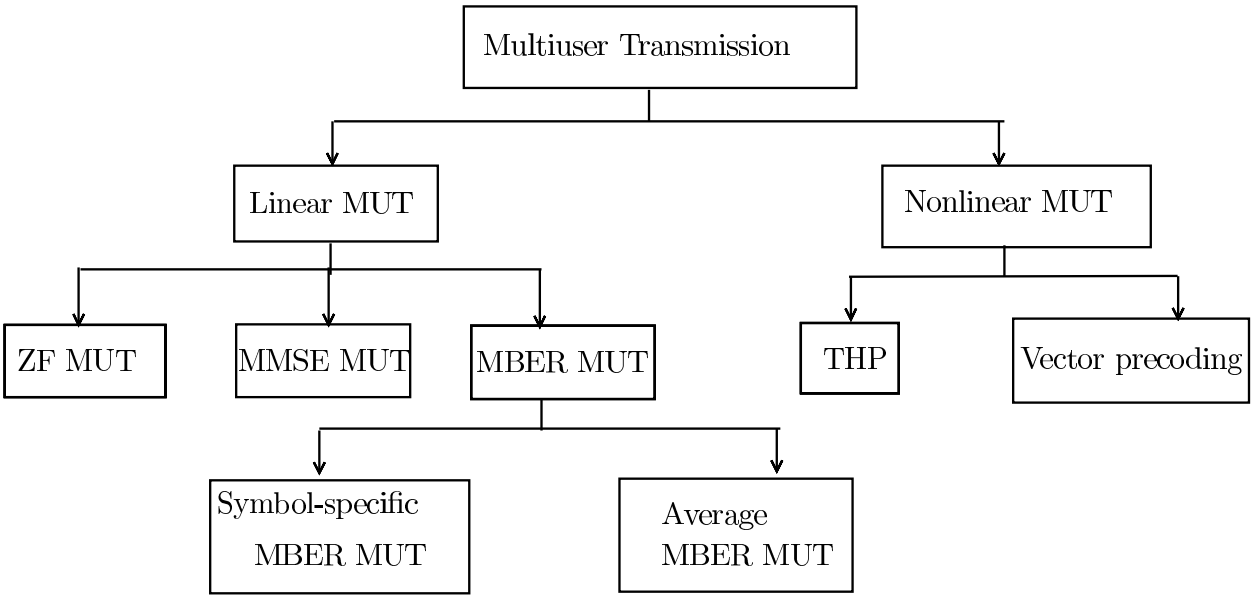

Figure 1.4: The family-tree of MUT schemes. MUT: multiuser transmission, MBER: for minimum bit error rate, THP: Tomlison-Harashima precoding.

Following our literature review in Chapter 2, we will highlight the open research areas in the field of MUT, with particular emphasis on the following two main aspects:

1. Computational complexity reduction in linear and nonlinear MUT algorithms;
2. Novel MUT algorithms will be designed, which are capable of improving the overall system performance.

In the field of linear MUT algorithms, MMSE-MUT schemes [25] are designed to minimize the mean square error between the legitimate transmitted signal and received signal. They are popular owing to their appealing simplicity. However, since we are more interested in the achievable BER performance, than in the achievable MSE, a better strategy is to directly minimize the system's BER. This motivates the design of MBER-MUT algorithms [19, 20]. The MBER-MUT design is detailed later in Chapter 2, which constitutes

a constrained nonlinear optimization problem [5, 26], where the Sequential Quadratic Programming (SQP) algorithm of [27] may be used for generating the precoder's coefficients for the MBER-MUT [5, 24, 26]. Moreover, the computational complexity of this algorithm may become excessive for employment in a real-time system [24]. This motivated our work reported in [28] in the field of MBER-MUT, where the Particle Swarm Optimization (PSO) [29, 30] technique was invoked for finding the near-optimal MBER-MUT weights, despite substantially reducing the computational complexity imposed.

On the other hand, nonlinear MUT techniques were found to be more powerful in terms of approaching the maximum attainable rate of the optimum dirty paper coding (DPC) scheme [31] than linear MUT schemes. Vector Precoding (VP) [23] constitutes a promising technique, which achieves a substantial system performance gain compared to linear MUT algorithms. The family of classic VP algorithms based on the traditional zero forcing criterion (ZF-VP) [23] and on the MMSE criterion (MMSE-VP) [32] employs a so-called sphere encoding algorithm [23] to find the optimal pertubation vector, which will be introduced in detail in Chapter 4. To elaborate a little further, the sphere encoding algorithm may be deemed to be the counterpart of the reduced-complexity sphere decoding (SD) [33] algorithm, which is a popular near-ML MUD algorithm. Despite dispensing with the brute-force full-search ML strategy, the computational complexity imposed by the sphere encoding algorithm was shown to be relatively high [23] and hence at the time of writing it may not be suitable for real-time systems [4]. Although several complexity reduction algorithms have been proposed [4, 34] at the cost of sacrificing the attainable system performance, our motivation is that of proposing a powerful algorithm, which achieves a similar system performance as that obtained by the high-complexity sphere encoding algorithm, while reducing the computational complexity imposed.

Although ZF-VP and MMSE-VP constitute state-of-the-art algorithms in the field of VP, yet, precoding schemes designed based on the MBER criterion by directly minimizing the BER of the system may be deemed attractive, since the BER is the ultimate system performance indicator. Linear MBER-MUT schemes were proposed in [19, 20]. An advanced VP scheme was conceived in [35] for improving the BER in a quasi-static fading environment, which was based on the assumption that the BER may be expressed as a direct function of the average MSE, hence this solution naturally does not lead to the true BER expression, since the MUI distribution is typically non-Gaussian. Therefore, we embark on deriving the BER expression for the system and demonstrate that the perturbation vector may indeed be chosen based on the MBER criterion [36]. Then, based on these findings, we will proceed to propose the design of the MBER criterion based vector precoding technique, which we referred to as the generalized MBER vector precoding algorithm (G-MBER-VP) in [37].

As a promising technique, VP has also been invoked in nonlinear MIMO transceiver designs [8, 38] in order to mitigate the interference at the transmitter. A nonlinear transceiver design based on the geometric mean decomposition (GMD) technique was proposed in [6]. The GMD is a channel decomposition algorithm, which was proposed as an improvement of the traditional singular value decomposition (SVD) algorithm [39]. The GMD technique was also shown to be capable of beneficially diagonalizing the MIMO channel matrix, leading to identical diagonal elements, hence offering identical subchannel gains. As a further advance, uniform channel decomposition (UCD) was proposed in [7] for improving the GMD. The

UCD maintains the highest possible capacity at any signal-to-noise ratio (SNR), and it achieves the maximal attainable diversity gain [7]. A brief introduction to the GMD and the UCD algorithms can be found in Chapter 2, where their advantages over the traditional SVD scheme are also discussed. The solutions proposed in [8] extended the idea of [6] to a GMD MMSE-VP (GMD-MMSE-VP) based transceiver design by invoking the MMSE-VP algorithm. Again, the schemes designed by directly minimizing the BER of the system may be deemed attractive. It is also expected that a UCD based VP design will outperform a GMD based VP design, since the UCD algorithm may be deemed to be an improved GMD scheme based on the MMSE criterion. Although the authors of [7] proposed a UCD based THP design (UCD-THP), to the best of our knowledge, no UCD aided VP transceiver design was proposed to date in the open literature. Against this background, we propose a novel joint UCD-MBER-VP transceiver design by combining the UCD and the MBER based VP [38].

In summary, the novel contributions of this thesis are listed as follows:

- In Chapter 3, we demonstrate that the employment of PSO in deriving both the symbol-specific and the average linear MBER-MUT precoder's coefficients is capable of substantially reducing the computational complexity, when compared to their counterparts using the traditional SQP approach [27], which is achieved without eroding the system performance [28, 40, 41].

- In Chapter 4, we invoke the PSO algorithm in order to find the optimal perturbation vector of both ZF-VP and MMSE-VP. We demonstrate that our approach achieves a similar performance to that of using the potentially excessive-complexity sphere encoding algorithm [23], at a reduced computational complexity. The proposed solution will be contrasted to several benchmark schemes found in the literature [4, 34], which aim for reducing the computational complexity imposed at the cost of achieving a sub-optimum performance, when compared to that of the sphere encoding algorithm.

- In a practical communication system, the BER is the ultimate indicator of the attainable system performance, hence algorithms designed based on the MBER criterion by minimizing the BER of the system are attractive [19–21]. There are numerous MBER MUD algorithms in the literature [12, 42–44]. Several contributions based on the MBER criterion can also be found in the research literature of linear MUTs [19, 20]. Yet, to the best of our knowledge, no VP algorithm was proposed to date based on the direct minimization of the BER in the open literature. Against this background, we propose a novel G-MBER-VP design based on directly minimizing the BER of the system [36, 37, 45]. The resultant G-MBER-VP design turns out to be a non-convex continuous-valued optimization problem. Hence, we adopt the PSO algorithm for efficiently solving this challenging nonlinear MUT design problem.

- In Chapter 5, we extend our proposed G-MBER-VP concept into MIMO transceiver designs and propose a joint UCD-MBER-VP transceiver by combining the UCD and the MBER based VP [38].

- In Chapter 6, we also demonstrate that our proposed G-MBER-VP and UCD-MBER-VP designs are capable supporting more users than the number of transmit antennas employed at the BS, which constitutes a pratical rank-deficient scenario, where the number of MSs supported is higher than the number of transmit antennas employed [37, 38, 45]. We demonstrate that our design outperforms

all the benchmark designs, especially in the challenging rank-deficient scenario, where the number of DL transmit antennas is lower than the number of users supported. The simulations demonstrate that in such challenging scenarios, conventional algorithms encounter error floors, while the proposed schemes do not.

1.3 Thesis Outline

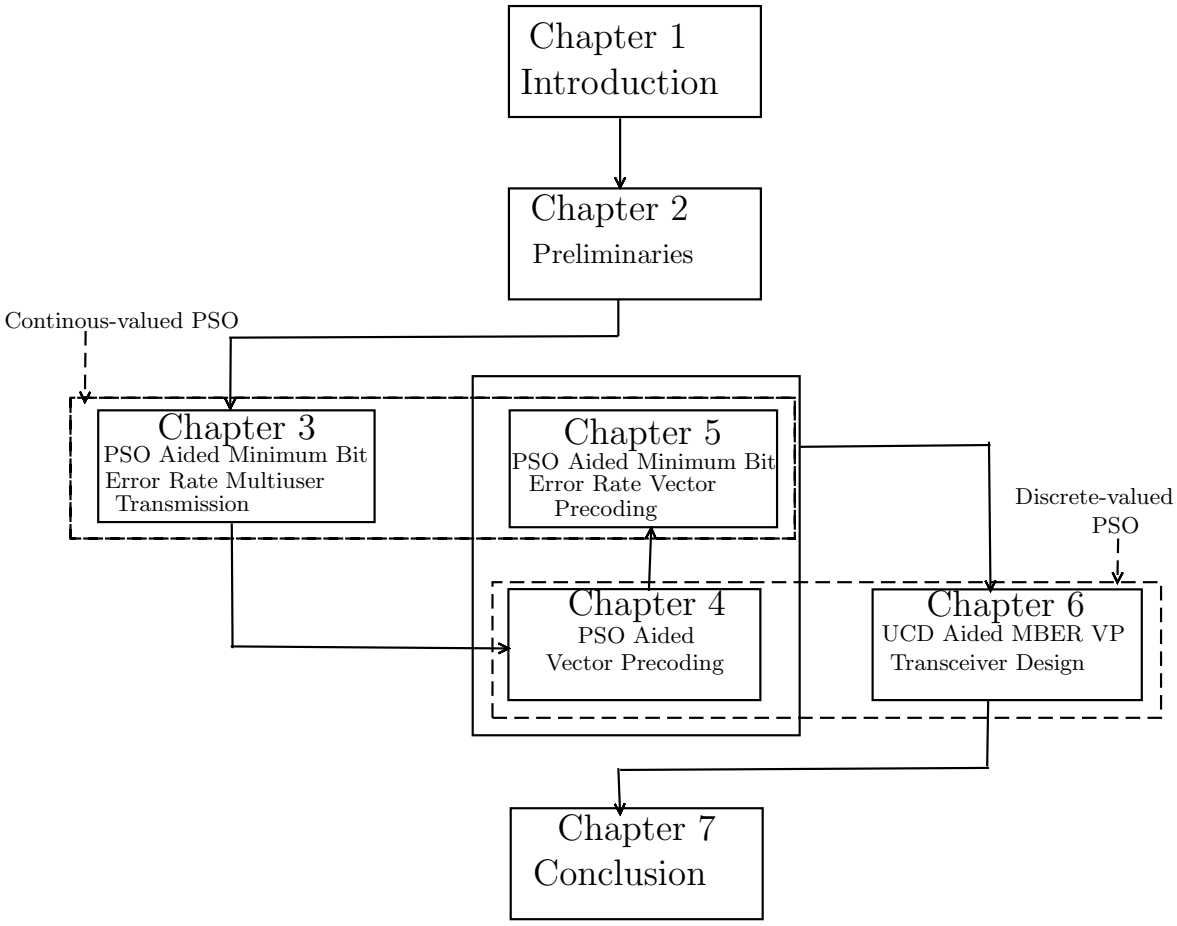

Figure 1.5: The structure of the thesis.

The structure of the thesis can be seen in Fig. 1.5. An overview of both linear and nonlinear MUT schemes is provided in Chapter 2. In Section 2.1, we describe several classic MUT algorithms and compare both their achievable BER performance as well as their computational complexity. Generally speaking, nonlinear MUT algorithms are capable of achieving better BER performances than their linear MUT counterparts, while linear MUT algorithms benefit from a lower computational complexity. In other words, there is always a trade-off between the achievable BER performance and the computational complexity imposed by the MUT, which is similar to the trade-offs observed for MUDs. An introduction to PSO is provided in Section 2.2, which constitute a population based stochastic optimization method inspired by the social behaviour of bird flocks or fish schools. They are capable of substantially reducing the search space, hence have the ability to rapidly converge and they are also capable of 'steering clear' of local minima. More

specifically, our introduction covers the family of both continous-valued as well as discrete-valued PSO. Finally, Section 6.2 is devoted to the provision of the foundamental knowledge concerning the GMD and UCD algorithms, both of which are based on the well-known SVD scheme.

The computational complexity reduction issues of linear MBER-MUTs are addressed in Chapter 3. Since the state-of-the-art SQP algorithm [27] imposes a high complexity, when calculating the coefficients of both the symbol-specific and of the average MBER-MUT precoders, we propose continuous-valued PSO aided symbol-specific MBER-MUT solutions in Section 3.4.1 and continuous-valued PSO assisted average MBER-MUT designs in Section 3.4.2. It is shown in Section 3.7 that our approaches are capable of achieving the same BER performance as the SQP algorithm [27] while imposing a lower computational complexity.

In Chapter 4, we focus our attention on the computational complexity reduction of the nonlinear VP MUT alogrithm. Deriving the best pertubation vector in VP is challenging, which was solved by using the sphere encoding algorithm of [23], which imposes a potentionally excessive computational complexity. Although several complexity reduction schemes have been proposed in the literature [4, 34], again, they can only achieve a sub-optimum BER performance, when compared to that achieved by invoking the sphere encoding algorithm. We show that by using our proposed discrete-valued PSO approach, we may achieve a similar BER performance to that of the sphere encoding algorithm, while imposing a significantly reduced computational complexity.

The architecture of the ZF-VP and MMSE-VP is then further developed to conceive the VP based MBER scheme in Chapter 5. More specifically, in Section 5.2 we first introduce the MBER criterion for the design of VP scheme, then show how to find the perturbation vector based on this novel MBER criterion, noting that the calculation of the precoding matrix still follows the approach of MMSE-VP. In Section 5.3, we propose the direct generation of the effective symbol vector based on the proposed MBER criterion, given the knowledge of the channel state information and the current information symbol vector to be transmitted, rather than using the previously proposed two-step optimization process of the ZF-VP and MMSE-VP. It is shown in Section 5.5 that our approach achieves a better BER performance than the benchmark algorithms and it is capable of supporting rank deficient systems, where the number of users supported in the DL is higher than that of the antennas employed at the DL transmitter.

The previously proposed MIMO transceiver designs based on GMD [6] and UCD [7] all assumed that the number of antennas employed at the transmitter is equal to or larger than the number of antennas employed at the receiver. In other words, practical rank-deficient scenarios have not been considered. It is shown in Section 6.6 that all the benchmark algorithms proposed in the literature are unable to support rank deficient systems, hence result in error floors. Against this background, in Section 6.4 we further extend the employment of our proposed MBER criterion based VP into MIMO transceiver designs. More specifically, in our proposed UCD-MBER-VP scheme, the precoding and equalization matrices are calculated by the UCD method, while the perturbation vector is chosen based directly on the MBER criterion. We demonstrate that our proposed algorithm outperforms the existing benchmark schemes, especially for rank-deficient systems, which is achieved at a similar computational complexity as that of the existing benchmark schemes.

The thesis is concluded in Chapter 7, along with a range of future work suggestions.

Chapter 2

Preliminaries

In this chapter, the underlying fundamentals of this thesis are introduced. These cover the three major aspects of multiuser transmission (MUT), particle swarm optimization (PSO) as well as geometric mean decomposition (GMD) and uniform channel decomposition (UCD). A rudimentary introduction to MUT is provided in Section 2.1, where we commence from introducing classic linear MUT algorithms in Section 2.1.1, namely ZF-MUT and MMSE-MUT. Linear MUT schemes benefit from implementational simplicity, but they achieve a limited BER performance, when compared to that of their nonlinear MUT counterparts. One of the promising nonlinear MUT schemes known as vector precoding or vector perturbation (VP) is introduced next in Section 2.1.2, followed by the characterization of our powerful optimization tool, namely the PSO algorithm in Section 2.2. More specifically, the continous-valued PSO scheme, which is more suitable for solving continous-valued optimization problems, is introduced in Section 2.2.1, while the introduction of the discrete-valued PSO algorithm invoked for solving combinatorial optimization problems is covered in Section 2.2.2. This chapter is concluded in Section 2.3.

2.1 Multiuser Transmission

Motivated by the achievable performance gains of MUD [9, 10] in the uplink (UL), in recent years the so-called transmitter preprocessing philosophy was conceived for MUT, in order to mitigate the multiuser interference at the transmitter by pre-compensating for the effect of the channel to be encountered for the downlink (DL) at the transmitter, which has drawn wide attention [3, 18, 46–49]. The advantages of employing MUT techniques were discussed in Section 1.2, but again, one of its most substantial benefit is that it is possible to employ low-complexity single-user matched-filter (MF) based receivers at the MSs for mobile broadcast channels [50]. However, in MUT, the transmitter requires the knowledge of the DL channels associated with each of the MSs in order to carry out transmit preprocessing. The assumption that the downlink channel's impulse response is known at the BS may be deemed valid in time division duplex (TDD) systems, such as for example in combined TDD-code division multiple access (TDD-CDMA, [51]) or in time division aided CDMA (TD-CDMA, [52]). This is because the UL and the DL share the same frequency band. Thus in the absence of strong interference, all channel parameters are similar for the UL and DL [53–55],

provided that the coherence time [56] of the channel is sufficiently long, so that the channel estimate of the UL receiver is still valid, when it is used by the DL transmit preprocessing algorithm.

Since the broadcast DL channels spanning from the BS to MSs can be estimated by exploiting its reciprocity with respect to the multiple access UL channels spanning from the MSs to the BS, MUT may be deemed suited for DL transmission in a cellular wireless communications system using TDD. By contrast, for systems using for example frequency division duplex (FDD), where the uplink and downlink channels may not be considered reciprocal, CSI feedback is required from the MS's receivers to the BS's transmitter. To elaborate a little further, the DL MUT techniques may also be viewed as the DL counterpart of the UL SDMA arrangements. More explicitly, in the UL a MUD is employed at the BS to detect all of the K UL signals by exploiting the unique, user-specific Channel Impulse Responses (CIR) for differentiating the users. The same principle may be exploited for uniquely and unambiguously differentiating the K users also at the BS's DL MUT, provided that all the K users signal their CIRs back to the BS.

In the next section, some well-established MUT techniques, including linear MUTs and nonlinear MUT algorithms are briefly reviewed.

2.1.1 Linear Multiuser Transmission

We commence by introducing the system model of linear MUT algorithms, which may be classified according to the family-tree of Fig. 1.4.

2.1.1.1 System Model

The DL of a SDMA system supporting non-cooperative mobile receivers is considered here. The BS is equipped with N DL transmit antennas and communicates with K MSs, each employing a single receive antenna. The corresponding system model is depicted in Fig. 2.1.

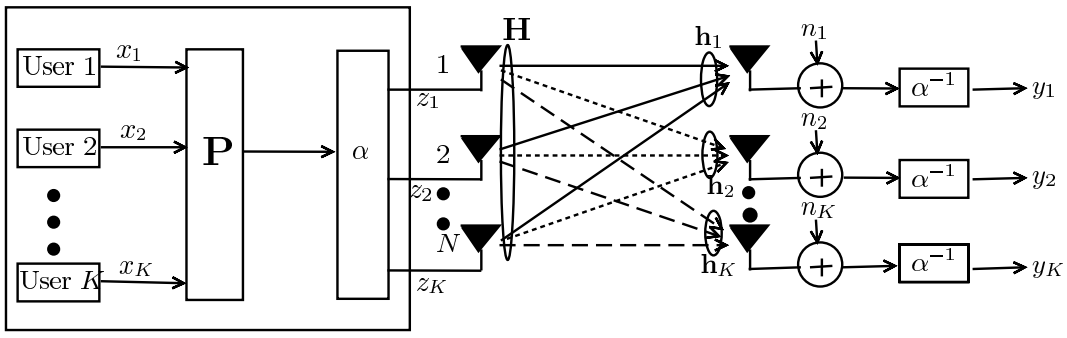

Figure 2.1: Schematic of the SDMA DL using linear preprocessing based MUT at the BS. The system employs N transmit antennas to communicate with K non-cooperative MSs.

The vector of K-element information symbols $\mathbf{x}$ transmitted in the DL is given by

$$\mathbf{x} = [x_1, x_2, \cdots, x_K]^T, \tag{2.1}$$

where x_k, $1 \leq k \leq K$ denotes the transmitted symbol of the kth MS, and the symbol energy is given by $E[|x_k|^2] = \sigma_x^2$, for $1 \leq k \leq K$, where x_k is an independently and identically distributed (i.i.d.) uniform random variable. $E[\bullet]$ denotes the expectation operator.

The $(K \times N)$-element channel matrix $\mathbf{H}$ is given by

$$\mathbf{H} = [\mathbf{h}_1, \mathbf{h}_2, \cdots, \mathbf{h}_K]^T, \tag{2.2}$$

where $\mathbf{h}_k$, $1 \leq k \leq K$ is the kth user's CIR also referred to as the spatial signature, which is given by

$$\mathbf{h}_k = [h_{k,1}, h_{k,2}, \cdots, h_{k,N}], k = 1, 2, \cdots, K. \tag{2.3}$$

We assume that the CIR taps $h_{k,i}$, for $1 \leq k \leq K$ and $1 \leq i \leq N$ are independent of each other and obey the complex Gaussian distribution associated with $E[|h_{k,i}|^2] = 1$.

The $(N \times K)$-element MUT precoding matrix $\mathbf{P}$ is given by

$$\mathbf{P} = [\mathbf{p}_1, \mathbf{p}_2, \cdots, \mathbf{p}_K], \tag{2.4}$$

where $\mathbf{p}_k$, $1 \leq k \leq K$ represents the precoder coefficient vector to be used for the kth user's data stream. More explicitly, given the knowledge of all CIRs, the K precoding vectors pre-compensate for the DL MUT at the BS, so that the MS can use a single-user MR-based receiver.

Given a total transmit power $\mathrm{E_T}$ at the BS, an appropriate scaling factor should be used after precoding to fulfill our transmit power constraint of having an identical transmit power to that of the traditional transmitter dispensing with MUT.

At the receiver, the reciprocal of the scaling factor, namely α^{-1}, is employed to compensate for this power scaling at the receiver invoking for example a classic automatic gain control mechanism, so that unity-gain transmission is ensured.

The Gaussian noise vector $\mathbf{n}$ is given by

$$\mathbf{n} = [n_1, n_2, \cdots, n_K]^T, \tag{2.5}$$

where $n_k, 1 \leq k \leq K$ is a complex Gaussian random variable associated with a zero mean and $E[|n_k|^2] = 2\sigma_n^2 = \mathrm{N_o}$. Thus, the baseband model of the system can be described as

$$\mathbf{y} = \mathbf{HPx} + \alpha^{-1}\mathbf{n}, \tag{2.6}$$

where $\mathbf{y} = [y_1\ y_2 \cdots y_K]^T$ denotes the received signal vector, and y_k, $1 \leq k \leq K$, constitutes sufficient statistics for the kth MS to detect the transmitted data symbol x_k. Finally, the detector simply subjects the symbols to hard-decisions according to the modulated signal constellation for symbol estimation.

2.1.1.2 Zero Forcing Multiuser Transmission

Similar to ZF-MUD, the aim for Zero forcing MUT (ZF-MUT) is to eliminate the interference at the receivers, which is imposed by transmitting

$$\mathbf{z} = \alpha_{zf}\mathbf{P}_{zf}\mathbf{x}, \tag{2.7}$$

where $\mathbf{x}$ is the original information symbol vector, $\mathbf{P}_{zf}$ is the precoding matrix of the ZF-MUT scheme, which is given by [25]

$$\mathbf{P}_{zf} = \mathbf{H}^H(\mathbf{H}\mathbf{H}^H)^{-1}, \tag{2.8}$$

yielding,

$$\mathbf{H}\mathbf{P}_{zf} = \mathbf{I}. \tag{2.9}$$

The role of the normalization factor α_{zf} is to fullfill the sum-power constraint $\mathrm{E_T}$ at the transmitter, which is given by

$$\alpha_{zf} = \sqrt{\frac{\mathrm{E_T}}{tr[(\mathbf{H}\mathbf{H}^H)^{-1}\mathbf{R_x}]}}, \tag{2.10}$$

where the covariance matrix of $\mathbf{x}$ is defined as $\mathbf{R_x} = E[\mathbf{x}\mathbf{x}^H]$.

Therefore, an example can be provided for the purpose of demonstration. We consider the transmission of a symbol vector of a simple (2×2)-element MIMO system, when QPSK modulation scheme is employed. The information bit of the first user is $[0\ \ 1]$, while the information bit of the other user is $[1\ \ 1]$. Thus, the information symbol vector is $\mathbf{x} = [-0.5 + j0.5, 0.5 + j0.5]^T$. The transmissions take place over a flat Rayleigh fading channel, where $\mathbf{H}$ can be expressed as:

$$\mathbf{H} = \begin{bmatrix} -0.06 + j0.39 & 0.10 - j0.00 \\ -0.76 + j0.45 & -0.35 + j0.87 \end{bmatrix}$$

When the system is operating at $\mathbf{E_b/N_o}$=6 $\mathbf{dB}$, the instantaneous noise vector may be expressed as $\mathbf{n} = [0.005 - j0.03, -0.16 - j0.28]^T$.

The ZF criterion based precoding matrix can be computed according to Equation 2.8, yielding:

$$\mathbf{P}_{zf} = \mathbf{H}^H(\mathbf{H}\mathbf{H}^H)^{-1} = \begin{bmatrix} -1.06 - j2.53 & 0.20 - j0.21 \\ -0.63 + j2.53 & -0.67 - j0.94 \end{bmatrix}.$$

Suppose the transmit power constraint $\mathrm{E_T}$ is normalized to be 1, namely $\mathrm{E_T} = 1$, then the value of the normalization factor α_{zf} can be computed according to Equation 2.10, yielding:

$$\alpha_{zf} = \sqrt{\frac{\mathrm{E_T}}{tr[(\mathbf{H}\mathbf{H}^H)^{-1}\mathbf{R_x}]}} = 0.30.$$

Hence, the received signal $\mathbf{y}$ can be calculated according to Equation 2.6 as:

$$\begin{aligned} \mathbf{y} &= \alpha^{-1}\mathbf{H}\alpha\mathbf{P}\mathbf{x} + \alpha^{-1}\mathbf{n} = \mathbf{x} + \alpha^{-1}\mathbf{n} \\ &= [-0.48 + j0.37,\ -0.05 - j0.43]^T. \end{aligned}$$

The resultant bits for the two users are then decoded by simply retaining the polarity of the signals, yielding $[0\ \ 1]$ and $[0\ \ 0]$, respectively. Two errors may be observed amongst the four transmitted bits.

It is worth noting that since the ZF MUT assumes that the only signal-contamination is the MUI, in the presence of AWGN it imposes a performance degradation owing to the classic noise-amplification phenomenon.

Fig.2.2 shows the BER performance of the zero-forcing MUT and MUD under the assumption of perfect CIR knowledge. We considered a (4×4)-element MIMO system communicating over an independent flat Rayleigh fading channel, when a QPSK modulation scheme is employed. In the presence of perfect CSI knowledge, the two schemes share the same BER performance.

2.1.1.3 MMSE Multiuser Transmission

In MMSE multiuser transmission, the aim is to preprocess the transmitted signal in order to minimize the MSE between the original information symbol vector and the received signal. Hence, the optimization problem to be solved may be formulated as

$$\{\mathbf{P}_{mmse}, \alpha_{mmse}\} = \arg\min_{\mathbf{P},\alpha} E[\|\alpha^{-1}(\mathbf{HPx}+\mathbf{n}) - \mathbf{x}\|^2]; s.t. : E[\|\mathbf{Px}\|^2] = \mathrm{E_T}. \tag{2.11}$$

To solve this problem, we may introduce the Lagrange multiplier λ and then find the minimum of the following function:

$$\begin{aligned} L\{\mathbf{P},\alpha,\lambda\} &= E[\|\alpha^{-1}(\mathbf{HPx}+\mathbf{n}) - \mathbf{x}\|^2] + \lambda\{E[\|\mathbf{Px}\|^2] - \mathrm{E_T}\} \\ &= tr(\alpha^{-2}\mathbf{HPR_xP}^H\mathbf{H}^H + \mathbf{R_x} + \alpha^{-2}\mathbf{R_n} - \alpha^{-1}\mathbf{HPR_x} - \alpha^{-1}\mathbf{R_xP}^H\mathbf{H}^H \\ &\quad +\lambda\mathbf{PR_xP}^H) - \lambda\mathrm{E_T}, \end{aligned} \tag{2.12}$$

where we define $\mathbf{R_n} = E[\mathbf{nn}^H]$. By setting this Lagrangian function's gradient with respect to $\mathbf{P}$ to zero, after some manipulations we arrive at [24]:

$$(\alpha^{-2}\mathbf{H}^H\mathbf{H} + \lambda\mathbf{I})\mathbf{P} = \alpha^{-1}\mathbf{H}^H. \tag{2.13}$$

Then, the precoding matrix can be expressed as:

$$\mathbf{P}_{mmse} = \alpha\mathbf{H}^H(\mathbf{HH}^H + \alpha^2\lambda\mathbf{I})^{-1}. \tag{2.14}$$

The gradient of the Lagrangian function with respect to α can be expressed as

$$\begin{aligned} \bigtriangledown_\alpha L\{\mathbf{P},\alpha,\lambda\} &= \frac{\partial L\{\mathbf{P},\alpha,\lambda\}}{\partial\alpha} \\ &= tr(2\alpha^{-3}\mathbf{HPR_xP}^H\mathbf{H}^H + 2\alpha^{-3}\mathbf{R_n} \\ &\quad -\alpha^{-2}\mathbf{HPR_x} - \alpha^{-2}\mathbf{R_xP}^H\mathbf{H}^H), \end{aligned} \tag{2.15}$$

setting the above gradient to zero and then using the power constraint $E[\|\mathbf{Px}\|^2] = tr(\mathbf{PR_xP}^H) = \mathrm{E_T}$, we may arrive at

$$\alpha^2\lambda = \frac{tr(\mathbf{R_n})}{\mathrm{E_T}}. \tag{2.16}$$

Thus, the solution of the optimization problem formulated in Equation 2.11 becomes [25]

$$\mathbf{P}_{mmse} = \alpha_{mmse}\mathbf{H}^H(\mathbf{HH}^H + \frac{2\sigma_n^2}{\mathrm{E_T}}\mathbf{I})^{-1}, \tag{2.17}$$

where the normalization factor α_{mmse} of Equation 2.11 is given by [24]

$$\alpha_{mmse} = \sqrt{\frac{\mathrm{E_T}}{tr(\mathrm{FF}^H)}}, \tag{2.18}$$

where $\mathrm{F} = \mathbf{H}^H(\mathbf{H}\mathbf{H}^H + \frac{2\sigma_n^2}{\mathrm{E_T}}\mathbf{I})^{-1}$.

Let us now return to the example provided in Section 2.1.1.2. According to Equation 2.18, the normalization factor α_{mmse} may be calculated as:

$$\alpha_{mmse} = \sqrt{\frac{\mathrm{E_T}}{tr(\mathrm{FF}^H)}} = 0.57, \tag{2.19}$$

while the MMSE criterion based precoding matrix can be computed according to Equation 2.17, yielding:

$$\mathbf{P}_{mmse} = \alpha_{mmse}\mathbf{H}^H(\mathbf{H}\mathbf{H}^H + \frac{2\sigma_n^2}{\mathrm{E_T}}\mathbf{I})^{-1} = \begin{bmatrix} -0.54 - j1.35 & -0.10 - j0.22 \\ -0.28 + j1.24 & -0.42 - j0.69 \end{bmatrix}.$$

Hence, the received signal $\mathbf{y}$ can be calculated according to Equation 2.6 as:

$$\begin{aligned} \mathbf{y} &= \mathbf{H}\mathbf{P}_{mmse}\mathbf{x} + \alpha_{mmse}^{-1}\mathbf{n} \\ &= [-0.18 + j0.18,\ 0.10 - j0.03]^T. \end{aligned}$$

The resultant bits for the two users are then decoded by simply retaining the polarity of the signals, yielding $[0 \quad 1]$ and $[1 \quad 0]$, respectively. In contrast to the ZF-MUT example, there is now only one error amongst the four transmitted bits.

Fig.2.2 portrays the BER performance of the MMSE MUT and MUD. We considered a (4×4)-element MIMO system communicating over flat Rayleigh fading channels, when a QPSK modulation scheme was employed. As expected, in the presence of perfect CIR knowledge, the MMSE MUT and MUD exhibit the same BER performance.

2.1.1.4 MBER Multiuser Transmission

The MMSE-MUT was designed to minimize the mean square error between the legitimate transmitted signal and received signal. However, we are more interested in minimizing the BER, rather than the MSE. Hence we set out to directly minimize the system's BER. This motivates the design of the MBER-MUT. There are two basic types of MBER-MUT. One of them is a symbol-by-symbol MBER multiuser transmission scheme [21], which frequently updates the MUT array weights, namely for each new symbol vector. The other scheme is the so-called average MBER-MUT, which minimizes the BER averaged over the entire legitimate signals. This is the direct counterpart of the MBER-MUD, which is a generalized MBER-MUT [5]. They will be detailed in Section 3.4.1 and Section 3.4.2, respectively.

In the next section, we will briefly highlight some of the seminal contributions in the open literature up to date on linear MUT schemes.

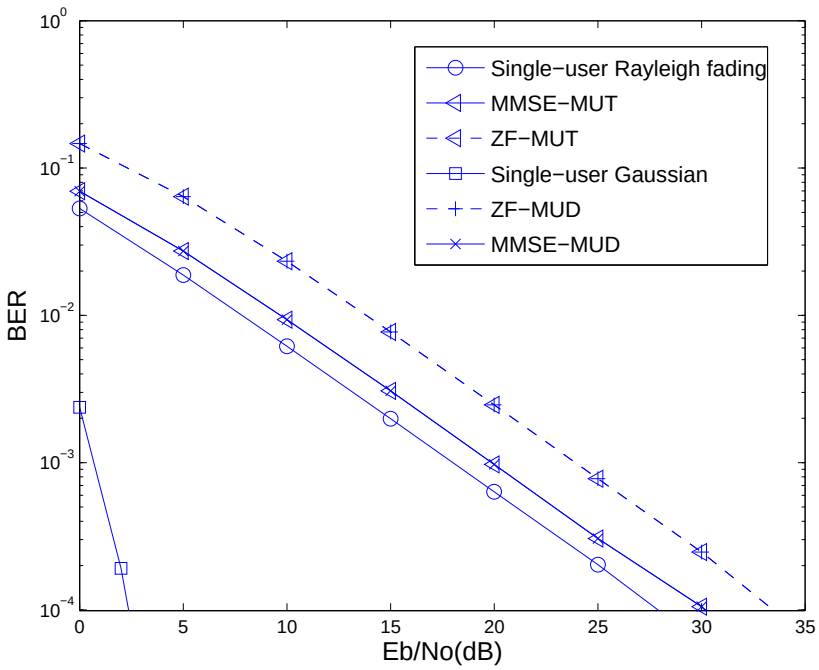

Figure 2.2: BER performances of the several linear MUTs and MUDs. The scenario of a (4×4)-element MIMO system communicating over an independent flat Rayleigh fading channel is considered and QPSK modulation scheme was employed. The single-user BER performances of transmitting over Gaussian and Rayleigh fading channels are also included.

2.1.1.5 Contributions in linear MUT design

A range of novel concepts were introduced in [57] for establishing the relationship between MUDs and MUTs, arguing that for any linear MUD scheme, there exists a linear MUT counterpart, which can be readily designed from the original linear MUD. In the rest of this subsection, some linear MUT schemes are reviewed. Table 2.1 and Table 2.2 briefly show the evolution of linear MUT techniques.

2.1.2 Nonlinear Multiuser Transmission

One of the most promising and popular nonlinear MUT techniques is known as vector precoding [35] or vector perturbation [66] (VP). In this section, a brief rudimentary introducation on VP is provided commencing from the system model.

2.1.2.1 System Model

The DL of an SDMA system supporting non-cooperative mobile receivers is considered here, where the BS is equipped with N DL transmit antennas and transmits over frequency-flat fading channels to K non-cooperative MSs. Each MS employs a single receive antenna and a modulo device, which will be introduced later. The corresponding system model is depicted in Fig. 2.3.

Table 2.1: Selected contributions on linear MUT algorithms (Part 1)

Year	Author(s)	Contributions
1998	[58] Vojčić and Jang	Proposed a transmitter preprocessing scheme, which represents a linear transformation of the transmitted signals, where the mean squared errors recorded at the output of all the MS receivers are minimized. It was shown that when either a conventional MF-based single-user receiver or a RAKE receiver is employed, both the multiple access and the intersymbol interference can be eliminated. The authors also discussed the possibility of including a specific transmit power constraint, hence the resultant solution was referred to as the constrained MMSE transmit filter.
1999	[59] Karimi, Sandell and Salz	Introduced the concept of the transmit Wiener filter method. The transmit MMSE filter was obtained by simply incorporating a weighted identity matrix in the transmit zero-forcing solution in an intuitive way.
2001	[60] Barreto and Fettweis	Two precoding schemes were proposed for the downlink of CDMA systems, which assist in reducing the multiuser interference by jointly preprocessing the transmitted signal based on the knowledge of the downlink channel. Also proposed an unequal transmit power constraint and stated that the resultant optimization problem has no closed form solution.
2002	[25] Joham *et al.*	Derived the transmit Wiener filter concept for DS-CDMA systems, which takes into account the noise power encountered at the receivers. Demonstrated that the transmit Wiener filter converges to the transmit matched filter and to the transmit zero-forcing filter for low and high SNRs, respectively.
2003	[19] Irmer *et al.*	A MBER-MUT scheme was proposed for the TDD code-division multiple-access DL designed for frequency-selective channels.
2003	[21] Irmer *et al.*	Extended the symbol-specific MBER transmission to multiple transmit and receive antennas. The multiple antenna aided MUT schemes were compared, when combined with the application of PreRAKE, RAKE and Singular Value Decomposition (SVD) aided eigen-mode preprocessing.

Table 2.2: Selected contributions on linear MUT algorithms (Part 2)

Year	Author(s)	Contributions
2004	[2] Irmer *et al.*	Extended the symbol-specific MBER transmission concept from the symbol-by-symbol optimization to the more general chip-by-chip MBER concept using a phase-only MUT scheme, which imposes a considerably reduced computational complexity.
2005	[5] Hjørungnes and Diniz	Proposed an average MBER prefilter design for wireless Finite Impulse Response (FIR) MIMO communication systems.
2005	[49] Joham *et al.*	Compared three different types of linear transmit processing schemes designed for MIMO systems.
2007	[61] Habendorf and Fettweis	Proposed a new framework for the unconstrained optimization of systems obeying a fixed transmit power constraint. The linear MBER MUT was also extended to higher-order modulation schemes.
2007	[57] Yang	Introduced novel concepts for finding the relationship between MUDs and MUTs. For any given linear MUD scheme, there exists a linear MUT counterpart, which can be readily designed from the original linear MUD.
2008	[62] Richter *et al.*	Considered the spread-spectrum TDD-CDMA downlink using 4-QAM transmission.
2009	[63] Azzam and Adve	Developed an effective linear precoding algorithm for multiuser, multi-cell, MIMO systems.
2009	[64] Masouros and Alsusa	Introduced a novel channel inversion (CI) based precoding scheme for the DL of phase shift keying (PSK)-based MIMO systems.
2010	[65] Ryu and Choi	Proposed a linear MUT scheme for the DL of cellular systems replying on a decode and forward (DF) based relaying, where the available information at a BS and a relay station (RS) is asymmetric.

When we compare the system model seen in Fig. 2.3 to the linear MUT seen in Fig. 2.1, we can find that there are two new components here. At the transmitter, we have a new component which is used to perturb the information vector, in order to find its most appropriate perturbed version is the sense of the CF used. Its effect will be removed at the receiver by the modulo device, which is the other new component in Fig. 2.3. The combined effect of these two new components will be explained with the aid of Fig. 2.4 later in this section.

Our goal is now to find a simple way of modifying or perturbing the symbol vector by exploiting the knowledge of the CIRs in a conducive way, which allows us to minimize the detrimental impact of MUI at the receiver. More explicitly, the information symbol vector to be perturbed is given by

$$\mathbf{x} = [x_1, x_2, \cdots, x_K]^T, \tag{2.20}$$

where x_k denotes the transmitted symbol destined for the kth MS, and the symbol energy is given by

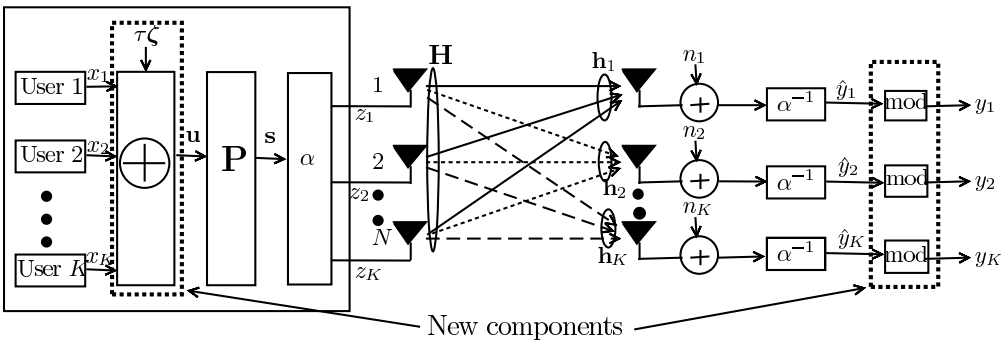

Figure 2.3: Schematic of the SDMA DL using ZF-VP (and/or MMSE-VP) at the BS. The system employs N transmit antennas to communicate with K decentralized non-cooperative MSs. It is worth noting that, when compared to the linear MUT schematic of Fig. 2.1, there are two new components. One of them is the perturbation component in the dashed-dot at the transmitter which perturbs the information vector, while the other is the modulo component in the dashed-dot at the receiver, which removes the effect of the perturbation imposed at the transmitter.

$E[|x_k|^2] = \sigma_x^2$, for $1 \leq k \leq K$, where x_k is an i.i.d. uniform random variable.

The perturbed symbol vector $\mathbf{u}$ having a dimension of K as can be seen in Fig. 2.3 is given by

$$\mathbf{u} = \mathbf{x} + \boldsymbol{\omega}, \tag{2.21}$$

so suppose $\mathbf{x} = [0.5 + j0.5]$ and $\boldsymbol{\omega} = [2 - j2]$, then we have $\mathbf{u} = \mathbf{x} + \boldsymbol{\omega} = [2.5 - j1.5]$. Here $\boldsymbol{\omega}$ is the perturbation vector found by using a certain criterion, such as the ZF criterion in [23], the MMSE criterion of [32], etc. The perturbation vector $\boldsymbol{\omega}$ may be chosen to be [23]

$$\boldsymbol{\omega} = \tau\boldsymbol{\zeta}, \tag{2.22}$$

where $\boldsymbol{\zeta}$ is a complex-valued vector, whose components are $a+jb$, with a and b being integers. For example, $\boldsymbol{\zeta} = [1 - j1]$, $\tau = 2$, then $\boldsymbol{\omega} = [2 - j2]$.

The $(K \times N)$-element channel matrix $\mathbf{H}$ is given by

$$\mathbf{H} = [\mathbf{h}_1, \mathbf{h}_2, \cdots, \mathbf{h}_K]^T, \tag{2.23}$$

where $\mathbf{h}_k$, $1 \leq k \leq K$ is the kth user's CIR, which is given by

$$\mathbf{h}_k = [h_{k,1}, h_{k,2}, \cdots, h_{k,N}], k = 1, 2, \cdots, K. \tag{2.24}$$

The CIR taps $h_{k,i}$, for $1 \leq k \leq K$ and $1 \leq i \leq N$ are independent of each other and obey the complex Gaussian distribution associated with $\mathrm{E}[|h_{k,i}|^2] = 1$.

The $(N \times K)$-element precoding matrix $\mathbf{P}$ is given by

$$\mathbf{P} = [\mathbf{p}_1, \mathbf{p}_2, \cdots, \mathbf{p}_K], \tag{2.25}$$

where $\mathbf{p}_k$, $1 \leq k \leq K$ represents the precoder coefficient vector derived for the kth user's data stream.

Given a total transmit power of $\mathrm{E_T}$ at the BS, an appropriate power scaling factor should be used after precoding in order to fulfill our transmit power constraint of having an identical transmit power to that of the classic case of dispensing with MUT.

At the receiver, the reciprocal of the scaling factor, namely α^{-1} is invoked, in order to compensate for the MUT's power scaling action at the receiver, so that unity-gain transmission is ensured.

The Gaussian noise vector $\mathbf{n}$ is given by

$$\mathbf{n} = [n_1, n_2, \cdots, n_K]^T, \tag{2.26}$$

where $n_k, 1 \leq k \leq K$ is a complex Gaussian random variable associated with a zero mean and $E[|n_k|^2] = 2\sigma_n^2 = \mathrm{N_o}$. Thus, the received signal vector before the modulo operation can be described as

$$\hat{\mathbf{y}} = \mathbf{HPu} + \alpha^{-1}\mathbf{n}. \tag{2.27}$$

The received signal vector $\mathbf{y} = [y_1\ y_2 \cdots y_K]^T$ after the modulo operation is given by

$$\mathbf{y} = mod_\tau(\hat{\mathbf{y}}), \tag{2.28}$$

and y_k, $1 \leq k \leq K$, constitutes sufficient statistics for the kth MS to detect the transmitted information symbol x_k.

The simple transmit-symbol perturbation of Equation (2.21) and the low-complexity nonlinear modulo operation invoked at the receiver side for eliminating the perturbation is capable of facilitating substantial performance gains. Explicitly, the effect of the perturbation vector of Equation (2.21) can be removed by the modulo operator employed at the receiver. To elaborate a little further, the modulo operator of Fig. 2.3 maps any element of the received signal vector into the fundamental Voronoi region of $\nu = \{a + ib | a, b \in [-\tau/2, \tau/2)\}$. Its operation can be described by [23]

$$\mathrm{mod}_\tau(\hat{\mathrm{y}}_\mathrm{k}) = \hat{\mathrm{y}}_\mathrm{k} - \lfloor \frac{\Re[\hat{\mathrm{y}}_\mathrm{k}] + \tau/2}{\tau} \rfloor \tau - \mathrm{j} \lfloor \frac{\Im[\hat{\mathrm{y}}_\mathrm{k}] + \tau/2}{\tau} \rfloor \tau, \tag{2.29}$$

where $\lfloor \bullet \rfloor$ denotes the largest integer less than or equal to its argument, and τ is a positive number determined as a function of the modulation constellation employed. This tehcnique was suggested by the authors of [23] based on their simulations to be chosen according to

$$\tau = 2(|c|_{max} + \Delta/2), \tag{2.30}$$

where $|c|_{max}$ is the absolute value of the original unperturbed modulated symbol having the largest magnitude and Δ is the spacing between the constellation points seen in Fig. 2.4.

Then, a certain degree of freedom is provided at the transmitter for minimizing the MUI at the MS's receiver by appropriately choosing any of the perturbed phasers representing the same original symbol in Fig. 2.4. More explicitly, a set of perturbed alternative symbols represent the same original 4-QAM data [32]. Therefore, the original 4-QAM constellation may be viewed as being periodically extended, as seen in Fig. 2.4.

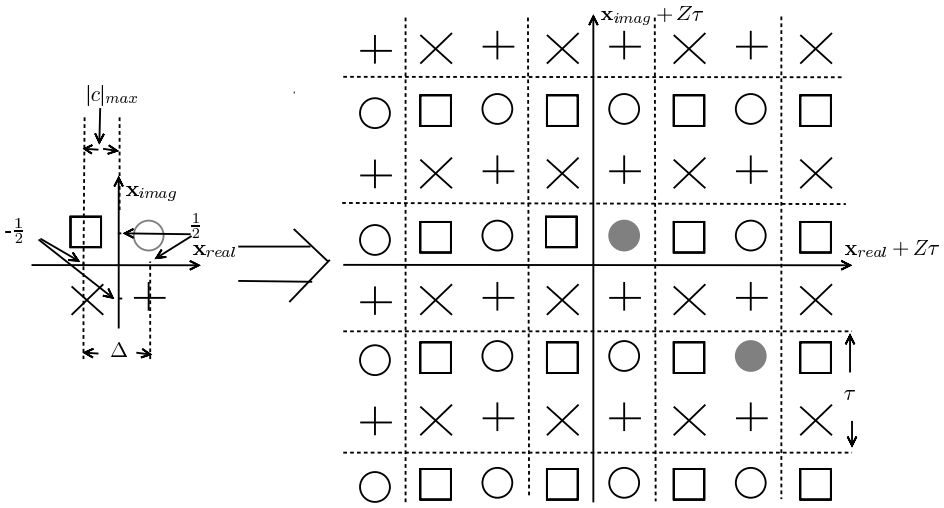

Figure 2.4: Standard 4-QAM constellation and the periodically extended 4-QAM constellation when using vector precoding. All symbols from the extended constellation associated with the same marker represent the same data [67]. The filled points of $0.5 + 0.5i$ and $2.5 - 1.5i$ are plotted in grey for illustration.

More specifically, consider the original 4-QAM scheme of Fig. 2.4 having the amplitude of $\{\pm 1/2\}^2$ for the complex-valued model. The values of $|c|_{max}$ and Δ are $|c|_{max} = \frac{1}{2}$ and $\Delta = 1$, respectively. Hence, according to Equation (2.30), we have $\tau = 2$.

Let us consider $\boldsymbol{\zeta} = [1 - i]$ when the original information symbol is $\mathbf{x} = [0.5 + 0.5i]$. Then, the discrete perturbation vector of Equation (2.22) becomes $\boldsymbol{\omega} = \tau\boldsymbol{\zeta} = [2 - 2i]$. Hence, the perturbed transmitted signal in Fig 2.4 becomes $\mathbf{u} = \mathbf{x} + \boldsymbol{\omega} = [2.5 - 1.5i]$.

Assuming that transmissions take place over an ideal channel, the received signal becomes $\hat{\mathbf{y}} = [2.5 - 1.5i]$. Then, taking the modulo function according to Equation (2.29) we have $\mathbf{y} = [0.5 + 0.5i]$, which is the same as the transmitted signal $\mathbf{x}$. This example demonstrated that the perturbed constellation points of $2.5 - 1.5i$ and $0.5 + 0.5i$ seen in Fig. 2.4 indeed represent the same data, when taking the modulo function of Equation (2.29) into account.

By contrast, if the transmission channel is not ideal, the contaminated received signal may become $\hat{\mathbf{y}} = [2.1 - 0.9i]$. Then, after the modulo operation of Equation (2.29), we have $\mathbf{y} = [0.1 - 0.9i]$. Hence, compared to the value of $\mathbf{x} = [0.5 + 0.5i]$, we can see that a quadrature-phase component error occurs. Hence the received signal is mapped into the wrong fundamental Voronoi region of $\nu = \{a + ib | a, b \in [-\tau/2, \tau/2)\}$ after the modulo operation.

2.1.2.2 Zero-Forcing Vector Precoding

The concept of ZF-VP was proposed in [23], where the authors observed that the problems imposed by inverting the channel's attenuation in a linear ZF-MUT when $N = K$ are due to the inverse of the normalization factor α^{-1}, which often becomes large owing to the large singular values in the inverse of the channel matrix $\mathbf{H}$. This may result in an amplified effective additive noise. The authors then found a way of overcoming this problem by 'perturbing' the data in a symbol-dependent way. More specifically, the intention is to form a perturbed vector of $\mathbf{u} = \mathbf{x} + \boldsymbol{\omega}$ from the information symbol vector $\mathbf{x}$, so that $\mathbf{z} = \mathbf{H}^{-1}\mathbf{u}$

has a norm, which is much smaller than the norm of $\mathbf{H}^{-1}\mathbf{x}$, while the entries of $\mathbf{u}$ can still be individually decoded at the receivers. As we have shown in Section 2.1.2.1, the degree of freedom in choosing $\mathbf{u} = \mathbf{x}+\boldsymbol{\omega}$ to convey the information symbols is provided by invoking the modulo operation seen in Fig. 2.4. Another interpretation of this method is to choose a perturbed vector of $\mathbf{u} = \mathbf{x} + \boldsymbol{\omega}$, which minimizes the required transmission power.

Hence, the cost function of ZF-VP may be formulated as [23]:

$$\boldsymbol{\omega}_{ZF} = \arg\min_{\boldsymbol{\omega}} \|\mathbf{H}^H(\mathbf{H}\mathbf{H}^H)^{-1}(\mathbf{x}+\boldsymbol{\omega})\|_2^2, \tag{2.31}$$

where $\boldsymbol{\omega} = \tau\boldsymbol{\zeta}$ and τ is a constant for a fixed modulation scheme. Hence the above equation may be re-written as [23]:

$$\boldsymbol{\zeta}_{ZF} = \arg\min_{\boldsymbol{\zeta}} \|\mathbf{H}^H(\mathbf{H}\mathbf{H}^H)^{-1}(\mathbf{x}+\tau\boldsymbol{\zeta})\|_2^2. \tag{2.32}$$

Interestingly, the authors of [32] demonstrated that the VP scheme proposed in [23] is actually a zero-forcing VP scheme. More explicitly, the authors of [32] considered the transmission of a block of N_B data symbols, during which the scaling factor α is kept constant. The received symbols are

$$\hat{\mathbf{y}} = \alpha^{-1}\mathbf{H}\mathbf{z} + \alpha^{-1}\mathbf{n}. \tag{2.33}$$

The transmit power constraint is then imposed by averaging over the block of N_B symbols as follows:

$$\frac{1}{N_B}\sum_{n=1}^{N_B} \| \mathbf{z} \|_2^2 \leq \mathrm{E_T}, \tag{2.34}$$

where we have

$$\mathbf{z} = \alpha\mathbf{P}\mathbf{u} = \alpha\mathbf{P}(\mathbf{x}+\boldsymbol{\omega}). \tag{2.35}$$

The error to be minimized at the receiver by appropriately selecting the MUT weights is defined as the difference between the desired virtual symbol $\mathbf{u}$ and the received symbol $\hat{\mathbf{y}}$ before the modulo operation of Fig. 2.4, when the interference is completely cancelled, i.e. when we have

$$\alpha^{-1}\mathbf{H}\mathbf{z} = \mathbf{u}. \tag{2.36}$$

Then, the MSE evaluated for a given data symbol block by averaging the symbol-based MSE over the entire N_B-symbol block is given by:

$$\begin{aligned} \varepsilon(\boldsymbol{\omega}, \mathbf{z}, \alpha^{-1}) &= \frac{1}{N_B}\sum_{n=1}^{N_B} E\left[\| \hat{\mathbf{y}} - \mathbf{u} \|_2^2 | \mathbf{x}\right] \\ &= \alpha^{-2} tr(\mathbf{R_n}). \end{aligned} \tag{2.37}$$

Hence, the optimization problem becomes

$$\{\boldsymbol{\omega}_{ZF}, \mathbf{z}_{ZF}, \alpha_{ZF}^{-1}\} = \arg\min_{\{\boldsymbol{\omega},\mathbf{z},\alpha^{-1}\}} \varepsilon(\boldsymbol{\omega}, \mathbf{z}, \alpha^{-1}); s.t. : \frac{1}{N_B}\sum_{n=1}^{N_B} \| \mathbf{z} \|_2^2 \leq \mathrm{E_T}. \tag{2.38}$$

Upon invoking the method of Lagrangian multipliers, the authors of [32] found the following solutions for $\mathbf{z}_{ZF}$ and α_{ZF}^{-1}:

$$\mathbf{z}_{ZF} = \alpha \mathbf{H}^H (\mathbf{H}\mathbf{H}^H)^{-1}\mathbf{u}, \tag{2.39}$$

and

$$\alpha_{ZF}^{-1} = \sqrt{\frac{\sum_{n=1}^{N_B} \mathbf{u}^H (\mathbf{H}\mathbf{H}^H)^{-1}\mathbf{u}}{N_B \mathrm{E_T}}}. \tag{2.40}$$

Thus, Equation (2.37) can be re-written as

$$\varepsilon(\boldsymbol{\omega}, \mathbf{z}, \alpha^{-1}) = \frac{tr(\mathbf{R_n})}{N_B \mathrm{E_T}} \sum_{n=1}^{N_B} \{(\mathbf{x}+\boldsymbol{\omega})^H (\mathbf{H}\mathbf{H}^H)^{-1}(\mathbf{x}+\boldsymbol{\omega})\}. \tag{2.41}$$

Therefore, the optimum perturbation vector should satisfy [32]:

$$\boldsymbol{\omega}_{ZF} = \arg\min_{\boldsymbol{\omega}} \|\mathbf{H}^H (\mathbf{H}\mathbf{H}^H)^{-1}(\mathbf{x}+\boldsymbol{\omega})\|_2^2, \tag{2.42}$$

which is identical to Equation (2.31). Hence the solution provided in [23] indeed, constitutes a ZF-VP.

Let us now return again to the example provided in Section 2.1.1.2. When the ZF-VP scheme is invoked, the precoding matrix is identical to that of ZF-MUT:

$$\mathbf{P} = \mathbf{H}^{-1} = \begin{bmatrix} -1.06 - j2.53 & 0.20 - j0.21 \\ -0.63 + j2.53 & -0.67 - j0.94 \end{bmatrix}$$

.

The perturbation vector $\boldsymbol{\omega}_{ZF}$ may be chosen to be $\boldsymbol{\omega}_{ZF} = [0 + j0, \quad -2 - j2]^T$.

Then, the scaling factor α can be calculated to be $\alpha = 0.47$. Therefore, the received signal may be expressed as:

$$\begin{aligned} \mathbf{y} &= mod_\tau\left[\alpha^{-1}\mathbf{H}\alpha\mathbf{P}(\mathbf{x}+\boldsymbol{\omega}_{ZF}) + \alpha^{-1}\mathbf{n}\right] \\ &= [-0.48 + j0.42, \;\; 0.14 - j0.09]^T. \end{aligned}$$

The resultant bits for the two users are then decoded by simply retaining the polarity of the signals, yielding $[0 \;\; 1]$ and $[1 \;\; 0]$, respectively. There is one error among the four transmitted bits.

2.1.2.3 MMSE Vector Precoding

The concept of MMSE vector precoding was proposed in [32]. In [32], the authors considered the transmission of a block of N_B data symbols, during which the scaling factor α was kept constant. The received symbols are

$$\hat{\mathbf{y}} = \alpha^{-1}\mathbf{H}\mathbf{z} + \alpha^{-1}\mathbf{n}. \tag{2.43}$$

The transmit power constraint was imposed by averaging over the block of N_B data symbols as follows:

$$\frac{1}{N_B}\sum_{n=1}^{N_B} \| \mathbf{z} \|_2^2 \leq \mathrm{E_T}, \tag{2.44}$$

where we have:

$$\mathbf{z} = \alpha \mathbf{P}\mathbf{u} = \alpha \mathbf{P}(\mathbf{x} + \boldsymbol{\omega}). \tag{2.45}$$

The error to be minimized at the receiver by appropriately selecting the MUT weights is defined as the difference between the desired virtual symbol $\mathbf{u} = \mathbf{x} + \boldsymbol{\omega}$ and the received symbol $\hat{\mathbf{y}}$ before the modulo operation. Then, the MSE evaluated for a given data symbol block by averaging the symbol MSE over the whole block becomes

$$\varepsilon(\boldsymbol{\omega}, \mathbf{z}, \alpha^{-1}) = \frac{1}{N_B} \sum_{n=1}^{N_B} E\left[\| \hat{\mathbf{y}} - \mathbf{u} \|_2^2 | \mathbf{x} \right]. \tag{2.46}$$

This can be further expanded to

$$\varepsilon(\boldsymbol{\omega}, \mathbf{z}, \alpha^{-1}) = \frac{1}{N_B} \sum_{n=1}^{N_B} (\mathbf{u}^H \mathbf{u} - 2\alpha^{-1} \Re(\mathbf{u}^H \mathbf{H}\mathbf{z}) + \alpha^{-2} \mathbf{z}^H \mathbf{H}^H \mathbf{H}\mathbf{z}) + \alpha^{-2} tr(\mathbf{R_n}). \tag{2.47}$$

Hence the MMSE VP optimization problem becomes

$$\{\boldsymbol{\omega}_{MMSE}, \mathbf{z}_{MMSE}, \alpha_{MMSE}^{-1}\} = \arg \min_{\{\boldsymbol{\omega}, \mathbf{z}, \alpha^{-1}\}} \varepsilon(\boldsymbol{\omega}, \mathbf{z}, \alpha^{-1}); s.t. : \frac{1}{N_B} \sum_{n=1}^{N_B} \| \mathbf{z} \|_2^2 \leq \mathrm{E_T}. \tag{2.48}$$

Our approach is then to find the joint optimum of $\{\boldsymbol{\omega}_{MMSE}, \mathbf{z}_{MMSE}, \alpha_{MMSE}^{-1}\}$ in two steps. Firstly, we assume that $\boldsymbol{\omega}$ are given and then minimize the MSE of Equation (2.46) over both $\mathbf{z}_{MMSE}$ and α^{-1}, by taking the transmit power constraint into account. This process would require the application of Lagrangian multipliers. It may be shown that these conditions lead to a unique solution [23]. Secondly, the MSE of Equation (2.46) is minimized by searching over the legitimate range of $\boldsymbol{\omega}$ under the assumption of a specific $\mathbf{z}$ and α^{-1}.

The corresponding Lagrangian function can be formulated as

$$L(\boldsymbol{\omega}, \mathbf{z}, \alpha^{-1}, \lambda) = \varepsilon(\boldsymbol{\omega}, \mathbf{z}, \alpha^{-1}) + \lambda(\frac{1}{N_B} \sum_{n=1}^{N_B} \mathbf{z}^H \mathbf{z} - \mathrm{E_T}), \tag{2.49}$$

where λ is the Lagrangian multiplier. When we set the derivatives of Equation (2.49) with respect to $\mathbf{z}$ and α^{-1} to zero, the following optimality conditions are obtained:

$$\frac{\partial L}{\partial \mathbf{z}} = \frac{1}{N_B}(-\alpha^{-1} \mathbf{H}^T \mathbf{u}^* + \alpha^{-2} \mathbf{H}^T \mathbf{H}^* \mathbf{z}^* + \lambda \mathbf{z}^*) = \mathbf{0}_N, \tag{2.50}$$

and

$$\frac{\partial L}{\partial \alpha^{-1}} = \frac{1}{N_B}(-2\Re(\mathbf{u}^H \mathbf{H}\mathbf{z}) + 2\alpha^{-1} \mathbf{z}^H \mathbf{H}^H \mathbf{H}\mathbf{z}) + 2\alpha^{-1}\beta = 0, \tag{2.51}$$

while the third optimality condition is that

$$\lambda(\frac{1}{N_B} \sum_{n=1}^{N_B} \mathbf{z}^H \mathbf{z} - \mathrm{E_T}) = 0. \tag{2.52}$$

Taking the transpose of Eq.(2.50) and multiplying it from the right with $\mathbf{z}N_B\alpha$, we then arrive at

$$-\mathbf{u}^H\mathbf{H}\mathbf{z} + \alpha^{-1}\mathbf{z}^H\mathbf{H}^H\mathbf{H}\mathbf{z} + \frac{\lambda}{\alpha^{-1}}\mathbf{z}^H\mathbf{z} = 0. \tag{2.53}$$

The Lagrangian multiplier may then be expressed from Equation (2.50) as follows:

$$\lambda = \alpha^{-2}\frac{tr(\mathbf{R_n})}{\frac{1}{N_B}\sum_{n=1}^{N_B}\mathbf{z}^H\mathbf{z}} = \alpha^{-2}\frac{tr(\mathbf{R_n})}{\mathrm{E_T}} = \alpha^{-2}\xi, \tag{2.54}$$

where $\xi = \frac{tr(\mathbf{R_n})}{\mathrm{E_T}}$.

Upon substituting Equation (2.54) into Equation (2.50) and Equation (2.51), we then arrive at:

$$\mathbf{z}_{MMSE} = \alpha\mathbf{H}^H(\mathbf{H}\mathbf{H}^H + \xi\mathbf{I}_c)^{-1}\mathbf{u}, \tag{2.55}$$

where $\mathbf{I}_c$ is the complex-valued identity matrix, and

$$\alpha_{MMSE}^{-1} = \sqrt{\frac{\sum_{n=1}^{N_B}\mathbf{u}^H\mathbf{H}\mathbf{H}^H(\mathbf{H}\mathbf{H}^H + \xi\mathbf{I}_c)^{-2}\mathbf{u}}{N_B\mathrm{E_T}}}. \tag{2.56}$$

The authors of [32] pointed out that regardless of what the best desired virtual symbol vectors $\mathbf{u} = \mathbf{x} + \boldsymbol{\omega}$ are, the optimum transmit symbols can be obtained by linearly filtering $\mathbf{u}$ with the aid of an appropriate MF, where only the scaling factor α_{MMSE}^{-1} depends on $\mathbf{u}$, but not the structure of the MF.

Assuming that the optimum gain factor and MUT vectors are obtained, the MSE function of Equation (2.46) can be simplified to

$$\begin{aligned}\varepsilon(\boldsymbol{\omega}, \mathbf{z}_{MMSE}, \alpha_{MMSE}^{-1}) &= \frac{1}{N_B}\sum_{n=1}^{N_B}(\mathbf{u}^H\mathbf{u} - \mathbf{u}^H\mathbf{H}\mathbf{H}^H(\mathbf{H}\mathbf{H}^H + \xi\mathbf{I}_c)^{-1}\mathbf{u}) \\ &= \frac{\xi}{N_B}\sum_{n=1}^{N_B}\mathbf{u}^H(\mathbf{H}\mathbf{H}^H + \xi\mathbf{I}_c)^{-1}\mathbf{u} \\ &= \frac{\xi}{N_B}\sum_{n=1}^{N_B}(\mathbf{x}+\boldsymbol{\omega})^H(\mathbf{H}\mathbf{H}^H + \xi\mathbf{I}_c)^{-1}(\mathbf{x}+\boldsymbol{\omega}).\end{aligned} \tag{2.57}$$

Upon introducing the notation of

$$\mathbf{L}^H\mathbf{L} = (\mathbf{H}\mathbf{H}^H + \xi\mathbf{I}_c)^{-1}, \tag{2.58}$$

where $\mathbf{L}$ can be obtained via Cholesky factorisation [39], the problem of finding the optimum MMSE $\boldsymbol{\omega}$ value can be written as

$$\boldsymbol{\omega}_{MMSE} = \arg\min_{\boldsymbol{\omega}} \|\mathbf{L}(\mathbf{x}+\boldsymbol{\omega})\|_2^2. \tag{2.59}$$

Again, when τ is given, the above equation may be re-written as:

$$\boldsymbol{\zeta}_{MMSE} = \arg\min_{\boldsymbol{\zeta}} \|\mathbf{L}(\mathbf{x}+\tau\boldsymbol{\zeta})\|_2^2. \tag{2.60}$$

The search for the optimal perturbation vector in both the ZF and MMSE vector precoding schemes finds the legitimate virtual transmit symbol, which is closest to the would-be received symbol, given the

CSI, as suggested in [23] and [32]. Instead of using the brute-force full-search based ML solution, the MUT-based counterpart of the SD may be invoked, which is referenced to as the so-called *sphere encoding* (SE) algorithm [23]. The conceptually appealing SE philosophy is that depending on the SINR experienced, virtual contellation points are tentatively tested within the SE's search radius in order to find the best virtual transmit symbol.

Let us continue the example provided in Section 2.1.1.2. When the MMSE-VP scheme is invoked, the precoding matrix can be computed from Equation (2.55):

$$\mathbf{P} = \mathbf{H}^H(\mathbf{H}\mathbf{H}^H + \xi\mathbf{I}_c)^{-1} = \begin{bmatrix} -0.48 - j1.21 & -0.13 - j0.22 \\ -0.24 + j1.09 & -0.39 - j0.66 \end{bmatrix}$$

.

The perturbation vector $\boldsymbol{\omega}_{MMSE}$ may be chosen to be $\boldsymbol{\omega}_{MMSE} = [0 + j0, \quad -2 + j0]^T$.

Then, the scaling factor α can be calculated to be $\alpha = 0.70$, therefore, the received signal can be expressed as:

$$\begin{aligned} \mathbf{y} &= mod_\tau\left[\alpha^{-1}\mathbf{H}\alpha\mathbf{P}(\mathbf{x} + \boldsymbol{\omega}_{MMSE}) + \alpha^{-1}\mathbf{n}\right] \\ &= [-0.26 + j0.37, \;\; 0.28 + j0.03]^T. \end{aligned}$$

The resultant bits for the two users are then decoded by simply retaining the polarity of the signals, yielding $[0 \;\; 1]$ and $[1 \;\; 1]$, respectively. There are now no errors amongst the four transmitted bits.

2.1.2.4 Simulation Results

In this section, the BER performances of several algorithms invoked in a (4×4)-element MIMO system employing QPSK modulation for communicating over an independent flat Rayleigh fading channel are examined in Fig. 2.5.

From Fig. 2.5, it is clear that the nonlinear ZF-VP is capable of achieving a substantial SNR gain over the linear ZF-MUT, especially at high SNRs. This shows the BER performance advantage of the nonlinear MUT schemes over the class of linear MUT schemes. Yet again, this performance gain is obtained at the expense of a significantly higher computational complexity. It can also be observed in Fig. 2.5 that the MMSE-VP algorithm outperforms the ZF-VP scheme at all SNRs by a margin of 2 $\mathbf{dB}$ SNR gain.

2.1.2.5 Contributions in Vector Precoding Design

VP was proposed in [23], and it has become a hot research topic since its conception. Selected contributions on vector precoding are summarized in Table 2.3 and Table 2.4. Detailed discussions on our novel contributions of this treatise can be found in Chapter 4 and Chapter 5.

Table 2.3: Selected contributions on vector precoding algorithms (Part 1)

Year	Author(s)	Contributions
2005	[23] Hochwald *et al.*	This pioneering contribution proposed VP, which was later termed as zero-forcing VP in [32].
2005	[32] Schmidt *et al.*	Proposed a new VP framework based on minimizing the MSE, which may be deemed to be the predominant MMSE VP scheme.
2006	[66] Kim *et al.*	Proposed another VP precoder design which minimize the total MSE.
2006	[68] Yuen and Hochwald	The statistical properties of the VP scheme were analyzed and guidelines for choosing its parameters in a systematic manner were provided. These properties suggest that a large perturbation-parameter is capable of improving the attainable performance at low SNRs. The benefit of these improvements is that the scheme operates approximately 1.5 dB closer to capacity than ZF-VP.
2006	[35] Callard *et al.*	Proposed an algorithm to minimize the MSE instead of the transmit power in VP, and improvements of about 2 dB were reported in a rapidly fading propagation scenario.
2006	[69] Habendorf *et al.*	Proposed to estimate the search radius in VP based on the statistics of the preceded symbols in order to reduce the number of legitimate transmit symbol combinations. The computational complexity was shown to be reduced.
2007	[70] Habendorf *et al.*	Designed suboptimum VP schemes having an upper bounded complexity.
2007	[4] Liu *et al.*	Proposed a lattice-reduction-aided (LRA) MMSE VP for multiple input multiple output (MIMO) systems.
2007	[71] Chua *et al.*	Proposed an algorithm, which was capable of finding a continuous-valued perturbation vector that minimizes the MSE of the received signal.
2008	[72] Ryan *et al.*	Provided a new lattice-theoretic approach for analyzing the performance of VP in the presence of Rayleigh fading.
2008	[73] Rico *et al.*	Proposed a rapidly-converging least-squares solution-seeker algorithm for finding the perturbation vector of VP, which reduced the computational complexity.

Table 2.4: Selected contributions on vector precoding algorithms (Part 2)

Year	Author(s)	Contributions
2008	[74] Muller *et al.*	Minimized the transmit energy by selecting the transmitted symbols from an increased alphabet for precoding, which preserved the minimum distance of the transmitted symbols. The average energy savings achieved for the transmission over random MIMO channels under the assumption of a large system were estimated. It was found that significant gains can be achieved.
2009	[75] Ryan *et al.*	Proposed both lattice-theoretic and rate-distortion based approaches for analyzing the performance of VP systems, taking into account the practical restrictions imposed by limited CIR feedback and pilot-based CIR-estimation training. Showed that the attainable performance was primarily determined by the ratio between the number of users and the number of transmit antennas.
2009	[76] Lu *et al.*	Studied the symbol error ratio (SER) performance of VP aided systems using quantized channel feedback.
2009	[77] Han *et al.*	Proposed an improved VP technique having a low complexity for the downlink of a MIMO system.
2009	[78] de Miguel *et al.*	Proposed different convex alphabet relaxation schemes for VP using binary, quaternary and octal modulation. An alternative channel inversion technique was proposed, which assited purely real-valued binary alphabets in performing similarly well to their complex-valued extensions, resulting in reduced optimization complexity.
2010	[79] Razi *et al.*	Derived expressions for the sum rate in terms of the average energy of the precoded vector, and used this to derive a closed-form upper bound for the high-SNR region. Proposed a modification of VP, where different transmission rates could be allocated to different users. Also proposed a low-complexity user selection algorithm that attempted to maximize the high-SNR sum- rate upper bound.
2010	[80] de Miguel *et al.*	Addressed the scenario of MUTs having less antennas than the number of users supported for the transmission over MIMO channels. while keeping the received signal free from interference with a certain probability.

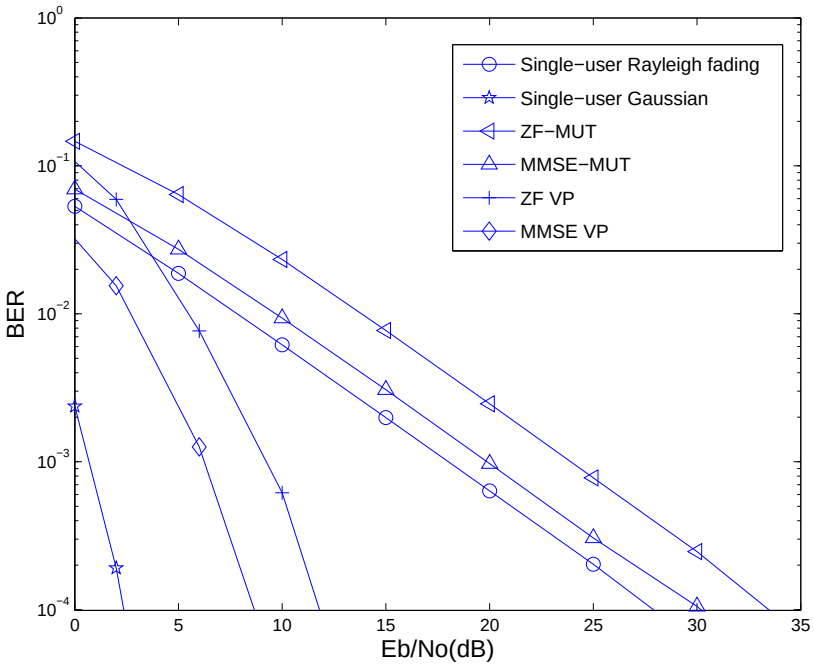

Figure 2.5: BER performances of the ZF-MUT, MMSE-MUT, ZF-VP and MMSE-VP. The scenario of a (4×4)-element MIMO system communicating over an independent flat Rayleigh fading channel is considered and a QPSK modulation scheme is employed. The single-user BER performances of transmitting over Gaussian and Rayleigh fading channels are also included.

2.2 Particle Swarm Optimization

Optimization plays an important role in our daily life, since many problems in our regular activities, social life, scientific, as well as in economic and engineering problems have parameters that can be tuned to produce a more desirable result. Given the fact that the complexity of the problems we attempt to solve has been increasing over the past few decades, there is a need for improved optimization algorithms. Hence, numerous optimization techniques have been proposed to solve the above-mentioned diverse problems, some of which drew their inspiration by mimicking processes found in nature. In this treatise, we invoke a relatively novel optimization technique, namely Particle Swarm Optimization (PSO).

PSO was originally proposed by Eberhart and Kennedy [29, 30] in the context of optimizing continuous nonlinear functions, and it was discovered through simulation of a bird flock trying to find food. To elaborate a little further, numerous scientists investigated various interpretations of the movement of organisms in a bird flock or fish school before Eberhart and Kennedy. Both Reynolds [85] and Heppner [85] studied the model of bird flocks based on their oberservation and understanding of large numbers of birds flying synchronously, often changing direction suddenly, then scattering and regrouping, etc. These models relied heavily on manipulation of the 'inter-individual' distances. The synchronous flocking behavior was thought to be a function of the birds' efforts to maintain an 'optimum' distance between themselves and their neighbors. However, as observed by Wilson [86] in fish schooling, any particle in the school should benefit from the discoveries and previous experience of all other members of the school during the search for food. More

Table 2.5: Selected contributions related to PSO in the research field of wireless communications.

Year	Author(s)	Contributions
2004	[17] Lu and Yan	Proposed a new binary PSO algorithm (BEPD) and applied it to solve multiuser detection problems in a CDMA system.
2005	[16] El-Mora *et al.*	Presented a novel MUD based on the PSO algorithm (MUDPSO).
2005	[15] Zhao and Zheng	Focused on the problem of MUD using the modified PSO algorithm for direct-sequence code-division multiple-access (DS-CDMA) systems with STBC.
2007	[13] Soo *et al.*	PSO was used to develop a suboptimal MUD strategy, where the decorrelating detector or linear minimum mean square error detector was used as the first stage to initialize the PSO-based MUD.
2008	[81] Liu and Li	Proposed a PSO-based MUD for receive-diversity aided STBC systems.
2008	[11] Xu	Advocated a near-optimal, reduced-complexity turbo multiuser receiver for space-time block-coded MC-CDMA uplink systems operating over frequency- selective fading environments based on the PSO algorithm.
2008	[82] Huang *et al.*	Presented an algorithm capable of efficient decoding of convolutional codes, which were based on PSO. The algorithm decided the number of decoding paths to be explored by appropriately adjusting the population size M in order to reduce the search complexity of the trellis-based decoding. Hence it was deemed beneficial for decoding high-constraint length convolutional codes.
2009	[83] Hei *et al.*	A new grouping strategy based on PSO was proposed for the multiuser MIMO downlink.
2009	[28] Yao *et al.*	PSO was invoked to solve the constrained nonlinear optimization problem for the MBER MUT.
2010	[84] Gao *et al.*	Proposed an algorithm based on an improved discrete PSO technique (I-DPSO) for the PAPR reduction of OFDM systems.

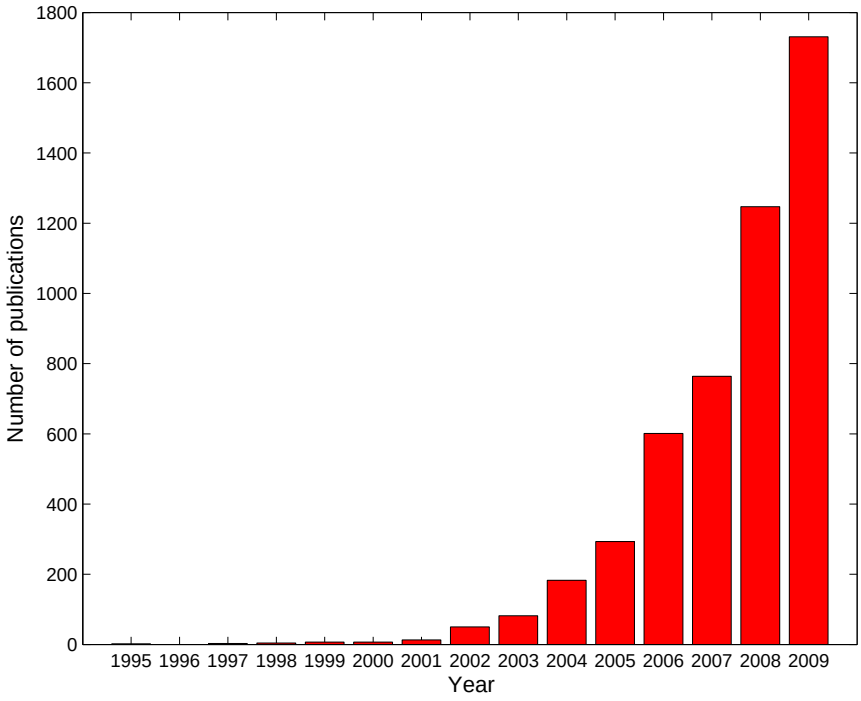

Figure 2.6: Number of publications related to PSO from 1995 to 2009. Results were obtained from IEEEXplore.

explicitly, the social sharing of the information among all the particles should be taken into account, which is the motivation of PSO.

In contrast to popular gradient-based optimization algorithms, such as for example the Conjugate Gradient (CG) algorithm [87] and the family of quasi-Newton algorithms [88, 89], but similarly to GAs [90], PSO also constitutes a stochastic algorithm, which does not require any gradient-related information. This provides PSO with an advantage in challenging applications, where there are numerous local optima, or where the gradient is either unavailable or computationally expensive to derive. Since its introduction, the popularity of PSO has been increasing, because it is easy to implement, it has the ability to rapidly converge and it is capable of 'steering clear' of local minima. Fig. 2.6 shows the number of publications related to PSO from 1995 to 2009, clearly indicating its increasing popularity. More specifically, in Table 2.5 we summarized some of the seminal contributions related to PSO in the research field of wireless communications. PSO was firstly invoked in wireless communications in 2004 [16, 17, 91]. Therefore, compared to other optimization techniques, PSO is still a relatively new tool, but its benefits in solving complex wireless communication optimization problems has already been clearly demonstrated. This also motivates the work proposed in this treatise, demonstrating that PSO is indeed an attractive optimization algorithm in the field of wireless communications.

Generally speaking, in a PSO aided system, a swarm of individuals, known as particles, 'fly' through the search space and try to find the best location quantified in terms of a given cost function (CF). PSO algorithms typically commence their operation with the random initialization of a population of individuals

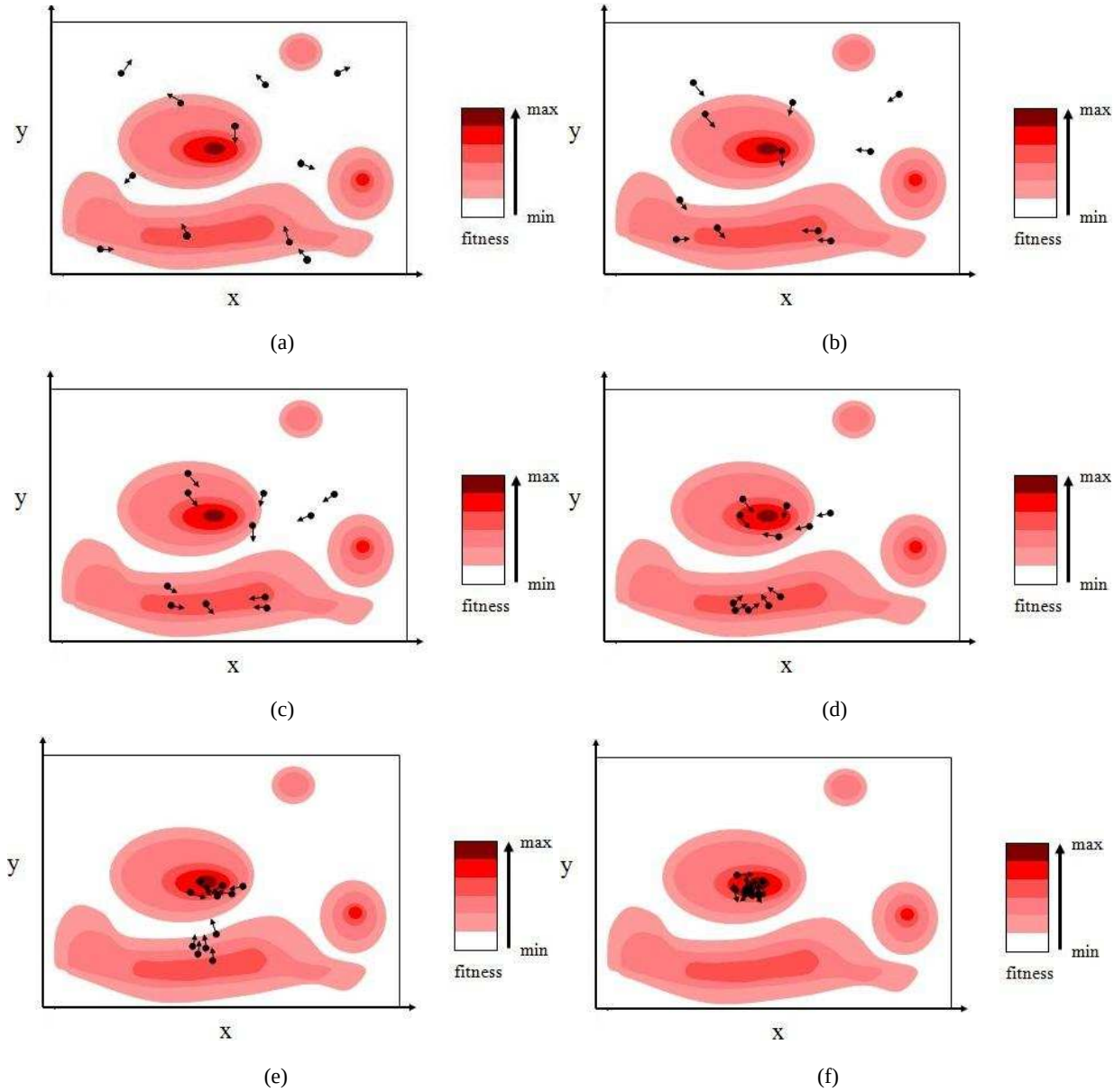

Figure 2.7: An example illustrating how PSO operates.

representing legitimate potential solutions. These may be based on random guesses to the problem's solutions, although often more meritorious suboptimum solutions are also available. Based on a previously defined social network structure, which determines the way each individual interacts with the rest of the particle swarm, each particle endeavours to find a globally optimal solution by gradually adjusting its flight trajectory towards its own best location (its own experience) and towards the best position of the entire swarm (the experience of the entire swarm of particles) at each evolutionary optimization step.

Fig. 2.7 shows a simple illustration of the way PSO works. As seen in Fig. 2.7, there are at least two sub-optimum solutions (local minima for instance) and one optimum solution which has the maximum 'fitness' value in the optimization problem in terms of having the best CF value. Again, at the beginning, several particles are randomly dropped in the search space, as seen in Fig. 2.7(a). Each particle will have its own initial search direction and speed or velocity. In the next evolutionary optimization step seen in

Fig. 2.7(b), every particle adjusts its search direction and velocity after exchanging information with other particles according to the communication structure of the swarm. Fig. 2.7(c) shows what happens in the next iteration. When we compare Fig. 2.7(c) to Fig. 2.7(a), it is quite clear that the particles start to exhibit a tendency to converge as some of them are moving towards the global optimum, while the rest are moving towards one of the local optimum. After further adjustments and search of each particle, we can see in Fig. 2.7(d) that the particles can be divided into two groups, which converge to different locations. More specifically, the particles in the first group converge towards the global optimum, while the particles in the other group converge to a local optimum. The optimization process does not stop here, however. In the next evolutionary optimization step observed in Fig. 2.7(e), the group of particles that converged to the local optimum starts to move towards the global optimum, after the particles exchanged their information, while the group of particles that already converged to the global optimum is wandering around the global optimum. This shows the ability of PSO to abandon a local optimum. Finally, every particle in the swarm converges to the global optimum, as shown in Fig. 2.7(f), and the optimization process is concluded here.

The employment of PSO is not limited to the solution of continuous-valued optimization problems. It can also be invoked in the field of solving discrete-valued optimization problems by using its discrete-valued version. Let us commence by highlighting the operation of continuous-valued PSOs, and then move to discrete-valued PSO.

2.2.1 Continuous-valued Particle Swarm Optimization

2.2.1.1 Contributions on Continuous-valued Particle Swarm Optimization

Continuous-valued PSO is the most popular form of PSO. Contributions on the development of continuous-valued PSO are summarized in Table 2.6, Table 2.7, Table 2.8 and Table 2.9. As we may observe in the example shown in Fig. 2.7, there are several parameters that control the behavior of the particles. Let us now commence our more detailed discourse by introducing the parameters of the PSO algorithm.

2.2.1.2 Parameters of Particle Swarm Optimization

Numerous parameters may be used in PSO, some of which are basic core parameters, while others may be used optionally to enhance the attainable performance of PSO.

- Basic parameters of PSO

    1. Population size S;

       Represents the total number of particles used in a single iteration of the PSO algorithm, which is typically kept constant. The population size might be interpreted as, for example, the number of birds flying in a specific formation before they change direction during their next synchronisation iteration. In the example seen in Fig. 2.7, there are eleven particles, so $S = 11$;
    2. Fitness value of a particle $\{F(\check{\mathbf{P}}_i^{(l)})\}_{i=1}^{S}$;

Table 2.6: Selected contributions on the development of continuous-valued PSO (Part 1).

Year	Author(s)	Contributions
1995	[29, 30] Eberhart and Kennedy	The original contributions which introduced PSO.
1997	[92] Kennedy	Introduced PSO and invoked it in the context of neural networks. PSO was shown to be capable of optimizing network weights.
1997	[93] Salerno	PSO was invoked for parsing natural language phrases.
1998	[94] Shi and Eberhart	The parameter referenced to as inertia weight was introduced into PSO. Simulations showed the beneficial impact of this parameter on the attainable performance of PSO.
1998	[95] He *et al.*	PSO was invoked to implement knowledge acquisition from input-output samples in a four-layer fuzzy neural network.
1999	[96] Shi and Eberhart	The performance of PSO was empirically studied in the context of four different benchmark functions in conjunction with asymmetric initial search range settings. Suggested to use an adaptive inertia weight for improving the achievable PSO performance in the vicinity of the optimum.
1999	[97] Clerc	Presented a low-complexity iterative PSO algorithm, which relied on a single equation and a social parameter.
2000	[98] Eberhart	The performance of particle swarm optimization using an inertia weight was compared to that of five benchmark functions.
2001	[99] Eberhart and Shi	Provided a review on the applications of PSO in engineering and computer science

It quantifies the fitness value of the ith particle at the lth iteration based on the related cost function. For a specific minimization problem, a particle position yielding a reduced cost function value is regarded as having a higher fitness;

3. $\{\mathbf{P}b_i^{(l)}\}_{i=1}^{S}$

   It identifies the best position that the ith particle has ever visited until the lth iteration, yielding the highest fitness value so far for this particle. More explicitly, it represents the best experience of the ith particle during the optimization process;

4. $\mathbf{G}b^{(l)}$

   It represents the best particle position that any of the particles has ever visited until the lth iteration, i.e. the position exhibiting the best CF value so far for all particles. It provides the 'social information', which is shared among all the particles in the swarm;

5. The velocity of a particle $\{\mathbf{V}_i^{(l)}\}_{i=1}^{S}$;

Table 2.7: Selected contributions on the development of continuous-valued PSO (Part 2)

Year	Author(s)	Contributions
2001	[100] Shi and Eberhart	Designed a fuzzy system for dynamically adapting the inertia weight of the PSO. The experimental results showed that the adaptive fuzzy PSO was a particularly promising optimization method for dynamic problems
2002	[101] Coello and Lechuga	Extended the heuristic PSO to deal with multi-objective optimization problems by using the concept of Pareto dominance to determine the most beneficial flight direction of a particle.
2002	[102] Krink *et al.*	Introduced an improvement in the PSO in order to overcome premature convergence to a local optimum in iterative optimization.
2003	[103] Janson and Middendorf	A hierarchical version of the PSO method (H-PSO) was introduced, where the particles are arranged in a dynamic hierarchy used for defining a neighborhood structure. Depending on the quality or fitness of their so far best value, the particles are encouraged to move in the most promising direction in the hierarchy to ensure that the highest-fitness particles have a higher influence on the entire swarm.
2003	[104] Stacey *et al.*	Proposed the improvement of mutations in PSO in order to speed up convergence and to escape from local minima.
2004	[105] Parsopoulos *et al.*	Presented an approach for effectively finding the global minimum with the aid of PSO.
2004	[106] van den Bergh *et al.*	Exploited the cooperative behavior of the particles, in order to significantly improve the attainable performance of the original PSO algorithm.
2004	[107] Ratnaweera *et al.*	Time-varying acceleration coefficients (TVAC) were introduced in addition to the time-varying inertia weighting factors in PSO. Based on TVAC, two different strategies were discussed in order to improve the performance of the PSO. Firstly, mutation-based PSO was combined with TVAC (MPSO-TVAC); secondly, the concept of ”self-organizing hierarchical particle swarm optimization” was combine with TVAC (HPSO-TVAC).

Table 2.8: Selected contributions on the development of continuous-valued PSO (Part 3)

Year	Author(s)	Contributions
2005	[108] Yang and Simon	Based on this proposal, each particle adjusted its position according to both its own previous worst solution and based on its group's previous worst solution to find the optimal particle position.
2005	[109] Breaban and Luchian	Transformed PSO into a self-adaptive algorithm based on specific swarm-inspired operators, which improved the PSO's efficiency, especially when applied to multimodal functions.
2005	[110] Hendtlass	This algorithm made each wave of particles partially independent, hence the algorithm advocated became suitable for problems having multiple local optima.
2006	[111] Yang *et al.*	Proposed a hybrid algorithm combining PSO and simulated annealing [112].
2006	[113] Maeda and Kuratani	Proposed two hybrid algorithms based on the PSO and the so-called simultaneous perturbation optimization method [114].
2006	[115] Pei *et al.*	Presented a hybrid PSO algorithm, which relied on some element of the simplex optimization algorithm designed for nonlinear bilevel programming.
2007	[116] Kang *et al.*	Defined so-called gravitation field model and proposed a new PSO algorithm based on this model.
2007	[117] Xie *et al.*	A hybrid evolutionary optimization algorithm based on the combination of PSO and GAs was presented to solve the biclustering problem [118].
2008	[119] Ho *et al.*	The Orthogonal PSO (OPSO) concept was proposed for solving otherwise intractable large parameter optimization problems.

It is the velocity of the moving particles, i.e. birds. At the lth iteration, the velocity of the ith particle is denoted by $\mathbf{V}_i^{(l)}$. It is updated from iteration-to-iteration, while at the initial stage, it is common to set $\{\mathbf{V}_i^{(0)}\}_{i=1}^{S} = 0$.

6. The position of a particle $\{\check{\mathbf{P}}_i^{(l)}\}_{i=1}^{S}$;

   It represents a candidate solution to the corresponding optimization problem. At the lth iteration, the position of the ith particle is denoted by $\check{\mathbf{P}}_i^{(l)}$, which is updated at every iteration.

7. The acceleration coefficients c_1, c_2;

   The acceleration coefficients represent the weighting of the stochastic acceleration terms in order to move the particle towards its best individual visted location $\{\mathbf{P}b_i^{(l)}\}_{i=1}^{S}$ and towards the best ever visited location of the entire swarm $\mathbf{G}b^{(l)}$. Low acceleration coefficients of c_1 and c_2 allow particles to roam far from their target regions before being slowly pulled back, whereas high

Table 2.9: Selected contributions on the development of continuous-valued PSO (Part 4)

Year	Author(s)	Contributions
2008	[120] Fang *et al.*	A novel formula was introduced for updating the particle velocity, allowing the majority of the particles to adjust their movements during the search process.
2008	[121] Chen *et al.*	Introduced the concept of cultural cooperative PSO based on a beneficial combination of the cooperative PSO and the cultural algorithm [122].
2009	[123] Wu *et al.*	Proposed to use PSO in solving multi-stage stochastic financial optimization problems.
2009	[124] Tang and Zhao	Presented a hybrid PSO by applying a novel adaptive mutation operator. Experimental results demonstrated the efficiency of the proposed algorithm.
2009	[125] Hao and Hu	Proposed an improved PSO algorithm which exhibited both global and local search capabilities. As part of the global search process, the algorithm also enhanced the local search capability by improving random perturbations on the local search.
2010	[126] Bai and Ding	Presented an improved PSO algorithm by using a novel learning strategy. Namely, each particle relies on its own experiences, such as its previous best individual position and previous swarm best position.
2010	[127] Liu *et al.*	Proposed to partition the swarm into a set of composite particles based on their similarity and demonstrated its efficiency in solving dynamic optimization problems.

values result in abrupt tugging movement toward or away from the target region. If $c_1 < c_2$ holds for the ith particle, then the movement of particle $\check{\mathbf{P}}_i$ will be directed more towards the best position found so far by the whole swarm, namely, towards $\mathbf{G}b$ rather than towards its own best position $\mathbf{P}b_i$, and vice versa for the case of $c_1 > c_2$.

- Control parameters of Particle Swarm Optimization

  1. Inertia weight $w^{(l)}$;

     It is used to control the impact of the velocity of previous iterations on the velocity of the current iteration. This parameter balances the global and local exploration capabilities of the particle and controls the smoothness of the exploration trajectory, of a single bird, when searching for food. For the initial stage of the search process, employing a large inertia weight is recommended in order to enhance the global exploration capability, whereas for later stages, the inertia weight is reduced for the sake of achieving an improved local exploration.

  2. Maximum velocity V_{max};

     The particle velocity is limited by the maximum velocity V_{max}, which determines the resolution of the search. The value of V_{max} is usually selected empirically.

3. Maximum value of legitimate particle positions P_{max};

   This parameter limits the search to the legitimate search space.

2.2.1.3 Search Process of Particle Swarm Optimisation

Let us consider a general complex-valued optimization problem, rather than a real-valued optimization problem, since the complex-valued one is more general. The optimum solution is the one, which minimizes the CF $F(\check{\mathbf{P}})$ formulated as:

$$\check{\mathbf{P}}_{opt} = \arg\min_{\check{\mathbf{P}}} F(\check{\mathbf{P}}); \quad s.t. : \check{\mathbf{P}} \in \mathsf{S}^{N\times K}, \tag{2.61}$$

where $\check{\mathbf{P}}$ is a $\mathsf{S} = (N \times K)$-element complex-valued particle-position matrix to be optimized, and

$$\mathsf{S} = [-P_{\max},\ P_{\max}] + j[-P_{\max},\ P_{\max}], \tag{2.62}$$

defines the search range for each element of the S-element particle-position matrix $\check{\mathbf{P}}$. The flow chart of the PSO algorithm is shown in Fig. 2.8. A swarm of particles $\{\check{\mathbf{P}}_i^{(l)}\}_{i=1}^{S}$ which represents the set of legitimate potential solutions is evolved across the entire search space $\mathsf{S}^{N\times K}$, where S is the swarm size and the index l denotes the iteration index. The search process of PSO proceeds as follows:

1) The swarm initialization. With $l = 0$, the initial particles, $\{\check{\mathbf{P}}_i^{(0)}\}_{i=1}^{S}$, are randomly generated in the search space $\mathsf{S}^{N\times K}$ as seen in block 1 of Fig. 2.8.

2) The swarm evaluation. Each particle position $\check{\mathbf{P}}_i^{(l)}$ has a fitness value $F(\check{\mathbf{P}}_i^{(l)})$ associated with it, which is evaluated in block 2 of Fig. 2.8 according to the cost function. Each particle at position $\check{\mathbf{P}}_i^{(l)}$ remembers its best position visited so far, denoted as $\mathbf{P}b_i^{(l)}$, which provides the so-called cognitive information. Every particle is also assumed to know the best position visited so far by the entire swarm, denoted as $\mathbf{G}b^{(l)}$, which resulted in the best CF value. This provides the so-called social information. The best particle and swarm position $\{\mathbf{P}b_i^{(l)}\}_{i=1}^{S}$ and $\mathbf{G}b^{(l)}$ are updated at each iteration as follows:

For ($i = 1$; $i \leq S$; i++)
  If ($F(\check{\mathbf{P}}_i^{(l)}) < F(\mathbf{P}b_i^{(l)})$) $\mathbf{P}b_i^{(l)} = \check{\mathbf{P}}_i^{(l)}$;
End for;
$i^* = \arg\min_{1\leq i\leq S} F(\mathbf{P}b_i^{(l)})$;
If ($F(\mathbf{P}b_{i^*}^{(l)}) < F(\mathbf{G}b^{(l)})$) $\mathbf{G}b^{(l)} = \mathbf{P}b_{i^*}^{(l)}$;

3) The swarm update. Each particle position $\check{\mathbf{P}}_i^{(l)}$ is associated with a velocity, denoted as $\mathbf{V}_i^{(l)}$, which determines its flight-speed. The velocity and position of the ith particle are updated in each iteration in block 3 of Fig. 2.8 according to [92]:

$$\begin{aligned}\mathbf{V}_i^{(l+1)} &= w^{(l)} \cdot \mathbf{V}_i^{(l)} + rand() \cdot c_1 \cdot [\mathbf{P}b_i^{(l)} - \check{\mathbf{P}}_i^{(l)}] \\ &\quad + rand() \cdot c_2 \cdot [\mathbf{G}b^{(l)} - \check{\mathbf{P}}_i^{(l)}], \qquad (2.63)\\ \check{\mathbf{P}}_i^{(l+1)} &= \check{\mathbf{P}}_i^{(l)} + \mathbf{V}_i^{(l+1)}, \qquad (2.64)\end{aligned}$$

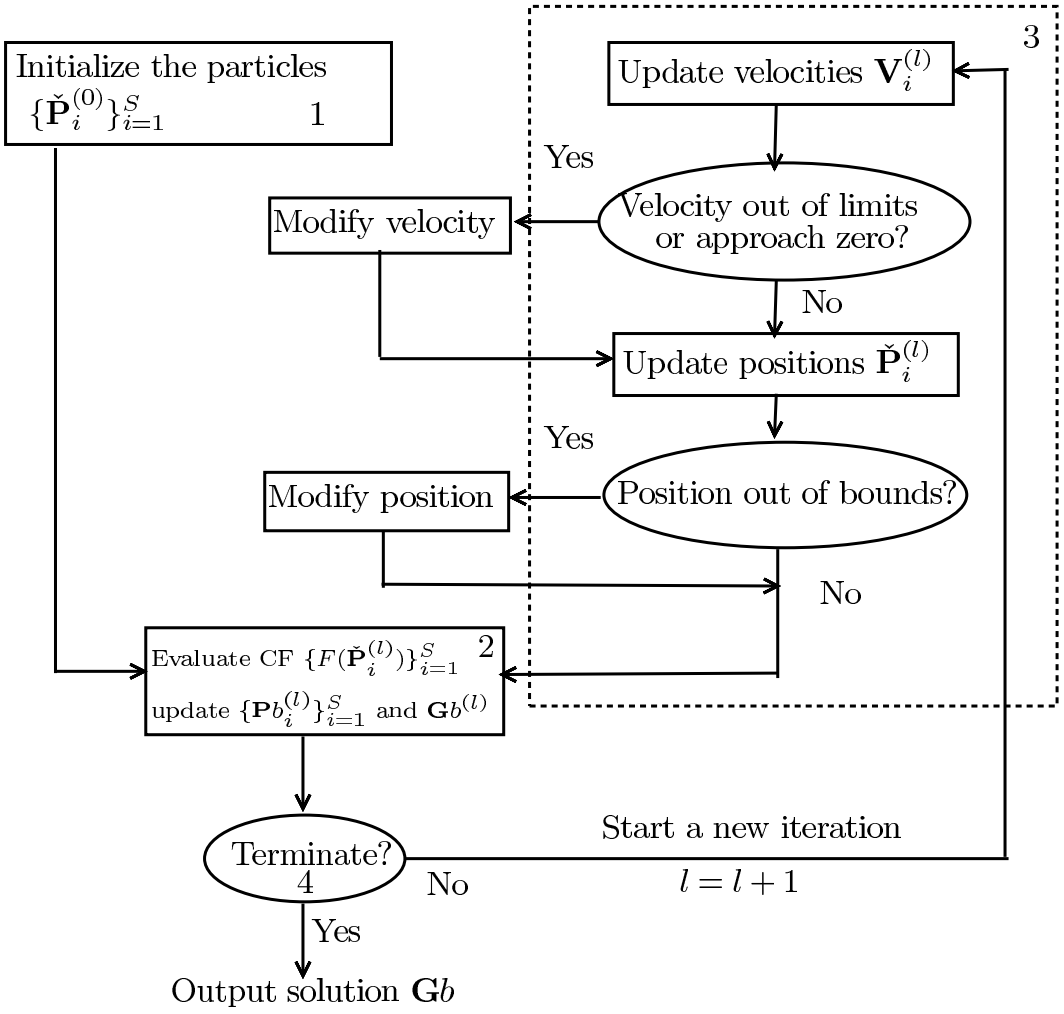

Figure 2.8: Flow chart of PSO algorithm

where $rand()$ denotes a uniform by distributed random number between 0 and 1. The physical interpretation of Equation 2.63 is that in its first term, we take into account the weighted velocity $\mathbf{V}_i^{(l)}$ of the lth iteration, which is then randomly adjusted by taking into account the particles' deviation $[\mathbf{P}b_i^{(l)} - \check{\mathbf{P}}_i^{(l)}]$ from its best ever position according to the 2nd term, after weighting it by the accelaration c_1. The third term is the dual pair of the 2nd one, where the deviation $[\mathbf{G}b^{(l)} - \check{\mathbf{P}}_i^{(l)}]$ from the overall best position is weighted by c_2. In order to avoid the excessive roaming of particles beyond the search space [128], a velocity range, $\mathsf{V} = [-V_{\max},\ V_{\max}] + j[-V_{\max},\ V_{\max}]$, is imposed on each element of $\mathbf{V}_i^{(l+1)}$ so that we have

$$
\begin{aligned}
&\text{If } (\Re[\mathbf{V}_i^{(l+1)}|_{p,q}] > V_{\max}) \quad \Re[\mathbf{V}_i^{(l+1)}|_{p,q}] = V_{\max};\\
&\text{If } (\Re[\mathbf{V}_i^{(l+1)}|_{p,q}] < -V_{\max}) \quad \Re[\mathbf{V}_i^{(l+1)}|_{p,q}] = -V_{\max};\\
&\text{If } (\Im[\mathbf{V}_i^{(l+1)}|_{p,q}] > V_{\max}) \quad \Im[\mathbf{V}_i^{(l+1)}|_{p,q}] = V_{\max};\\
&\text{If } (\Im[\mathbf{V}_i^{(l+1)}|_{p,q}] < -V_{\max}) \quad \Im[\mathbf{V}_i^{(l+1)}|_{p,q}] = -V_{\max}.
\end{aligned}
$$

Moreover, if the velocity approaches zero, it is reinitialised proportionally to $V_{\max}$ with the aid of a small scaling factor as follows: γ

$$\mathbf{V}_i^{(l+1)}|_{p,q} = \pm rand() \cdot \gamma \cdot (V_{\max} + jV_{\max}). \tag{2.65}$$

Similarly, each element of $\check{\mathbf{P}}_i^{(l+1)}$ is checked to ensure that it stays inside the search space S:

If $(\Re[\check{\mathbf{P}}_i^{(l+1)}|_{p,q}] > P_{\max})$
$\Re[\check{\mathbf{P}}_i^{(l+1)}|_{p,q}] = rand() \cdot P_{\max}$;
If $(\Re[\check{\mathbf{P}}_i^{(l+1)}|_{p,q}] < -P_{\max})$
$\Re[\check{\mathbf{P}}_i^{(l+1)}|_{p,q}] = -rand() \cdot P_{\max}$;
If $(\Im[\check{\mathbf{P}}_i^{(l+1)}|_{p,q}] > P_{\max})$
$\Im[\check{\mathbf{P}}_i^{(l+1)}|_{p,q}] = rand() \cdot P_{\max}$;
If $(\Im[\check{\mathbf{P}}_i^{(l+1)}|_{p,q}] < -P_{\max})$
$\Im[\check{\mathbf{P}}_i^{(l+1)}|_{p,q}] = -rand() \cdot P_{\max}$.

That is, if a particle is outside the search space, it is randomly moved back inside the search space, rather than forcing it to stay at the border. This is similar to the scheme proposed in [128].

4) Termination condition check. If the maximum number of iterations, $I_{\max}$, is reached, terminate the algorithm with the solution $\mathbf{G}b^{(I_{\max})}$; otherwise, set $l = l + 1$ and go to Step *2) of* Fig. 2.8.

2.2.1.4 Particle Update Examples

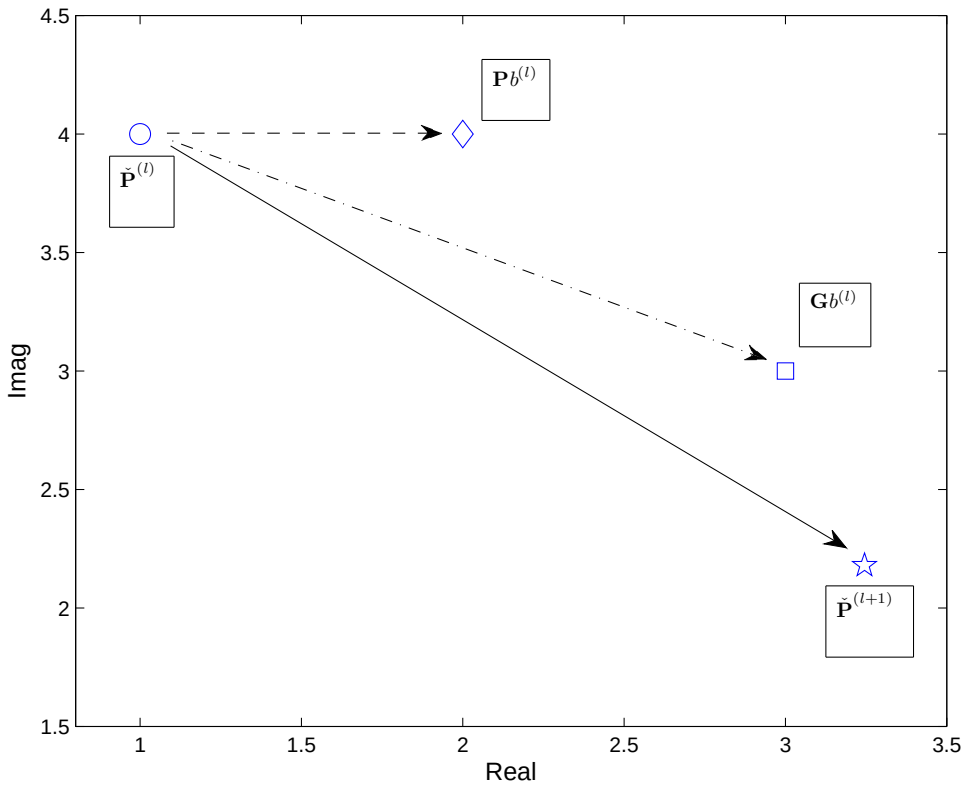

Figure 2.9: An example to show the particle update operation, which is based on block 3 of Fig. 2.8.

The core operations of PSO are based on Equation (2.63) for the particle velocity update and on Equation (2.64) for the particle position update. In Equation (2.63), the term $rand() \cdot c_1 \cdot [\mathbf{P}b_i^{(l)} - \check{\mathbf{P}}_i^{(l)}]$ is associated

with cognition, since it only takes into account the individual particle's own experiences. Hence, if the PSO algorithm is constructed in such way that it only makes use of the cognitive information, then we have $c_2 = 0$ and Equation (2.63) would be simplified to:

$$\mathbf{V}_i^{(l+1)} = w^{(l)} \cdot \mathbf{V}_i^{(l)} + rand() \cdot c_1 \cdot [\mathbf{P}b_i^{(l)} - \check{\mathbf{P}}_i^{(l)}]. \tag{2.66}$$

Moreover, the performance obtained by the simplified PSO model of Equation (2.66), which is based on the cognition-only model, is substantially improved by the model of Equation (2.63), because the latter exploits the interaction between different particles. More explicitly, the term $rand() \cdot c_2 \cdot [\mathbf{G}b^{(l)} - \check{\mathbf{P}}_i^{(l)}]$ in Equation (2.63) represents the social interaction amongst the particles.

It should be pointed out that in a complex-valued optimization problem, the velocity is also complex-valued, but the update of the real and imaginary parts of the velocity should be carried out seperately, since there should be no correlation between the real and imaginary parts. In the following, a simple example is used for demonstrating, how the particle update is implemented, as detailed in Fig. 2.9.

Let us now consider a complex-valued optimization problem. We assume that the position of a particle in Fig. 2.9 at the lth iteration is $\check{\mathbf{P}}^{(l)} = 1 + j4$ and that its best ever visited position is $\mathbf{P}b_i^{(l)} = 2 + j4$, while the best ever visited position of the entire swarm is $\mathbf{G}b^{(l)} = 3 + j3$. We firstly proceed to the velocity update operation of block 3 in Fig. 2.8, let $w^{(l)} = 0$. Then the impact of the previous velocity on the current one is minimized. Then Equation (2.63) is simplified to:

$$\mathbf{V}_i^{(l+1)} = rand() \cdot c_1 \cdot (\mathbf{P}b_i^{(l)} - \check{\mathbf{P}}_i^{(l)}) + rand() \cdot c_2 \cdot (\mathbf{G}b^{(l)} - \check{\mathbf{P}}_i^{(l)}). \tag{2.67}$$

Furthermore, let $c_1 = c_2 = 2$, the two variables returned by the function $rand()$ are randomly chosen to be $0.80 + j0.25$ and $0.91 + j0.43$ respectively. Then the value of the cognitive information part can be calculated as:

$$rand() \cdot c_1 \cdot [\mathbf{P}b_i^{(l)} - \check{\mathbf{P}}_i^{(l)}] = 0.51 + j0, \tag{2.68}$$

where again, the update of the real and imaginary parts is carried out seperately, while the value of the social information is calculated as:

$$rand() \cdot c_2 \cdot [\mathbf{G}b^{(l)} - \check{\mathbf{P}}_i^{(l)}] = 1.72 - j1.82. \tag{2.69}$$

Then the velocity for this specific particle is adjusted according to Equation (2.63) and block 3 of Fig. 2.8 as:

$$\begin{aligned} \mathbf{V}_i^{(l+1)} &= rand() \cdot c_1 \cdot [\mathbf{P}b_i^{(l)} - \check{\mathbf{P}}_i^{(l)}] + rand() \cdot c_2 \cdot [\mathbf{G}b^{(l)} - \check{\mathbf{P}}_i^{(l)}] \\ &= 2.24 - j1.82. \end{aligned} \tag{2.70}$$

Let us now proceed to the update of the particle's position in Fig. 2.9. According to Equation (2.64) and block 3 of Fig. 2.8, the new particle position can be calculated as:

$$\check{\mathbf{P}}_i^{(l+1)} = \check{\mathbf{P}}_i^{(l)} + \mathbf{V}_i^{(l+1)} = 3.24 + j2.17. \tag{2.71}$$

Table 2.10: Particle positions during the optimization process

Particles	1	2	3	4
Initialized positions	4.41	-2.31	2.45	4.09
Positions in iteration 1	2.41	-2.31	0.99	2.09
Positions in iteration 2	1.52	-0.31	0.99	1.67
Positions in iteration 3	-0.47	-0.31	0.76	0.54
Positions in iteration 4	-0.40	-0.31	-1.22	-0.17
Positions in iteration 5	-0.15	-0.25	0.01	-0.17
Positions in iteration 6	0.11	-0.02	0.01	-0.08
Positions in iteration 7	-0.04	0.05	0.01	0.03
Positions in iteration 8	0.02	-0.04	0.01	-0.00
Positions in iteration 9	0.01	-0.02	-0.00	-0.00
Positions in iteration 10	0.00	0.01	-0.00	-0.00
Personal best position	0.00	0.01	-0.00	-0.00

This particle's update during the lth iteration is then completed, as also seen in Fig. 2.9, where the distances covered by the particles are proportional to the velocity calculated in Equation (2.70).

After the review of the position and velocity update of a single particle, now a simple one-dimensional search problem is formulated, in order to show how the entire swarm of particles acts in unison, in order to find the global optimum.

As a rudimentary example, the minimization of the objective function $y = x^2$ is considered, where $S = 4$ particles are used, which are initialized randomly in the range of $[-5,\ 5]$, and V_{max} is set to 2, $c_1 = c_2 = 2$ and $w = 0$. The positions of the particles during the optimization process based on Fig. 2.8 are listed in Table 2.10.

It can be seen from Table 2.10 that the particles gradually improve their position in terms of finding the optimal point. We may notice that at early stages of the search, the velocities are typically large, hence the particles are wandering across a relatively large area attempting to find a better position associated with an improved CF. The positions of the four particles at initialization as well as at, the 3rd, 6th and 10th iteration are plotted in Fig. 2.10. It may be observed that the PSO algorithm rapidly converges to the optimal point.

2.2.2 Discrete-valued Particle Swarm Optimization

In the previous section, we imposed no constraint on the value of the particles. However, many real world optimization problems have to operate on discrete values, hence there is an increasing demand for developing algorithms regarding this type of optimization problems. The contributions on the development of discrete-valued PSO are summarized in Table 2.11.

Table 2.11: Selected contributions on the development of discrete-valued PSO

Year	Author(s)	Contributions
1997	[129] Kennedy and Eberhart	The discrete binary version of the particle swarm algorithm was proposed.
2004	[130] Pang *et al.*	A discrete PSO algorithm was derived for solving the travelling salesman problem.
2005	[131] Afshinmanesh *et al.*	A binary particle swarm optimization method based on the theory of immunity in biology was advocated.
2006	[132] Huang and Tung	Discrete PSO was combined with GA-style mutation to solve optimization problems.
2007	[133] Jafarpour *et al.*	Proposed a cellular learning automata [134] based discrete PSO.
2007	[135] Veeramachaneni *et al.*	Presented an effective, discrete, multi-valued PSO, which used probabilistic transition rules to move from one discrete value to another.
2008	[136] Li *et al.*	A discrete PSO based on quantum evolution concept [137] was introduced.
2008	[138] Xu *et al.*	Designed an improved discrete PSO based on cooperative swarms, which partition the search space into lower-dimensional subspaces in order to reduce the complexity.
2009	[139] Song *et al.*	Presented a multi-level, discrete-valued PSO algorithm and demonstrated its performance compared to genetic algorithm.
2010	[140] Chen *et al.*	Proposed a PSO algorithm featuring two beneficial characteristics. Firstly, the set-based representation scheme allow the PSO to characterize the discrete search space of combinatorial optimization problems. Secondly, the candidate solution and velocity were defined as a crisp set, and a set with possibilities, respectively.

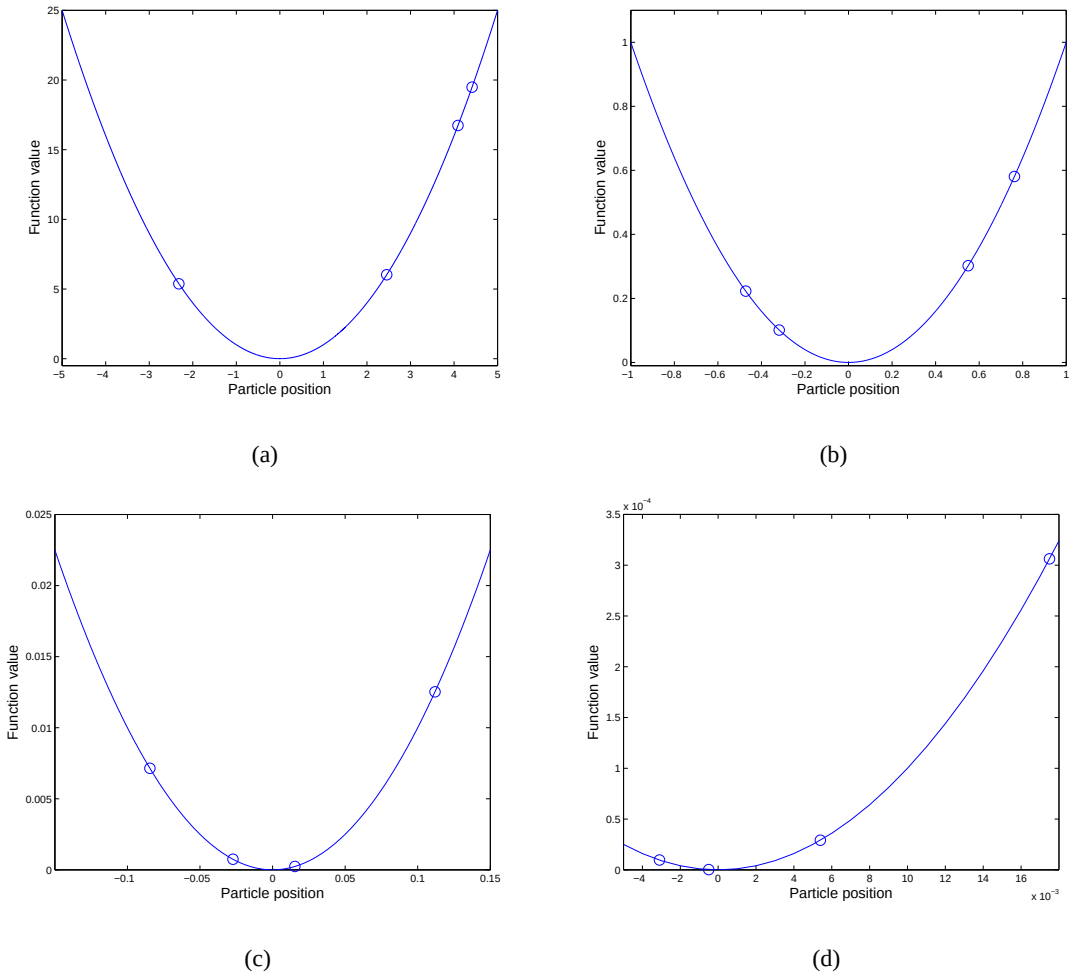

Figure 2.10: A PSO example minimizing the function $y = x^2$. (a): Initial particle positions. (b): Positions at 3rd itertion. (c): Positions at 6th itertion. (d): Positions at 10th itertion.

2.2.2.1 Binary Particle Swarm Optimization

PSO was firstly designed for solving nonlinear optimization problems, in order to find the optimum continuous value [30]. With the aim of extending its applications to discrete optimization problems, Kennedy proposed a discrete binary version of PSO [129], which may be invoked for example to find a K-bit BPSK vector in a MUD or MUT problem, as detailed later in this section. The velocity $\{\mathbf{V}_i^{(l)}\}_{i=1}^{S}$ of a particle may be updated according to the same equation as that used for continuous-valued PSO, namely Equation (2.63), which is repeated here for convenience [129]:

$$\begin{aligned}\mathbf{V}_i^{(l+1)} &= \mathbf{V}_i^{(l)} + rand() \cdot c_1 \cdot [\mathbf{P}b_i^{(l)} - \check{\mathbf{P}}_i^{(l)}] \\ &\quad + rand() \cdot c_2 \cdot [\mathbf{G}b^{(l)} - \check{\mathbf{P}}_i^{(l)}].\end{aligned}$$

The velocity is then transformed into a number within the range of $[0 \cdots 1]$, where the resultant normalized velocity is then used for updating the particle's position. This transformation may be carried out for

Table 2.12: The parameter values of the ith particle

$\check{\mathbf{P}}_i^{(l)}$	$\mathbf{V}_i^{(l)}$	c_1	rand()	c_2	rand()	$\mathbf{P}b_i^{(l)}$	$\mathbf{G}b^{(l)}$
1	0.67	2	0.54	2	0.97	1	0

example by using the sigmoid function given by [129]:

$$sig(\mathbf{V}_i^{(l+1)}) = \frac{1}{1+e^{-\mathbf{V}_i^{(l+1)}}}, \tag{2.72}$$

which is plotted in Fig. 2.11. Then, the particle's position update may be carried out according to [129]:

$$\check{\mathbf{P}}_i^{(l+1)} = \begin{cases} 0, & \text{if} \quad z \geq sig(\mathbf{V}_i^{(l+1)}), \\ 1, & \text{if} \quad z < sig(\mathbf{V}_i^{(l+1)}), \end{cases} \tag{2.73}$$

where z is a random uniformly distributed number assuming the binary values of $[0,\ 1]$.

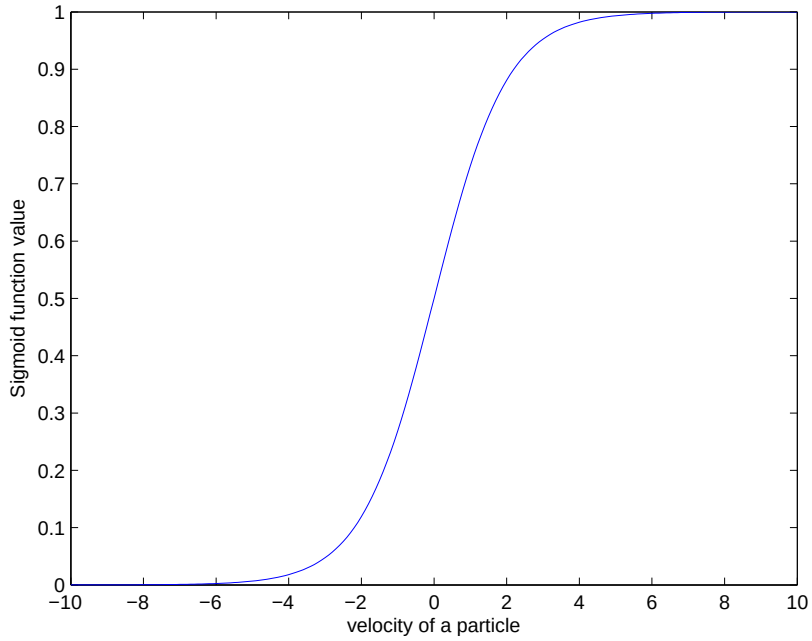

Figure 2.11: Sigmoid function value.

The decision regarding the position and velocity update of the particle at position $\check{\mathbf{P}}_i$ is now probabilistic, implying that the higher the value of the velocity $\mathbf{V}_i$, the higher the value of $sig(\mathbf{V}_i)$ becomes, albeit it still remains within the continuous range of $[0, \cdots 1]$. Hence the probability of opting for '1' for $\mathbf{s}_i|_q$ is increased. Again, the sigmoid function is plotted in Fig. 2.11. We may observe several properties of the sigmoid function from the figure, namely, that for $x \to \infty$, we have $sig(x) \to 1$; when $x = 0$, $sig(x) = \frac{1}{2}$; and for $x \to -\infty$, $sig(x) \to 0$.

Let us now consider an example, demonstrating the velocity and position update of the ith particle in a specific iteration. The parameter values considered are listed in Table 2.12.

According to Table 2.12, the new velocity can be calculated as:

$$\begin{aligned}\mathbf{V}_i^{(l+1)} &= \mathbf{V}_i^{(l)} + rand() \cdot c_1 \cdot [\mathbf{P}b_i^{(l)} - \check{\mathbf{P}}_i^{(l)}] + rand() \cdot c_2 \cdot [\mathbf{G}b^{(l)} - \check{\mathbf{P}}_i^{(l)}] \\ &= -1.27. \end{aligned} \tag{2.74}$$

Then we have

$$sig(\mathbf{V}_i^{(l+1)}) = \frac{1}{1 + e^{-\mathbf{V}_i^{(l+1)}}} = 0.2178. \tag{2.75}$$

Assuming that the uniformly distributed random number in Equation (2.73) is $z = 0.4529$, therefore, the new position for this particle becomes $\check{\mathbf{P}}_i^{(l+1)} = 0$.

The discrete binary PSO has been invoked for example for MUD [16, 17]. Next, a simple MIMO MUD example is considered in order to demonstrate the operation of the discrete binary PSO algorithm. Let us consider the transmission of a symbol vector $\mathbf{x} = [x_1 \;\; x_2 \;\; x_3 \;\; x_4 \;\; x_5]^T$ in a (5×5)-element MIMO system employing BPSK modulation communicating over an independent flat Rayleigh fading channel, where the received signal $\mathbf{y}$ can be expressed as $\mathbf{y} = \mathbf{H}\mathbf{x} + \mathbf{n}$. The related parameters are summarized in Table 2.13.

Note that in the step of calculating the particle's fitness in block 2 of Fig. 2.8 according to the ML fitness function based on the ML detection formula of:

$$F(\mathbf{x}) = \|\mathbf{y} - \mathbf{H}\mathbf{x}\|_2^2, \tag{2.76}$$

the positions of the particles have to be mapped to a BPSK symbol, namely, $0 \rightarrow -1$ and $1 \rightarrow 1$.

When the first iteration commences, we have:

1. For particle 1: According to block 3 of the flow-chart in Fig. 2.8,

   - For the 1st element, we have:
     The velocity is $\mathbf{V}_{(1,1)}^1 = \mathbf{V}_{(1,1)}^{(0)} + rand() \cdot c_1 \cdot [\mathbf{P}b_{(1,1)}^{(0)} - \check{\mathbf{P}}_{(1,1)}^{(0)}] + rand() \cdot c_2 \cdot [\mathbf{G}b^{(0)} - \check{\mathbf{P}}_{(1,1)}^{(0)}] = 0 + 2 \cdot 0.91 \cdot 0 + 2 \cdot 0.45 \cdot -1 = -0.91$. Then according to Equation (2.72), $sig(\mathbf{V}_{(1,1)}^1) = 0.82$, and assuming that the random number is $z = 0.90$, the new particle position becomes now $\check{\mathbf{P}}_{(1,1)}^{(1)} = 0$.
   - For the 2nd element:
     The velocity becomes $\mathbf{V}_{(1,2)}^1 = 0 + 2 \cdot 0.29 \cdot 0 + 2 \cdot 0.78 \cdot 1 = 1.56$. Then $sig(\mathbf{V}_{(1,2)}^1) = 0.2863$, the random number is $z = 0.05$, hence, the new position is now $\check{\mathbf{P}}_{(1,2)}^{(1)} = 1$.
   - For the 3rd element:
     The velocity is $\mathbf{V}_{(1,3)}^1 = 0 + 2 \cdot 0.21 \cdot 0 + 2 \cdot 0.77 \cdot 0 = 0$. Then $sig(\mathbf{V}_{(1,3)}^1) = 0.5$, the random number is $z = 0.6968$, hence the new position becomes now $\check{\mathbf{P}}_{(1,3)}^{(1)} = 0$.
   - For the 4th element:
     The velocity is $\mathbf{V}_{(1,4)}^1 = 0 + 2 \cdot 0.90 \cdot 0 + 2 \cdot 0.60 \cdot 0 = 0$. Then $sig(\mathbf{V}_{(1,4)}^1) = 0.5$, the random number is $z = 0.5446$, hence the new position is now $\check{\mathbf{P}}_{(1,4)}^{(1)} = 0$.

Table 2.13: The parameters of the $K = 5$-user MUD example

Related parameters	Value
SNR	$10\ \mathbf{dB}$
Symbol vector $\mathbf{x}$	$[1 \quad 1 \quad -1 \quad 1 \quad -1]^T$
Received signal $\mathbf{y}$	$\begin{bmatrix} -2.3794 - j1.5611 \\ -0.0936 + j0.4151 \\ 1.7978 + j1.3970 \\ 0.5584 + j0.5969 \\ 1.9298 + j0.9380 \end{bmatrix}$
Fitness funcion $F(\mathbf{x})$	$\|\mathbf{y} - \mathbf{H}\mathbf{x}\|_2^2$
c_1	2
c_2	2
Size of particle swarm S	4
Initial position for particle 1: $\check{\mathbf{P}}_1^{(0)}$	$[1 \quad 0 \quad 1 \quad 0 \quad 0]^T$
Initial fitness value for particle 1	7.83
Initial position for particle 2: $\check{\mathbf{P}}_2^{(0)}$	$[0 \quad 0 \quad 1 \quad 0 \quad 1]^T$
Initial fitness value for particle 2	9.09
Initial position for particle 3: $\check{\mathbf{P}}_3^{(0)}$	$[0 \quad 1 \quad 1 \quad 0 \quad 0]^T$
Initial fitness value for particle 3	6.25
Initial position for particle 4: $\check{\mathbf{P}}_4^{(0)}$	$[0 \quad 0 \quad 1 \quad 1 \quad 0]^T$
Initial fitness value for particle 4	6.69
Initial global best position: $\mathbf{G}b^{(0)}$	$[0 \quad 1 \quad 1 \quad 0 \quad 0]^T$
Initial fitness value for $\mathbf{G}b^{(0)}$	6.25
Maximum velocity $\|V_{max}\|$	6

- For the 5th element:
  The velocity is $\mathbf{V}_{(1,5)}^1 = 0 + 2 \cdot 0.75 \cdot 0 + 2 \cdot 0.87 \cdot 0 = 0$. Then $sig(\mathbf{V}_{(1,5)}^1) = 0.5$, the random number is $z = 0.8938$, hence the new position is now $\check{\mathbf{P}}_{(1,5)}^{(1)} = 0$.
  Therefore, the position for the 1st 5-bit particle at the 1st iteration is $\check{\mathbf{P}}_1^{(1)} = [0 \quad 1 \quad 0 \quad 0 \quad 0]^T$. The associated fitness function value calculated according to Equation (2.76) becomes then 5.71. Since this CF value is lower than the previous value of 7.83 in Table 2.13 for the 1st particle, the best visited position of this particle is updated from $[1 \quad 0 \quad 1 \quad 0 \quad 0]^T$ to $\mathbf{P}b_1^{(1)} = [0 \quad 1 \quad 0 \quad 0 \quad 0]^T$.

2. For particle 2: According to block 3 of the flow-chart in Fig. 2.8,

   - For the 1st element:
     The velocity is $\mathbf{V}_{(2,1)}^1 = \mathbf{V}_{(2,1)}^{(0)} + rand() \cdot c_1 \cdot [\mathbf{P}b_{(2,1)}^{(0)} - \check{\mathbf{P}}_{(2,1)}^{(0)}] + rand() \cdot c_2 \cdot [\mathbf{G}b^{(0)} - \check{\mathbf{P}}_{(2,1)}^{(0)}] = 0 + 2 \cdot 0.85 \cdot 0 + 2 \cdot 0.68 \cdot 0 = 0$. Then according to Equation (2.72), $sig(\mathbf{V}_{(2,1)}^1) = 0.5$, and assuming that the random number is $z = 0.40$, the new particle position becomes now $\check{\mathbf{P}}_{(2,1)}^{(1)} = 1$.

- For the 2nd element:
  The velocity becomes $\mathbf{V}^1_{(2,2)} = 0 + 2 \cdot 0.04 \cdot 0 + 2 \cdot 0.23 \cdot 1 = 0.47$. Then $sig(\mathbf{V}^1_{(2,2)}) = 0.61$, the random number is $z = 0.01$, hence the new position is now $\check{\mathbf{P}}^{(1)}_{(2,2)} = 1$.
- For the 3rd element:
  The velocity is $\mathbf{V}^1_{(2,3)} = 0 + 2 \cdot 0.38 \cdot 0 + 2 \cdot 0.90 \cdot 0 = 0$. Then $sig(\mathbf{V}^1_{(2,3)}) = 0.5$, the random number is $z = 0.30$, hence the new position becomes now $\check{\mathbf{P}}^{(1)}_{(2,3)} = 1$.
- For the 4th element:
  The velocity is $\mathbf{V}^1_{(2,4)} = 0 + 2 \cdot 0.86 \cdot 0 + 2 \cdot 0.14 \cdot 0 = 0$. Then $sig(\mathbf{V}^1_{(2,4)}) = 0.5$, the random number is $z = 0.30$, hence the new position is now $\check{\mathbf{P}}^{(1)}_{(2,4)} = 1$.
- For the 5th element:
  The velocity is $\mathbf{V}^1_{(2,5)} = 0 + 2 \cdot 0.41 \cdot 0 + 2 \cdot 0.21 \cdot -1 = -0.42$. Then $sig(\mathbf{V}^1_{(2,5)}) = 0.39$, the random number is $z = 0.76$, hence the new position is now $\check{\mathbf{P}}^{(1)}_{(2,5)} = 0$.

  Therefore, the position for the 2nd 5-bit particle at the 1st iteration is $\check{\mathbf{P}}^{(1)}_2 = [1 \quad 1 \quad 1 \quad 1 \quad 0]^T$. The associated fitness function value calculated according to Equation (2.76) becomes 3.59. Since this CF value is lower than the previous value of 9.09 in Table 2.13 for the 2nd particle, the best visited position of this particle is updated from $[0 \quad 0 \quad 1 \quad 0 \quad 1]^T$ to $\mathbf{P}b^{(1)}_2 = [1 \quad 1 \quad 1 \quad 1 \quad 0]^T$.

3. For particle 3: According to block 3 of the flow-chart in Fig. 2.8,

- For the 1st element:
  The velocity is $\mathbf{V}^1_{(3,1)} = \mathbf{V}^{(0)}_{(3,1)} + rand() \cdot c_1 \cdot [\mathbf{P}b^{(0)}_{(3,1)} - \check{\mathbf{P}}^{(0)}_{(3,1)}] + rand() \cdot c_2 \cdot [\mathbf{G}b^{(0)} - \check{\mathbf{P}}^{(0)}_{(3,1)}] = 0 + 2 \cdot 0.24 \cdot 0 + 2 \cdot 0.88 \cdot 0 = 0$. Then according to Equation (2.72), $sig(\mathbf{V}^1_{(3,1)}) = 0.5$, and assuming that the random number is $z = 0.29$, the new particle position is now $\check{\mathbf{P}}^{(1)}_{(3,1)} = 1$.
- For the 2nd element:
  The velocity is $\mathbf{V}^1_{(3,2)} = 0 + 2 \cdot 0.19 \cdot 0 + 2 \cdot 0.72 \cdot 0 = 0$. Then $sig(\mathbf{V}^1_{(3,2)}) = 0.5$, the random number is $z = 0.95$, hence the new position is now $\check{\mathbf{P}}^{(1)}_{(3,2)} = 0$.
- For the 3rd element:
  The velocity is $\mathbf{V}^1_{(3,3)} = 0 + 2 \cdot 0.90 \cdot 0 + 2 \cdot 0.70 \cdot 0 = 0$. Then $sig(\mathbf{V}^1_{(3,3)}) = 0.5$, the random number is $z = 0.81$, hence the new position is now $\check{\mathbf{P}}^{(1)}_{(3,3)} = 0$.
- For the 4th element:
  The velocity is $\mathbf{V}^1_{(3,4)} = 0 + 2 \cdot 0.86 \cdot 0 + 2 \cdot 0.88 \cdot 0 = 0$. Then $sig(\mathbf{V}^1_{(3,4)}) = 0.5$, the random number is $z = 0.23$, hence the new position is now $\check{\mathbf{P}}^{(1)}_{(3,4)} = 1$.
- For the 5th element:
  The velocity is $\mathbf{V}^1_{(3,5)} = 0 + 2 \cdot 0.62 \cdot 0 + 2 \cdot 0.24 \cdot 0 = 0$. Then $sig(\mathbf{V}^1_{(3,5)}) = 0.5$, the random number is $z = 0.44$, hence the new position is now $\check{\mathbf{P}}^{(1)}_{(3,5)} = 1$.

  Therefore, the position for the 3rd 5-bit particle at the 1st iteration is $\check{\mathbf{P}}^{(1)}_3 = [1 \quad 0 \quad 0 \quad 1 \quad 1]^T$. The associated fitness function value calculated according to Equation (2.76) becomes 6.33. Since this CF value is higher than the previous value of 6.25 in Table 2.13 for the 3rd particle, the best visited position is still $\mathbf{P}b^{(1)}_3 = [0 \quad 1 \quad 1 \quad 0 \quad 0]^T$.

4. For particle 4: According to block 3 of the flow-chart in Fig. 2.8,

   - For the 1st element:
     The velocity is $\mathbf{V}^1_{(4,1)} = \mathbf{V}^{(0)}_{(4,1)} + rand() \cdot c_1 \cdot [\mathbf{P}b^{(0)}_{(4,1)} - \check{\mathbf{P}}^{(0)}_{(4,1)}] + rand() \cdot c_2 \cdot [\mathbf{G}b^{(0)} - \check{\mathbf{P}}^{(0)}_{(4,1)}] = 0 + 2 \cdot 0.78 \cdot 0 + 2 \cdot 0.71 \cdot 0 = 0$. Then according to Equation (2.72), $sig(\mathbf{V}^1_{(4,1)}) = 0.5$, and assuming that the random number is $z = 0.24$, the new particle position is now $\check{\mathbf{P}}^{(1)}_{(4,1)} = 1$.
   - For the 2nd element:
     The velocity is $\mathbf{V}^1_{(4,2)} = 0 + 2 \cdot 0.73 \cdot 0 + 2 \cdot 0.90 \cdot 1 = 1.81$. Then $sig(\mathbf{V}^1_{(4,2)}) = 0.86$, the random number is $z = 0.84$, hence the new position is now $\check{\mathbf{P}}^{(1)}_{(4,2)} = 1$.
   - For the 3rd element:
     The velocity is $\mathbf{V}^1_{(4,3)} = 0 + 2 \cdot 0.97 \cdot 0 + 2 \cdot 0.14 \cdot 0 = 0$. Then $sig(\mathbf{V}^1_{(4,3)}) = 0.5$, the random number is $z = 0.85$, hence the new position is now $\check{\mathbf{P}}^{(1)}_{(4,3)} = 0$.
   - For the 4th element:
     The velocity is $\mathbf{V}^1_{(4,4)} = 0 + 2 \cdot 0.76 \cdot 0 + 2 \cdot 0.76 \cdot -1 = -1.52$. Then $sig(\mathbf{V}^1_{(4,4)}) = 0.17$, the random number is $z = 0.4594$, hence the new position is now $\check{\mathbf{P}}^{(1)}_{(4,4)} = 0$.
   - For the 5th element:
     The velocity is $\mathbf{V}^1_{(4,5)} = 0 + 2 \cdot 0.38 \cdot 0 + 2 \cdot 0.10 \cdot 0 = 0$. Then $sig(\mathbf{V}^1_{(4,5)}) = 0.39$, the random number is $z = 0.12$, hence, the new position is now $\check{\mathbf{P}}^{(1)}_{(4,5)} = 1$.
     Therefore, the position for the 4th 5-bit particle at the 1st iteration is $\check{\mathbf{P}}^{(1)}_4 = [1 \quad 1 \quad 0 \quad 0 \quad 1]^T$. The associated fitness function value calculated according to Equation (2.76) becomes 5.28. Since this CF value is lower than the previous value of 6.69 in Table 2.13 for the 4th particle, the best visited particle position is updated from $[0 \quad 0 \quad 1 \quad 1 \quad 0]^T$ to $\mathbf{P}b^{(1)}_4 = [1 \quad 1 \quad 0 \quad 0 \quad 1]^T$.

5. Update of $\mathbf{G}b^{(1)}$
   Since now the best ever visited position is $\mathbf{P}b^{(1)}_2 = [1 \quad 1 \quad 1 \quad 1 \quad 0]^T$, which is associated with a fitness value of 3.59 and hence it is lower than that of $\mathbf{G}b^{(0)}$ given by 6.25 in Table 2.13. Therefore, the global best ever visited position after the 1st iteration is updated to $\mathbf{G}b^{(1)} = [1 \quad 1 \quad 1 \quad 1 \quad 0]^T$.

Then the algorithm proceeds to its 2nd iteration:

1. For particle 1:
   The position for the 1st 5-bit particle at the 2nd iteration is found to be $\check{\mathbf{P}}^{(2)}_1 = [1 \quad 1 \quad 1 \quad 0 \quad 0]^T$. The associated fitness function value calculated according to Equation (2.76) becomes 5.82. Since this CF value is higher than the previous value of 5.71 for the 1st particle, the best visited position is still $\mathbf{P}b^{(2)}_1 = [0 \quad 1 \quad 0 \quad 0 \quad 0]^T$.

2. For particle 2:
   The position for the 2nd 5-bit particle at the 2nd iteration is found to be $\check{\mathbf{P}}^{(2)}_2 = [0 \quad 1 \quad 1 \quad 0 \quad 0]^T$. The associated fitness function value calculated according to Equation (2.76) becomes 6.25. Since this CF value is higher than the previous value of 3.59 for the 2nd particle, the best visited position is still $\mathbf{P}b^{(2)}_2 = [1 \quad 1 \quad 1 \quad 1 \quad 0]^T$.

3. For particle 3:
   The position for the 3rd 5-bit particle at the 2nd iteration is found to be $\check{\mathbf{P}}_3^{(2)} = [0 \quad 1 \quad 0 \quad 0 \quad 1]^T$. The associated fitness function value calculated according to Equation (2.76) becomes 7.65. Since this CF value is higher than the previous value of 6.25 for the 3rd particle, the best visited position is still $\mathbf{P}b_3^{(2)} = [0 \quad 1 \quad 1 \quad 0 \quad 0]^T$.

4. For particle 4:
   The position for the 4th 5-bit particle at the 2nd iteration is found to be $\check{\mathbf{P}}_4^{(2)} = [1 \quad 0 \quad 0 \quad 0 \quad 0]^T$. The associated fitness function value calculated according to Equation (2.76) becomes 5.15. Since this CF value is lower than the previous value of 5.28 for the 4th particle, the best visited position is updated to $\mathbf{P}b_4^{(2)} = [1 \quad 0 \quad 0 \quad 0 \quad 0]^T$.

5. Update of $\mathbf{G}b^{(2)}$
   Since now the best ever visited position is still $\mathbf{P}b_2^{(2)} = [1 \quad 1 \quad 1 \quad 1 \quad 0]^T$, which is associated with a fitness value of 3.59 which is equal to that of $\mathbf{G}b^{(1)}$, therefore, the global best ever visited position after 2nd iteration stays the same, which is $\mathbf{G}b^{(2)} = [1 \quad 1 \quad 1 \quad 1 \quad 0]^T$.

The algorithm then proceeds to its 3rd iteration:

1. For particle 1:
   The position for the 1st 5-bit particle at the 3rd iteration is found to be $\check{\mathbf{P}}_1^{(3)} = [0 \quad 1 \quad 0 \quad 1 \quad 1]^T$. The associated fitness function value calculated according to Equation (2.76) becomes 7.91. Since this CF value is higher than the previous value of 5.71 for the 1st particle, the best visited position is still $\mathbf{P}b_1^{(3)} = [0 \quad 1 \quad 0 \quad 0 \quad 0]^T$.

2. For particle 2:
   The position for the 2nd 5-bit particle at the 3rd iteration is found to be $\check{\mathbf{P}}_2^{(3)} = [1 \quad 1 \quad 1 \quad 1 \quad 0]^T$.This is its best visited position, so $\mathbf{P}b_2^{(3)} = [1 \quad 1 \quad 1 \quad 1 \quad 0]^T$.

3. For particle 3:
   The position for the 3rd 5-bit particle at the 3rd iteration is found to be $\check{\mathbf{P}}_3^{(3)} = [0 \quad 1 \quad 1 \quad 1 \quad 0]^T$. The associated fitness function value calculated according to Equation (2.76) becomes 5.49. Since this CF value is lower than the previous value of 6.25 for the 3rd particle, the best visited position is updated from $[0 \quad 1 \quad 1 \quad 0 \quad 0]^T$ to $\mathbf{P}b_3^{(3)} = [0 \quad 1 \quad 1 \quad 1 \quad 0]^T$.

4. For particle 4:
   The position for the 4th 5-bit particle at the 3rd iteration is found to be $\check{\mathbf{P}}_4^{(3)} = [1 \quad 1 \quad 1 \quad 1 \quad 1]^T$. The associated fitness function value calculated according to Equation (2.76) becomes 6.02. Since this CF value is higher than the previous value of 5.15 for the 4th particle, the best visited position is still $\mathbf{P}b_4^{(3)} = [1 \quad 0 \quad 0 \quad 0 \quad 0]^T$.

5. Update of $\mathbf{G}b^{(3)}$
   Since now the best ever visited position is still $\mathbf{P}b_2^{(3)} = [1 \quad 1 \quad 1 \quad 1 \quad 0]^T$, which is associated with

a fitness value of 3.59 which is equal to that of $\mathbf{G}b^{(2)}$, therefore, the global best ever visited position after 3rd iteration stays the same, which is $\mathbf{G}b^{(3)} = [1 \quad 1 \quad 1 \quad 1 \quad 0]^T$.

The algorithm then proceeds to its 4th iteration:

1. For particle 1:
   The position for the 1st 5-bit particle at the 4th iteration is found to be $\check{\mathbf{P}}_1^{(4)} = [0 \quad 0 \quad 1 \quad 1 \quad 0]^T$. The associated fitness function value calculated according to Equation (2.76) becomes 6.69. Since this CF value is higher than the previous value of 5.71 for the 1st particle, the best visited position is still $\mathbf{P}b_1^{(4)} = [0 \quad 1 \quad 0 \quad 0 \quad 0]^T$.

2. For particle 2:
   The position for the 2nd 5-bit particle at the 4th iteration is found to be $\check{\mathbf{P}}_2^{(4)} = [1 \quad 1 \quad 0 \quad 1 \quad 0]^T$. The associated fitness function value calculated according to Equation (2.76) becomes 0.54. Since this CF value is lower than the previous value of 3.59 for the 2nd particle, the best visited position is updated from $[1 \quad 1 \quad 1 \quad 1 \quad 0]^T$ to $\mathbf{P}b_2^{(4)} = [1 \quad 1 \quad 0 \quad 1 \quad 0]^T$.

3. For particle 3:
   The position for the 3rd 5-bit particle at the 4th iteration is found to be $\check{\mathbf{P}}_3^{(4)} = [1 \quad 1 \quad 1 \quad 1 \quad 0]^T$. The associated fitness function value calculated according to Equation (2.76) becomes 3.59. Since this CF value is lower than the previous value of 5.49 for the 3rd particle, the best visited position is updated from $[0 \quad 1 \quad 1 \quad 1 \quad 0]^T$ to $\mathbf{P}b_3^{(4)} = [1 \quad 1 \quad 1 \quad 1 \quad 0]^T$.

4. For particle 4:
   The position for the 4th 5-bit particle at the 4th iteration is found to be $\check{\mathbf{P}}_4^{(4)} = [1 \quad 1 \quad 1 \quad 0 \quad 0]^T$. The associated fitness function value calculated according to Equation (2.76) becomes 5.82. Since this CF value is higher than the previous value of 5.15 for the 4th particle, the best visited position is still $\mathbf{P}b_4^{(4)} = [1 \quad 0 \quad 0 \quad 0 \quad 0]^T$.

5. Update of $\mathbf{G}b^{(4)}$
   Since now the best ever visited position becomes $\mathbf{P}b_2^{(4)} = [1 \quad 1 \quad 0 \quad 1 \quad 0]^T$, which is associated with a fitness value of 0.54 and hence it is lower than the value of $\mathbf{G}b^{(3)}$. Therefore, the global best ever visited position after the 4th iteration is updated to $\mathbf{G}b^{(4)} = [1 \quad 1 \quad 0 \quad 1 \quad 0]^T$. We may also notice that the solution is the ML solution, hence the optimum position (solution) has been found in the 4th iteration.

The above example shows how the discrete binary PSO algorithm operates and the entire update process is summarized in Table 2.14. Let us now consider some other aspects of this algorithm. In the above example, it took the algorithm of Fig. 2.8 $I = 4$ iterations to find the ML solution. However, since PSO constitutes a stochastic optimization algorithm, the number of iterations it needs to find the optimum solution may vary in each single simulation. Hence, a histogram showing the number of iterations the discrete binary PSO algorithm required to find the ML solution may help us to arrive at a better understanding of the capabilities of this algorithm, which can be seen in Fig. 2.12. The parameter values are the same as in Table 2.13.

Table 2.14: Particles update process

	1st particle $\check{\mathbf{P}}_1$	2nd particle $\check{\mathbf{P}}_2$
Initial position (fitness)	$\mathbf{P}b_1^{(0)} = [1\,0\,1\,0\,0]^T$ (7.83)	$\mathbf{P}b_2^{(0)} = [0\,0\,1\,0\,1]^T$ (9.09)
Best position after 1st iteration (fitness)	$\mathbf{P}b_1^{(1)} = [0\,1\,0\,0\,0]^T$ (5.71)	$\mathbf{P}b_2^{(1)} = [1\,1\,1\,1\,0]^T$ (3.59)
Best position after 2nd iteration (fitness)	$\mathbf{P}b_1^{(2)} = [0\,1\,0\,0\,0]^T$ (5.71)	$\mathbf{P}b_2^{(2)} = [1\,1\,1\,1\,0]^T$ (3.59)
Best position after 3rd iteration (fitness)	$\mathbf{P}b_1^{(3)} = [0\,1\,0\,0\,0]^T$ (5.71)	$\mathbf{P}b_2^{(3)} = [1\,1\,1\,1\,0]^T$ (3.59)
Best position after 4th iteration (fitness)	$\mathbf{P}b_1^{(4)} = [0\,1\,0\,0\,0]^T$ (5.71)	$\mathbf{P}b_2^{(4)} = [1\,1\,0\,1\,0]^T$ (0.54)
	3rd particle $\check{\mathbf{P}}_3$	4th particle $\check{\mathbf{P}}_4$
Initial position (fitness)	$\mathbf{P}b_3^{(0)} = [0\,1\,1\,0\,0]^T$ (6.25)	$\mathbf{P}b_4^{(0)} = [0\,0\,1\,1\,0]^T$ (6.69)
Best position after 1st iteration (fitness)	$\mathbf{P}b_3^{(1)} = [0\,1\,1\,0\,0]^T$ (6.33)	$\mathbf{P}b_4^{(1)} = [1\,1\,0\,0\,1]^T$ (5.28)
Best position after 2nd iteration (fitness)	$\mathbf{P}b_3^{(2)} = [0\,1\,1\,0\,0]^T$ (6.33)	$\mathbf{P}b_4^{(2)} = [1\,0\,0\,0\,0]^T$ (5.15)
Best position after 3rd iteration (fitness)	$\mathbf{P}b_3^{(3)} = [0\,1\,1\,1\,0]^T$ (5.49)	$\mathbf{P}b_4^{(3)} = [1\,0\,0\,0\,0]^T$ (5.15)
Best position after 4th iteration (fitness)	$\mathbf{P}b_3^{(4)} = [1\,1\,1\,1\,0]^T$ (3.59)	$\mathbf{P}b_4^{(4)} = [1\,0\,0\,0\,0]^T$ (5.15)
	Global best particle	
Initial position (fitness)	$\mathbf{G}b^{(0)} = [0\,1\,1\,0\,0]^T$ (6.25)	
Best position after 1st iteration (fitness)	$\mathbf{G}b^{(1)} = [1\,1\,1\,1\,0]^T$ (3.59)	
Best position after 2nd iteration (fitness)	$\mathbf{G}b^{(2)} = [1\,1\,1\,1\,0]^T$ (3.59)	
Best position after 3rd iteration (fitness)	$\mathbf{G}b^{(3)} = [1\,1\,1\,1\,0]^T$ (3.59)	
Best position after 4th iteration (fitness)	$\mathbf{G}b^{(4)} = [1\,1\,0\,1\,0]^T$ (0.54)	

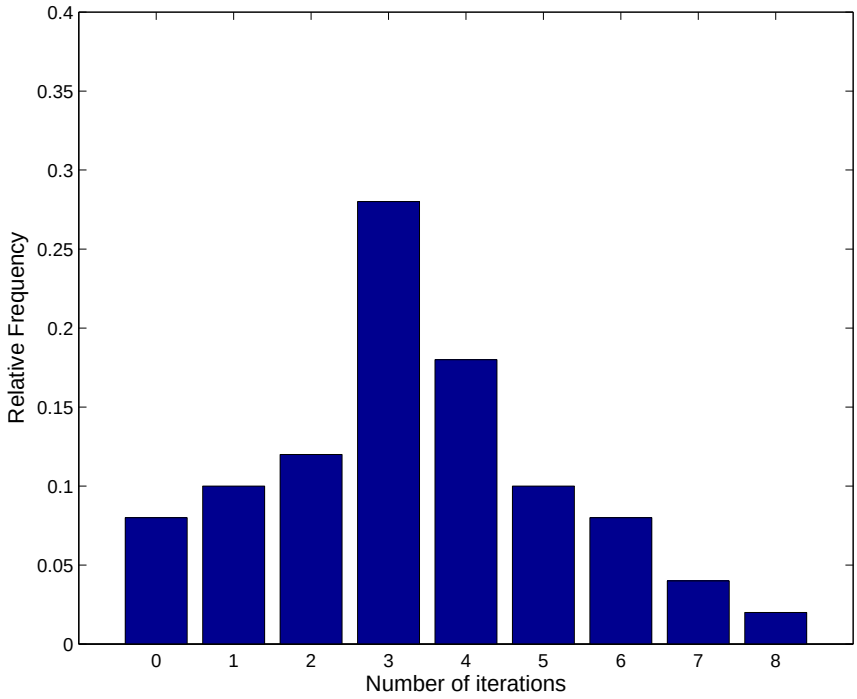

Figure 2.12: The histgram showing the number of iterations the discrete binary PSO algorithm needs to find the ML solution. 50 random simulation runs are used to obtain the result.

Table 2.15: Pairs of MUT shemes and MUD schemes

	MUD algorithms	MUT algorithms
Linear approaches	ZF-MUD	ZF-MUT
	MMSE-MUD	MMSE-MUT
	MBER-MUD	MBER-MUT
Nonlinear approaches	VP	SD

A total of 50 simulations were carried out in order to generate Fig. 2.12. It can observed that 14 of them needed as few as three iterations to find the ML solution, while nine of them required four iterations. On average, it may take the algorithm around four iterations to find the ML solution. However, we also note that it requires more than eight iterations to guarantee that the ML solution is found. Bearing in mind that more iterations impose an increased computational complexity, there is naturally a tradeoff between the computational complexity imposed and the achievable performance when using PSO.

2.2.2.2 Integer Particle Swarm Optimization

This discrete binary PSO algorithm [129] is specifically designed for a binary system. It can be argued that arbitrary multi-level discrete variables can be transformed into an equivalent binary representation, and then the binary PSO can be used. However, the range of the discrete variables often does not match the upper limit of the equivalent binary representation. For example, a discrete variable assuming values of [0,1,2,3,4,5] requires a three-bit binary representation, which ranges between [0-7]. Thus, special measures are required to handle the values outside the original range of the discrete variable. Secondly, the Hamming distance between two discrete values undergoes a nonlinear transformation, when an equivalent binary representation is used instead. This often increases the complexity of the search process. The third reason is that the above-mentioned binary representation increases the dimension of the particle. For these reasons, an extension to the original discrete, but binary-valued PSO converting it to a discrete multi-valued PSO is necessary.

Several researchers have proposed discrete multi-valued PSO algorithms [135, 139]. In our work, we follow the proposal in [135] and invoke their discrete multi-valued PSO algorithm in the context of vector precoding, which is detailed in Chapter 4.

2.3 Conclusions

In this chapter, the preliminary knowledge required for the detailed discussions of this treatise was provided. More specifically, in Section 2.1, we offered a rudimentary introduction to MUT covering the family of linear MUT schemes, namely ZF-MUT, MMSE-MUT and MBER-MUT, as well as the nonlinear VP MUT algorithm. The MUD counterparts of the MUT algorithms can be seen in Table 2.15. It has been shown in [57] that several linear MUT schemes may be readily designed from their linear MUD counterparts, including the ZF-MUT and MMSE-MUT provided that the number of antennas at the BS is no less than that of

the MSs supported. Generally speaking, nonlinear MUT schemes are capable of achieving a better attainable BER performance than linear MUT algorithms at the expense of higher computational complexity as stated in Section 2.1. In Section 2.2, the PSO algorithm was introduced, where it was splited into two parts, focused on continuous-valued PSO and discrete-valued PSO, respectively. More specifically, the continuous-valued PSO scheme which is more suitable for solving continuous-valued optimization problems, was introduced in Section 2.2.1, while Section 2.2.2 covered the introduction of the discrete-valued PSO algorithm invoked for solving combinatorial optimization problems. The PSO algorithm is a promising optimization tool and has been invoked in our research intensively, which will be discussed in later chapters. In the next chapter, we are going to address the computational complexity reduction issues in linear MBER-MUTs, namely in the context of the symbol-specific MBER-MUT scheme and average MBER-MUT algorithm.

Chapter 3

Particle Swarm Optimization Aided Minimum Bit Error Rate Multiuser Transmission

3.1 Introduction

In this chapter, an MBER-MUT designed for the Down-Link (DL) of SDMA systems will be discussed. More explicitly, PSO is invoked for deriving the MUT precoder's coefficients with the aim of directly minimizing the system's BER as well as for reducing the related computational comlexity imposed by using the state-of-the-art SQP algorithm.

The MMSE-MUT has been introduced in Chapter 2, where the coefficients of the precoder are chosen to minimize the mean square error between the transmitted signal and received signal. Since the BER is the ultimate system performance indicator, the research community's interest in MBER based MUT techniques has increased recently. More specifically, in [19, 20], an MBER-MUT was proposed for the Time Division Duplex Code Division Multiple Access (TDD-CDMA) DL communicating in frequency-selective channels. Later, this work was extended to multiple transmit and receive antennas in [21]. Then, a chip-level MBER-MUT scheme was proposed in [2], and a phase-only chip-level MBER-MUT scheme having a reduced computational complexity was also conceived in [2]. Reference [141] showed that the number of spatio-temporal dimensions given by the number of transmit antennas and time-slots can be exceeded in certain circumstances by using the MBER-MUT, for the sake of supporting more users in the DL than the number of transmit antennas. The array-weights of these MBER-MUT techniques were designed for the given MIMO transmit symbol vector and therefore the coefficients of the precoder have to be specifically calculated for every transmit symbol vector. An MBER-MUT design minimizing the average BER was proposed for Binary Phase Shift Keying (BPSK) in [5] and for Quadrature Phase Shift Keying (QPSK) in [26], where the coefficients of the precoder only have to be re-calculated, when the channel coefficients have changed.

We will show in Section 3.4 that the MBER-MUT design constitutes a constrained nonlinear optimiza-

tion problem [5, 26], and the SQP algorithm [27] may be used to obtain the precoder's coefficients for the MBER-MUT [5,24,26]. However, the computational complexity of this algorithm may be deemed excessive at the time of writing for a real-time system [24]. This motivates the work introduced in this chapter in the field of MBER-MUT, with the aim of finding an efficient algorithm which imposes a reduced computational complexity by invoking the PSO algorithm [30].

In Section 3.2, the MBER criterion is introduced. The system model used throughout this chapter is detailed in Section 3.3, followed by the description of the cost functions of the symbol-specific MBER-MUT and the average MBER-MUT in Section 3.4, respectively. The PSO aided MBER-MUT method is introduced in Section 3.5. Section 3.6 quantifies the computational complexity of the SQP approach and of our PSO approach for both the symbol-specific MBER-MUT and for the average MBER-MUT. Our simulation results are provided in Section 3.7, followed by our discussions and the chapter conclusions in Section 3.8.

3.2 Minimum Bit Error Rate Criterion

Let us continue with a simple example to demonstrate the importance of the MBER criterion.

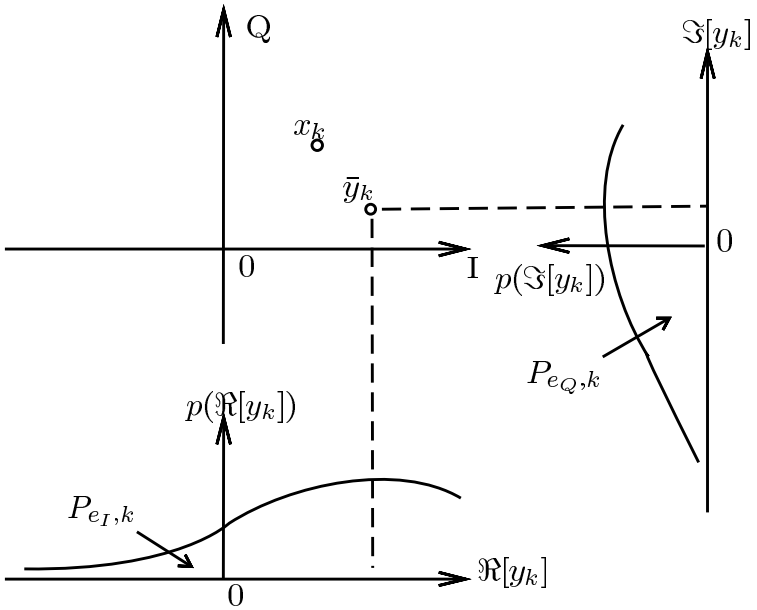

Figure 3.1: Symbol x_k of a QPSK constellation with the interference-contaminated expectation $\bar{y}_k$ of the estimated signal y_k and the PDFs of the in-phase and quadrature-phase component of the estimated signal.

Consider a QPSK system associated with the constellation of $\pm\frac{1}{2} \pm j\frac{1}{2}$, where the desired user's symbol x_k is $\frac{1}{2} + j\frac{1}{2}$. Fig. 3.1 shows the desired symbol x_k, the interference-contaminated expectation $\bar{y}_k$ of the estimated signal y_k and the Probability Density Functions (PDF) of the in-phase and quadrature-phase component of the estimated signal. The error probabilities of the in-phase and quadrature-phase component are denoted by $P_{e_I,k}$ and $P_{e_Q,k}$, respectively, while $P_{e,k}$ denotes the average error probability of the system.

We commence from the calculation of the in-phase error probability $P_{e_I,k}$. When the real part of the received symbol $\Re[y_k]$ falls in the interval of $(-\infty,\ 0]$ due to the effect of the Gaussian noise, we have

$\text{sgn}(\Re[x_k])\Re[y_k] < 0$, therefore it is clear that an error occurs. Hence, $P_{e_I,k}$ is given by [26]:

$$P_{e_I,k} = \text{Prob}\{\text{sgn}(\Re[x_k])\Re[y_k] < 0\}, \tag{3.1}$$

where $\Re[\bullet]$ denotes the real part, while when the imaginary part of the received symbol $\Im[y_k]$ falls in the interval of $(-\infty,\ 0]$ due to the effect of the Gaussian noise, we have $\text{sgn}(\Im[x_k])\Im[y_k] < 0$, hence again, an error occurs. Thus, $P_{e_Q,k}$ is given by [26]:

$$P_{e_Q,k} = \text{Prob}\{\text{sgn}(\Im[x_k])\Im[y_k] < 0\}, \tag{3.2}$$

where $\Im[\bullet]$ denotes the imaginary part.

Then the error probability of this QPSK system $P_{e,k}$ can be obtained by averaging $P_{e_I,k}$ and $P_{e_Q,k}$, which is given by [26]:

$$P_{e,k} = (P_{e_I,k} + P_{e_Q,k})/2 \ . \tag{3.3}$$

3.3 System Model

The system to be considered throughout Chapter 3 will be introduced here, where the DL of a SDMA system supporting non-cooperative mobile receivers is considered. The BS is equipped with N DL transmit antennas and communicates with K MSs, each employing a single receive antenna. The corresponding system model is depicted in Fig. 2.1 . The vector of information symbols $\mathbf{x}$ transmitted in the DL is given by

$$\mathbf{x} = [x_1, x_2, \cdots, x_K]^T, \tag{3.4}$$

where $x_k,\ 1 \leq k \leq K$ denotes the transmitted symbol of the kth MS, and the symbol energy is given by $E[|x_k|^2] = \sigma_x^2$, for $1 \leq k \leq K$.

The $(N \times K)$-element MUT precoder matrix $\mathbf{P}$ is given by

$$\mathbf{P} = [\mathbf{p}_1, \mathbf{p}_2, \cdots, \mathbf{p}_K], \tag{3.5}$$

where $\mathbf{p}_k$, $1 \leq k \leq K$ represents the precoder coefficient vector for the kth user's data stream, as exemplified in Equation (2.8) and Fig. 2.1.

Given a total transmit power E_T at the BS, an appropriate scaling factor should be used after precoding to fulfill our transmit power constraint of having an identical transmit power to that of the scenario operating without a precoder, which is defined as

$$\alpha = \sqrt{\frac{\text{E}_T}{E[\|\mathbf{Px}\|^2]}}, \tag{3.6}$$

for the average MBER-MUT, and as

$$\alpha = \sqrt{\frac{\text{E}_T}{\|\mathbf{Px}\|^2}}, \tag{3.7}$$

for the symbol-specific MBER-MUT.

At the receiver, the reciprocal of the scaling factor, namely α^{-1}, is used to scale the received signal to ensure unity-gain transmission. The channel matrix $\mathbf{H}$ is given by

$$\mathbf{H} = [\mathbf{h}_1, \mathbf{h}_2, \cdots, \mathbf{h}_K]^T, \tag{3.8}$$

where $\mathbf{h}_k$, $1 \leq k \leq K$ is the kth user's CIR, which is given by

$$\mathbf{h}_k = [h_{k,1}, h_{k,2}, \cdots, h_{k,N}], k = 1, 2, \cdots, K. \tag{3.9}$$

The CIR taps $h_{k,i}$, for $1 \leq k \leq K$ and $1 \leq i \leq N$ are independent of each other and obey the complex Gaussian distribution associated with $E[|h_{k,i}|^2] = 1$.

The Gaussian noise vector $\mathbf{n}$ is given by

$$\mathbf{n} = [n_1, n_2, \cdots, n_K]^T, \tag{3.10}$$

where $n_k, 1 \leq k \leq K$ is a complex Gaussian random variable with zero mean and $E[|n_k|^2] = 2\sigma_n^2 = \mathrm{N_o}$. The SNR of the DL is defined as $\mathrm{SNR} = \mathrm{E_b}/\mathrm{N_o}$, where $\mathrm{E_b} = \mathrm{E_T}/(N\log_2 M)$ is the energy per bit per antenna for M-ary modulation. Thus, the baseband model of the system can be described as

$$\mathbf{y} = \mathbf{HPx} + \alpha^{-1}\mathbf{n}, \tag{3.11}$$

where $\mathbf{y} = [y_1\ y_2 \cdots y_K]^T$ denotes the received signal vector, and y_k, $1 \leq k \leq K$, constitutes sufficient statistics for the kth MS to detect the transmitted data symbol x_k. Finally, the detector simply subjects the symbols to hard-decision according to the phase constellation for symbol estimation.

Two main MBER-MUT strategies exist in the literature. The first design may be referred to as the symbol-specific MBER MUT [24], while the other one may be referred to as the average MBER MUT [5, 26], which are outlined below.

3.4 Cost Functions of the Minimum Bit Error Rate Multiuser Transmission Algorithms

In this section, the cost functions of both the symbol-specific MBER-MUT and of the average MBER-MUT algorithms derived for BPSK and QPSK systems are introduced. We show that the resultant opmization probelms are constrained by the transmit power constraint, hence a penalty function approach is adopted to convert the constrained optimization processes into unconstrained ones and to automatically perform power allocation in order to meet the transmit power constraint. This approach is quite similar to the Lagrange multiplier based method used in [26].

3.4.1 Symbol-specific MBER-MUT

The symbol-specific MBER-MUT approach was developed based on the fact that the information symbols to be transmitted are known exactly at the transmitter. Given the knowledge of the CIRs to be encountered by

the individual antenna elements, the precoding matrix can be specifically chosen for the given K-component MIMO symbol vector $\mathbf{x}$ so that the BER is minimized. In the rest of this subsection, we will provide the derivation of the cost function of the symbol-specific MBER-MUT.

First, let us consider a BPSK system. Based on the system model established in Section 3.3, only the real part of the received signal $\mathbf{y}$ should be taken into account. According to the MBER criterion depicted in Section 3.2, when the real part of the received signal $\Re[y_k], 1 \leq k \leq K$ falls in the interval of $(-\infty,\ 0]$, namely, when we have $\text{sgn}(\Re[x_k])\Re[y_k] < 0, 1 \leq k \leq K$, errors occur. Hence, the error probability $P_{e_I,k}$ of the in-phase component associated with the kth user, where $1 \leq k \leq K$, is given by [26]:

$$\begin{aligned} P_{e_I,k} &= \text{Prob}\{\text{sgn}(\Re[x_k])\Re[y_k] < 0\} \\ &= \text{Prob}\{z_R^k < 0\}, \end{aligned} \tag{3.12}$$

where z_R^k is the signed decision variable given by:

$$z_R^k = \text{sgn}(\Re[x_k])\Re[y_k]. \tag{3.13}$$

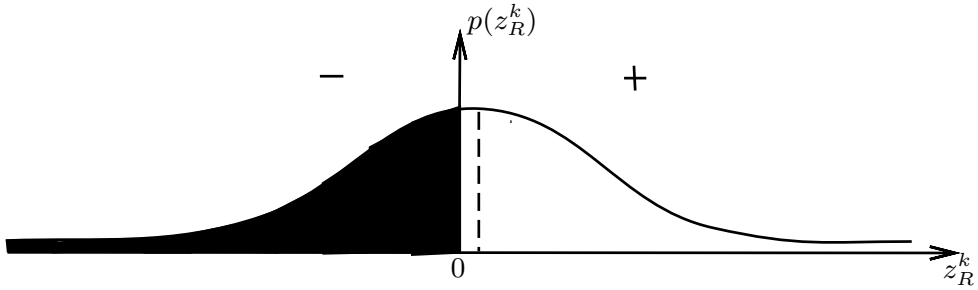

Figure 3.2: Probability density function of the decision variable z_R^k, where the shaded area represents the BER.

The decision variable z_R^k, according to central limit theorem, obeys the Gaussian distribution associated with the mean of $c_R^k = \text{sgn}(\Re[x_k])\Re[\mathbf{h}_k\mathbf{P}\mathbf{x}]$, its probability density function (PDF) can be seen in Fig. 3.2. More explicitly, the PDF of the decision variable z_R^k is given by [26]:

$$p(z_R^k) = \frac{1}{\sigma_n\sqrt{2\pi}} \exp\left(-\frac{(z_R^k - c_R^k)^2}{2\sigma_n^2}\right). \tag{3.14}$$

The erroneous decision events are associated with the area under the PDF curve in the interval $(-\infty,\ 0]$, namely, the shaded area shown in Fig. 3.2. Hence, Equation (3.12) can be rewritten as [26]:

$$\begin{aligned} P_{e_I,k} &= \text{Prob}\{z_R^k < 0\} = \int_{-\infty}^{0} p(z_R^k) dz_R^k \\ &= Q\left(\frac{c_R^k}{\sigma_n}\right), \end{aligned} \tag{3.15}$$

where $Q(\bullet)$ is the standard Gaussian error function.

As we mentioned, in the symbol-specific MBER-MUT, the precoding matrix $\mathbf{P}$ is specifically chosen for the current K-component MIMO symbol vector $\mathbf{x}$. Hence, given the symbol vector $\mathbf{x}$ to be transmitted, the average BER of the in-phase component at the receiver is [19]

$$P_{e_I,\mathbf{x}} = \frac{1}{K}\sum_{k=1}^{K} Q\left(\frac{c_R^k}{\sigma_n}\right). \tag{3.16}$$

Thus, the BER of BPSK signalling is given by

$$P_{e,\mathbf{x}} = P_{e_I,\mathbf{x}}. \tag{3.17}$$

Let us now consider a QPSK system, where the BER of the in-phase component has already been introduced above, and the BER of the quadrature-phase component can be derived in a similar way. Let us furthermore introduce the notation of

$$\begin{aligned} z_I^k &= \text{sgn}(\Im[x_k])\Im[y_k], & (3.18)\\ c_I^k &= \text{sgn}(\Im[x_k])\Im[\mathbf{h}_k\mathbf{P}\mathbf{x}], & (3.19) \end{aligned}$$

then, the error probability $P_{e_Q,k}$ of the quadrature-phase component associated with the kth user, where $1 \leq k \leq K$, is given by [26]:

$$\begin{aligned} P_{e_Q,k} &= \text{Prob}\{\text{sgn}(\Im[x_k])\Im[y_k] < 0\} \\ &= \text{Prob}\{z_I^k < 0\} \\ &= \int_{-\infty}^{0} p(z_I^k)dz_I^k \\ &= Q\left(\frac{c_I^k}{\sigma_n}\right), \end{aligned} \tag{3.20}$$

where we have

$$p(z_I^k) = \frac{1}{\sigma_n\sqrt{2\pi}} \exp\left(-\frac{(z_I^k - c_I^k)^2}{2\sigma_n^2}\right). \tag{3.21}$$

Hence, given the symbol vector $\mathbf{x}$ to be transmitted, the average BER of the quadrature-phase component of $\mathbf{y}$ is [19]:

$$P_{e_Q,\mathbf{x}} = \frac{1}{K}\sum_{k=1}^{K} Q\left(\frac{c_I^k}{\sigma_n}\right). \tag{3.22}$$

Thus, the BER of QPSK signalling is given by

$$P_{e,\mathbf{x}} = (P_{e_I,\mathbf{x}} + P_{e_Q,\mathbf{x}})/2. \tag{3.23}$$

Therefore, the solution of the symbol-specific MBER-MUT weight optimization is defined as

$$\begin{aligned} \mathbf{P}_{\text{TxMBER},\mathbf{x}} &= \arg\min_{\mathbf{P}} P_{e,\mathbf{x}} \\ &\text{s.t.} \quad \|\mathbf{P}\mathbf{x}\|^2 = \mathrm{E}_T. \end{aligned} \tag{3.24}$$

As we mentioned, the so-called penalty function approach is adopted here to convert the constrained optimization process of Equation (3.24) into an unconstrained one and to perform power allocation for the sake of meeting the transmit power constraint. To introduce the cost function for this optimization problem, we define the following penalty function for the power constraint

$$F(\mathbf{P}) = P_{e,\mathbf{x}}(\mathbf{P}) + G_{\mathbf{x}}(\mathbf{P}) \tag{3.25}$$

with the penalty function given by

$$G_{\mathbf{x}}(\mathbf{P}) = \begin{cases} 0, & \|\mathbf{Px}\|^2 - \mathrm{E}_T \leq 0, \\ \lambda(\|\mathbf{Px}\|^2 - \mathrm{E}_T), & \|\mathbf{Px}\|^2 - \mathrm{E}_T > 0, \end{cases} \tag{3.26}$$

where the penalty factor $\lambda > 0$ should be chosen appropriately so that the symbol-specific MBER-MUT design of Equation (3.24) becomes the following unconstrained optimization

$$\mathbf{P}_{\text{TxMBER},\mathbf{x}} = \arg\min_{\mathbf{P}} \{P_{e,\mathbf{x}}(\mathbf{P}) + G_{\mathbf{x}}(\mathbf{P})\}. \tag{3.27}$$

3.4.2 Average MBER-MUT

The problem associated the symbol-specific MBER-MUT approach is that for every transmitted symbol vector $\mathbf{x}$, the precoder matrix $\mathbf{P}$ must be calculated by solving our optimization problem of Equation (3.27), which imposes a high computational complexity in the long run, as discussed later in Section 3.6.

To avoid the computational complexity associated with the K-component MIMO symbol-specific MBER MUT scheme, in this section we introduce the average MBER-MUT, where the precoder matrix remains optimal in terms of minimizing the average BER for all the legitimate transmission symbol vectors.

Let us commence by considering a BPSK system. As stated in Section 3.4.1, when we introduce the definitions of

$$z_R^k = \text{sgn}(\Re[x_k])\Re[y_k], \tag{3.28}$$

$$c_R^k = \text{sgn}(\Re[x_k])\Re[\mathbf{h}_k\mathbf{Px}], \tag{3.29}$$

then, the error probability $P_{e_I,k}$ of the quadrature-phase component associated with the kth user, where $1 \leq k \leq K$, is given by [26]:

$$P_{e_I,k} = Q\left(\frac{c_R^k}{\sigma_n}\right), \tag{3.30}$$

where we have

$$p(z_R^k) = \frac{1}{\alpha^{-1}\sigma_n\sqrt{2\pi}} \exp\left(-\frac{(z_R^k - c_R^k)^2}{2\sigma_n^2\alpha^{-2}}\right). \tag{3.31}$$

In the average MBER-MUT, the precoder matrix remains optimal in terms of minimizing the average BER for all the legitimate transmission symbol vectors. Therefore, the average BER of the in-phase component of $\mathbf{y}$ at the receiver can be shown to be [142]

$$P_{e_I} = \frac{1}{KM^K} \sum_{q=1}^{M^K} \sum_{k=1}^{K} Q\left(\frac{\text{sgn}(\Re[x_k^{(q)}])\Re[\mathbf{h}_k\mathbf{Px}^{(q)}]}{\sigma_n}\right). \tag{3.32}$$

Here M^K is the number of equiprobable legitimate transmit symbol vectors $\mathbf{x}^{(q)}$ for M-ary PSK signalling and $x_k^{(q)}$ is the kth element of $\mathbf{x}^{(q)}$, with $1 \leq q \leq M^K$. Thus, the BER of BPSK signalling is

$$P_e = P_{e_I}, \tag{3.33}$$

with $M^K = 2^K$.

Similarly, the average BER of the quadrature-phase component of $\mathbf{y}$ is given by [142]

$$P_{e_Q} = \frac{1}{KM^K} \sum_{q=1}^{M^K} \sum_{k=1}^{K} Q\left(\frac{\text{sgn}(\Im[x_k^{(q)}])\Im[\mathbf{h}_k \mathbf{P}\mathbf{x}^{(q)}]}{\sigma_n} \right), \tag{3.34}$$

and the BER recorded for QPSK signalling is given by

$$P_e = (P_{e_I} + P_{e_Q})/2, \tag{3.35}$$

with $M^K = 4^K$.

Hence, the average MBER MUT solution is defined as

$$\begin{aligned} \mathbf{P}_{\text{TxMBER}} &= \arg\min_{\mathbf{P}} P_e \\ &\text{s.t.} \quad E[\|\mathbf{P}\mathbf{x}\|^2] = \mathrm{E}_T. \end{aligned} \tag{3.36}$$

To introduce our cost function used for this optimization problem, we define the following penalty function for incorporating the power constraint

$$G(\mathbf{P}) = \begin{cases} 0, & E[\|\mathbf{P}\mathbf{x}\|^2] - \mathrm{E}_T \leq 0, \\ E[\|\mathbf{P}\mathbf{x}\|^2] - \mathrm{E}_T, & E[\|\mathbf{P}\mathbf{x}\|^2] - \mathrm{E}_T > 0, \end{cases} \tag{3.37}$$

which assists us, when the precoder's output power $E[\|\mathbf{P}^*\mathbf{x}\|^2]$ exceeds the total power constraint, for every possible symbol vector $\{x_i\}_{i=1}^{M^K}$.

Then the cost function is given by

$$F = P_e + \lambda G(\mathbf{P}), \tag{3.38}$$

which allows us to convert Equation (3.36) into the unconstrained optimization of

$$\mathbf{P}_{\text{TxMBER}} = \arg\min_{\mathbf{P}} \{P_e + \lambda G(\mathbf{P})\}, \tag{3.39}$$

where λ is the penalty factor and its value should be chosen to ensure rapid convergence.

3.5 PSO assisted MBER-MUT

In this section, PSO assisted symbol-specific (PSO-SS) MBER-MUT and PSO assisted average (PSO-A) MBER-MUT algorithms are proposed.

The process of the proposed PSO aided MBER-MUT algorithm may be decribed by the flow chart seen in Fig. 2.8. A swarm of particles, $\{\check{\mathbf{P}}_i^{(l)}\}_{i=1}^{S}$, that represents the set of potential solutions is evolved in the search space $\mathsf{S}^{N\times K}$, where

$$\mathsf{S} = [-P_{\max},\ P_{\max}] + j[-P_{\max},\ P_{\max}] \tag{3.40}$$

is the square area in the complex plane that defines the search range for each element of the precoder coefficient matrix, S is the swarm size and l denotes the iteration index. Our empirical results suggest that

the search limit can be set to $P_{\max} = 1$ for our application, as shown quantitatively in Section 3.7.Let us briefly revisit Fig. 2.8 here with reference to the specifically numbered blocks as follows:

1) The swarm initialization-block 1 of Fig. 2.8.
With $l = 0$, set $\check{\mathbf{P}}_1^{(0)}$ to the MMSE-MUT solution, while the rest of the initial particles, $\{\check{\mathbf{P}}_i^{(0)}\}_{i=2}^{S}$, are randomly generated in the search space $\mathsf{S}^{N\times K}$. Another potential solution might be using 'hill-climbing', where every single bit of the MMSE-MUT is inverted and as a result, if the CF was improved, the related solution is retained.

2) The swarm evaluation-block 2 of Fig. 2.8.
Each particle $\check{\mathbf{P}}_i^{(l)}$ has a cost $F(\check{\mathbf{P}}_i^{(l)})$ associated with it, which is evaluated according to either Equation (3.27) or Equation (3.39), depending on whether the symbol-specific or the average MBER-MUT design is considered. Each particle $\check{\mathbf{P}}_i^{(l)}$ remembers its best position visited so far, denoted as $\mathbf{P}b_i^{(l)}$, which provides the cognitive information. Every particle also knows the best position visited so far when considering all individuals of the entire swarm, denoted as $\mathbf{G}b^{(l)}$, which provides the social information. $\{\mathbf{P}b_i^{(l)}\}_{i=1}^{S}$ and $\mathbf{G}b^{(l)}$ are updated at each iteration.

Firstly, the entire particle set's position $\{\mathbf{P}b_i^{(l)}\}_{i=1}^{S}$ is updated. For the ith particle, where we have $1 \leq i \leq S$, the CF value of $F(\check{\mathbf{P}}_i^{(l)})$ and that of $F(\mathbf{P}b_i^{(l)})$ are compared as in block 2 of Fig. 2.8, and if the value of $F(\check{\mathbf{P}}_i^{(l)})$ is equal to or higher than that of $F(\mathbf{P}b_i^{(l)})$, this means that the new position visited by the ith particle at the lth iteration yields a higher CF value. This higher CF value represents a lower fitness in our case, hence the most recently visited position is no better than the ith particle's previously visited best position during the previous $(l-1)$ iterations. Hence the value of $F(\mathbf{P}b_i^{(l)})$ and $\mathbf{P}b_i^{(l)}$ will remain at their previous values, namely at $F(\mathbf{P}b_i^{(l-1)})$ and $\mathbf{P}b_i^{(l-1)}$, respectively. If, however, the value of $F(\check{\mathbf{P}}_i^{(l)})$ is lower than that of $F(\mathbf{P}b_i^{(l)})$, the new position that the ith particle visited at the lth iteration yields a reduced CF value. This corresonds to an increased fitness, hence the new visited position is better than the ith particle's previously visited best position during its $(l-1)$ previous iterations. As a result, the value of $F(\mathbf{P}b_i^{(l)})$ and $\mathbf{P}b_i^{(l)}$ will be replaced by those of $F(\mathbf{P}b_i^{(l)})$ and $\mathbf{P}b_i^{(l)}$, respectively in block 2 of Fig. 2.8.

Following the update of $\{\mathbf{P}b_i^{(l)}\}_{i=1}^{S}$, $\mathbf{G}b^{(l)}$ is also updated in block 2 of Fig. 2.8. The best individual particle position $\mathbf{P}b_{i^*}^{(l)}$ found at the lth iteration provides the lowest CF value, namely the highest fitness value. Then, the CF value of $F(\mathbf{P}b_{i^*}^{(l)})$ is compared to that of $F(\mathbf{G}b^{(l)})$ in block 2 of Fig. 2.8. If the CF value of $F(\mathbf{P}b_{i^*}^{(l)})$ is found to be lower than that of $F(\mathbf{G}b^{(l)})$, the best position that all members of the whole swarm ever visited at the lth iteration results in a lower CF value, namely a higher fitness value. Hence the individual particle position of $\mathbf{P}b_{i^*}^{(l)}$ results in a better CF value than the whole swarm's previously visited best position $\mathbf{G}b^{(l-1)}$ during its previous $(l-1)$ iterations. Consequently, the CF value of $F(\mathbf{G}b^{(l)})$ and $\mathbf{G}b^{(l)}$ will be replaced by those of $F(\mathbf{P}b_{i^*}^{(l)})$ and $\mathbf{P}b_{i^*}^{(l)}$, respectively. Otherwise, $F(\mathbf{G}b^{(l)})$ and $\mathbf{G}b^{(l)}$ will remain as those of $F(\mathbf{G}b^{(l-1)})$ and $\mathbf{G}b^{(l-1)}$, respectively. The related pseudocode explicitly describing the operations is as follows:

For ($i = 1$; $i \leq S$; i++)
    If ($F(\check{\mathbf{P}}_i^{(l)}) < F(\mathbf{P}b_i^{(l)})$) $\mathbf{P}b_i^{(l)} = \check{\mathbf{P}}_i^{(l)}$;
End for;

$i^* = \arg\min_{1 \le i \le S} F(\mathbf{P}b_i^{(l)})$;
If $(F(\mathbf{P}b_{i^*}^{(l)}) < F(\mathbf{G}b^{(l)}))$ $\mathbf{G}b^{(l)} = \mathbf{P}b_{i^*}^{(l)}$;

3) The swarm update-block 3 of Fig. 2.8.
Each particle $\check{\mathbf{P}}_i^{(l)}$ has a velocity, denoted as $\mathbf{V}_i^{(l)}$, which controls its 'flight'. The velocity and position of the ith particle are updated in each iteration according to Equation (2.63) and Equation (2.64), respectively.

It was reported in [107] that using a time varying acceleration coefficient (TVAC) enhances the attainable performance of PSO. We adopt this mechanism, in which c_1 decreases from 2.5 to 0.5 and c_2 varies from 0.5 to 2.5 during the iterative procedure according to [107]:

$$\begin{aligned} c_1 &= (0.5 - 2.5) \cdot l/I_{\max} + 2.5, \\ c_2 &= (2.5 - 0.5) \cdot l/I_{\max} + 0.5. \end{aligned} \tag{3.41}$$

This TVAC mechanism was found to perform well in our application. We also remove the influence of the previous iteration's velocity by setting $w = 0$, as suggested in [107].

In order to avoid the excessive roaming of particles beyond the search space [128], we limit the velocity range according to $\mathsf{V} = [-V_{\max},\ V_{\max}] + j[-V_{\max},\ V_{\max}]$. Given this choice of particle positions, the velocity limit can be set to $V_{\max} = 1$, which is imposed on each element of $\mathbf{V}_i^{(l+1)}$ so that when the velocity exceeds its limit, it would be constrainted to its maximum legitimate range, namely to:

If $(\Re[\mathbf{V}_i^{(l+1)}|_{p,q}] > V_{\max})$ $\Re[\mathbf{V}_i^{(l+1)}|_{p,q}] = V_{\max}$;
If $(\Re[\mathbf{V}_i^{(l+1)}|_{p,q}] < -V_{\max})$ $\Re[\mathbf{V}_i^{(l+1)}|_{p,q}] = -V_{\max}$;
If $(\Im[\mathbf{V}_i^{(l+1)}|_{p,q}] > V_{\max})$ $\Im[\mathbf{V}_i^{(l+1)}|_{p,q}] = V_{\max}$;
If $(\Im[\mathbf{V}_i^{(l+1)}|_{p,q}] < -V_{\max})$ $\Im[\mathbf{V}_i^{(l+1)}|_{p,q}] = -V_{\max}$.

Moreover, if the velocity in Equation (2.63) approaches zero, it is reinitialized proportional by to $V_{\max}$ with the aid of a scaling factor γ

$$\mathbf{V}_i^{(l+1)}|_{p,q} = \pm rand() \cdot \gamma \cdot (V_{\max} + jV_{\max}), \tag{3.42}$$

where an appropriate value of the scaling factor γ in Equation (3.42) which would allow us to avoid having a zero velocity was found to be $\gamma = 0.1$ in our experiments to be detailed in Section 3.7. The reason for avoiding zero velocity is quite plausible, since a zero velocity at this iteration would imply that the particle will not move, hence discarding an opportunity to explore the search space and, as a result, potentially would delay convergence.

Similarly, each element of $\check{\mathbf{P}}_i^{(l+1)}$ is checked to ensure that it stays inside the search space S. More explicitly, if a particle is outside the search space, it is moved back inside the search space to a random position, rather than forcing it to stay at the border. This is similar to the philosophy of the scheme proposed in [128]. The related pseudocode of block 3 in Fig. 2.8 is as follows:

If $(\Re[\check{\mathbf{P}}_i^{(l+1)}|_{p,q}] > P_{\max})$
$\Re[\check{\mathbf{P}}_i^{(l+1)}|_{p,q}] = rand() \cdot P_{\max}$;

If ($\Re[\check{\mathbf{P}}_i^{(l+1)}|_{p,q}] < -P_{\max}$)
$\Re[\check{\mathbf{P}}_i^{(l+1)}|_{p,q}] = -rand() \cdot P_{\max}$;
If ($\Im[\check{\mathbf{P}}_i^{(l+1)}|_{p,q}] > P_{\max}$)
$\Im[\check{\mathbf{P}}_i^{(l+1)}|_{p,q}] = rand() \cdot P_{\max}$;
If ($\Im[\check{\mathbf{P}}_i^{(l+1)}|_{p,q}] < -P_{\max}$)
$\Im[\check{\mathbf{P}}_i^{(l+1)}|_{p,q}] = -rand() \cdot P_{\max}$;

4) Termination condition check-block 4 of Fig. 2.8.
Still referring to Fig. 2.8, if the maximum number of iterations, $I_{\max}$, is reached, terminate the algorithm with the solution $\mathbf{G}b^{(I_{\max})}$; otherwise, set $l = (l+1)$ and go to Step *2)* of Fig. 2.8.

The corresponding pseudocode of the algorithm can be written as follows:

Step (1). Initialize the positions of the particles, $\{\check{\mathbf{P}}_i^{(0)}\}_{i=1}^{S}$, set all the $\{F(\mathbf{P}b_i^0)\}_{i=1}^{S}$ and $F(\mathbf{G}b_i^0)$ to a large positive number;
For ($l = 0$; $l < I_{\max}$; l++)
Step (2). Evaluate $\{F(\check{\mathbf{P}}_i^{(l)})\}_{i=1}^{S}$ for all the particles according to Equation (3.27) in PSO-SS MBER-MUT optimization or Equation (3.39) in PSO-A MBER-MUT optimization;
Step (3). For ($i = 1$; $i \leq S$; i++)
If $[F(\check{\mathbf{P}}_i^{(l)}) < F(\mathbf{P}b_i^{(l)})]$
$\mathbf{P}b_i^{(l)} = \check{\mathbf{P}}_i^{(l)}$;
End if;
End for;
$i^* = \arg\min_{1 \leq i \leq S} F(\mathbf{P}b_i^{(l)})$;
If $[F(\mathbf{P}b_{i^*}^{(l)}) < F(\mathbf{G}b^{(l)})]$
$\mathbf{G}b^{(l)} = \mathbf{P}b_{i^*}^{(l)}$;
End if;
$c_1 = (0.5 - 2.5) \cdot l/I_{\max} + 2.5$;
$c_2 = (2.5 - 0.5) \cdot l/I_{\max} + 0.5$;
For ($i = 1$; $i \leq S$; i++)
$\mathbf{V}_i^{(l+1)} = w \cdot \mathbf{V}_i^{(l)} + rand() \cdot c_1 \cdot [\mathbf{P}b_i^{(l)} - \check{\mathbf{P}}_i^{(l)}] + rand() \cdot c_2 \cdot [\mathbf{G}b^{(l)} - \check{\mathbf{P}}_i^{(l)}]$;
If ($\mathbf{V}_i^{(l+1)}|_{p,q} == 0$)
If ($rand() < 0.5$)
$\mathbf{V}_i^{(l+1)}|_{p,q} = rand() \cdot \gamma \cdot (V_{\max} + jV_{\max})$;
Else
$\mathbf{V}_i^{(l+1)}|_{p,q} = -rand() \cdot \gamma \cdot (V_{\max} + jV_{\max})$;
End if;
End if;
If ($\Re[\mathbf{V}_i^{(l+1)}|_{p,q}] > V_{\max}$)
$\Re[\mathbf{V}_i^{(l+1)}|_{p,q}] = V_{\max}$;
End if;
If ($\Re[\mathbf{V}_i^{(l+1)}|_{p,q}] < -V_{\max}$)

$\Re[\mathbf{V}_i^{(l+1)}|_{p,q}] = -V_{\max}$;
End if;
If ($\Im[\mathbf{V}_i^{(l+1)}|_{p,q}] > V_{\max}$)
$\Im[\mathbf{V}_i^{(l+1)}|_{p,q}] = V_{\max}$;
End if;
If ($\Im[\mathbf{V}_i^{(l+1)}|_{p,q}] < -V_{\max}$)
$\Im[\mathbf{V}_i^{(l+1)}|_{p,q}] = -V_{\max}$;
End if;
$\check{\mathbf{P}}_i^{(l+1)} = \check{\mathbf{P}}_i^{(l)} + \mathbf{V}_i^{(l+1)}$;
If ($\Re[\check{\mathbf{P}}_i^{(l+1)}|_{p,q}] > P_{\max}$)
$\Re[\check{\mathbf{P}}_i^{(l+1)}|_{p,q}] = rand() \cdot P_{\max}$;
End if;
If ($\Re[\check{\mathbf{P}}_i^{(l+1)}|_{p,q}] < -P_{\max}$)
$\Re[\check{\mathbf{P}}_i^{(l+1)}|_{p,q}] = -rand() \cdot P_{\max}$;
End if;
If ($\Im[\check{\mathbf{P}}_i^{(l+1)}|_{p,q}] > P_{\max}$)
$\Im[\check{\mathbf{P}}_i^{(l+1)}|_{p,q}] = rand() \cdot P_{\max}$;
End if;
If ($\Im[\check{\mathbf{P}}_i^{(l+1)}|_{p,q}] < -P_{\max}$)
$\Im[\check{\mathbf{P}}_i^{(l+1)}|_{p,q}] = -rand() \cdot P_{\max}$;
End if;
End for;
End for;

3.6 Computational Complexity

In this section the computational complexity of the symbol-specific MBER-MUT and of the average MBER-MUT algorithms using SQP and PSO are studied. Our computational complexity calculation follows the suggestions in [26]:

"For the sake of fair comparisons of the MUD algorithms, the number of real-valued operations is used as the unit of complexity, and the complexities imposed by a real-valued multiplication and a real-valued addition might be considered equivalent. A single complex-valued addition's complexity is equivalent to that of two real-valued operations, and a complex-valued multiplication's complexity is equivalent to that of six real-valued operations."

3.6.1 Symbol-specific MBER-MUT

The computational complexity per iteration of the SQP-based symbol-specific MBER MUT scheme, extracted from [26] and that of our proposed PSO-SS MBER MUT scheme, are listed in Table 4.4 for QPSK

modulation. The total computational complexity equals the number of iterations that the algorithm required in order to arrive at a globally optimal solution multiplied by this complexity per iteration.

Table 3.1: Computational complexity per iteration of two symbol-specific MBER MUT designs for QPSK signalling, where N is the number of transmit antennas, K is the number of mobile users, and S is the particle size.

Algorithm	Flops
SQP	$\mathcal{O}[8 \cdot K^3 \cdot N^3] + 8 \cdot K^3 \cdot N^2 + 8 \cdot N^2 \cdot K^2 + 22 \cdot K^2 \cdot N + 8 \cdot K \cdot N^2$ $+14 \cdot K^2 + 18 \cdot K \cdot N - 2 \cdot N^2 + 2 \cdot K + N + 11$
PSO	$(38 \cdot N \cdot K + 8 \cdot N + 7 \cdot K + 3) \cdot S + 8$

More explicitly, a detailed complexity calculation table for our proposed PSO-SS MBER MUT scheme per iteration is listed in Table 3.2, which considers the most complex operations. Naturally, the total complexity depends on the number of transmit antennas N, the number of users K and on the size of the swarm S, which is often set between S =20 and 40.

Table 3.2: Detailed computational complexity per iteration for PSO-SS MBER MUT designs for QPSK signalling, where N is the number of transmit antennas, K the number of mobile users, and S is the particle size. The numbers in () indicate the index of the corresponding block in Fig. 2.8.

Stage	Flops
Evaluate fitness (2)	$(8 \cdot N \cdot K + 7 \cdot K) \cdot S$
Update c_1, c_2 (3)	$4 \cdot 2$
Update velocities (3)	$2 \cdot 7 \cdot N \cdot K \cdot S$
Update positions (3)	$2 \cdot N \cdot K \cdot S$

3.6.2 Average MBER-MUT

The computational complexity per iteration of the SQP-based average MBER MUT algorithm, extracted from [26] and that of our proposed PSO-A MBER MUT scheme, are listed in Table 3.3 for QPSK modulation. The total computational complexity equals the number of iterations multiplied by the complexity per iteration. It should be pointed out that for the symbol-specific MBER-MUT the precoding matrix has to be recalculated for every symbol vector to be transmitted, while for the average MBER-MUT, the precoding matrix only has to be recalculated when the channel's complex envelope has changed. Hence the symbol-specific MBER-MUT exhibits a significantly higher computational complexity. On the other hand, it is expected that the symbol-specific MBER-MUT design provides a slightly better performance, which will be demonstrated in Section 3.7.

More explicitly, the detailed complexity calculations for our proposed PSO-A MBER MUT algorithm per iteration are listed in Table 3.4. Naturally, its complexity depends on the number of transmit antennas N, the number of users K, the size of symbol constellation M and the size S of the swarm.

Table 3.3: Computational complexity per iteration of two average MBER MUT designs for QPSK signalling, where N is the number of transmit antennas, K is the number of mobile users, $M = 4$ is the size of symbol constellation and S is the particle size.

Algorithm	Flops
SQP	$K \times (8 \cdot N^2 \cdot K^2 + 6 \cdot N \cdot K + 6 \cdot N + 8 \cdot K + 4) \cdot M^K$ $+\mathcal{O}[8 \cdot N^3 \cdot K^3] + 8 \cdot N^2 \cdot K^2 + 16 \cdot N \cdot K^2 + 8 \cdot N^2 \cdot K$ $+12 \cdot N \cdot K + 6 \cdot K^2 - 2 \cdot N^2 + N - 2 \cdot K + 11$
PSO	$[(16 \cdot N \cdot K + 7 \cdot K + 6 \cdot N + 1) \cdot M^K + 20 \cdot N \cdot K + 2] \cdot S + 8$

Table 3.4: Detailed computational complexity per iteration for PSO-A MBER MUT designs for QPSK signalling, where N is the number of transmit antennas, K is the number of mobile users, $M = 4$ is the size of the symbol constellation and S is the particle size. The numbers in () indicate the index of the corresponding block in Fig. 2.8.

Stage	Flops
Evaluate fitness (2)	$[(16 \cdot N \cdot K + 7 \cdot K + 6 \cdot N + 1) \cdot M^K + 2] \cdot S$
Update c_1, c_2 (3)	$4 \cdot 2$
Update velocities (3)	$2 \cdot 7 \cdot N \cdot K \cdot S$
Update positions (3)	$2 \cdot N \cdot K \cdot S$

3.7 Simulation Results and Discussion

In this section, our simulation results are provided along with our related discussions. Since the terms "TxMBER" and "TxMMSE" can also be seen in the literature [24], the nomenclature "TxMBER" and "MBER-MUT" are used interchangeably, and so are "TxMMSE" and "MMSE-MUT".

3.7.1 The choice of $P_{\max}$

The appropriate choice of $P_{\max}$ for the PSO-SS MBER-MUT and PSO-A MBER-MUT algorithms is considered here. The distribution of the absolute value of $\check{\mathbf{P}}_i|_{p,q}$ recorded for the PSO-SS MBER-MUT scheme can be seen in Fig. 3.3, where 100 PSO-SS MBER-MUT precoding matrices were taken into account for the system employing N=4 transmit antennas to support K=4 QPSK users for communicating over flat Rayleigh fading MIMO channels. It can be seen that among all the $N \cdot K \cdot 2 \cdot 100 = 3200$ absolute values, 2496 fall in the interval of $(0,\ 0.5]$, 704 fall in the interval of $(0.5,\ 1.0]$, while none of them exceeds 1.0. This suggests that setting the value of $P_{\max}$ to be $|P_{\max}| = 1$ for the PSO-SS MBER-MUT scheme should be appropriate.

The distribution of the absolute value of $\check{\mathbf{P}}_i|_{p,q}$ of the PSO-A MBER-MUT scheme can be seen in Fig. 3.4, where 100 PSO-A MBER-MUT precoding matrix are taken into account for the system employing N=4 transmit antennas to support K=4 QPSK users for communicating over flat Rayleigh fading MIMO channels. It can be seen that, among all the 3200 absolute values, 2621 fall in the interval of $(0,\ 0.5]$, 579 fall in the interval of $(0.5,\ 1.0]$, while none of them goes above 1.0. These suggest that setting the value of

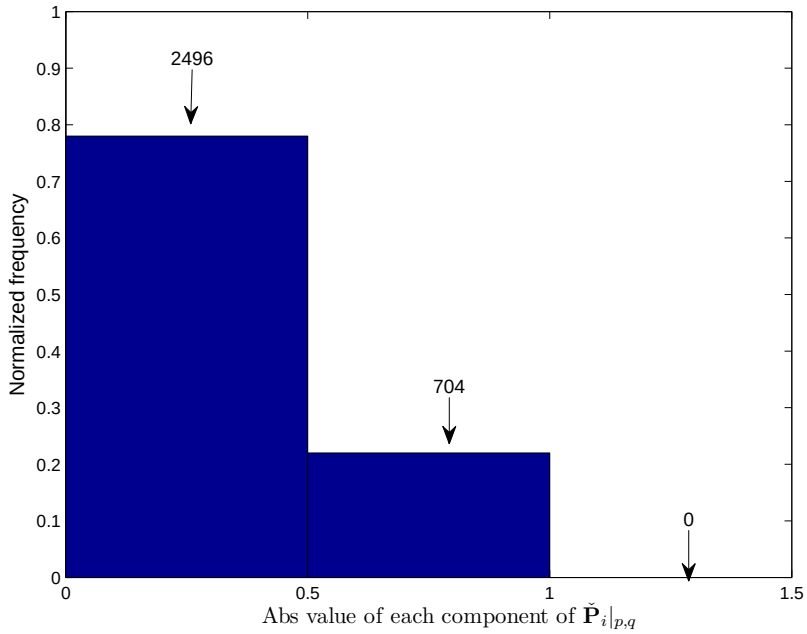

Figure 3.3: The distribution of the absolute value of $\check{\mathbf{P}}_i|_{p,q}$ of the PSO-SS MBER-MUT scheme, where 100 PSO-SS MBER-MUT precoding matrices were taken into account for the system employing N=4 transmit antennas to support K=4 QPSK users for communicating over flat Rayleigh fading MIMO channels.

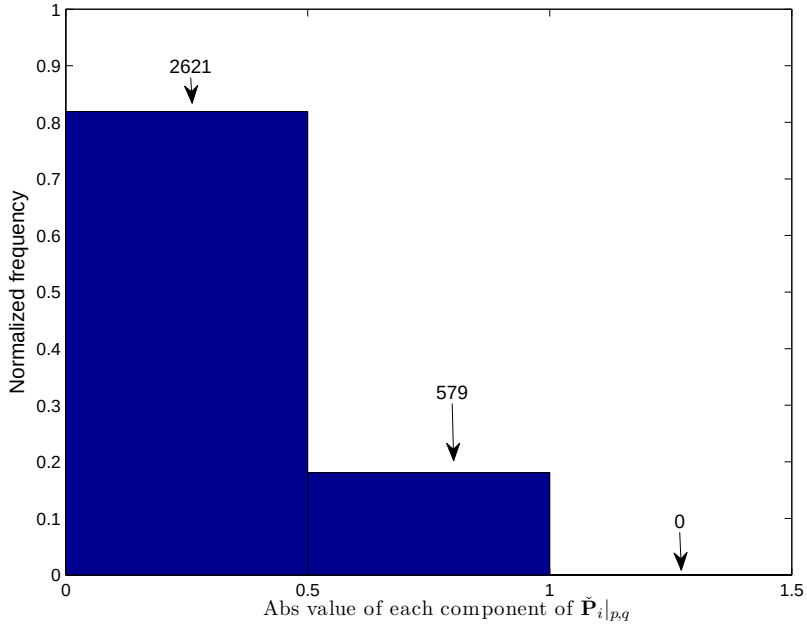

Figure 3.4: The distribution of the absolute value of $\check{\mathbf{P}}_i|_{p,q}$ of the PSO-A MBER-MUT scheme. 100 PSO-A MBER-MUT precoding matrices were taken into account for the system employing N=4 transmit antennas to support K=4 QPSK users for communicating over flat Rayleigh fading MIMO channels. We may notice that the result is similar to what we have seen in Fig. 3.3.

Table 3.5: Simulation parameters summary. CSIT means CSI at the transmitter side.

Parameter	Value or Type
System	
Modulation scheme	QPSK
Transmit antennas	4
Receive end users	4
Channel	flat Rayleigh fading
CSIT knowledge	perfect
Channel realizations	100
PSO	
$P_{\max}$	1
$V_{\max}$	1

$P_{\max}$ to be $|P_{\max}| = 1$ for the PSO-A MBER-MUT algorithm is sufficient.

3.7.2 The effect of TVAC

The effects of TVAC described in Section 3.5 on the for PSO-SS MBER-MUT and PSO-A MBER-MUT algorithms are considered here. The simulation parameters are listed in Table 3.5.

The effect of TVAC on the performance of the PSO-SS MBER-MUT scheme for the system employing N=4 transmit antennas for supporting K=4 QPSK users communicating over flat Rayleigh fading MIMO channels at Eb/No=15dB can be seen in Fig. 3.5. The performances are obtained by averaging over 100 channel realizations.

It can be observed in Fig. 3.5 that, when the TVAC scheme is adopted, the PSO-SS MBER-MUT algorithm converges to the optimal solution slightly earlier namely after around 30 iterations. This suggests that the TVAC scheme is capable of slightly enhancing the attainable performance of our PSO-SS MBER-MUT approach.

The effect of TVAC on the performance of the PSO-A MBER-MUT scheme for the system employing N=4 transmit antennas for supporting K=4 QPSK users communicating over flat Rayleigh fading MIMO channels at Eb/No=15dB can be seen in Fig. 3.6. The achieved performance was obtained averaged over 100 channel realizations. As we can see in Fig. 3.6, the PSO-A MBER-MUT algorithm converges to the optimal solution after around 40 iterations when the TVAC scheme is adopted, slightly earlier than without the TVAC scheme. This shows that the TVAC scheme is capable of modestly enhancing the performance of PSO in our PSO-A MBER-MUT approach.

3.7.3 The choice of γ

The effect of the parameter γ described in Equation (3.42) of Section 3.5 on the for PSO-SS MBER-MUT and PSO-A MBER-MUT algorithms is considered in this part using the simulation parameters of Table 3.5.

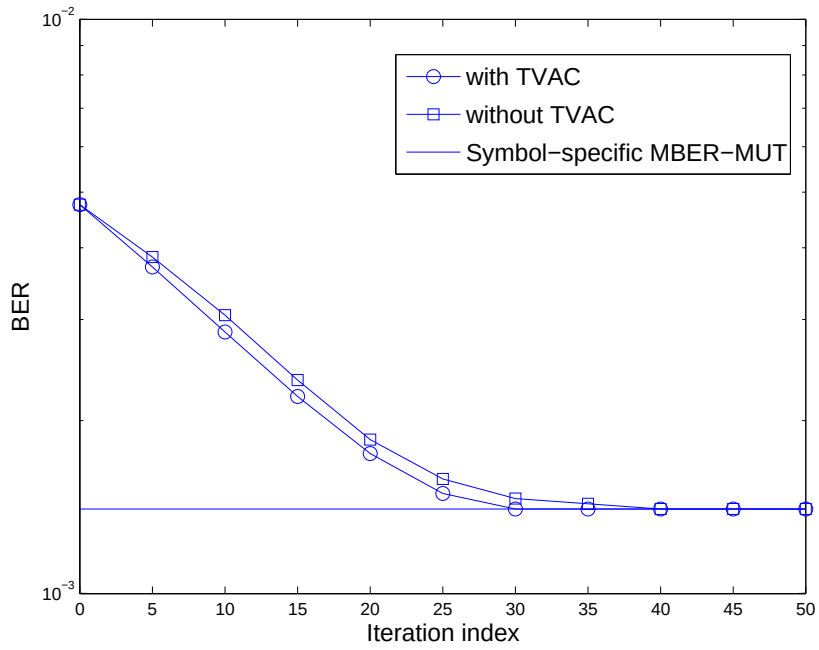

Figure 3.5: The effect of TVAC on the performance of the PSO-SS MBER-MUT scheme for the system employing N=4 transmit antennas to support K=4 QPSK users for communicating over flat Rayleigh fading MIMO channels at Eb/No=15dB. The benchmark performance of the symbol-specific MBER-MUT at Eb/No=15dB which can be observed in Fig. 3.16 is also shown in this figure. All system parameters are summarized in Table 3.5.

The effect of the choice of γ in Equation (3.42) on the performance of the PSO-SS MBER-MUT scheme for the system employing N=4 transmit antennas to support K=4 QPSK users for communicating over flat Rayleigh fading MIMO channels at Eb/No=10dB is shown in Fig. 3.7. Again, the performance averaged over 100 channel realizations. It can be seen in Fig. 3.7 that for $\gamma = 0.1$, the PSO-SS MBER-MUT algorithm converges to the optimal solution after about 20 iterations, while requiring slightly more iterations for $\gamma = 0.05$ and $\gamma = 0.2$. Hence, we can conclude that in this case, $\gamma = 0.1$ is the best design option.

The effect of the choice of γ on the performance of the PSO-A MBER-MUT scheme for the system employing N=4 transmit antennas to support K=4 QPSK users for communicating over flat Rayleigh fading MIMO channels at Eb/No=10dB can be seen in Fig. 3.8. The BER performance was averaged over 100 channel realizations. Again, it is clear that for $\gamma = 0.1$, the PSO-A MBER-MUT algorithm converges to the optimal solution after about 20 iterations, while requiring slightly more iterations for $\gamma = 0.05$ and $\gamma = 0.2$. Therefore, we can see that $\gamma = 0.1$ is also the best choice in this case.

3.7.4 The choice of S

The effect of the swarm size S for the PSO-SS MBER-MUT and PSO-A MBER-MUT algorithms are quantified in this part using the simulation parameters of Table 3.5.

The influence of the swarm size S on the attainable performance of the PSO-SS MBER-MUT scheme

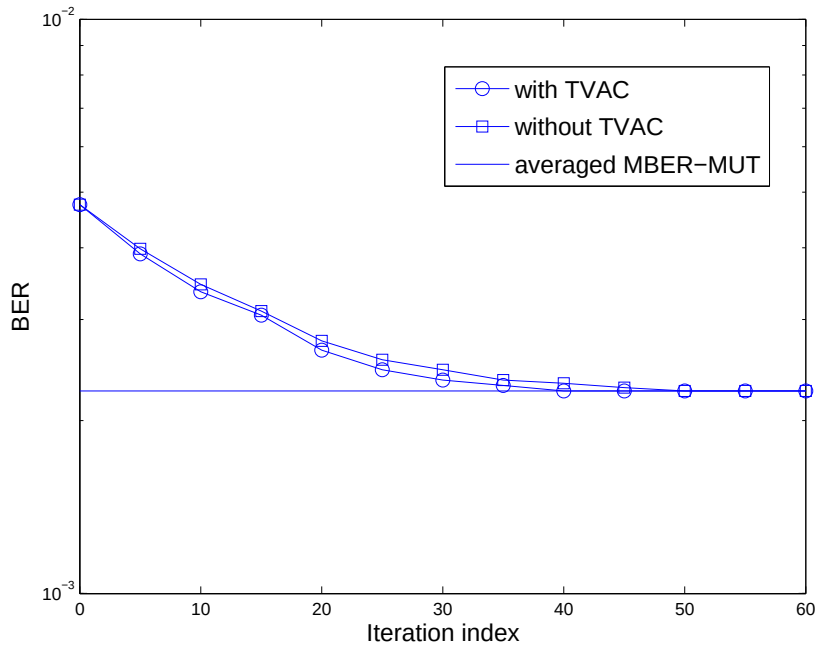

Figure 3.6: The effect of TVAC on the performance of the PSO-A MBER-MUT scheme for the system employing N=4 transmit antennas to support K=4 QPSK users for communicating over flat Rayleigh fading MIMO channels at Eb/No=15dB. Again, the benchmark performance of the average MBER-MUT at Eb/No=15dB which can be observed in Fig. 3.16 is also shown in this figure. All system parameters are summarized in Table 3.5.

for the system employing N=4 transmit antennas to support K=4 QPSK users for communicating over flat Rayleigh fading MIMO channels at Eb/No=15dB can be seen in Fig. 3.9 along with the associated computational complexity. The related performances were recorded upon averaging over 100 channel realizations.

Observe in Fig. 3.9, that S = 10 failed to ensure convergence to the optimal solution, while the algorithm associated with S = 20, 30 and 40 converged to the optimal PSO-SS MBER MUT solution. In conjunction with S = 20, the algorithm converged after about 28 iterations at a complexity cost of 375,984 Flops, while for S = 30 and 40, the algorithm converged after 20 iterations at the complexity costs of 402,760 Flops and 536,960 Flops, respectively. In this case the best design choice is $S = 20$.

The effect of the swarm size S on the performance of the PSO-A MBER-MUT scheme recorded for the system employing N=4 transmit antennas to support K=4 QPSK users for communicating over flat Rayleigh fading MIMO channels at Eb/No=15dB can be seen in Fig. 3.10, in conjunction with the related computational complexity. The performances were obtained by averaging the results over 100 channel realizations.

It can also be observed that S = 10 failed to ensure convergence to the optimal solution while the algorithm associated with S = 20, 30 and 40 converged to the optimal PSO-A MBER MUT solution. When using S = 20, the algorithm converged after around 40 iterations at a computational cost of 63,541,120 Flops, for S = 30, the algorithm converged after 27 iterations at the costs of 64,335,276 Flops, while for S = 40, the scheme requires 79,426,200 Flops to converge after 25 iterations. Hence, in this case, the best choice of

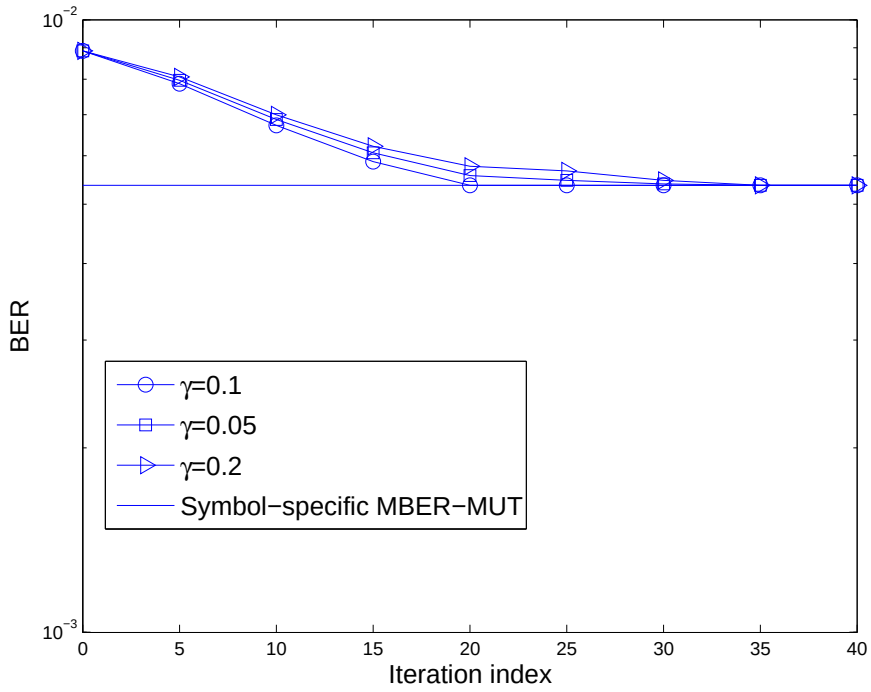

Figure 3.7: The effect of the choice of γ in Equation (3.42) on the performance of the PSO-SS MBER-MUT scheme for the system employing N=4 transmit antennas to support K=4 QPSK users for communicating over flat Rayleigh fading MIMO channels at Eb/No=10dB. The benchmark performance of the symbol-specific MBER-MUT at Eb/No=10dB which can be observed in Fig. 3.16 is also shown in this figure. All system parameters are summarized in Table 3.5.

Table 3.6: Simulation parameters in showing the BER cost function surfaces.

Parameter	Value or Type
Modulation scheme	QPSK
Transmit (or receive) antennas	1
Number of users	1
Channel	flat Rayleigh fading
CSIT (or CSIR) knowledge	perfect
Channel	$[-1.09678 + j0.481258]$

S is also 20.

3.7.5 Single-user BER cost function surface

Here, three types of BER CF surfaces are shown for a (1×1)-element system, namely, the one for the MBER-MUD [143], the one for the average MBER-MUT as well as those of the symbol-specific MBER-MUT concerning each of the four legitimate transmitted symbols, when the baseband received signals are expressed in the form of Equation 3.43. The simulation parameters are listed in Table 3.6. Let us now

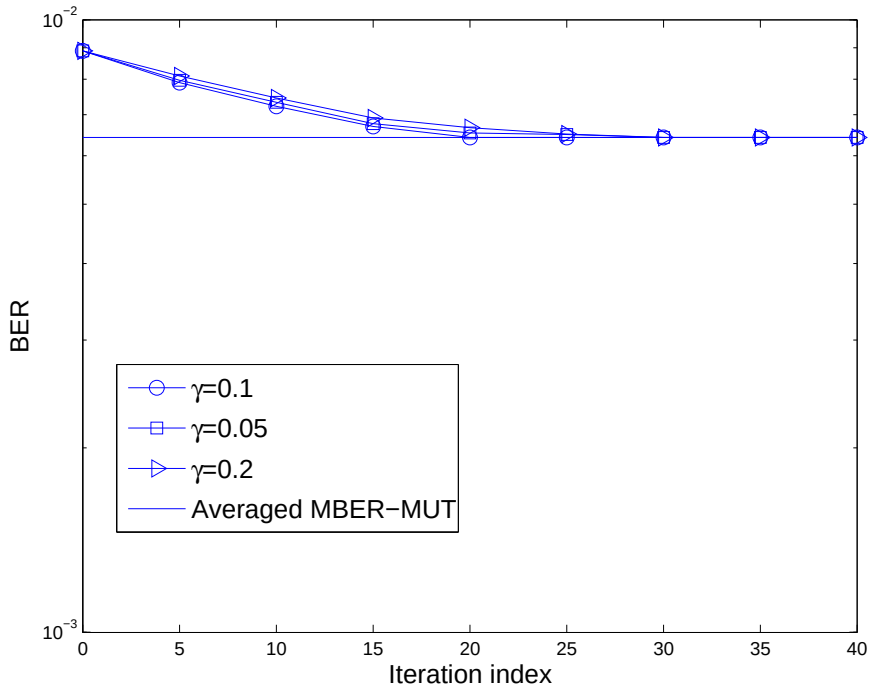

Figure 3.8: The effect of the parameter γ in Equation (3.42) on the performance of the PSO-A MBER-MUT scheme for the system employing N=4 transmit antennas to support K=4 QPSK users for communicating over flat Rayleigh fading MIMO channels at Eb/No=10dB. Again, the benchmark performance of the average MBER-MUT at Eb/No=10dB which can be observed in Fig. 3.16 is also shown in this figure. All system parameters are summarized in Table 3.5.

consider the MUD and MUT scenarios formulated as:

$$\begin{aligned} \mathbf{y} &= \mathbf{W}(\mathbf{Hx}+\mathbf{n}) \quad forMUD \\ \mathbf{y} &= \mathbf{HPx}+\alpha^{-1}\mathbf{n} \quad forMUT. \end{aligned} \tag{3.43}$$

First of all, the BER CF surface of the system invoking the MBER-MUD algorithm and employing N=1 receive antenna to support K=1 QPSK user communicating over a flat Rayleigh fading channel at Eb/No=5dB is shown in Fig. 3.11. Both the MMSE-MUD and the MBER-MUD solutions are characterized. The BER CF does not have a closed-form solution for the MBER-MUD weights for transmission over Rayleigh fading channels. Hence, an iterative strategy based on the steepest-descent gradient method can be adopted for finding the MBER solution [26]. It is observed in Fig. 3.11 that the MMSE-MUD solution does not coincide with the MBER-MUD solution, since the output of the detection is not Gaussian distributed. It can also be observed from Fig. 3.11 that there are infinite number of MBER solutions.

The BER cost function surfaces for the system invoking the symbol-specific MBER-MUT algorithm and employing N=1 transmit antenna to support K=1 QPSK user for communicating over flat Rayleigh fading MIMO channels at Eb/No=5dB is shown in Fig. 3.13. All the BER surfaces of the four legitimate transmission symbols can be seen. Both the MMSE-MUT and the MBER-MUT solutions are characterized. As for the MBER-MUD characterized in Fig. 3.11, the BER CF surfaces exhibit less smoothly evolving

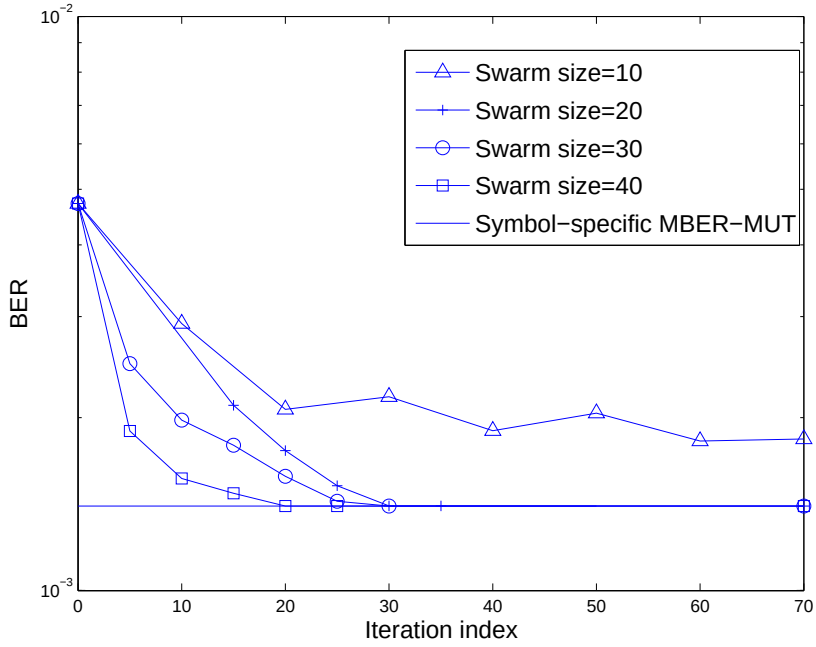

(a)

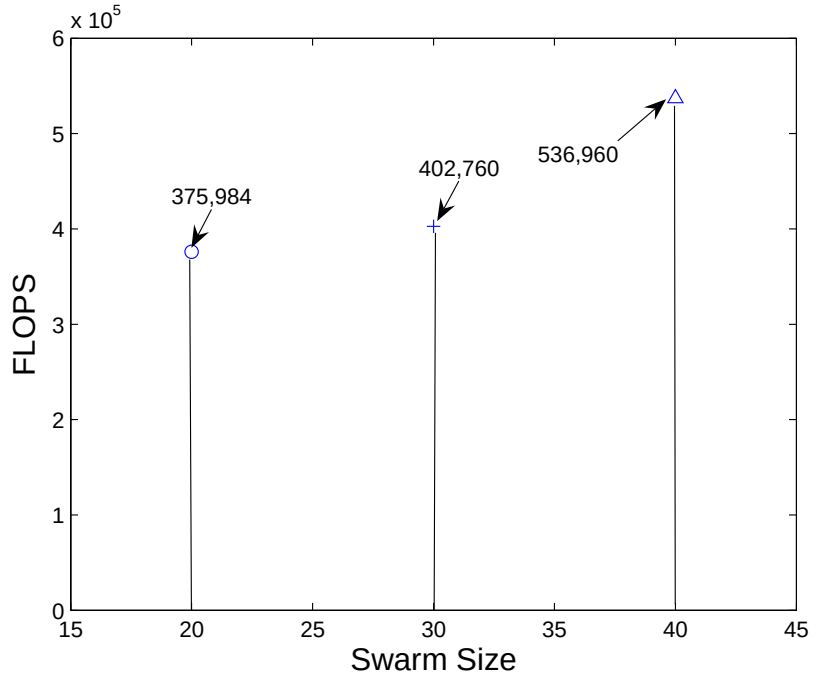

(b)

Figure 3.9: (a)The effect of the choice of S on the performance of the PSO-SS MBER-MUT scheme for the system employing N=4 transmit antennas to support K=4 QPSK users for communicating over flat Rayleigh fading MIMO channels at Eb/No=15dB. The benchmark performance of the symbol-specific MBER-MUT at Eb/No=15dB which can be observed in Fig. 3.16 is shown in this figure as well. (b) The related computational complexity. All system parameters are summarized in Table 3.5.

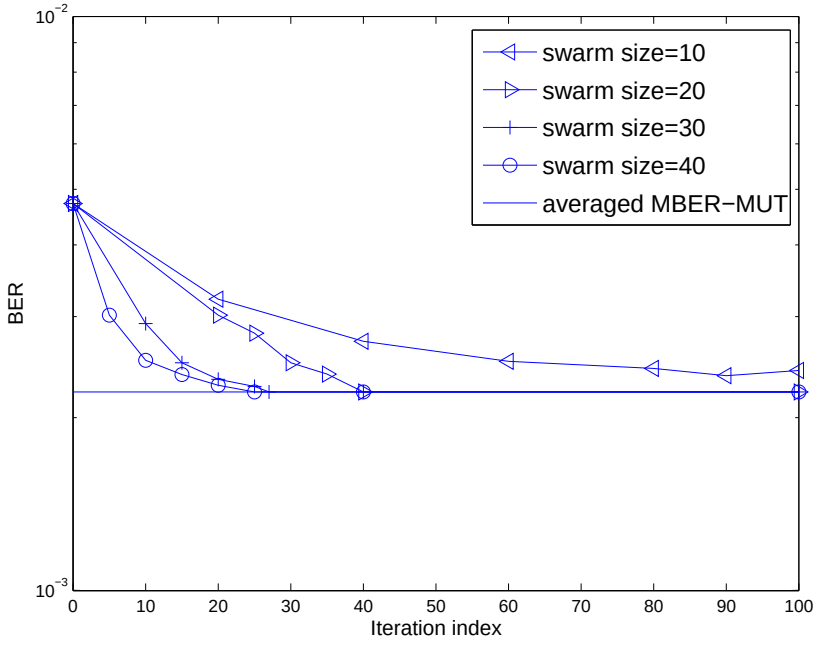

(a)

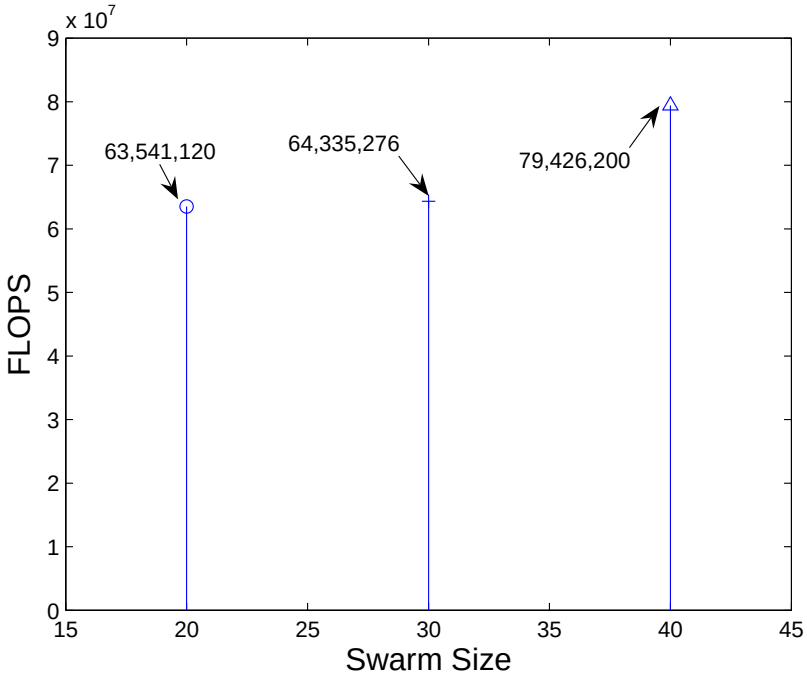

(b)

Figure 3.10: (a) The effect of the swarm size S on the performance of the PSO-A MBER-MUT scheme for the system employing N=4 transmit antennas to support K=4 QPSK users for communicating over flat Rayleigh fading MIMO channels at Eb/No=15dB. Again, the benchmark performance of the average MBER-MUT at Eb/No=15dB which can be observed in Fig. 3.16 is also shown in this figure. (b) The related computational complexity. All system parameters are summarized in Table 3.5.

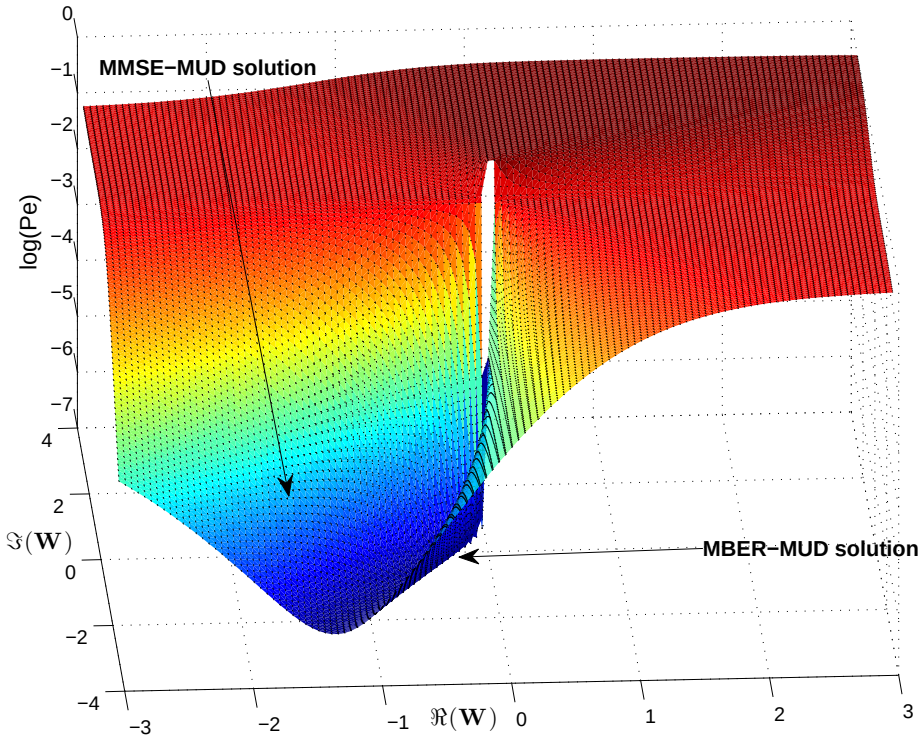

Figure 3.11: The BER cost function surface for the system invoking the MBER-MUD [143] algorithm and employing N=1 receive antenna to support K=1 QPSK user for communicating over flat Rayleigh fading channel at Eb/No=5dB. The channel coefficient is $\mathbf{H} = [-1.09678 + j0.481258]$. Since the cost function is undefined when $\mathbf{W} = [0 + j0]$, hence there is a blank point in the figure.

shapes than say the typical paraboloid-like MMSE surfaces. Hence we are unable to derive closed-form solutions for the weights of the precoding matrix of the symbol-specific MBER-MUT scheme of Section 3.4.1. As a solution, an iterative strategy is used. Interestingly, we can observe in Fig. 3.13 that in this (1×1)-element system, the BER cost function surfaces for the four legitimate transmitted symbol are identical. This phenomenon suggests that in a (1×1)-element single-user system, the shape of the BER cost function surface is only affected by the CIR as well as the SNR, namely, the noise level.

The BER cost function surface for the system invoking average MBER-MUT algorithm of Section 3.4.2 and employing N=1 transmit antennas to support K=1 QPSK users for communicating over flat Rayleigh fading MIMO channels at Eb/No=5dB is shown in Fig. 3.12. This was recorded by averaging the BER cost function surfaces of all legitimate transmission symbols. The MMSE-MUT solution is also characterized. Again, both the symbol-specific MBER-MUT and the average MBER-MUT algorithm outperformed the MMSE-MUT solution. It is quite interesting to see in Fig. 3.12 and Fig. 3.13 that, although there is a power constraint, there are again infinite number of MBER solutions for the precoder's coefficients for this 1×1 system.

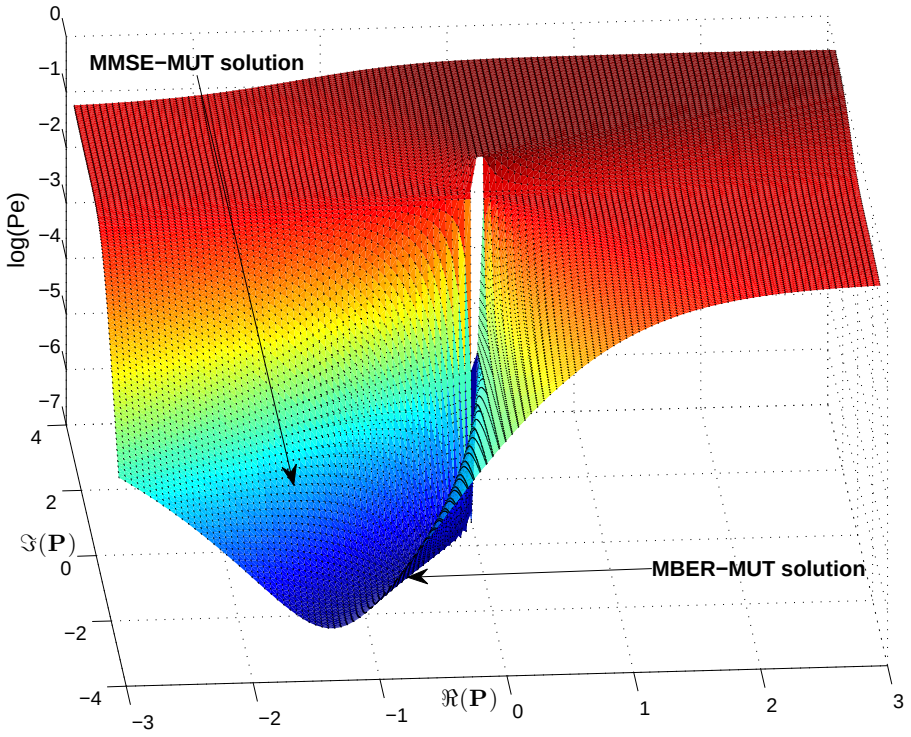

Figure 3.12: The BER cost function surface for the system invoking the average MBER-MUT algorithm and employing N=1 transmit antenna to support K=1 QPSK user for communicating over flat Rayleigh fading channel at Eb/No=5dB. The channel coefficient is $\mathbf{H} = [-1.09678 + j0.481258]$. The cost function is undefined when $\mathbf{W} = [0 + j0]$, therefore there is a blank point in the figure.

3.7.6 Two-user scenario

In the above example, we showed that the BER cost function surfaces of the MBER-MUD, the symbol-specific MBER-MUT and average MBER-MUT are identical for a (1×1)-element single user QPSK system, hence resulting in the same MBER solution. The same conclusions remain valid, when more users are supported, namely, also in the scenario when MUI is imposed. In this part, a two-user scenario is considered, where there are $M^K = 4^2$=16 legitimate transmission symbol vectors. The simulation parameters are listed in Table 3.7. The CIRs of the (2×2)-element system are:

$$\mathbf{H} = \begin{bmatrix} 0.045 + j0.121 & -0.797 - j0.435 \\ -0.574 - j0.340 & -0.262 - j1.920 \end{bmatrix}.$$

If the baseband received signals are expressed in the form given in Equation 3.43, for the MUD receiver weights $\mathbf{W}_{mmse}$, we have

$$\mathbf{W}_{mmse} = \begin{bmatrix} 1.865 - j0.004 & -0.562 + j0.726 \\ -0.459 + j0.533 & -0.140 + j0.169 \end{bmatrix}, \tag{3.44}$$

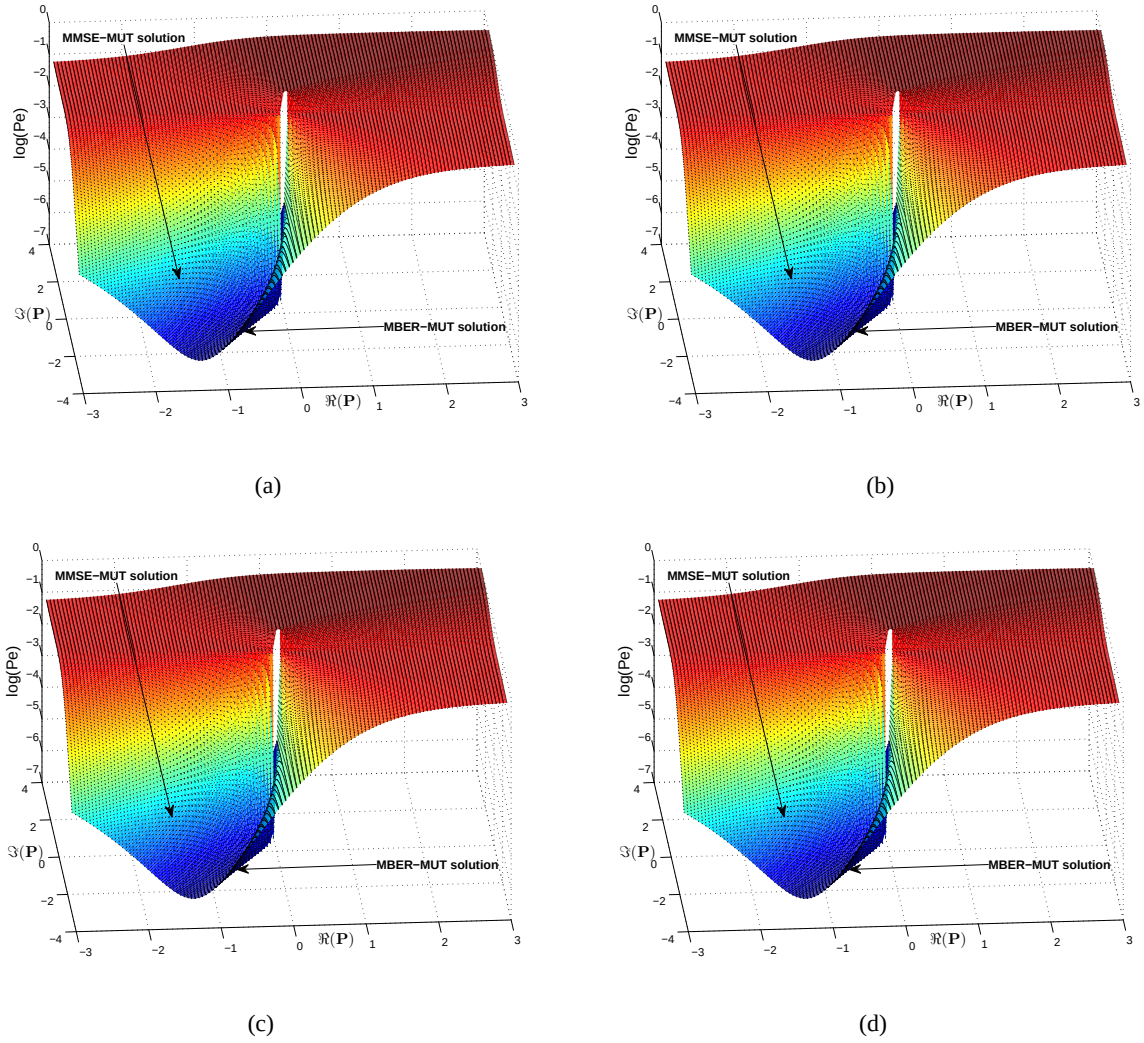

Figure 3.13: The BER cost function surfaces for the system invoking the symbol-specific MBER-MUT algorithm and employing N=1 transmit antenna to support K=1 QPSK user for communicating over flat Rayleigh fading channel at Eb/No=5dB. The channel coefficient is $\mathbf{H} = [-1.09678 + j0.481258]$. (a) $\mathbf{x} = [\frac{\sqrt{2}}{2} + j\frac{\sqrt{2}}{2}]$. (b) $\mathbf{x} = [\frac{\sqrt{2}}{2} - j\frac{\sqrt{2}}{2}]$. (c) $\mathbf{x} = [-\frac{\sqrt{2}}{2} + j\frac{\sqrt{2}}{2}]$. (d) $\mathbf{x} = [-\frac{\sqrt{2}}{2} - j\frac{\sqrt{2}}{2}]$. Since the cost function is undefined when $\mathbf{W} = [0 + j0]$, hence there are blank points in these figures.

and

$$\mathbf{W}_{mber} = \begin{bmatrix} 1.074 - j0.053 & -0.470 + j0.612 \\ -0.328 + j0.333 & -0.115 + j0.113 \end{bmatrix}. \tag{3.45}$$

By contrast, in the case of the MMSE-MUT and the average MBER-MUT algorithms, the precoder weights are:

$$\mathbf{P}_{mmse} = \begin{bmatrix} 1.865 - j0.004 & -0.562 + j0.726 \\ -0.459 + j0.533 & -0.140 + j0.169 \end{bmatrix}, \tag{3.46}$$

and

$$\mathbf{P}_{a-mber} = \begin{bmatrix} 1.074 - j0.053 & -0.470 + j0.612 \\ -0.328 + j0.333 & -0.115 + j0.113 \end{bmatrix}. \tag{3.47}$$

Table 3.7: Simulation parameters in the $K = 2$ users case.

Parameter	Value or Type
Modulation scheme	QPSK
Transmit (or receive) antennas	2
Number of users	2
Channel	flat Rayleigh fading
CSIT (or CSIR) knowledge	perfect
SNR	10 dB

When the symbol-specific MBER-MUT algorithm is considered, we arrive at different results emerging from our simulations. When $\mathbf{x} = [\frac{\sqrt{2}}{2} + j\frac{\sqrt{2}}{2} \quad \frac{\sqrt{2}}{2} + j\frac{\sqrt{2}}{2}]^T$ or $\mathbf{x} = [-\frac{\sqrt{2}}{2} - j\frac{\sqrt{2}}{2} \quad -\frac{\sqrt{2}}{2} - j\frac{\sqrt{2}}{2}]^T$ or $\mathbf{x} = [\frac{\sqrt{2}}{2} - j\frac{\sqrt{2}}{2} \quad \frac{\sqrt{2}}{2} - j\frac{\sqrt{2}}{2}]^T$ or $\mathbf{x} = [-\frac{\sqrt{2}}{2} + j\frac{\sqrt{2}}{2} \quad -\frac{\sqrt{2}}{2} + j\frac{\sqrt{2}}{2}]^T$, the values for the precoding matrix are:

$$\mathbf{P}_{ss-mber,1} = \begin{bmatrix} 1.058 + j0.090 & -0.287 + j0.496 \\ -0.440 + j0.264 & -0.115 + j0.258 \end{bmatrix}. \tag{3.48}$$

By Contrast, for $\mathbf{x} = [\frac{\sqrt{2}}{2} - j\frac{\sqrt{2}}{2} \quad \frac{\sqrt{2}}{2} + j\frac{\sqrt{2}}{2}]^T$ or $\mathbf{x} = [-\frac{\sqrt{2}}{2} + j\frac{\sqrt{2}}{2} \quad -\frac{\sqrt{2}}{2} - j\frac{\sqrt{2}}{2}]^T$ or $\mathbf{x} = [\frac{\sqrt{2}}{2} + j\frac{\sqrt{2}}{2} \quad -\frac{\sqrt{2}}{2} + j\frac{\sqrt{2}}{2}]^T$ or $\mathbf{x} = [-\frac{\sqrt{2}}{2} - j\frac{\sqrt{2}}{2} \quad \frac{\sqrt{2}}{2} - j\frac{\sqrt{2}}{2}]^T$, the values for the precoding matrix are:

$$\mathbf{P}_{ss-mber,2} = \begin{bmatrix} 1.118 - j0.061 & -0.394 + j0.430 \\ -0.425 + j0.398 & -0.004 + j0.252 \end{bmatrix}. \tag{3.49}$$

For $\mathbf{x} = [-\frac{\sqrt{2}}{2} + j\frac{\sqrt{2}}{2} \quad \frac{\sqrt{2}}{2} + j\frac{\sqrt{2}}{2}]^T$ or $\mathbf{x} = [\frac{\sqrt{2}}{2} - j\frac{\sqrt{2}}{2} \quad -\frac{\sqrt{2}}{2} - j\frac{\sqrt{2}}{2}]^T$ or $\mathbf{x} = [\frac{\sqrt{2}}{2} + j\frac{\sqrt{2}}{2} \quad \frac{\sqrt{2}}{2} - j\frac{\sqrt{2}}{2}]^T$ or $\mathbf{x} = [-\frac{\sqrt{2}}{2} - j\frac{\sqrt{2}}{2} \quad -\frac{\sqrt{2}}{2} + j\frac{\sqrt{2}}{2}]^T$, the values for the precoding matrix are:

$$\mathbf{P}_{ss-mber,3} = \begin{bmatrix} 1.001 + j0.180 & -0.245 + j0.872 \\ -0.158 + j0.258 & -0.213 - j0.087 \end{bmatrix}. \tag{3.50}$$

Finally, for $\mathbf{x} = [-\frac{\sqrt{2}}{2} - j\frac{\sqrt{2}}{2} \quad \frac{\sqrt{2}}{2} + j\frac{\sqrt{2}}{2}]^T$ or $\mathbf{x} = [\frac{\sqrt{2}}{2} + j\frac{\sqrt{2}}{2} \quad -\frac{\sqrt{2}}{2} - j\frac{\sqrt{2}}{2}]^T$ or $\mathbf{x} = [\frac{\sqrt{2}}{2} - j\frac{\sqrt{2}}{2} \quad -\frac{\sqrt{2}}{2} + j\frac{\sqrt{2}}{2}]^T$ or $\mathbf{x} = [-\frac{\sqrt{2}}{2} + j\frac{\sqrt{2}}{2} \quad \frac{\sqrt{2}}{2} - j\frac{\sqrt{2}}{2}]^T$, the values for the precoding matrix are:

$$\mathbf{P}_{ss-mber,4} = \begin{bmatrix} 1.017 - j0.258 & -0.823 + j0.365 \\ -0.156 + j0.212 & -0.067 - j0.108 \end{bmatrix}. \tag{3.51}$$

As we can see, the weights of the MBER-MUD and those of the average MBER-MUT are identical, since they are obtained by averaging over all the 16 legitimate transmission symbol vectors. Moreover, those of the latter are more difficult to derive in practice owing to the additional total transmit power constraint of Equation (3.6).

For the symbol-specific MBER-MUT scheme, there are four different sets of precoding matrices $\mathbf{P}$ based on the 16 legitimate transmission symbol vectors considered. This fact suggests that different sets of legitimate transmission symbol vectors may results in the same precoding matrices. Nevertheless, this precoding matrix is specifically designed for these sets of legitimate transmission symbol vectors, which

is in contrast to the more generic average MBER-MUT solution. This explains the BER performance gain of the symbol-specific MBER-MUT over the average MBER-MUT, which is achieved at the expense of an increased computational complexity.

3.7.7 Convergence and complexity

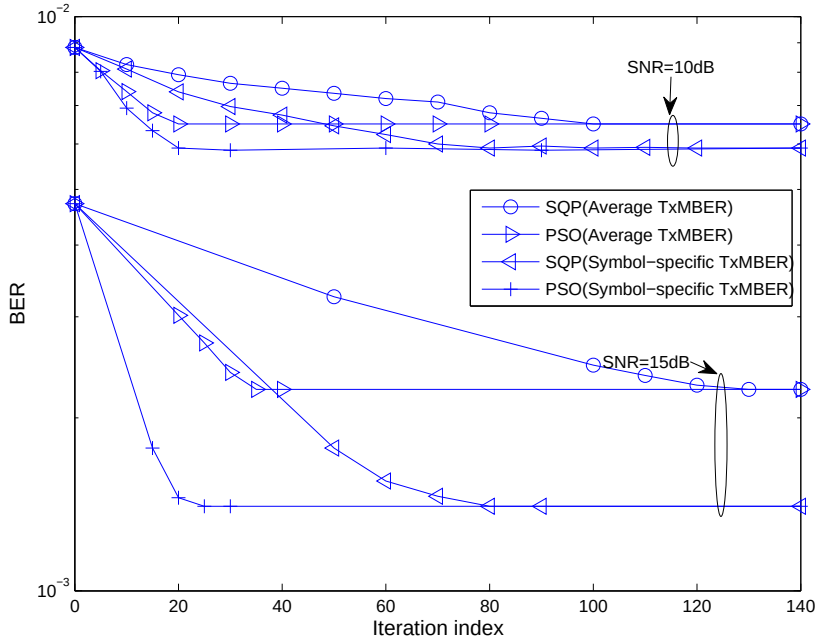

Figure 3.14: Convergence performance of the SQP as well as PSO-SS and PSO-A MBER-MUT schemes for the system employing $N = 4$ transmit antennas to support $K = 4$ QPSK mobile users over flat Rayleigh fading channels at Eb/No=10 dB and 15 dB, repsectively. All system parameters are summarized in Table 3.5.

In this section, we provide a convergence and complexity study for the SQP as well as for the PSO-SS and PSO-A MBER-MUT schemes for the system employing $N = 4$ transmit antennas to support $K = 4$ QPSK mobile users communicating over flat Rayleigh fading channels. The simulation parameters are listed in Table 3.5.

Fig. 3.14 compares the convergence performance of the SQP as well as PSO based symbol-specific and average MBER MUT schemes, operating at the SNR values of 10 dB and 15 dB, respectively. For the symbol-specific MBER MUT communicating at SNR$=$ 10 dB, it can be seen from Fig. 3.14 that the SQP algorithm converged to the optimal solution after 70 iterations, while its PSO counterpart arrived at the same optimal solution after 20 iterations. In the case of the average MBER-MUT design operating at SNR$=$ 10 dB, the SQP algorithm converged to the optimal solution after 100 iterations, while the PSO algorithm arrived at the same optimal solution after 20 iterations.

Fig. 3.15 shows the complexity versus iteration index for the four MBER-MUT designs studied at the SNR value of 10 dB. For the symbol-specific MBER MUT communicating at SNR$=$ 10 dB, the SQP

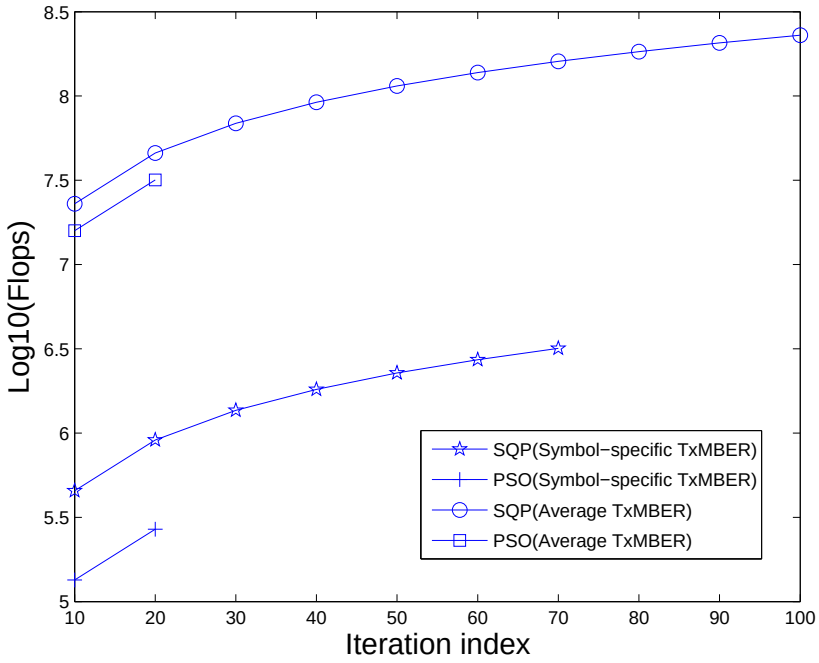

Figure 3.15: Complexity versus iteration index comparison of the SQP as well as PSO-SS and PSO-A MBER-MUT schemes for the system employing $N = 4$ transmit antennas to support $K = 4$ QPSK mobile users over flat Rayleigh fading channels at Eb/No=10 dB. All system parameters are summarized in Table 3.5.

algorithm required 3,180,170 Flops to converge to the optimal solution, while the PSO aided algorithm converged to the same optimal solution at the cost of 268,560 Flops. Hence the PSO-aided symbol-specific MBER-MUT design imposed an approximately twelve times lower complexity than its SQP counterpart for this case. For the average MBER MUT design operating at SNR$=10$ dB, the SQP algorithm needed 229,351,100 Flops to converge to the optimal solution, while the PSO aided algorithm converged at the cost of 34,561,760 Flops. Therefore, the PSO-aided average MBER-MUT design imposed an approximately seven times lower complexity than its SQP counterpart in the scenario investigated.

It can also be seen from Fig. 3.14 that at SNR$=15$ dB the SQP based symbol-specific MBER MUT converged after 80 iterations, which required 3,634,480 Flops, while the PSQ-aided symbol-specific MBER MUT achieved convergence after 30 iterations, which required 402,840 Flops. Thus, the PSO-aided symbol-specific MBER-MUT design imposed an approximately nine times lower complexity than its SQP counterpart for the SNR value of 15 dB. Similarly, it can be seen from Fig. 3.14 that at SNR$=15$ dB the SQP based average MBER MUT algorithm took 140 iterations to converge at a total complexity cost of 321,091,540 Flops, while the PSO-aided average MBER MUT design needed 40 iterations to converge at a total cost of 63,541,120 Flops. It was then plausible that the PSO-aided average MBER-MUT design imposed an approximately five times lower complexity than its SQP-based counterpart investigated in this scenario.

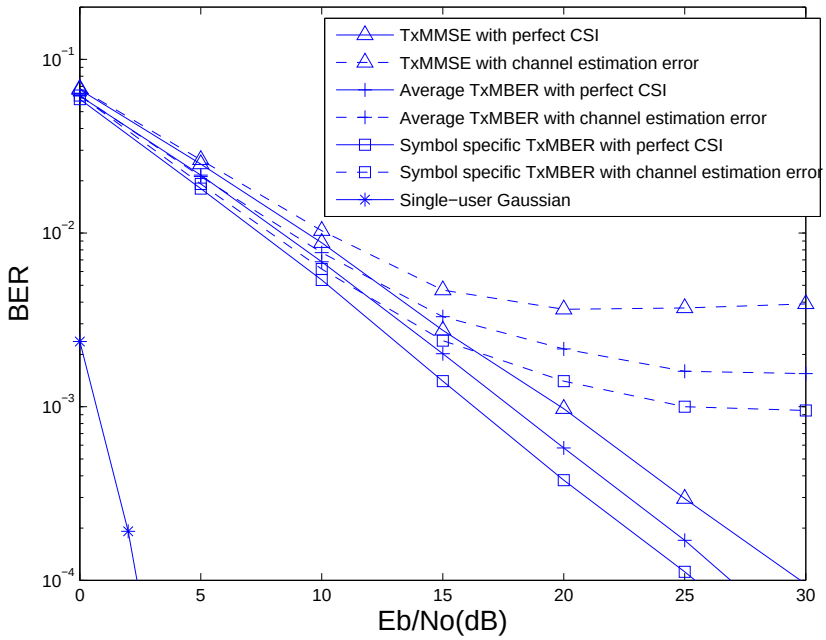

Figure 3.16: BER versus SNR performance of the PSO-SS MBER-MUT and PSO-A MBER-MUT communicating over flat Rayleigh fading channels using $N = 4$ transmit antennas to support $K = 4$ QPSK mobile users, in comparison with the benchmark MMSE-MUT. The channel estimation error was assumed to be Gaussian and had a standard deviation of 0.05 er noise-dimension. All system parameters are summarized in Table 3.5.

3.7.8 Performance and Discussions

The BER versus SNR performances of the PSO-SS MBER-MUT and PSO-A MBER-MUT schemes communicating over flat Rayleigh fading channels using $N = 4$ transmit antennas to support $K = 4$ QPSK mobile users, can be seen in Fig. 3.16 in comparison to the benchmark MMSE-MUT scheme. The simulation parameters are listed in Table 3.5.

Fig. 3.16 compares the BER performance of the MMSE-MUT scheme to those of the PSO-SS MBER-MUT and PSO-A MBER-MUT schemes, assuming a perfect CSI knowledge at the BS. It is seen that the PSO-SS MBER-MUT achieved an SNR gain of 4.5 dB over the MMSE-MUT at the target BER of 10^{-4}, while the PSO-A MBER-MUT provided an SNR gain of 3 dB over the MMSE-MUT scheme at the same target BER level. The robustness of the two PSO-aided MBER-MUT schemes to channel estimation error was also investigated by adding a Gaussian white noise with a standard deviation of 0.05 per dimension to each channel tap $h_{i,k}$ to represent channel estimation error. The BERs of the MMSE-MUT and the two PSO based MBER-MUT schemes under this channel estimation error are also plotted in Fig. 3.16. It can be seen that both the PSO-SS and PSO-A MBER-MUT designs were no more sensitive to channel estimation error than the MMSE-MUT design.

3.8 Conclusions

Table 3.8: Computational complexity summary.

	Complexity(Flops)/SNR	Complexity(Flops)/SNR
SQP (Average MBER-MUT)	229,351,100/10dB	321,091,540/15dB
PSO (Average MBER-MUT)	34,561,760/10dB	63,541,120/15dB
SQP (Symbol-specific MBER-MUT)	3,180,170/10dB	3,634,480/15dB
PSO (Symbol-specific MBER-MUT)	268,560/10dB	402,840/15dB

In this chapter, we focused our attention on the computational complexity reduction of linear MBER-MUTs, namely that of the symbol-specific MBER-MUT and of the average MBER-MUT. The MUT using the MMSE criterion is popular owing to its implementational and concept simplicity. However, since the BER is the ultimate system performance indicator, we are more interested in the MBER-MUT design. Unlike the MBER-MUD, the MBER-MUT design encounters a power constrained nonlinear optimization problem. The SQP algorithm [24] may be used to obtain the precoder's coefficients. However, the computational complexity of the SQP based MBER-MUT solution may be excessive for high-rate systems. Hence, as an attractive design alternative, in this chapter, continuous-valued PSO was invoked in order to find the MBER-MUT's precoder matrix $\mathbf{P}$ for reducing its computational complexity.

Two PSO aided MBER-MUTs were designed and characterized in this chapter. The first one may be referred to as the symbol-specific MBER-MUT, while the other one as the average MBER-MUT. Simulation results of Fig. 3.15 demonstrated that both of our designs provide an improvement in comparison to conventional linear MUT schemes at a reduced complexity compared to the state-of-art SQP based MBER-MUT. More explicitly, in the case of the symbol-specific MBER-MUT of Section 3.4.1, for example, in a (4×4)-element MIMO system communicating over flat Rayleigh fading channels at an SNR of $\frac{Eb}{No} = 10$dB when a QPSK modulation scheme is adopted, observe in Fig. 3.14 that our PSO aided MBER-MUT algorithm arrives at the MBER-MUT solution at a twelve times lower complexity than the SQP based MBER-MUT design as seen in Table 3.8. Similarly, observe in Table 3.8 that its computational complexity is nine times lower than that of the SQP based approach when the operating SNR is $\frac{Eb}{No} = 15$ dB. In the case of the average MBER-MUT scheme of Section 3.4.2, for example, in a (4×4)-element MIMO system communicating over flat Rayleigh fading channels at an given SNR of $\frac{Eb}{No} = 10$dB when a QPSK modulation scheme is adopted, our PSO aided MBER-MUT algorithm arrives at the MBER-MUT solution at a seven times lower complexity than the SQP based MBER-MUT design. Similarly, its computational complexity is seen to be five times lower in Fig. 3.14 than that of the SQP based approach, when the operating SNR is $\frac{Eb}{No} = 15$dB, again, these are summarized in Table 3.8.

These results demonstrated the efficiency of using continous-valued PSO algorithms in deriving the linear MBER-MUT's precoder weights at a reduced computational complexity. In the next chapter, we will look into the application of discrete-valued PSO algorithm in the area of the promising nonlinear MUT scheme, namely vector precoding.

Chapter 4

Particle Swarm Optimization Aided Vector Precoding

4.1 Introduction and Relevance to Previous Chapters

In Chapter 3, we demonstrated the efficiency of using continous-valued PSO algorithms in deriving the linear MBER-MUT's precoder weights at a reduced computational complexity. However, the computational complexity becomes potentially higher fir the VP considered in this chapter, which constitutes a nonlinear MUT.

As we argued in Section 2.1.2.3, the classic sphere encoding algorithm [23], which has a similar reduced-search philosophy to that of the sphere decoding algorithm [33] used in MUD [1], is indeed capable of achieving the optimum performance. However, its computational complexity may become prohibitive in high-dimensional problems. Several suboptimum algorithms have been proposed in order to reduce the average complexity at the expense of some performance degradation. In [34], the authors adopted the lattice reduction method [144] and Babai's approximate closest point solution [144] for the sake of reducing the complexity of the nonlinear VP, following a similar philosophy to those of [145] and [146]. The authors of [4] extended these solutions to MMSE-VP based on [32].

Against this background, in this chapter we embark on designing a low-complexity search algorithm based on the discrete-valued PSO instead of the sphere encoding algorithm of [23] for finding the optimum perturbation vector in order to reduce the computational complexity imposed. This approach provides a flexible computational complexity as a benefit of its iterative optimization, while the lattice-reduction approach of [4] has a non-reconfigurable complexity.

The system model is introduced in Section 4.2 and we revisit the cost functions for VP in Section 4.3. In Section 4.4, a rudimentary introduction to the discrete multi-valued PSO is provided. The discrete multi-valued PSO aided low-complexity VP design is proposed in Section 4.5 and the corresponding computational complexity is discussed in Section 4.6. Our simulation results are provided in Section 4.7, followed by our discussions and the chapter conclusions in Section 4.8.

4.2 System Model

As previously detailed in the context of Fig. 2.3 in Section 2.1.2.1, the DL of an SDMA system supporting non-cooperative mobile receivers is considered here, where the BS equipped with N transmit antennas communicates with K non-cooperative MSs over frequency-flat fading channels, each employing a single receive antenna and a modulo device. The system model used throughout this chapter is the same as the one we introduced in Section 2.1.2.1, which is repeatly described in the following for the reader's convenience.

The K-element information symbol vector to be perturbed is given by $\mathbf{x} = [x_1, x_2, \cdots, x_K]^T$, where the symbol energy is $E[|x_k|^2] = \sigma_x^2$, for $1 \leq k \leq K$, and x_k is an i.i.d. uniformly distributed random variable. Recall from Section 2.1.2.1 that the perturbed symbol vector $\mathbf{u}$ having a dimension of K is given by $\mathbf{u} = \mathbf{x} + \boldsymbol{\omega}$, where $\boldsymbol{\omega}$ is the perturbation vector given as [23] $\boldsymbol{\omega} = \tau\boldsymbol{\zeta}$. The $(N \times K)$-element precoding matrix $\mathbf{P}$ is denoted as $\mathbf{P} = [\mathbf{p}_1, \mathbf{p}_2, \cdots, \mathbf{p}_K]$, where $\mathbf{p}_k$, $1 \leq k \leq K$ represents the precoder's coefficient vector configured for the kth user's data stream. The $(K \times N)$-element channel matrix $\mathbf{H}$ is denoted as $\mathbf{H} = [\mathbf{h}_1, \mathbf{h}_2, \cdots, \mathbf{h}_K]^T$, where $\mathbf{h}_k$, $1 \leq k \leq K$ is the kth user's CIR, which is given by $\mathbf{h}_k = [h_{k,1}, h_{k,2}, \cdots, h_{k,N}], k = 1, 2, \cdots, K$. The CIR taps $h_{k,i}$, for $1 \leq k \leq K$ and $1 \leq i \leq N$ are independent of each other and obey the complex-valued Gaussian distribution associated with $\mathrm{E}[|h_{k,i}|^2] = 1$. The Gaussian noise vector $\mathbf{n}$ is given by $\mathbf{n} = [n_1, n_2, \cdots, n_K]^T$, where $n_k, 1 \leq k \leq K$ is a complex-valued Gaussian random variable with zero mean and $E[|n_k|^2] = 2\sigma_n^2 = \mathrm{N_o}$. When the total transmit power is constrained to be $\mathrm{E_T}$ at the BS, an appropriate scaling factor is used to fulfill this transmit power constraint, which is defined as $\alpha = \sqrt{\mathrm{E_T}/\|\mathbf{d}\|^2}$. At the receiver, the reciprocal of the scaling factor, namely α^{-1}, is used to scale the received signal in order to maintain a unity-gain transmission, again, as detailed in Section 2.1.2.1.

Thus, the signal vector before the modulo operation can be described as $\hat{\mathbf{y}} = \mathbf{HPu} + \alpha^{-1}\mathbf{n}$, the received signal vector $\mathbf{y} = [y_1\ y_2 \cdots y_K]^T$ after the modulo operation is given by $\mathbf{y} = mod_\tau(\hat{\mathbf{y}})$, and y_k, $1 \leq k \leq K$, constitutes sufficient statistics for the kth MS to detect the transmitted information data symbol x_k through quantization.

4.3 Cost Functions for Vector Precoding

The cost functions for ZF-VP and MMSE-VP have been introduced in Section 2.1.2.2 and Section 2.1.2.3, respectively. More explicitly, the cost function of ZF-VP was formulated in Equation (2.31) as:

$$\boldsymbol{\omega}_{ZF} = \arg\min_{\boldsymbol{\omega}} \|\mathbf{H}^H(\mathbf{H}\mathbf{H}^H)^{-1}(\mathbf{x} + \boldsymbol{\omega})\|_2^2,$$

while the cost function of MMSE-VP was given in Equation (2.59) as:

$$\boldsymbol{\omega}_{MMSE} = \arg\min_{\boldsymbol{\omega}} \|\mathbf{L}(\mathbf{x} + \boldsymbol{\omega})\|_2^2.$$

The perturbation vector is given by $\boldsymbol{\omega} = \tau\boldsymbol{\zeta}$, where τ is a positive number determined by the modulation constellation employed. More explicitly, if the M-point square-shaped Gray coded quadrature amplitude modulation (QAM) constellation of

$$\Big\{ \pm\frac{1}{2}, \cdots, \pm\frac{\sqrt{M}-1}{2} \Big\} + j\Big\{ \pm\frac{1}{2}, \cdots, \pm\frac{\sqrt{M}-1}{2} \Big\}$$

is used, the modulo operation parameter can be set to $\tau = \sqrt{M}$ [4, 32], and $\boldsymbol{\zeta}$ is a complex-valued vector whose components are $a + jb$, where a and b are integers.

4.4 Discrete Multi-Valued PSO

Typical discrete particle swarm optimization algorithms are designed for binary-valued optimization problems [129]. As we will show in Section 4.7, for each corresponding search space of the real and imaginary part of the K-element complex-valued $\boldsymbol{\zeta}$ may be restricted to be $[-2, -1, 0, 1, 2]^{2\times K}$. If the binary-valued PSO is employed [129], this five-element set requires a three-bit binary representation, which ranges between [0-7] covering 8 integers, while we only need five of them in our case. Thus, special measures would be required to handle the values outside the original five-element range of the discrete variable. Hence, binary-valued PSO techniques are not ideal for our problem and we adopted a discrete multi-valued PSO to solve our specific problem in this case. More explicitly, we follow the proposals outlined in [135] and invoke the authors' discrete multi-valued PSO algorithm after appropriate modifications in order to solve our problem. In the next section, the original discrete multi-valued PSO algorithm proposed in [135] is introduced.

4.4.1 Discrete Multi-Valued PSO

The discrete multi-valued PSO algorithm proposed in [135] deals with optimization problems, where the range of discrete variable values spans $[0, \quad (M-1)]$. Hence, this algorithm is capable of solving a generic discrete and complex-valued optimization problem formulated as:

$$\check{\mathbf{P}}_{opt} = \arg\min_{\check{\mathbf{P}}} F(\check{\mathbf{P}}); \quad s.t. : \check{\mathbf{P}} \in \mathsf{S}^{N\times K}, \tag{4.1}$$

where $\check{\mathbf{P}}$ is a $(N \times K)$-element discrete and complex-valued matrix to be optimized, and

$$\mathsf{S} = [0,\ M-1] + j[0,\ M-1] \tag{4.2}$$

defines the search range for each element of $\check{\mathbf{P}}$. The flow chart of the corresponding PSO algorithm is shown in Fig.4.1. A swarm of particles $\{\check{\mathbf{P}}_i^{(l)}\}_{i=1}^{S}$, which represents the potential solutions is evolved in the search space $\mathsf{S}^{N\times K}$, where S is the swarm size and the index l denotes the iteration index. The search process of this discrete multi-valued PSO is explained as follows:

1) The swarm initialization - block 1 of Fig. 4.1.

This step is similar to what we have introduced for block 1 of Fig. 2.8 in the context of the MBER-MUT. In other words, the procedures of the MBER-MUT are also applicable for the VP design of this chapter. For the reader's convenience we repeat these procedures here. At $l = 0$, the initial particles, $\{\check{\mathbf{P}}_i^{(0)}\}_{i=1}^{S}$, are randomly generated in the search space $\mathsf{S}^{N\times K}$. More explicitly, the real and imaginary part of every element of the particles $\{\check{\mathbf{P}}_i^{(0)}\}_{i=1}^{S}$ is initialized to a discrete number within the range $[0 \quad M-1]$.

2) The swarm evaluation - block 2 of Fig. 4.1.

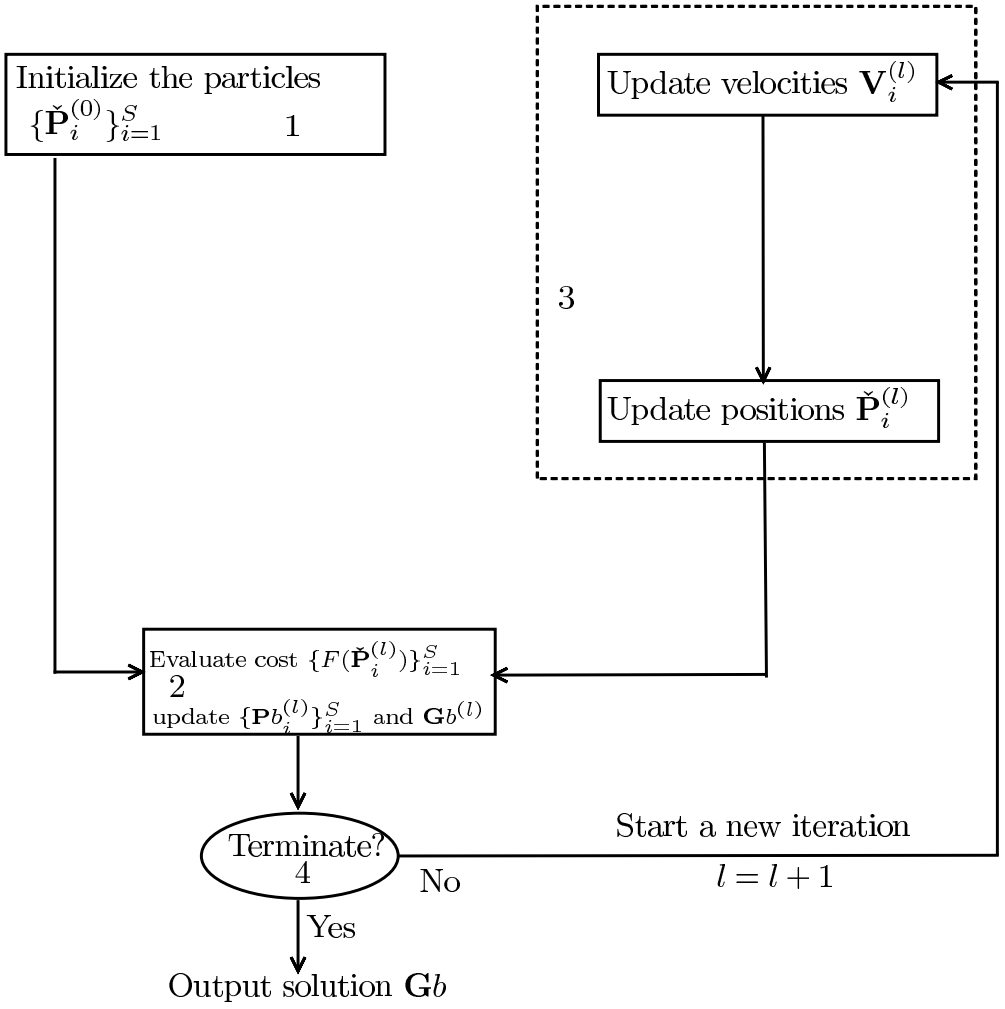

Figure 4.1: Flow chart of the discrete multi-valued PSO algorithm

Again, this part of the PSO-aided VP is identical to the one we have already introduced in block 2 of Fig. 2.8 in Section 2.2.1.3. More explicitly, each particle $\check{\mathbf{P}}_i^{(l)}$ is associated with a fitness value $F(\check{\mathbf{P}}_i^{(l)})$, which is evaluated based on the cost function given in Equation (2.31) for the ZF-VP and by Equation (2.59) for the MMSE-VP. Each particle $\check{\mathbf{P}}_i^{(l)}$ is capable of remembering its best individual position visited so far, denoted as $\mathbf{P}b_i^{(l)}$, which provides the cognitive information. Every particle also remembers the best position visited so far by the entire swarm, denoted as $\mathbf{G}b^{(l)}$, which provides the social information. As seen in Fig. 4.1, both $\{\mathbf{P}b_i^{(l)}\}_{i=1}^S$ and $\mathbf{G}b^{(l)}$ are updated in each iteration, if a better individual particle position and an improved swarm best position is found, respectively.

To elaborate a little further, $\{\mathbf{P}b_i^{(l)}\}_{i=1}^S$ is updated in block 2 of Fig. 4.1. For the ith particle, where $1 \leq i \leq S$, the CF values of $F(\check{\mathbf{P}}_i^{(l)})$ and $F(\mathbf{P}b_i^{(l)})$ are compared in block 2 of Fig. 4.1. If the CF value of $F(\check{\mathbf{P}}_i^{(l)})$ is equal to or higher than that of $F(\mathbf{P}b_i^{(l)})$, this implies that the new position that the ith particle visited during the lth iteration yields a higher CF value, i. e. a reduced fitness in our case. Hence the new visited position is no better than the ith particle's previously visited best position during its most recent $(l-1)$ iterations. Therefore the CF values of $F(\mathbf{P}b_i^{(l)})$ and $\mathbf{P}b_i^{(l)}$ will remain the same as their previous values, namely $F(\mathbf{P}b_i^{(l-1)})$ and $\mathbf{P}b_i^{(l-1)}$, respectively. If the CF value of $F(\check{\mathbf{P}}_i^{(l)})$ is lower than that of $F(\mathbf{P}b_i^{(l)})$, then the new position that the ith particle visited during the lth iteration yields a lower CF value,

i. e. an increased fitness, hence the new visited position is better than the ith particle's previously visited best position during its last $(l-1)$ iterations. Consequently the CF value of $F(\mathbf{P}b_i^{(l)})$ and $\mathbf{P}b_i^{(l)}$ will be replaced by those of $F(\mathbf{P}b_i^{(l)})$ and $\mathbf{P}b_i^{(l)}$, respectively.

As seen in block 2 of Fig. 4.1, after the update of $\{\mathbf{P}b_i^{(l)}\}_{i=1}^{S}$, $\mathbf{G}b^{(l)}$ is updated. The best individual particle position at the lth iteration $\mathbf{P}b_{i^*}^{(l)}$ is the one, which provides the lowest CF value, namely the highest fitness value. Then, the CF value of $F(\mathbf{P}b_{i^*}^{(l)})$ is compared to that of $F(\mathbf{G}b^{(l)})$. If the value of $F(\mathbf{P}b_{i^*}^{(l)})$ is lower than that of $F(\mathbf{G}b^{(l)})$, then the best position that the whole swarm visited during the lth iteration results in a reduced CF value, namely an increased fitness value. Hence the position of $\mathbf{P}b_{i^*}^{(l)}$ is better than the entire swarm's previously visited best position $\mathbf{G}b^{(l-1)}$ during its last $(l-1)$ iterations. Hence the CF value of $F(\mathbf{G}b^{(l)})$ and $\mathbf{G}b^{(l)}$ will be replaced by those of $F(\mathbf{P}b_{i^*}^{(l)})$ and $\mathbf{P}b_{i^*}^{(l)}$, respectively. Otherwise, $F(\mathbf{G}b^{(l)})$ and $\mathbf{G}b^{(l)}$ will remain the same $F(\mathbf{G}b^{(l-1)})$ and $\mathbf{G}b^{(l-1)}$, respectively. The related pseudocode is as follows:

For ($i = 1$; $i \leq S$; i++)
  If [$F(\check{\mathbf{P}}_i^{(l)}) < F(\mathbf{P}b_i^{(l)})$] $\mathbf{P}b_i^{(l)} = \check{\mathbf{P}}_i^{(l)}$;
End for;
$i^* = \arg\min_{1\leq i\leq S} F(\mathbf{P}b_i^{(l)})$;
If [$F(\mathbf{P}b_{i^*}^{(l)}) < F(\mathbf{G}b^{(l)})$] $\mathbf{G}b^{(l)} = \mathbf{P}b_{i^*}^{(l)}$;

3) The swarm update - block 3 of Fig. 4.1.

In contrast to block 1 and 2 of the MBER-MUT, this block of the VP design is different from what we observed in block 3 of Fig. 2.8 in Section 2.2.1.3. The difference lies in the process of updating the position $\check{\mathbf{P}}_i$ which is detailed in the following.

Explicitly, each particle $\check{\mathbf{P}}_i$ has a velocity $\mathbf{V}_i^{(l)}$ during the lth iteration, which controls its 'flight'. The velocity and position of the ith particle at the $(l+1)$st iteration are updated according to Equation (2.63), which is repeated here for convenience:

$$\mathbf{V}_i^{(l+1)} = w^{(l+1)} \cdot \mathbf{V}_i^{(l)} + rand() \cdot c_1 \cdot [\mathbf{P}b_i^{(l)} - \check{\mathbf{P}}_i^{(l)}] + rand() \cdot c_2 \cdot [\mathbf{G}b^{(l)} - \check{\mathbf{P}}_i^{(l)}],$$

where $rand()$ denotes the uniform random number between 0 and 1, and $c_1 = 1.0$ and $c_2 = 1.0$ are the two acceleration coefficients, $w^{(l+1)}$ is the inertia weight. The inertia weight is updated from iteration to iteration, according to the following equation [135]:

$$w^{(l)} = \frac{(w_{max} - 0.4) \cdot (I_{\max} - l)}{I_{\max} - 0.4}, \tag{4.3}$$

where $w_{max} = 0.9$ and $I_{\max}$ is the maximum number of iterations. The effect of this time-variant inertia weight is that in the early iterative stages, the particles would explore the entire search space, since the particles' momentum is preserved from the previous iteration, hence a global search is facilitated. By contrast, during the later iterative stages, the employment of a low inertia weight value would facilitate a rapidly converging local search. This allows the PSO algorithm to explore the entire legitimate search range, hence avoiding premature convergence to a local optimum.

In contrast to the approach adopted in Equation (2.64) in the context of continous-valued PSO aided MBER-MUT which produces continous-valued position and in Equation (2.73) in the context of binary PSO which generates binary-valued position, each element of the velocity vector $\mathbf{V}$ here is transformed into an integer number between $[0, \ M]$ using the sigmoid transformation [129]:

$$\begin{aligned} sig(\Re[\mathbf{V}_i^{(l+1)}|_{p,q}]) &= \frac{M}{1+e^{-(\Re[\mathbf{V}_i^{(l+1)}|_{p,q}])}}, \\ sig(\Im[\mathbf{V}_i^{(l+1)}|_{p,q}]) &= \frac{M}{1+e^{-(\Im[\mathbf{V}_i^{(l+1)}|_{p,q}])}}. \end{aligned} \tag{4.4}$$

The position of the particle $\check{\mathbf{P}}_i^{(l+1)}$ is updated also differently from Equation (2.64) as detailed below. More explicitly, each element of the complex-valued position $\Re[\check{\mathbf{P}}_i^{(l+1)}|_{p,q}]$ and $\Im[\check{\mathbf{P}}_i^{(l+1)}|_{p,q}]$ is generated using the Gaussian distribution with a mean and standard deviation of $N[sig(\Re[\mathbf{V}_i^{(l+1)}|_{p,q}]), \ \varrho(M-1)]$ or $N[sig(\Im[\mathbf{V}_i^{(l+1)}|_{p,q}]), \ \varrho(M-1)]$ respectively, where ϱ is a number to be chosen in order to enhance the algorithm's performance, and it was suggested to employ $\varrho = 0.2$ for a ternary system in [135]. The position of the particle $\check{\mathbf{P}}_i^{(l+1)}$ is updated according to the rules detailed in the next paragraph.

Let us consider the generation of the position $\Re[\check{\mathbf{P}}_i^{(l+1)}|_{p,q}]$ as an example. We randomly pick a number from the Gaussian distribution associated with the center or mean of $sig(\Re[\mathbf{V}_i^{(l+1)}|_{p,q}])$ and standard deviation of $(M-1)\cdot\varrho$. Then we "round" this number to the nearest integer. If the integer is less than 0, then the position $\Re[\check{\mathbf{P}}_i^{(l+1)}|_{p,q}]$ is set to 0, else if the integer is larger than $(M-1)$, then $\Re[\check{\mathbf{P}}_i^{(l+1)}|_{p,q}]$ is set to $(M-1)$, otherwise $\Re[\check{\mathbf{P}}_i^{(l+1)}|_{p,q}]$ is set to the closest integer. For example, if the search range of the problem encompasses the integer positions in the range of $[0, \ 4]$, and we have $\Re[\mathbf{V}_i^{(l+1)}|_{p,q}]$=0.8, then given the mean of $sig(\Re[\mathbf{V}_i^{(l+1)}|_{p,q}])$=3.4499, the center of the corresponding normal distribution is 3.4499. Furthermore, the standard deviation is $(M-1)\cdot\varrho = 0.2\cdot(5-1) = 0.8$. Assuming that the randomly picked number is 2, since it is in the range of $[0, \ 4]$, hence we have $\Re[\check{\mathbf{P}}_i^{(l+1)}|_{p,q}] = 2$. The corresponding pseudocode used for the VP, which has to be contrasted to Equation (2.64) of the MBER-MUT is as follows:

$$\Re[\check{\mathbf{P}}_i^{(l+1)}|_{p,q}] = round[sig(\Re[\mathbf{V}_i^{(l+1)}|_{p,q}]) + (M-1)\cdot\varrho\cdot randn())] \tag{4.5}$$

$$\Re[\check{\mathbf{P}}_i^{(l+1)}|_{p,q}] = \begin{cases} 0, & sig(\Re[\mathbf{V}_i^{(l+1)}|_{p,q}]) < 0, \\ M-1, & sig(\Re[\mathbf{V}_i^{(l+1)}|_{p,q}]) > M-1, \end{cases}$$

$$\Im[\check{\mathbf{P}}_i^{(l+1)}|_{p,q}] = round[sig(\Im[\mathbf{V}_i^{(l+1)}|_{p,q}]) + (M-1)\cdot\varrho\cdot randn())] \tag{4.6}$$

$$\Im[\check{\mathbf{P}}_i^{(l+1)}|_{p,q}] = \begin{cases} 0, & sig(\Im[\mathbf{V}_i^{(l+1)}|_{p,q}]) < 0, \\ M-1, & sig(\Im[\mathbf{V}_i^{(l+1)}|_{p,q}]) > M-1, \end{cases}$$

where $randn()$ is a random number generated from a standard normal distribution.

Observe from the above equations that both the real and imaginary value of the position is a discrete number between $[0, \ M-1]$. Then, for any given value of the position, there is a certain probability for choosing a number between $[0, \ M-1]$, which decreases as a function of its distance from the given value.

4) Termination condition check - block 4 of Fig. 4.1.

This block is also similar to block 4 of Fig. 2.8 in Section 2.2.1.3, which considered the MBER-MUT. If the maximum number of iterations, $I_{\max}$, is reached, terminate the algorithm with the solution $\mathbf{G}b^{(I_{\max})}$.

Another optional termination criterion is constituted by a pre-defined cost function value, namely, when we have $F(\mathbf{G}b^l) < r$, where r is the pre-defined cost function value. If the stopping criterion is not satisfied, set $l = l + 1$ and proceed to Step *2)* of Fig. 4.1.

As we mentioned, each element of the velocity vector $\mathbf{V}$ is transformed into an integer number between $[0, \ M]$, which will be the average of the normal distribution used for generating the corresponding position, while our search space for the position is $[0, \ M-1]$. We will show in Section 4.7 that the approach of transforming each element of the velocity vector $\mathbf{V}$ into a number between $[0, \ M]$ rather than between $[0, \ M-1]$ may limit the performance of the algorithm, since the latter approach provides an improved performance in our case. More explicitly, the velocity vector elements determine, how far a particle may move from its central position, which relates the velocity to the positions.

4.4.2 Example

Let us now use a simple example to show how this algorithm described by Fig. 4.1 operates. The two dimensional problem to be minimized is $\|\mathbf{x} - 2\|_2^2$, where the corresponding search space is defined as any integer between $[0, \ 5]^2$, it is clear that the global minimal point is $\mathbf{x} = [2 \ \ 2]$ associated with a fitness function value of $F(\mathbf{x}) = 0$. The related parameters are summarized in Table 4.1.

We would like to mention that a simple MUD example has been provided in Table 2.13 of Section 2.2.2.1 which used binary PSO. Therefore, the difference between these two examples is the that in the previous example, the search space is 0 or 1, while in the example below, the search space is defined as any integer between $[0, \ 5]^2$.

When the first search iteration starts, the value of the inertia weight is $w^{(1)} = \frac{(0.9-0.4)\cdot(5-1)}{5-0.4} = 0.43$,

1. For particle 1:

   - For 1st element:
     The velocity is calculated from Equation (2.63) as $\mathbf{V}^1_{(1,1)} = 0.43\cdot 0 + 1\cdot 0.74\cdot 0 + 1\cdot 0.39\cdot -3 = -1.17$. Then we have $sig(\mathbf{V}^1_{(1,1)}) = 1.41$, and after the "rounding" action, the new position becomes $\check{\mathbf{P}}^{(1)}_{(1,1)} = 0$.
   - For 2nd element:
     The velocity is calculated from Equation (2.63) as $\mathbf{V}^1_{(1,2)} = 0.43\cdot 0 + 1\cdot 0.55\cdot 0 + 1\cdot 0.73\cdot -1 = -0.73$. Hence we have $sig(\mathbf{V}^1_{(1,2)}) = 1.94$, and after the "rounding" action, the new position is $\check{\mathbf{P}}^{(1)}_{(1,2)} = 1$.
     Therefore, the position for the 1st particle at the 1st iteration is $\check{\mathbf{P}}^{(1)}_1 = [0 \ \ 1]$. The associated fitness function value is then $F = 5$. Since this value is lower than the previous one of $F = 8$ in Table 4.1 for the 1st particle, the personal best visited position is updated to $\mathbf{Pb}^{(1)}_1 = [0 \ \ 1]$.

2. For particle 2:

   - For 1st element:
     The velocity is calculated from Equation (2.63) as $\mathbf{V}^1_{(2,1)} = 0.43\cdot 0 + 1\cdot 0.61\cdot 0 + 1\cdot 0.58\cdot 0 = 0$.

Table 4.1: The related parameters of the optimization example using the algorithm proposed in [135]. Please note that a similar example has been provided in Table 2.13 of Section 2.2.2.1 which used binary PSO. However, we are using discrete multi-valued PSO here.

Related parameters	Value or Type
Fitness function $F(\mathbf{x})$	$\|\mathbf{x}-2\|_2^2$
Inertia weight $w^{(l)}$	$\frac{(w_{max}-0.4)\cdot(I_{\max}-l)}{I_{\max}-0.4}$
Maximum number of iterations $I_{\max}$	5
c_1	1
c_2	1
ϱ	0.2
Search space for each dimension	$[0,\ 5]$
Size of particle swarm S	4
Initial position for particle 1: $\check{\mathbf{P}}_1^{(0)}$	$[4\ \ 4]$
Initial fitness value for particle 1	8
Initial position for particle 2: $\check{\mathbf{P}}_2^{(0)}$	$[1\ \ 0]$
Initial fitness value for particle 2	5
Initial position for particle 3: $\check{\mathbf{P}}_3^{(0)}$	$[1\ \ 3]$
Initial fitness value for particle 3	2
Initial position for particle 4: $\check{\mathbf{P}}_4^{(0)}$	$[3\ \ 0]$
Initial fitness value for particle 4	5
Initial global best position: $\mathbf{G}b^{(0)}$	$[1\ \ 3]$
Initial fitness value for $\mathbf{G}b^{(0)}$	2

Then $sig(\mathbf{V}_{(2,1)}^1)=3$, and after the "rounding" action, the new position becomes $\check{\mathbf{P}}_{(2,1)}^{(1)}=2$.

- For 2nd element:
  The velocity quantified by Equation (2.63) $\mathbf{V}_{(2,2)}^1=0.43\cdot 0+1\cdot 0.07\cdot 0+1\cdot 0.37\cdot 3=1.12$. Then we have $sig(\mathbf{V}_{(2,2)}^1)=4.52$. Following the "rounding" action, the new position becomes $\check{\mathbf{P}}_{(2,2)}^{(1)}=5$.
  Therefore, the position for the 2nd particle at the 1st iteration is $\check{\mathbf{P}}_2^{(1)}=[2\ \ 5]$. The associated fitness function value is then $F=9$. Since this value is higher than the previous value of $F=5$ for the 2nd particle, the best individual position still remains $\mathbf{Pb}_2^{(1)}=[1\ \ 0]$.

3. For particle 3:

- For 1st element:
  The velocity is calculated from Equation (2.63) as $\mathbf{V}_{(3,1)}^1=0.43\cdot 0+1\cdot 0.03\cdot 0+1\cdot 0.40\cdot 0=0$. Then we have $sig(\mathbf{V}_{(3,1)}^1)=3$, and after the "rounding" action, the new position becomes $\check{\mathbf{P}}_{(3,1)}^{(1)}=4$.
- For 2nd element:
  The velocity is calculated from Equation (2.63) as $\mathbf{V}_{(3,2)}^1=0.43\cdot 0+1\cdot 0.65\cdot 0+1\cdot 0.57\cdot 0=0$.

Then $sig(\mathbf{V}^1_{(3,2)}) = 3$, and after the "rounding" action, the new position is $\check{\mathbf{P}}^{(1)}_{(3,2)} = 2$.

Therefore, the position for the 3rd particle at the 1st iteration is $\check{\mathbf{P}}^{(1)}_3 = [4\ \ 2]$. The associated fitness function value is then $F = 4$. Since this value is higher than the previous value of $F = 2$ for the 3rd particle, the individual best visited position remains $\mathbf{Pb}^{(1)}_3 = [1\ \ 3]$.

4. For particle 4:

   - For 1st element:

     The velocity is calculated from Equation (2.63) as $\mathbf{V}^1_{(4,1)} = 0.43 \cdot 0 + 1 \cdot 0.97 \cdot 0 + 1 \cdot 0.44 \cdot -2 = -0.88$. Then $sig(\mathbf{V}^1_{(4,1)}) = 1.75$, and after the "rounding" action, the new position becomes $\check{\mathbf{P}}^{(1)}_{(4,1)} = 3$.

   - For 2nd element:

     The velocity is calculated from Equation (2.63) as $\mathbf{V}^1_{(4,2)} = 0.43 \cdot 0 + 1 \cdot 0.77 \cdot 0 + 1 \cdot 0.56 \cdot 3 = 1.70$. Then we have $sig(\mathbf{V}^1_{(4,2)}) = 5.07$, following the "rounding" action, the new position is $\check{\mathbf{P}}^{(1)}_{(4,2)} = 5$.

     Therefore, the position for the 4th particle at the 1st iteration is $\check{\mathbf{P}}^{(1)}_4 = [3\ \ 5]$. The associated fitness function value is then 10. Since this value is higher than the previous one 5 for the 4th particle, the personal best visited position is still $\mathbf{P}b^{(1)}_4 = [3\ \ 0]$.

5. Update of $\mathbf{G}b^{(1)}$

   Since now the best individual ever visited position is still $\mathbf{P}b^{(1)}_3 = [1\ \ 3]$, associated with a fitness value of $F = 2$, which is identical to that of $\mathbf{G}b^{(0)}$. Therefore, the global best ever visited position after the 1st iteration is updated to $\mathbf{G}b^{(1)} = [1\ \ 3]$.

Then the algorithm proceeds to its 2nd iteration, while the value of the inertia weight $w^{(2)} = 0.32$,

1. For particle 1:

   The position for the 1st particle at the 2nd iteration is found to be $\check{\mathbf{P}}^{(2)}_1 = [5\ \ 2]$. The associated fitness function value is then $F = 9$. Since this value is higher than the previous value for the 1st particle, the best individual visited position is still $\mathbf{P}b^{(2)}_1 = [0\ \ 1]$.

2. For particle 2:

   The position for the 2nd particle at the 2nd iteration is found to be $\check{\mathbf{P}}^{(2)}_2 = [1\ \ 0]$. The associated fitness function value is then $F = 5$. Since this value is identical to the previous one for the 2nd particle, the individual best visited position still remains $\mathbf{P}b^{(2)}_2 = [1\ \ 0]$.

3. For particle 3:

   The position for the 3rd particle at the 2nd iteration is found to be $\check{\mathbf{P}}^{(2)}_3 = [1\ \ 5]$. The associated fitness function value is then $F = 10$. Since this value is higher than the previous value for the 3rd particle, the best individual visited position is still $\mathbf{P}b^{(2)}_3 = [1\ \ 3]$.

4. For particle 4:

   The position for the 4th particle at the 2nd iteration is found to be $\check{\mathbf{P}}^{(2)}_4 = [5\ \ 1]$. The associated fitness

function value is then $F = 10$. Since this value is higher than the previous one for the 4th particle, the individual best visited position is still $\mathbf{P}b_4^{(2)} = [3\ \ 0]$.

5. Update of $\mathbf{G}b^{(2)}$
   Since now the best individual ever visited position is still $\mathbf{P}b_3^{(2)} = [1\ \ 3]$, associated with a fitness value of $F = 2$, which is equal to that of $\mathbf{G}b^{(1)}$. Therefore, the global best ever visited position after the 2nd iteration stays the same, which is $\mathbf{G}b^{(2)} = [1\ \ 3]$.

Then the algorithm proceeds to its 3rd iteration, while the value of the inertia weight $w^{(3)} = 0.21$,

1. For particle 1:
   The position for the 1st particle at the 3rd iteration is found to be $\check{\mathbf{P}}_1^{(3)} = [0\ \ 2]$. The associated fitness function value is then $F = 4$. Since this value is lower than the previous value for the 1st particle, the best individual visited position is still $\mathbf{P}b_1^{(3)} = [0\ \ 2]$.

2. For particle 2:
   The position for the 2nd particle at the 3rd iteration is found to be $\check{\mathbf{P}}_2^{(3)} = [3\ \ 4]$. The associated fitness function value is then $F = 5$. Since this value is identical to the previous one for the 2nd particle, the personal best visited position is still $\mathbf{P}b_2^{(3)} = [1\ \ 0]$.

3. For particle 3:
   The position for the 3rd particle at the 3rd iteration is found to be $\check{\mathbf{P}}_3^{(3)} = [3\ \ 1]$. The associated fitness function value is then $F = 2$. Since this value is identical to the previous one for the 3rd particle, the best individual visited position is still $\mathbf{P}b_3^{(2)} = [1\ \ 3]$.

4. For particle 4:
   The position for the 4th particle at the 3rd iteration is found to be $\check{\mathbf{P}}_4^{(3)} = [2\ \ 4]$. The associated fitness function value is then $F = 4$. Since this value is lower than the previous one for the 4th particle, the individual best visited position is updated to be $\mathbf{P}b_4^{(3)} = [2\ \ 4]$.

5. Update of $\mathbf{G}b^{(3)}$
   Since now the best individual ever visited position is still $\mathbf{P}b_3^{(3)} = [1\ \ 3]$, associated with a fitness value of $F = 2$ which is equal to that of $\mathbf{G}b^{(2)}$. Therefore, the global best ever visited position after 3rd iteration stays the same, which is $\mathbf{G}b^{(3)} = [1\ \ 3]$.

Then the algorithm proceeds to its 4th iteration, while the value of the inertia weight $w^{(4)} = 0.10$,

1. For particle 1:
   The position for the 1st particle at the 4th iteration is found to be $\check{\mathbf{P}}_1^{(4)} = [3\ \ 3]$. The associated fitness function value is then $F = 2$. Since this value is lower than the previous value for the 1st particle, the individual best visited position is updated to be $\mathbf{P}b_1^{(4)} = [3\ \ 3]$.

2. For particle 2:
   The position for the 2nd particle at the 4th iteration is found to be $\check{\mathbf{P}}_2^{(4)} = [0\ \ 0]$. The associated fitness

function value is then $F = 8$. Since this value is higher than the previous value for the 2nd particle, the individual best visited position is still $\mathbf{P}b_2^{(4)} = [1 \;\; 0]$.

3. For particle 3:
   The position for the 3rd particle at the 4th iteration is found to be $\check{\mathbf{P}}_3^{(4)} = [2 \;\; 5]$. The associated fitness function value is then $F = 9$. Since this value is higher than the previous one for the 3rd particle, the best individual visited position is still $\mathbf{P}b_3^{(4)} = [1 \;\; 3]$.

4. For particle 4:
   The position for the 4th particle at the 4th iteration is found to be $\check{\mathbf{P}}_4^{(4)} = [5 \;\; 3]$. The associated fitness function value is then $F = 10$. Since this value is higher than the previous value for the 4th particle, the best individual visited position is still $\mathbf{P}b_4^{(4)} = [2 \;\; 4]$.

5. Update of $\mathbf{G}b^{(4)}$
   Since now the best individual ever visited position is still $\mathbf{P}b_3^{(4)} = [1 \;\; 3]$, associated with a fitness value of $F = 2$ which is equal to that of $\mathbf{G}b^{(3)}$. Therefore, the global best ever visited position after 4th iteration stays the same, which is $\mathbf{G}b^{(4)} = [1 \;\; 3]$.

Then the algorithm proceeds to its 5th iteration, while the value of the inertia weight $w^{(5)} = 0$,

1. For particle 1:
   The position for the 1st particle at the 5th iteration is found to be $\check{\mathbf{P}}_1^{(5)} = [0 \;\; 4]$. The associated fitness function value is then $F = 8$. Since this value is higher than the previous value for the 1st particle, the best individual visited position is still $\mathbf{P}b_1^{(5)} = [3 \;\; 3]$.

2. For particle 2:
   The position for the 2nd particle at the 5th iteration is found to be $\check{\mathbf{P}}_2^{(5)} = [5 \;\; 3]$. The associated fitness function value is then $F = 10$. Since this value is higher than the previous value for the 2nd particle, the individual best visited position still remains$\mathbf{P}b_2^{(5)} = [1 \;\; 0]$.

3. For particle 3:
   The position for the 3rd particle at the 5th iteration is found to be $\check{\mathbf{P}}_3^{(5)} = [2 \;\; 2]$. The associated fitness function value is then $F = 0$. Since this value is lower than the previous one for the 3rd particle, the best individual visited position is updated to be $\mathbf{P}b_3^{(5)} = [2 \;\; 2]$.

4. For particle 4:
   The position for the 4th particle at the 5th iteration is found to be $\check{\mathbf{P}}_4^{(5)} = [0 \;\; 1]$. The associated fitness function value is then $F = 5$. Since this value is higher than the previous value for the 4th particle, the individual best visited position still remains $\mathbf{P}b_4^{(5)} = [2 \;\; 4]$.

5. Update of $\mathbf{G}b^{(5)}$
   Since now the best individual ever visited position is $\mathbf{P}b_3^{(5)} = [2 \;\; 2]$, associated with a fitness value of $F = 0$, which is lower than that of $\mathbf{G}b^{(4)}$. Therefore, the global best ever visited position after 5th iteration is $\mathbf{G}b^{(5)} = [2 \;\; 2]$. We may also notice that this is the optimum solution, hence the optimum position (solution) has been found in the 5th iteration.

4.5 Discrete Multi-Valued PSO Aided VP

In this section, the appropriately adapted discrete multi-valued PSO algorithm is invoked for finding the optimum perturbation vector of the ZF-VP and MMSE-VP algorithms.

As we will show in Section 4.7, for each of the corresponding search spaces of the real and imaginary part of the K-element complex-valued $\boldsymbol{\zeta}$, its value may be restricted to the reduced-search-complexity range of $[-2, -1, 0, 1, 2]^{2\times K}$ rather than searching through the entire legitimate range. This search-range reduction is reminiscent of the action of the sphere decoder or encoder. It is interesting to see that a similar conclusion was made in [68]. Hence, to make the discrete multi-valued PSO algorithm applicable, the following mapping should be employed in the optimization process: $-2 \longrightarrow 0, -1 \longrightarrow 1, 0 \longrightarrow 2, 1 \longrightarrow 3, 2 \longrightarrow 4$. Hence, the search space now becomes $[0, 1, 2, 3, 4]^{2\times K}$.

The search procedure is identical to that of Fig. 4.1 introduced in Section 4.4, but we appropriately adapted the original algorithm proposed in [135] in order to enhance its performance, which will be demonstrated in Section 4.7. The modifications are highlighted as follows:

1. Value of c_1 and c_2, as defined in Equation (2.63)
   The original algorithm [135] suggested the choice of $c_1 = c_2 = 1$, yet in our case, it was found that $c_1 = c_2 = 0.5$ would provide a better performance;

2. Modification of Equation (4.4)
   We may notice in Equation (4.4), that the number generated from the corresponding velocity by using the sigmoid function may reside within the range of $[M-1,\ M]$ when our search space is $[0,\ M-1]$. Moreover, when we are searching for a number from the range of 1, 2 and 3 for example, there is certainly no point in trying 4 during the search procedure. Hence, in our approach, we changed Equation (4.4) based on our empirical results to be detailed in Section 4.7 as follows:

$$\begin{aligned} sig(\Re[\mathbf{V}_i^{(l+1)}|_{p,q}]) &= \frac{(M-1)}{1+e^{-(\Re[\mathbf{V}_i^{(l+1)}|_{p,q}])}}, \\ sig(\Im[\mathbf{V}_i^{(l+1)}|_{p,q}]) &= \frac{(M-1)}{1+e^{-(\Im[\mathbf{V}_i^{(l+1)}|_{p,q}])}}, \end{aligned} \tag{4.7}$$

   by replacing M with $(M-1)$ in Equation (4.4), so that the number generated from the corresponding velocity always assumes an integer, which falls within the range of $[0,\ M-1]$. This solution will be shown to be capable of providing a better performance in Section 4.7;

3. Modification of the inertia weight update equation
   We also modified the time-variant inertia weight update of Equation (4.3) to be [96]:

$$w^{(l)} = (w_{max} - w_{min})\frac{(I_{\max} - l)}{I_{\max}} + w_{min}, \tag{4.8}$$

   where $w_{max} = 0.9$ and $w_{min} = 0.4$.

   In order to augment the effects of these two different inertia weight update equations, we may consider an example. Let the maximum number of iterations be $I_{\max} = 5$, while the values of the inertia weight

Table 4.2: An example showing the inertia weight values at different iterations when Equation (4.3) [135] and Equation (4.8) [96] are used for the inertia weight update, provided that $I_{\max} = 5$.

Variable or Iteration index	w_{max}	w_{min}	1	2	3	4	5
Equation (4.3) (original)	0.9	N/A	0.43	0.32	0.21	0.10	0
Equation (4.8) (modified)	0.9	0.4	0.8	0.7	0.6	0.5	0.4

at different iterations are shown in Table 4.2. We can see, that of the original equation is used, the values of the inertia weight would decrease iteration by iteration to a final value of 0. By contrast, when the modified scheme is adopted, the values of the inertia weight would decrease iteration by iteration to a final value of 0.4. This implies that at the early stages, the values for the inertia weight of the latter approach are always larger than the ones using the original equation. Hence, the latter approach is capable of providing a better global search capability in the early stages [96]. Therefore, this modification slightly improves the algorithm's performance, which is further detailed in Section 4.7.

We already mentioned that during the update of the particle positions, such as $\Re[\check{\mathbf{P}}_i|_{p,q}]$ for example, for a given mean of $sig(\Re[\mathbf{V}_i|_{p,q}])$, there is a certain probability of choosing a number between $[0\ \ 4]$ in our case. The probability of selecting a specific number monotonically decreases based on its distance from the mean of $sig(\Re[\mathbf{V}_i|_{p,q}])$. In the following part, the relationship between the mean of $sig(\Re[\mathbf{V}_i|_{p,q}])$ and the probability of picking discrete values is discussed.

For a given mean of $sig(\Re[\mathbf{V}_i|_{p,q}])$, the probability of assigning $\Re[\check{\mathbf{P}}_i|_{p,q}] = 0$ is given by the integral of the probability over the interval $(-\infty,\ 0.5]$, namely by

$$\begin{aligned} P\Re[\check{\mathbf{P}}_i|_{p,q}] = 0 \mid sig(\Re[\mathbf{V}_i|_{p,q}]) &= \int_{-\infty}^{0.5} g(x)dx \\ &= 1 - Q(\tfrac{0.5 - sig(\Re[\mathbf{V}_i|_{p,q}])}{4\cdot\varrho}), \end{aligned} \tag{4.9}$$

where $g(x)$ is

$$g(x) = \frac{1}{\sqrt{2\pi\varrho^2 4^2}} e^{\frac{-(x - sig(\Re[\mathbf{V}_i|_{p,q}]))^2}{2\varrho^2 4^2}}. \tag{4.10}$$

Similarly, the probability of $\Re[\check{\mathbf{P}}_i|_{p,q}] = 1$ is given by the integral over the interval $(0.5,\ 1.5]$, namely by

$$\begin{aligned} P\Re[\check{\mathbf{P}}_i|_{p,q}] = 1 \mid sig(\Re[\mathbf{V}_i|_{p,q}]) &= \int_{0.5}^{1.5} g(x)dx \\ &= Q(\tfrac{0.5 - sig(\Re[\mathbf{V}_i|_{p,q}])}{4\cdot\varrho}) - Q(\tfrac{1.5 - sig(\Re[\mathbf{V}_i|_{p,q}])}{4\cdot\varrho}). \end{aligned} \tag{4.11}$$

On the same note, the probability of $\Re[\check{\mathbf{P}}_i|_{p,q}] = 2$ is determined by integrating over the interval of $(1.5,\ 2.5]$, yielding

$$\begin{aligned} P\Re[\check{\mathbf{P}}_i|_{p,q}] = 2 \mid sig(\Re[\mathbf{V}_i|_{p,q}]) &= \int_{1.5}^{2.5} g(x)dx \\ &= Q(\tfrac{1.5 - sig(\Re[\mathbf{V}_i|_{p,q}])}{4\cdot\varrho}) - Q(\tfrac{2.5 - sig(\Re[\mathbf{V}_i|_{p,q}])}{4\cdot\varrho}). \end{aligned} \tag{4.12}$$

Table 4.3: An example showing the probabilities of choosing different values for $\Re[\check{\mathbf{P}}_i|_{p,q}]$ when the original algorithm proposed in [135] and our modified algorithm are used, provided that $\Re[\mathbf{V}_i|_{p,q}]$ =-0.8 and $\varrho = 0.2$.

Value	$sig(\Re[\mathbf{V}_i|_{p,q}])$	0	1	2	3	4
Original algorithm [135]	1.55	0.09	0.38	0.40	0.11	0.00
Modified algorithm	1.24	0.17	0.44	0.31	0.05	0.00

Again, the probability of $\Re[\check{\mathbf{P}}_i|_{p,q}] = 3$ is quantified by the corresponding integration over the interval of $(2.5,\ 3.5]$, which is formulated as:

$$\begin{aligned} P\Re[\check{\mathbf{P}}_i|_{p,q}] = 3 \mid sig(\Re[\mathbf{V}_i|_{p,q}]) &= \int_{2.5}^{3.5} g(x)dx \\ &= Q(\tfrac{2.5-sig(\Re[\mathbf{V}_i|_{p,q}])}{4\cdot\varrho}) - Q(\tfrac{3.5-sig(\Re[\mathbf{V}_i|_{p,q}])}{4\cdot\varrho}). \end{aligned} \tag{4.13}$$

Finally, the probability of $\Re[\check{\mathbf{P}}_i|_{p,q}] = 4$ is corresponding the integrate over the interval of $(3.5,\ \infty)$, yielding:

$$\begin{aligned} P\Re[\check{\mathbf{P}}_i|_{p,q}] = 4 \mid sig(\Re[\mathbf{V}_i|_{p,q}]) &= \int_{3.5}^{\infty} g(x)dx \\ &= Q(\tfrac{3.5-sig(\Re[\mathbf{V}_i|_{p,q}])}{4\cdot\varrho}). \end{aligned} \tag{4.14}$$

Let us now consider an example of showing the probabilities of choosing different values for $\Re[\check{\mathbf{P}}_i|_{p,q}]$, when the original algorithm proposed in [135] and our modified algorithm are used, which can be seen in Table 4.3. The value of $\Re[\mathbf{V}_i|_{p,q}]$ is assumed to be -0.8 and we have $\varrho = 0.2$.

We can observe the difference between the results of the two algorithms. Compared to the result of the modified algorithm, the original algorithm always opts for larger integers. In the example, "1" is most likely to be chosen as the new position in the modified algorithm, while "2" is most likely to be chosen as the new position in the original algorithm.

Table 4.4: Computational complexity of the MMSE-VP using sphere encoding and our discrete multi-valued PSO approach for QPSK signalling, where N is the number of transmit antennas, K is the number of mobile users, I is the number of iterations, $D_{\mathrm{MMSE-VP}}$ denotes the extended constellation points visited, and S is the particle size.

Algorithm	Flops
Sphere encoding	$(\frac{7}{3}\cdot K^3 + 13\cdot K^2 + 13\cdot K - 1)D_{\mathrm{MMSE-VP}} + 9\cdot K^2\cdot N - 2\cdot K^2$
PSO	$(7\cdot K^2\cdot S + 31\cdot K\cdot S + 4)\cdot I + \frac{7}{3}\cdot K^3 + 9\cdot K^2\cdot N + 7\cdot K^2\cdot S$ $-K\cdot S - 2\cdot K^2$

4.6 Computational Complexity

The computational complexity of the MMSE-VP using sphere encoding and of our discrete multi-valued PSO approach is studied in this section. More explicitly, a detailed complexity summary of our proposed PSO aided MMSE-VP scheme per iteration is listed in Table 4.5, which most critical depends on the number

Table 4.5: Detailed computational complexity per iteration for the highest-complexity techniques within the PSO aided MMSE-VP design for QPSK signalling, where K is the number of mobile users, and S is the particle size. The numbers in () indicate the index of the corresponding block in Fig. 4.1.

Stage	Flops
Update of inertia weight (3)	4
Update of velocities (3)	$9 \cdot 2 \cdot K \cdot S$
Calculate the sigmoid function (3)	$3 \cdot 2 \cdot K \cdot S$
Update positions (3)	$3 \cdot 2 \cdot K \cdot S$
Evaluate fitness (2)	$2 \cdot K \cdot S + (7 \cdot K^2 - K) \cdot S$

Table 4.6: Simulation parameters employed

Parameter	Value or Type
System	
Modulation scheme	QPSK
No. of transmit antennas	4
No. of users	4
Channel	flat Rayleigh fading
CSIT knowledge	perfect
Channel realizations	100
PSO	
c_1, c_2	0.5
ϱ	0.2
Swarm size S	40
$I_{\max}$	40

of users K and on the size of the swarm S. However, it may be observed in the flow chart of Fig. 4.1 that the computational complexity of the discrete multi-valued PSO aided MMSE-VP depends not only on the number of users K and the size of the swarm S, but also on the number of iterations the algorithm requires to converge to the optimum point. This will be discussed in more detail in Section 4.7 with the aid of our simulation results.

4.7 Simulation Results and Discussions

In this section, we mainly focus our attention on the MMSE-VP scheme, since it is capable of achieving a significantly better performance than the ZF-VP scheme, while imposing a similar computational complexity as that of the ZF-VP scheme. Hence at the time of writing, it may be more amenable to employment in practical systems.

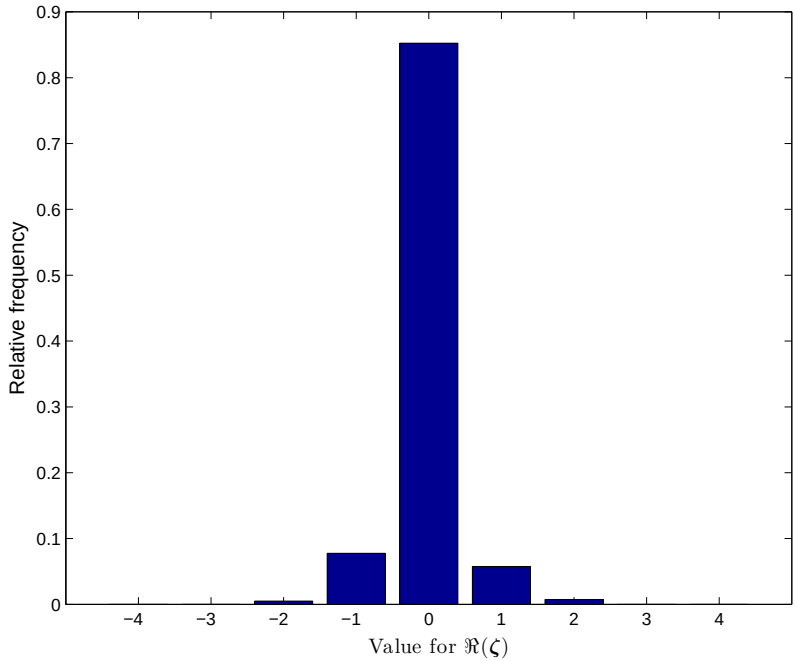

Figure 4.2: The distribution of the value of $\Re(\boldsymbol{\zeta})$ of the MMSE-VP scheme. 100 chosen perturbation vectors were taken into account for the system employing N=4 transmit antennas to support K=4 QPSK users for communicating over flat Rayleigh fading MIMO channels. All system parameters were summarized in Table 4.6.

4.7.1 MMSE-VP's search space for $\boldsymbol{\zeta}$

Recall that the search space of the PSO-aided MBER-MUT was defined in Equation (3.40) and discussed in Section 3.7.1. The MMSE-VP's search space defined in the context of Equation (2.60) for $\boldsymbol{\zeta}$ is discussed here. The search space in an optimization problem is closely related to its computational complexity. If the search space is large, the number of the legitimate candidates may be large leading to substantial search complexity. On the other hand, if the search space is appropriately small, then the corresponding complexity may be reduced. Hence, we are interested in finding the appropriate search space for $\boldsymbol{\zeta}$, in order to reduce the related computational complexity.

In Fig. 4.2, we considered the search space for $\Re(\boldsymbol{\zeta})$ in a system employing N=4 transmit antennas to support K=4 QPSK users for communicating over flat Rayleigh fading MIMO channels. 100 perturbation vectors generated by the MMSE-VP in 25 different SNR scenarios from $\frac{Eb}{No} = 5dB$ to $\frac{Eb}{No} = 29dB$ were taken into account. Since there was four elements in each perturbation vector presenting the value chosen for each user, there was $100 \times 4 = 400$ values. Explicitly, amongst the resultant 400 values, the relative frequency of choosing 0 was $\frac{341}{400}$=0.85, choosing 1 was $\frac{23}{400}$=0.05, choosing -1 was $\frac{31}{400}$=0.08 and choosing 2 and -2 were $\frac{3}{400}$=0.007 and $\frac{2}{400}$=0.005, respectively.

The search space for $\Im(\boldsymbol{\zeta})$ was considered in Fig. 4.2. Again, 100 perturbation vectors generated by the MMSE-VP in 25 different SNR scenarios from $\frac{Eb}{No} = 5dB$ to $\frac{Eb}{No} = 29dB$ in a system employing N=4 transmit antennas to support K=4 QPSK users for communicating over flat Rayleigh fading MIMO channels were taken into account. It may be observed from Fig. 4.2 that the relative frequency of choosing 0

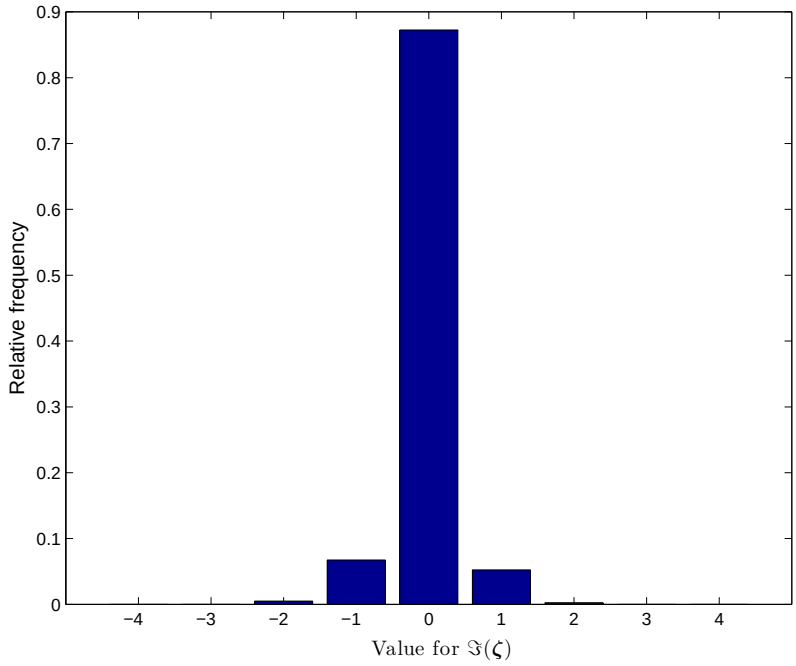

Figure 4.3: The distribution of the value of $\Im(\boldsymbol{\zeta})$ of the MMSE-VP scheme. 100 chosen perturbation vectors were taken into account for the system employing N=4 transmit antennas to support K=4 QPSK users for communicating over flat Rayleigh fading MIMO channels. All system parameters were summarized in Table 4.6. The result is similar to that shown in Fig. 4.2.

was $\frac{349}{400}$=0.87, choosing 1 was $\frac{21}{400}$=0.05, choosing -1 was $\frac{27}{400}$=0.08 and choosing 2 and -2 were $\frac{1}{400}$=0.002 and $\frac{2}{400}$=0.005, respectively.

By considering all the above results, it becomes clear that it may be a reasonable assumption that the value for $\Re(\boldsymbol{\zeta})$ and $\Im(\boldsymbol{\zeta})$ would only fall outside the range of $[-2,-1,0,1,2]$ with a vanishingly low probability. Therefore, we may restrict the search space to $[-2,-1,0,1,2]^{2\times K}$ without any undue performance degradation.

4.7.2 The effect of modified sigmoid function

The effects of using the original sigmoid function of Equation (4.4) and the modified one of Equation (4.7) are discussed here. The related system parameters are shown in Table 4.6, and the attainable performance of the MMSE-VP is characterized in Fig. 4.4, which was evaluated by averaging over 100 different channel realizations.

The test environment is the DL of a multiuser $(N\times K)$-element MIMO system employing N=4 transmit antennas at the BS, supporting K=4 QPSK users. Perfect CSI knowledge was assumed at the BS for transmission over the $(N\times K)$-element flat Rayleigh fading MIMO channel. The MMSE-VP MUT scheme is adopted for precoding. The size of the swarm here was chosen to be S=40 for the PSO algorithm, the maximum number of iterations was $I_{\max}$=40, and we used ϱ=0.2.

As we can observe from Fig. 4.4, our approach using Equation (4.7) to carry out the velocity transfor-

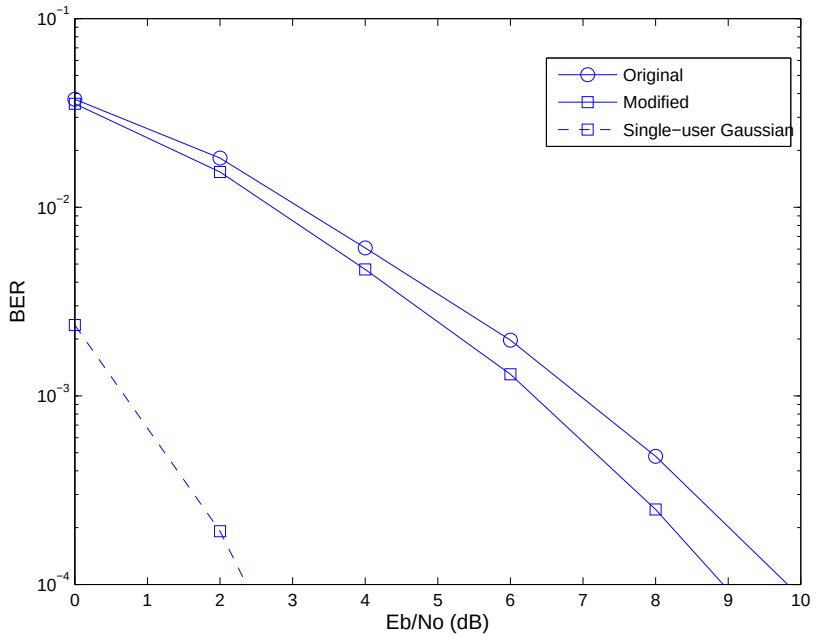

Figure 4.4: The achievable BER performance of using the original sigmoid function of Equation (4.4) and of the modified one in Equation (4.7) for finding the perturbation vector of the MMSE-VP for the system employing N=4 transmit antennas to support K=4 QPSK users for communicating over flat Rayleigh fading MIMO channels. A total number of $S = 40$ particles are used with a maximum number of $I_{\max} = 40$ iterations. All system parameters were summarized in Table 4.6. The performance of the MBER-MUT recorded in the same scenario was shown in Fig. 3.16.

mation outperforms the originally proposed approach of Equation (4.4) for the velocity transformation at all SNRs. More explicitly, at the target BER of 10^{-4}, our approach is capable of achieving a 1dB SNR gain over the original approach proposed in [135]. This performance enhancement is achieved by focussing the search scope to the range of $[0,\ M-1]$.

4.7.3 The effect of modified inertia weight update equation

The effect of using different inertia weight update schemes in Equation (4.3) and Equation (4.8) is discussed here. Again, the related system parameters are shown in Table 4.6, and the performance of the MMSE-VP can be seen in Fig. 4.5, which was recorded again by averaging over 100 different channel realizations. The only difference in comparison to the scenario considered in Fig. 4.4 is that we adopted Equation (4.7) as the velocity transformation equation.

A marginally better performance can be observed by using the modified inertia weight update formula of Equation (4.8) in Fig. 4.5 in comparison to Equation (4.3). These results showed that by using a larger inertia weight at the early stages is capable of improving the global search capability of the discrete multi-valued PSO algorithm, and hence provides a slightly better performance.

4.7.4 The choice of c_1, c_2

The appropriate choice of c_1, c_2 defined in Equation (2.63) is considered here. More explicitly, four sets of the values of c_1, c_2 are tested, namely, $c_1 = c_2 = 1$ as suggested in [135], $c_1 = c_2 = 0.2$, $c_1 = c_2 = 0.5$ and $c_1 = c_2 = 1.5$. The related parameters are shown again in Table 4.6, while the attainable performance can be seen in Fig. 4.6. The only difference in comparison to the scenario considered in Fig. 4.5 is that we used $\frac{(w_{max}-0.4)\cdot(I_{\max}-l)}{I_{\max}-0.4}$ to update the inertia weight.

It can be seen from the figure that the choices of $c_1 = c_2 = 0.5$ and $c_1 = c_2 = 1$ provide similar BER performances, while the performance recorded for $c_1 = c_2 = 0.2$ is slightly worse than that achieved by the former two. The worst performance obtained amongst the four settings is associated with $c_1 = c_2 = 1.5$. This suggests that setting $c_1 = c_2 = 0.5$ is a good choice.

4.7.5 The choice of ϱ

The beneficial choice of ϱ is considered here. First of all, let us re-consider the example provided in Table 4.3, where we considered the probabilities of choosing different values for $\Re[\check{\mathbf{P}}_i|_{p,q}]$ in conjunction with $\Re[\mathbf{V}_i|_{p,q}]$ =-0.8, and $sig(\Re[\mathbf{V}_i|_{p,q}]) = 1.2401$, when the modified velocity transformation equation is used. Here, we are interested in studying the effect of using different values for ϱ this time.

The relative frequency histogram of $\Re[\check{\mathbf{P}}_i|_{p,q}]$ recorded for different values of ϱ is portrayed in Fig. 4.7.

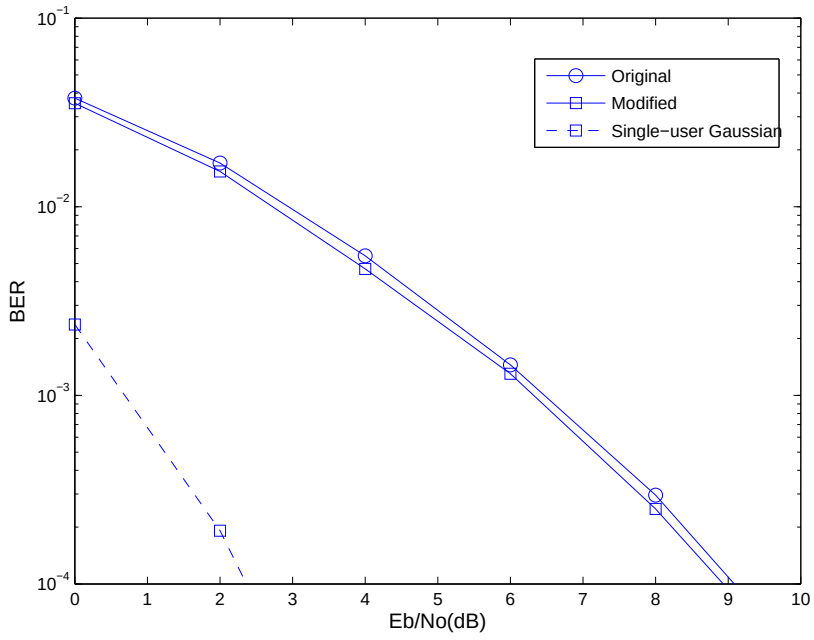

Figure 4.5: The achievable BER performance of using the original inertia update equation shown in Equation (4.3) and the modified inertia update equation shown in Equation (4.8) in MMSE-VP for the system employing N=4 transmit antennas to support K=4 QPSK users for communicating over flat Rayleigh fading MIMO channels. A total number of $S = 40$ particles are used with a maximum number of $I_{\max} = 40$ iterations. All system parameters were summarized in Table 4.6. The performance of the MBER-MUT recorded in the same scenario was shown in Fig. 3.16.

Table 4.7: An example showing the probabilities of choosing different values for $\Re[\check{\mathbf{P}}_i|_{p,q}]$ when different values for ϱ are taken into account, provided that $sig(\Re[\mathbf{V}_i|_{p,q}]) = 1.24$.

Value for ϱ	$sig(\Re[\mathbf{V}_i\|_{p,q}])$	0	1	2	3	4
0.1	1.24	0.03	0.70	0.25	$8.1704 \cdot 10^{-4}$	$8.0341 \cdot 10^{-9}$
0.2	1.24	0.17	0.44	0.31	0.05	0.002
0.3	1.24	0.26	0.31	0.26	0.11	0.02
0.4	1.24	0.32	0.24	0.22	0.13	0.07

We can see that as the value of ϱ increases, the probability of choosing other values for $\Re[\check{\mathbf{P}}_i|_{p,q}]$ rather than "1" is increasing, and this can also be seen from Fig. 4.7. It should be pointed out that based on what we can see from Fig. 4.7 and Table 4.7, the value of ϱ should be appropriately chosen. Too small a value of ϱ would limit the value of $\Re[\check{\mathbf{P}}_i|_{p,q}]$ and hence would limit the algorithm's performance. By contrast, an excessive value of ϱ seems too random, as seen in Table 4.7, where the probability of choosing "0" as the new position becomes even higher than the probability of choosing "1", despite the fact that the center of this distribution is more close to "1", when we have ϱ=0.4.

Let us now characterize the performance of choosing the above-mentioned four different values of ϱ in the context of MMSE-VP for the DL of a multiuser ($N \times K$)-element MIMO system employing N=4 transmit antennas at the BS, for supporting K=4 QPSK users. Perfect CSI knowledge was assumed at the

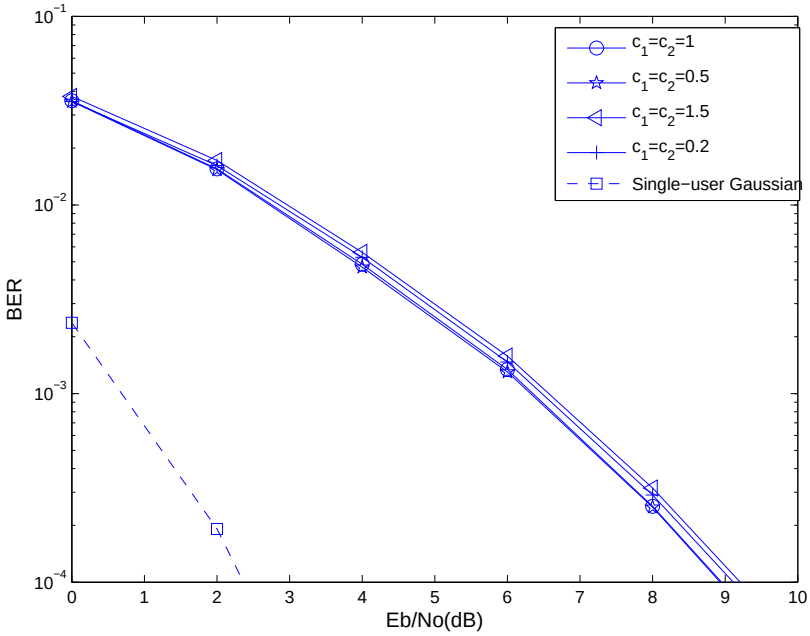

Figure 4.6: The performances of using four different choices for the value of c_1, c_2 in MMSE-VP for the system employing N=4 transmit antennas to support K=4 QPSK users for communicating over flat Rayleigh fading MIMO channels. A total number of $S = 40$ particles are used with a maximum number of $I_{\max} = 40$ iterations. All system parameters were summarized in Table 4.6. The performance of the MBER-MUT recorded in the same scenario was shown in Fig. 3.16.

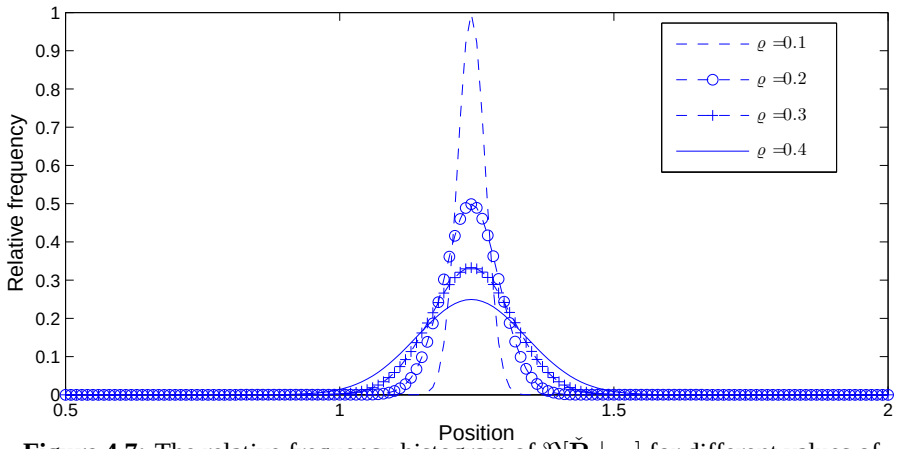

Figure 4.7: The relative frequency histogram of $\Re[\check{\mathbf{P}}_i|_{p,q}]$ for different values of ϱ.

Table 4.8: The computational complexities when different swarm sizes are considered.

Value for S	20	30	40	50
Required iterations to converge	90	60	40	40
Complexity (Flops)	428,010	428,970	382,770	478,250

BS for transmission over the $(N \times K)$-element flat Rayleigh fading MIMO channel. The size of the swarm was again chosen to be S=40 for the PSO algorithm. The maximum number of iterations was $I_{\max}$=40. All the parameters of the system are shown in Table 4.6. The only difference in comparison to the scenario considered in Fig. 4.6 is that we used $c_1 = c_2 = 0.5$.

Four different choices of ϱ, namely $\varrho = 0.1$, $\varrho = 0.2$, $\varrho = 0.3$ and $\varrho = 0.4$ are tested. The corresponding performances are show in Fig. 4.8. It is clear to see from this figure, that the performances when $\varrho = 0.2$ and $\varrho = 0.3$ are the best among the four, while the performance when $\varrho = 0.1$ is slightly worse than that achieved by the former two. The worst performance obtained among the four settings is $\varrho = 0.4$. This suggests that setting $\varrho = 0.2$ or $\varrho = 0.3$ are both good choices.

4.7.6 The choice of S

The choice of the swarm size S is considered here. The related system parameters are shown in Table 4.6, while the only difference in comparison to the scenario considered in Fig. 4.8 is that we used $\varrho = 0.3$ and the associated performance can be observed in Fig. 4.9. As seen from Fig. 4.9 that, at the target $Eb/No = 10$dB and for a swarm size of $S = 20$, it took the algorithm around $I = 90$ iterations to converge; when the swarm size was increased to $S = 30$, it took the algorithm around I =60 iterations to converge. When further increasing the swarm size to $S = 40$, the algorithm required around 40 iterations to converge. Finally, for the swarm size of $S = 50$, it took the algorithm also around 40 iterations to converge. The corresponding computational complexities, which were calculated based on Section 4.6, are summarized in Table 4.6. It becomes clear that the choice of $S = 40$ provides the lowest complexity, and hence it constitutes an attractive choice.

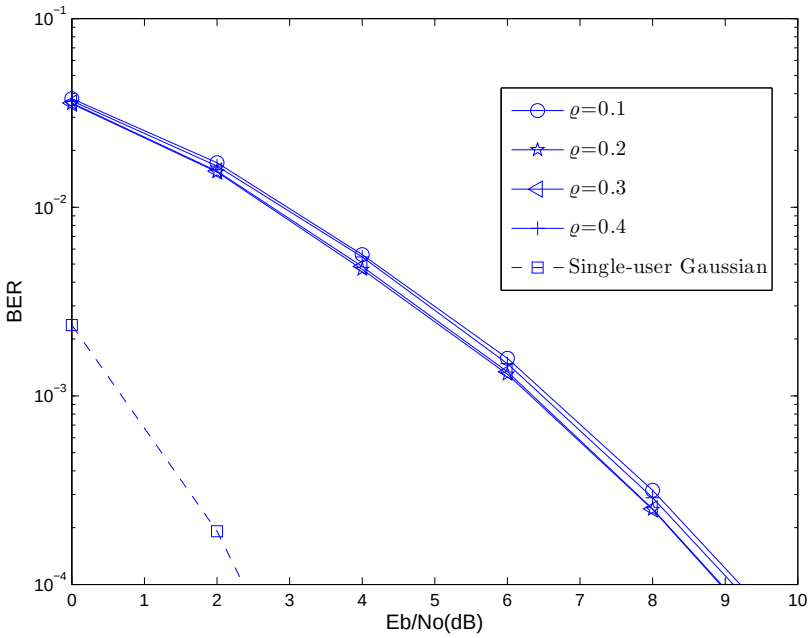

Figure 4.8: The performances obtained using four different choices for the value of ϱ in MMSE-VP for the system employing N=4 transmit antennas to support K=4 QPSK users for communicating over flat Rayleigh fading MIMO channels. A total number of $S = 40$ particles are used with a maximum number of $I_{\max} = 40$ iterations. All system parameters were summarized in Table 4.6. The performance of the MBER-MUT recorded in the same scenario was shown in Fig. 3.16.

4.7.7 Convergence and complexity

The covergence behavior of the proposed discrete multi-valued PSO aided MMSE-VP and the corresponding complexities are considered here. The parameters of the scenario considered are listed in Table 4.6. We, again, consider the DL of a multiuser $(N \times K)$-element MIMO system employing N=4 transmit antennas at the BS, supporting K=4 QPSK users. Perfect CSI knowledge was assumed at the BS for transmission over the $(N \times K)$-element flat Rayleigh fading MIMO channel. The convergence of the proposed discrete multi-valued PSO aided MMSE-VP algorithm characterized in the context of the system employing $N = 4$ transmit antennas for supporting $K = 4$ QPSK mobile users over flat Rayleigh fading channels at both Eb/No=6 dB and 10 dB are shown in Fig. 4.10. The swarm size was $S = 40$.

We can see from Fig. 4.10 that at the operating SNR of Eb/No=6 dB, the proposed algorithm needs I =30 iterations to converge, while it requires I =40 iterations to converge at Eb/No=10 dB. As shown in Section 4.6, the associated complexity was 288,330 and 382,770 Flops respectively. On the other hand, the averaged number of visited nodes, when sphere encoding was adopted, was 3193 and 3172, leading to 1,304,400 and 1,295,671 Flops, respecitvely. This implies that at Eb/No=6 dB, our proposed scheme is capable of reducing the computational complexity by $1 - \frac{288,330}{1,304,400} = 77.9\%$, while at Eb/No=10 dB by $1 - \frac{382,770}{1,295,671} = 70.46\%$. More explicitly, the complexity was reduced to 22.1% and 29.5%.

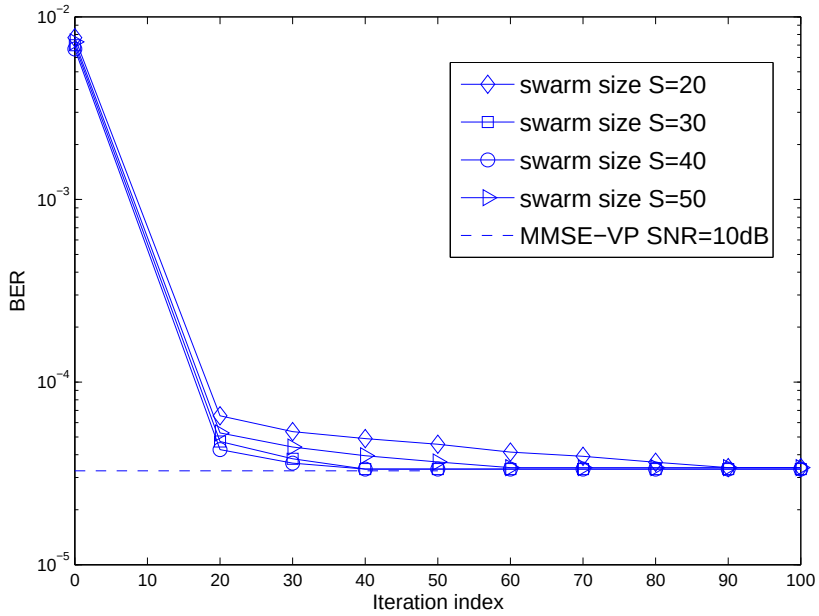

Figure 4.9: The BER versus iteration index performance obtained using different choices for the swarm size S in the MMSE-VP for the system employing N=4 transmit antennas to support K=4 QPSK users for communicating over flat Rayleigh fading MIMO channels when $Eb/No = 10$dB. The benchmark performance of the MMSE-VP at Eb/No=10dB which can be observed in Fig. 2.2 is also shown in this figure. All system parameters were summarized in Table 4.6. The performance of the MBER-MUT recorded in the same scenario was shown in Fig. 3.16.

4.7.8 Algorithmic performance

In this section, the performance of the MMSE-VP using the best parameter configurations found in our previous investigations for the proposed discrete multi-valued PSO aided scheme for transmission over the DL of the system employing $N = 4$ transmit antennas to support $K = 4$ QPSK mobile users over flat Rayleigh fading channels was considered. The related system parameters are summarized in Table 4.6. The BER performance results were obtained by averaging over 100 channel realizations, which are shown in Fig. 4.11.

It is clear by seen in Fig. 4.11 that our proposed discrete multi-valued PSO aided approach is capable of achieving the optimum sphere encoder based performance. More explicitly, in the scenario characterized in Fig. 4.11, where $S = 40$ particles and $I_{\max}$=40 maximum iterations are used, no SNR loss is observed for our approach when compared to the optimum performance of the MMSE-VP at the target BER of 10^{-5}, despite the fact that our approach benefits from a significantly lower computational complexity. For example, at the SNR of $Eb/No = 10$dB, our approach is capable of achieving the optimum sphere encoder based performance, at about 30% of the complexity compared to that imposed by sphere encoding as shown in Section 4.7.7.

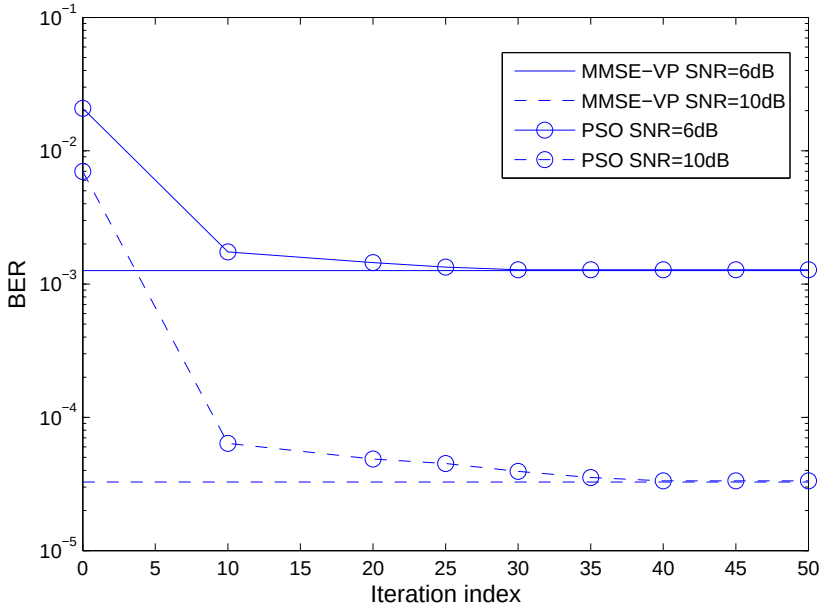

Figure 4.10: Convergence performances of the proposed PSO aided MMSE-VP algorithm for the system employing $N = 4$ transmit antennas to support $K = 4$ QPSK mobile users over flat Rayleigh fading channels at Eb/No=6 dB and 10 dB, repsectively. $S = 40$ particles are used. The benchmark performance of the MMSE-VP at Eb/No=6dB and Eb/No=10dB which can be observed in Fig. 2.2 is also shown in this figure. All system parameters were summarized in Table 4.6.

4.7.9 Performances at different maximum number of iterations

Let us now consider the achievable performance of our proposed discrete multi-valued PSO aided MMSE-VP scheme at different maximum number of iterations, when transmitting in the DL of the system employing $N = 4$ transmit antennas to support $K = 4$ QPSK mobile users over flat Rayleigh fading channels. The swarm size was S=40. The system parameters are summarized in Table 4.6, while the associated performance can be seen in Fig. 4.12.

We can see from Fig. 4.12 that as the number of iterations increases, the BER curve approaches the optimum one, especially at high SNRs. Interestingly, we can see that at the target BER of 10^{-5}, the performance attained, when using I =10 iterations is only about 1 dB away from the optimum sphere encoder based performance, while the computational complexity imposed is only 7.68% of that imposed by sphere encoding.

When we compare the curves associated with $I = 10$ and $I = 40$, it becomes clear that there is a less than 1 dB gap at all SNRs, hence when $I = 10$ is used for our proposed algorithm, a near optimum performance can be achieved, while we benefit from a significantly reduced computational complexity. In order to approach the optimum sphere encoder based performance, the number of iterations has to be further increased. For example, at the SNR of Eb/No=6 dB, the optimum performance may be closely approached by increasing the number of iterations to I =30.

This also means that our approach is capable of providing a flexible performance versus computational complexity trade-off, as a benefit of its iterative optimization regime. This feature is important, when there

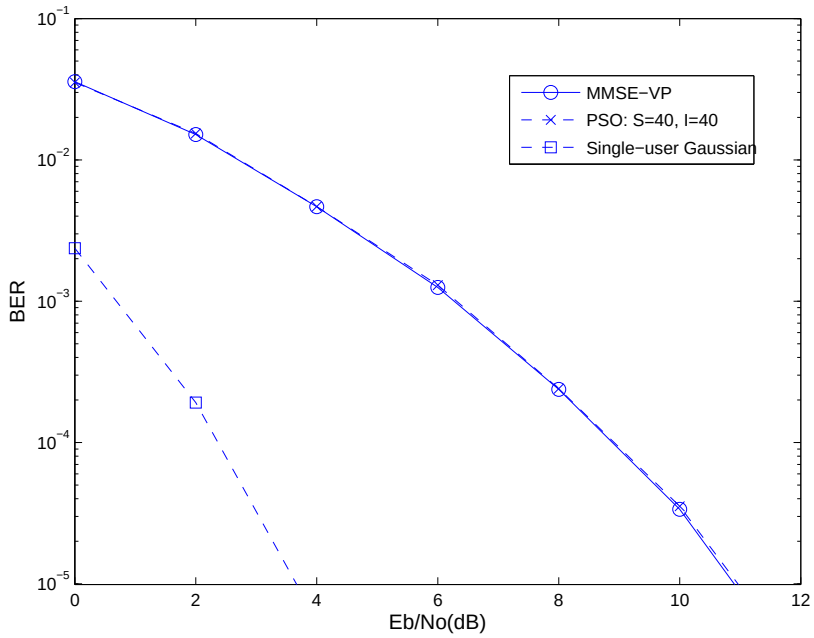

Figure 4.11: The performances of the MMSE-VP with optimum performance and our proposed discrete multi-valued PSO aided scheme where swarm size S=40, maximum iteraion number $I_{\max}$=40. The DL of the system employing $N = 4$ transmit antennas to support $K = 4$ QPSK mobile users over flat Rayleigh fading channels is considered. All system parameters were summarized in Table 4.6. The performance of the MBER-MUT recorded in the same scenario was shown in Fig. 3.16.

is a limited affordable computational complexity With the aid of our proposed algorithm, it is possible to tune the complexity to the affordable limit, while maintaining a near-optimum performance.

4.8 Conclusions

In Chapter 3 we successfully reduced the computational complexity imposed by linear MBER-MUTs by using PSO. Bearing in mind that the complexity reduction issue is more important in nonlinear MUTs, which are capable of achieving substantial BER performance improvement at the expense of a high complexity, in this chapter, we proposed discrete multi-valued PSO aided VP designs. More specifically, as a nonlinear MUT scheme, VP provides an attractive BER performance. However, the computational complexity imposed by the optimum shpere-encoder during the search for the optimal perturbation vector may become excessive. Hence it becomes necessary to find a reduced-complexity algorithm, while maintaining a near-optimum BER performance. Against this background, we developed a discrete multi-valued PSO aided MMSE-VP design, which was shown to be capable of approaching optimum sphere-encoder's performance at a significantly reduced computational complexity compared to that imposed by the sphere encoder. The system model was introduced in Section 4.2. Based on the system model, we may have the cost function in Equation (2.59) in Section 4.3. A rudimentary introduction to discrete multi-valued PSO algorithm was then provided in Section 4.4, followed by the description of the proposed discrete multi-valued PSO aided VP technique in Section 4.5. The corresponding computational complexity was discussed in Section 4.6. In Section 4.7, the simulation results were provided.

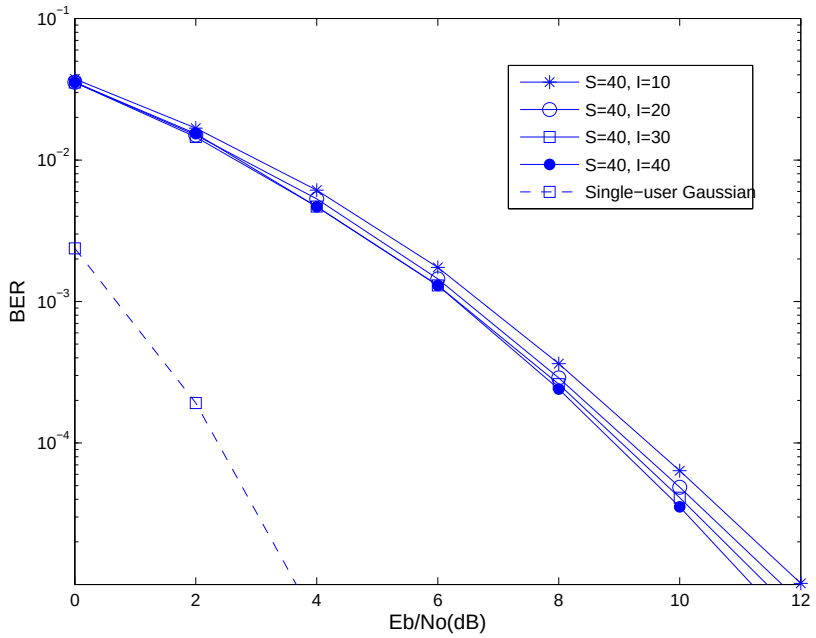

Figure 4.12: The performances of our proposed discrete multi-valued PSO aided MMSE-VP when different maximum number of iterations ($I = 10 - 40$) are considered, the swarm size S=40 and keeps constant. The DL of the system employing $N = 4$ transmit antennas to support $K = 4$ QPSK mobile users over flat Rayleigh fading channels is considered. All system parameters were summarized in Table 4.6. The performance of the MBER-MUT recorded in the same scenario was shown in Fig. 3.16.

Table 4.9: Computational complexity summary.

	Complexity(Flops)/SNR	Complexity(Flops)/SNR
sphere encoder	1,304,400/6dB	1,295,671/10dB
PSO	288,330/6dB	382,770/10dB

We focused our attention on the performance of the MMSE-VP in Section 4.7. The simulation results of Section 4.7.7 characterized the attainable performance in the case of employing N=4 transmit antennas at the BS for supporting K=4 QPSK users, while communicating over flat Rayleigh fading MIMO channel. Our approach is capable of finding the optimum perturbation vector at a reduced complexity of about 20% compared to that imposed by the sphere encoding at $Eb/No = 6$ dB. Similarly, the complexity compared to that imposed by sphere encoding was about 30% at $Eb/No = 10$ dB, while the total number of nodes in the search space was $5^8 = 390625$. This is summarized in Table 4.9. Hence, we conclude that our approach may be deemed to be a low-complexity near-optimum VP algorithm. Moreover, our approach can also strike a flexible BER performance versus complexity trade-off thanks to its iterative optimization.

Although MMSE-VP is an attractive nonlinear MUT design, which is capable of achieving a good BER performance, an improved design which directly minimizes the system's BER is conceptionally superior. Hence, in the next chapter, we will propose VP designs based on the MBER criterion.

Chapter 5

Minimum Bit Error Rate Vector Precoding

5.1 Introduction and Relevance to Previous Chapters

In previous chapters, we demonstrated the efficiency of PSO in solving optimization problems encountered in the context of wireless communications. More specifically, in Chapter 3 we successfully reduced the computational complexity imposed by linear MBER-MUTs by using continuous-valued PSO, the discrete multi-valued PSO was adopted in reducing the computational complexity imposed in MMSE-VP by sphere encoder [23] in Chapter 4. Compared the linear MUT algorithms family with the nonlinear VP schemes family we may notice that there is no VP algorithm proposed based on the MBER criterion. More explicitly, in ZF-VP, the precoding matrix was chosen to pre-equalize the channel using the zero-forcing criterion, while the perturbation vector was chosen to minimize the total transmit power. As an improvement of the ZF-VP, the MMSE-VP minimizes the total MSE of the system. However, since the BER is the ultimate system performance indicator, the concept precoding schemes designed by minimizing the MBER criterion is attractive. Despite its potential, to the best of our knowledge, no VP algorithm was proposed in the open literature based on the direct minimization of the BER.

Against this background, in this chapter, VP designs based on the MBER criterion were proposed to improve the BER performance of the system. We commence our discourse by introducing an improved MMSE-VP design based on the MBER criterion in Section 5.2. This transmit preprocessing scheme first invokes a regularized channel inversion and then superimposes a discrete-valued perturbation vector in order to minimize the BER of the system as an improvement of the well-known MMSE-VP scheme. To further improve the system's BER performance, an MBER-based continuous-valued generalized VP algorithm was proposed in Section 5.3. Given the knowledge of the information symbol vector and the CIR matrix, we consider the generation of the effective symbol vector to be transmitted by directly minimizing the BER of the system. The computational complexities of these two proposed algorithms are studied in Section 5.4. Simulation results are also provided in Section 5.5 in order to demonstrate the advantages of these two VP schemes based on the MBER criterion, especially for rank-deficient systems where the number of BS's transmit antennas is lower than the number of MSs supported. The robustness of these two designs to the CIR estimation error is also investigated.

5.2 Improved MMSE-VP Design Based on the MBER Criterion

In this section, the improved MMSE-VP design based on the MBER criterion is proposed. We firstly detail our system model in Section 5.2.1, continue by the introduction of the MBER criterion when modulo devices are employed at the non-cooperative MS receivers in Section 5.2.2. Finally, our proposed design is discussed in Section 5.2.3.

5.2.1 System Model

The schematic of the system model used throughout in this section is similar to the one we introduced in Section 2.1.2.1. It can be seen in Fig. 2.3 , which is repeated here for convenience, as in Fig. 5.1. However, in contrast to Fig. 2.3 , where the perturbation vector $\boldsymbol{\zeta}$ is chosen based on the MMSE criterion, the MBER criterion is used here and it remains the MMSE criterion in deriving the precoding matrix $\mathbf{P}$.

The DL of an SDMA system supporting non-cooperative mobile receivers is considered here, where the BS equipped with N transmit antennas communicates over frequency-flat fading channels with K non-cooperative MSs, each employing a single receive antenna and a modulo device.

The K-element information symbol vector of Fig. 5.1 to be perturbed is denoted by $\mathbf{x} = [x_1, x_2, \cdots, x_K]^T$, the symbol energy is given by $E[|x_k|^2] = \sigma_x^2$, for $1 \leq k \leq K$, where x_k is an i.i.d. uniform random variable. The perturbed symbol vector $\mathbf{u}$ having a dimension of K is given by $\mathbf{u} = \mathbf{x} + \boldsymbol{\omega}$, where $\boldsymbol{\omega}$ is the perturbation vector given as [23]: $\boldsymbol{\omega} = \tau\boldsymbol{\zeta}$. The $(N \times K)$-element precoding matrix $\mathbf{P}$ of Fig. 5.1 is denoted as $\mathbf{P} = [\mathbf{p}_1, \mathbf{p}_2, \cdots, \mathbf{p}_K]$, where $\mathbf{p}_k$, $1 \leq k \leq K$ represents the precoder coefficient vector for the kth user's data stream. The $(K \times N)$-element channel matrix $\mathbf{H}$ of Fig. 5.1 is denoted as $\mathbf{H} = [\mathbf{h}_1, \mathbf{h}_2, \cdots, \mathbf{h}_K]^T$, where $\mathbf{h}_k$, $1 \leq k \leq K$ is the kth user's CIR, which is given by $\mathbf{h}_k = [h_{k,1}, h_{k,2}, \cdots, h_{k,N}], k = 1, 2, \cdots, K$.. The CIR taps $h_{k,i}$, for $1 \leq k \leq K$ and $1 \leq i \leq N$ are independent of each other and obey the complex-valued Gaussian distribution associated with $\mathrm{E}[|h_{k,i}|^2] = 1$. The Gaussian noise vector $\mathbf{n}$ is given by $\mathbf{n} = [n_1, n_2, \cdots, n_K]^T$, where $n_k, 1 \leq k \leq K$ is a complex-valued Gaussian random variable with zero mean and $E[|n_k|^2] = 2\sigma_n^2 = \mathrm{N_o}$. When the total transmit power is constrained to be $\mathrm{E_T}$ at the BS, an appropriate scaling factor is used to fulfill this transmit power constraint, which is defined as $\alpha = \sqrt{\mathrm{E_T}/\|\mathbf{d}\|^2}$. At the receiver, the reciprocal of the scaling factor, namely α^{-1}, is used to scale the received signal in order to maintain a unity-gain transmission.

Note that the system model introduced above leads to a constrained optimization problem. The authors of [61] proposed a technique of transforming this constrained optimization problem into an unconstrained one by introducing the concept of effective noise. Since the signal vector before the modulo operation of Fig. 5.1 can be described as $\hat{\mathbf{y}} = \mathbf{HPu} + \alpha^{-1}\mathbf{n}$, let us introduce the notation of $\hat{\mathbf{n}} = \alpha^{-1}\mathbf{n}$, where $\hat{\mathbf{n}}$ is the effective noise. The reason for using this effective noise term is explained as follows. If the potential choice of $\boldsymbol{\omega}$ may result in the transmit power exceeding the power limit, then α would be assigned a relatively small value, leading to an amplified effective noise, which results in an increased BER. This choice of $\boldsymbol{\omega}$ is less likely to lead to the optimum perturbation vector. Therefore the perturbation vector chosen by using this effective noise based method should also satisfy the power constraint, hence now arrive at an unconstrained

optimization problem.

Again, the received signal vector $\mathbf{y} = [y_1\ y_2 \cdots y_K]^T$ of Fig. 5.1 after the modulo operation is given by $\mathbf{y} = mod_\tau(\hat{\mathbf{y}})$, and y_k, $1 \leq k \leq K$, constitutes sufficient statistics for the kth MS to detect the transmitted information data symbol x_k.

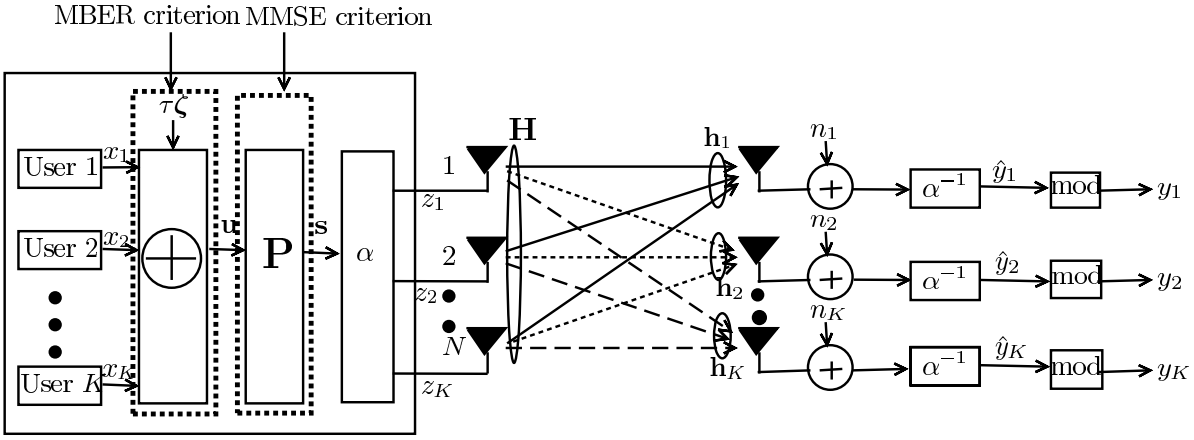

Figure 5.1: Schematic of the SDMA DL using the proposed ImMMSE-VP algorithm at the BS. The system employs N transmit antennas to communicate with K decentralized non-cooperative MSs. It is worth noting that in contrast to the schematic of Fig. 2.3, where the perturbation vector is chosen based on the MMSE criterion, here the MBER criterion is used.

5.2.2 The MBER Criterion combined with Modulo Devices

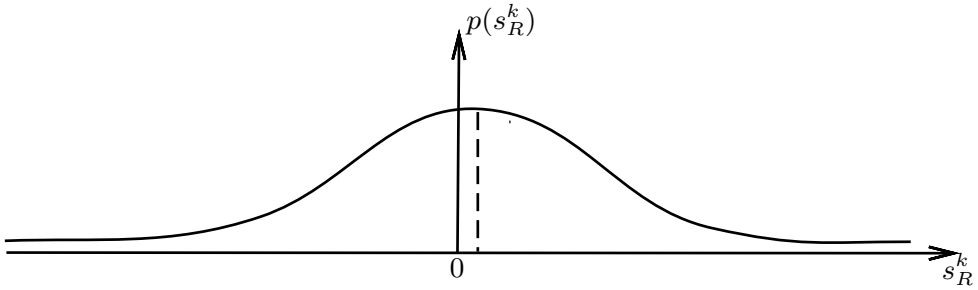

Figure 5.2: Probability density function of the decision variable s_R^k when the modulo operation is not used at the receiver side.

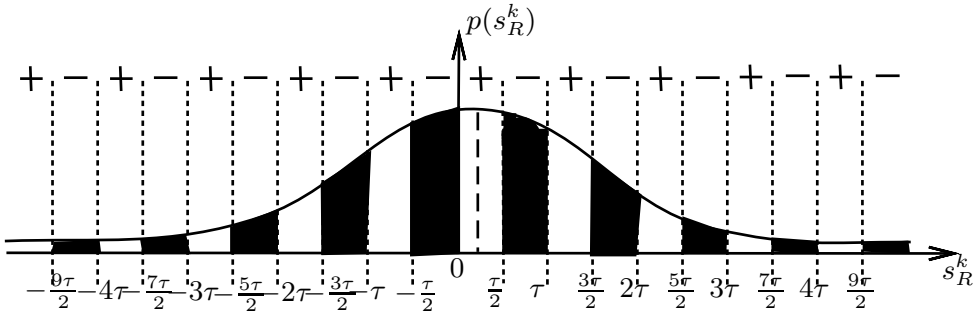

Figure 5.3: Probability density function of the decision variable s_R^k when the modulo operation of Fig. 2.3 explained with the aid of Fig. 2.4 is employed at the receiver. The shaded areas represent all the erroneous decision regions.

Here we only consider the MBER criterion combined with modulo device for the in-phase component. Its application to the quadrature-phase is straightforward. The description of the MBER criterion in the context of the in-phase component, when no modulo operation of Fig. 5.1 is employed at the receiver was already detailed in Section 3.4. Let the real part of the received signal before the modulo operation be denoted by $\Re[\hat{y}_k]$, while $\Re[y_k]$ represents the real part of the received signal after the modulo operation. When we have $\text{sgn}(\Re[x_k])\Re[y_k] < 0, 1 \leq k \leq K$, errors occur and according to the basic MBER criterion, we have:

$$P_{e_I,k}(\boldsymbol{\omega}) = \text{Prob}\{\text{sgn}(\Re[x_k])\Re[y_k] < 0\} = \text{Prob}\{z_R^k < 0\}, \tag{5.1}$$

where $z_R^k = \text{sgn}(\Re[x_k])\Re[y_k]$.

Hence, if we can estimate the distribution of z_R^k, the MBER detection problem of a modulo based receiver may be solved. However, this is not straightforward, since the transformation imposed by the modulo operation on the input signal is non-linear. Nonetheless, we can take advantage of the distribution of the signed decision variable $s_R^k = \text{sgn}(\Re[x_k])\Re[\hat{y}_k]$. Similar to Section 3.4, according to central limit theorem, the distribution of the decision variable s_R^k obeys the Gaussian distribution associated with the mean of $c_R^k = \text{sgn}(\Re[x_k])\Re[\mathbf{h}_k\mathbf{P}\mathbf{u}]$. The corresponding PDF can be seen in Fig. 5.2, which is formulated as:

$$p(s_R^k) = \frac{1}{\alpha^{-1}\sigma_n\sqrt{2\pi}} \exp\left(-\frac{(s_R^k - c_R^k)^2}{2\sigma_n^2\alpha^{-2}}\right). \tag{5.2}$$

Observe that Equation (5.2) is different from Equation (3.14), since here we invoked the effective noise of $\alpha^{-1}\sigma_n$.

Then, the relationship between the received signal before the modulo operation of Fig. 5.1 and the error probability should be explored in order to understand the nature of the MBER criterion in conjunction with the modulo operation. The following simple examples may be used to illustrate the solution to the problem, when we have say $\text{sgn}(\Re[x_k]) = 1$,

Example 1: if we have $\Re[\hat{y}_k] = 1.75\tau$, the signed decision variable is $s_R^k = 1.75\tau$, and after the modulo operation of Fig. 5.1, it is then mapped to $z_R^k = \text{sgn}(\Re[x_k])\Re[y_k] = -0.25\tau$. This means that s_R^k falls in the erroneous shaded area of Fig. 5.3, and an error occurs.

Example 2: if $\Re[\hat{y}_k] = -0.75\tau$, the signed decision variable $s_R^k = -0.75\tau$, after the modulo operation of Fig. 5.1, it is then mapped to $z_R^k = \text{sgn}(\Re[x_k])\Re[y_k] = 0.25\tau$, which means s_R^k falls in the the error-free area of Fig. 5.3, and no error.

Therefore, based on these two examples, we can see that encountering an error depends on where s_R^k would be after the modulo operation. If $z_R^k = mod_\tau(s_R^k)$ falls in the interval of $(-\infty,\ 0]$, then an error occurs. Otherwise, when $z_R^k = mod_\tau(s_R^k)$ falls in the interval of $(0,\ \infty)$, there is no error.

Let us now extend this idea further. It is clear that when s_R^k is in the intervals $[\frac{2m+1}{2}\tau,\ (m+1)\tau)$ for $-\infty < m < \infty$, then $z_R^k = mod_\tau(s_R^k)$ would fall into the interval of $(-\infty,\ 0]$, and errors occur. Again, Fig. 5.3 shows the erroneous areas for s_R^k after the modulo operation. Therefore, the BER of the in-phase

component associated with user k is

$$P_{e_I,k}(\boldsymbol{\omega}) = \sum_{m=-\infty}^{\infty} \int_{\frac{2m+1}{2}\tau}^{(m+1)\tau} p(s_R^k) ds_R^k. \tag{5.3}$$

Similarly, let us define $s_I^k = \text{sgn}(\Im[x_k])\Im[\hat{y}_k]$, the error probability of the quadrature-phase component can be expressed as:

$$P_{e_Q,k}(\boldsymbol{\omega}) = \sum_{m=-\infty}^{\infty} \int_{\frac{2m+1}{2}\tau}^{(m+1)\tau} p(s_I^k) ds_I^k. \tag{5.4}$$

5.2.3 Improved MMSE-VP Design

Let us now introduce our improved MMSE-VP (ImMMSE-VP) design, which is based on the MBER criterion detailed in the previous section. In this design, we are interested in choosing the perturbation vector based on the MBER criterion, rather than on the classic MMSE criterion of [32] which can be found in Section 2.1.2.3.

We consider a 4-QAM scheme having $M = 4$, based on the system model of Fig. 5.1 established in Section 5.2.1 and on the MBER criterion introduced in Section 5.2.2. Our goal is to set up the CF, which can be used to find the specific discrete-valued perturbation vector minimizing the system's BER.

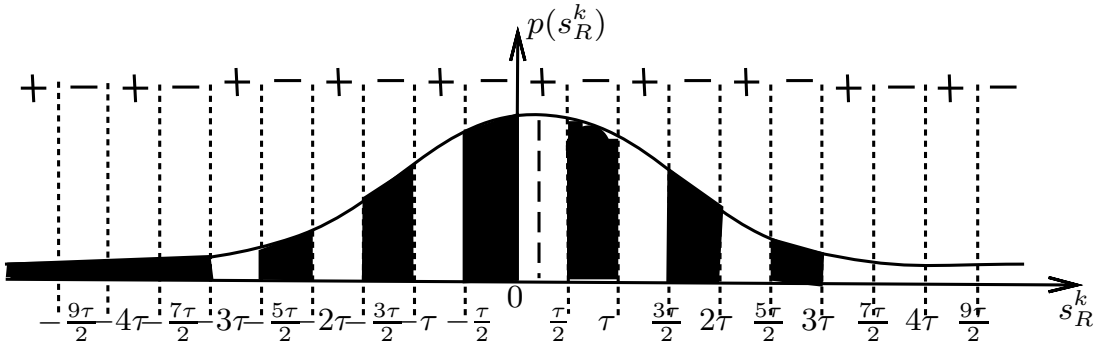

Figure 5.4: Probability density function of the decision variable s_R^k when the modulo operation is employed at the receivers, shaded areas represent the approximated erroneous decision regions, which can be contrasted to the exact regions of Fig. 5.3.

Let us commence by considering the in-phase component. It was shown in the previous section that the BER of the in-phase component associated with user k can be expressed as in Equation (5.3). However, the calculation of this BER involves a sum of an indefinite number of terms, and hence it is impossible to implement it in a real-time system. Hence, some form of approximation has to be employed, so that it can be calculated at a realistic complexity. Hence we used the approximation:

$$\begin{aligned} P_{e_I,k}(\boldsymbol{\omega}) &= \sum_{m=-\infty}^{\infty} \int_{\frac{2m+1}{2}\tau}^{(m+1)\tau} p(s_R^k) ds_R^k \approx \int_{-\infty}^{-3\tau} p(s_R^k) ds_R^k + \int_{-\frac{5\tau}{2}}^{-2\tau} p(s_R^k) ds_R^k + \int_{-\frac{3\tau}{2}}^{-\tau} p(s_R^k) ds_R^k \\ &+ \int_{-\frac{\tau}{2}}^{0} p(s_R^k) ds_R^k + \int_{\frac{\tau}{2}}^{\tau} p(s_R^k) ds_R^k + \int_{\frac{3\tau}{2}}^{2\tau} p(s_R^k) ds_R^k + \int_{\frac{5\tau}{2}}^{3\tau} p(s_R^k) ds_R^k, \end{aligned} \tag{5.5}$$

where the approximation occurs as we lump the integrations over all the error intervals in the range of $(-\infty,\ -3\tau)$ and $(3\tau,\ +\infty)$ into a single integration over the interval $(-\infty,\ -3\tau)$. This approximation is

accurate owing to the close symmetry of the PDF shown in Equation (5.2) in the two regions of $(3\tau,\ +\infty)$ and $(-\infty,\ -3\tau)$, as justified by our simulation results, which will be provided in Section 5.5. Furthermore, the last six integrates at the righthand side of the approximation are generally much larger than the first term.

The error probability of Equation (5.5), namely $P_{e_I,k}(\boldsymbol{\omega})$ can be further expressed as

$$\begin{aligned} P_{e_I,k}(\boldsymbol{\omega}) &\approx Q\left(\frac{c_R^k+3\tau}{\alpha^{-1}\sigma_n}\right)+Q\left(\frac{-\frac{5\tau}{2}-c_R^k}{\alpha^{-1}\sigma_n}\right)-Q\left(\frac{-2\tau-c_R^k}{\alpha^{-1}\sigma_n}\right)+Q\left(\frac{-\frac{3\tau}{2}-c_R^k}{\alpha^{-1}\sigma_n}\right) \\ &- Q\left(\frac{-\tau-c_R^k}{\alpha^{-1}\sigma_n}\right)+Q\left(\frac{-\frac{\tau}{2}-c_R^k}{\alpha^{-1}\sigma_n}\right)-Q\left(\frac{-c_R^k}{\alpha^{-1}\sigma_n}\right)+Q\left(\frac{\frac{\tau}{2}-c_R^k}{\alpha^{-1}\sigma_n}\right) \\ &- Q\left(\frac{\tau-c_R^k}{\alpha^{-1}\sigma_n}\right)+Q\left(\frac{\frac{3\tau}{2}-c_R^k}{\alpha^{-1}\sigma_n}\right)-Q\left(\frac{2\tau-c_R^k}{\alpha^{-1}\sigma_n}\right)+Q\left(\frac{\frac{5\tau}{2}-c_R^k}{\alpha^{-1}\sigma_n}\right) \\ &- Q\left(\frac{3\tau-c_R^k}{\alpha^{-1}\sigma_n}\right). \end{aligned} \tag{5.6}$$

Hence, the average BER of the in-phase component of $\mathbf{y}$ at the receivers is given by

$$P_{e_I,\mathbf{x}}(\boldsymbol{\omega}) = \frac{1}{K}\sum_{k=1}^{K} P_{e_I,k}(\boldsymbol{\omega}). \tag{5.7}$$

Similarly, let $c_I^k = \text{sgn}(\Im[x_k])\Im[\mathbf{h}_k\mathbf{P}\mathbf{u}]$. Then the BER of the quadrature-phase component for the kth user is given by

$$\begin{aligned} P_{e_Q,k}(\boldsymbol{\omega}) &\approx Q\left(\frac{c_I^k+3\tau}{\alpha^{-1}\sigma_n}\right)+Q\left(\frac{-\frac{5\tau}{2}-c_I^k}{\alpha^{-1}\sigma_n}\right)-Q\left(\frac{-2\tau-c_I^k}{\alpha^{-1}\sigma_n}\right)+Q\left(\frac{-\frac{3\tau}{2}-c_I^k}{\alpha^{-1}\sigma_n}\right) \\ &- Q\left(\frac{-\tau-c_I^k}{\alpha^{-1}\sigma_n}\right)+Q\left(\frac{-\frac{\tau}{2}-c_I^k}{\alpha^{-1}\sigma_n}\right)-Q\left(\frac{-c_I^k}{\alpha^{-1}\sigma_n}\right)+Q\left(\frac{\frac{\tau}{2}-c_I^k}{\alpha^{-1}\sigma_n}\right) \\ &- Q\left(\frac{\tau-c_I^k}{\alpha^{-1}\sigma_n}\right)+Q\left(\frac{\frac{3\tau}{2}-c_I^k}{\alpha^{-1}\sigma_n}\right)-Q\left(\frac{2\tau-c_I^k}{\alpha^{-1}\sigma_n}\right)+Q\left(\frac{\frac{5\tau}{2}-c_I^k}{\alpha^{-1}\sigma_n}\right) \\ &- Q\left(\frac{3\tau-c_I^k}{\alpha^{-1}\sigma_n}\right). \end{aligned} \tag{5.8}$$

Then the average BER of the quadrature-phase component of $\mathbf{y}$ at the receivers of the K MSs is given by

$$P_{e_Q,\mathbf{x}}(\boldsymbol{\omega}) = \frac{1}{K}\sum_{k=1}^{K} P_{e_Q,k}(\boldsymbol{\omega}). \tag{5.9}$$

The resultant average BER for 4-QAM signalling becomes

$$P_{e,\mathbf{x}}(\boldsymbol{\omega}) = (P_{e_I,\mathbf{x}}(\boldsymbol{\omega}) + P_{e_Q,\mathbf{x}}(\boldsymbol{\omega}))/2. \tag{5.10}$$

Hence, the optimal discrete-valued perturbation vector $\boldsymbol{\omega}_{\text{opt}}$ is found by solving the following optimization problem

$$\boldsymbol{\omega}_{\text{opt}} = \arg\min_{\boldsymbol{\omega}} P_{e,\mathbf{x}}(\boldsymbol{\omega}). \tag{5.11}$$

This discrete-valued optimization problem can be solved either by the sphere encoding algorithm [23] or by the proposed low complexity discrete multi-valued PSO algorithm of Chapter 4.

5.3 Generalized MBER Vector Precoder Design

The MBER generalised vector precoder design is detailed in this section. First of all, a new system model will be introduced in Section 5.3.1, where a generic vector precoder is used to replace the former precoding matrix and perturbation vector device illustrated in Fig. 5.1. The MBER-VP design is proposed in Section 5.3.2.

5.3.1 New System Model

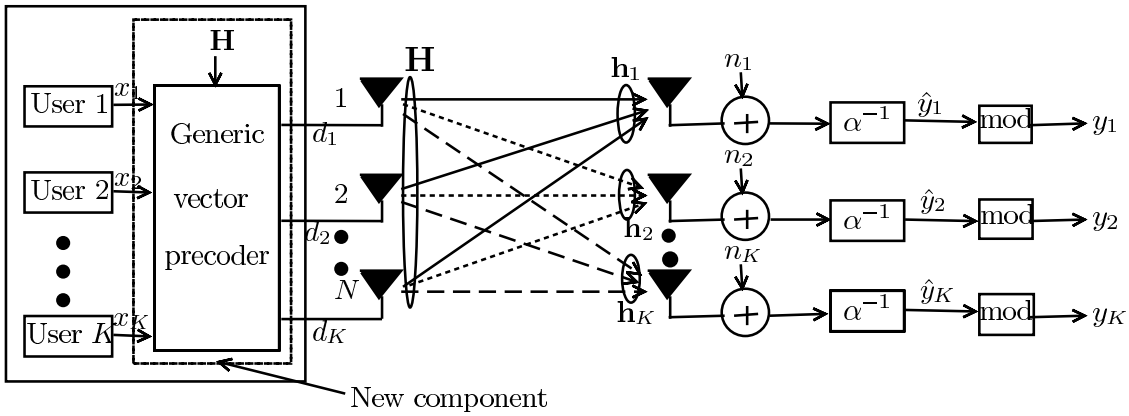

Figure 5.5: Schematic of the SDMA system's DL using generalized VP at the BS. The MUT-aided system employs N transmit antennas at the BS to communicate with K non-cooperative single-receive-antenna aided MSs, each equipped with a modulo device. When compared to Fig. 5.1, we can see that a generic vector precoder is used here.

As in Fig. 5.1 of Section 5.2.1, the DL of a SDMA system is considered here. The corresponding system model is depicted in Fig. 5.5. When compared to Fig. 5.1, we can see that a generic vector precoder is used here in Fig. 5.5. The BS equipped with N transmit antennas communicates over frequency-flat fading channels with K non-cooperative MSs, each employing a single receive antenna and a modulo device. The DL channel matrix $\mathbf{H}$ of the system seen in Fig. 5.5 is given by

$$\mathbf{H} = [\mathbf{h}_1\ \mathbf{h}_2 \cdots \mathbf{h}_K], \tag{5.12}$$

where $\mathbf{h}_k = [h_{1,k}\ h_{2,k} \cdots h_{N,k}]^T$, $1 \leq k \leq K$, is the kth user's spatial signature. The CIR taps $h_{i,k}$ for $1 \leq k \leq K$ and $1 \leq i \leq N$ are independent of each other and obey the complex-valued Gaussian distribution with $E[|h_{i,k}|^2] = 1$, where $E[\bullet]$ denotes the expectation operator. The K-element information symbol vector to be transmitted to the K MSs is given by $\mathbf{x} = [x_1\ x_2 \cdots x_K]^T$, where x_k is the information symbol for the kth MS.

Given the information symbol vector $\mathbf{x}$ and the DL CIR matrix $\mathbf{H}$ of Fig. 5.5, the generic VP generates the N-element continuous-valued effective symbol vector $\mathbf{d} = [d_1\ d_2 \cdots d_N]^T$, based on some criterion. In a conventional VP design seen in Fig. 2.4 of Section 2.1.2.1, such as the ZF-VP [23] and the MMSE-VP [32], the effective symbol vector $\mathbf{d}$ is expressed as

$$\mathbf{d} = \mathbf{P}(\mathbf{x} + \boldsymbol{\omega}), \tag{5.13}$$

where $\mathbf{P}$ is the $N \times K$ precoding matrix and $\boldsymbol{\omega}$ is the K-element discrete-valued perturbation vector. The goal of the design is to determine both $\mathbf{P}$ and $\boldsymbol{\omega}$ based on $\mathbf{H}$ and $\mathbf{x}$. The generic VP precoder presented here directly determines $\mathbf{d}$, which includes the conventional VP as a special case and, therefore, is referred to as the generalised VP.

The DL channel's white noise vector $\mathbf{n}$ is defined by $\mathbf{n} = [n_1\ n_2 \cdots n_K]^T$, where n_k, $1 \leq k \leq K$, is a complex-valued Gaussian random process with zero mean and a variance of $E[|n_k|^2] = 2\sigma_n^2 = \mathrm{N_o}$. Given a total transmit power constraint $\mathrm{E_T}$ at the BS, an appropriate scaling factor should be used to fullfill this transmit power constraint, which is defined as

$$\alpha = \sqrt{\mathrm{E_T}/\|\mathbf{d}\|^2}. \tag{5.14}$$

This definition is similar to Equation (3.7) in the context of the symbol-specific MBER-MUT, but different from Equation (3.6) in the context of the average MBER-MUT. The reason is that the value for the perturbation vector depends on the current information symbol vector as well as the current CIRs, hence it will change whenever either of the information symbol vector or the CIRs changes which is the same as we seen for the symbol-specific MBER-MUT in Section 3.4.1.

At the receiver, the reciprocal of the scaling factor, namely α^{-1}, is used to scale the received signal in order to maintain a unity-gain transmission. This leads to the effective noise $\hat{\mathbf{n}} = \alpha^{-1}\mathbf{n}$. The energy per bit per antenna is defined by $\mathrm{E_b} = \mathrm{E_T}/N \log_2 M$ for an M-ary modulation scheme.

The received signal vector $\hat{\mathbf{y}} = [\hat{y}_1\ \hat{y}_2 \cdots \hat{y}_K]^T$ before the modulo operation is given by

$$\hat{\mathbf{y}} = \mathbf{H}^T\mathbf{d} + \alpha^{-1}\mathbf{n}, \tag{5.15}$$

while the received signal vector $\mathbf{y} = [y_1\ y_2 \cdots y_K]^T$ after the modulo operation is given by

$$\mathbf{y} = mod_\tau(\hat{\mathbf{y}}), \tag{5.16}$$

and y_k, $1 \leq k \leq K$, constitutes sufficient statistics for the kth MS to detect the transmitted information data symbol x_k.

5.3.2 Generalised MBER Vector Precoding

The notations used in this section are similar to those introduced in Section 5.2.3, the difference is that the generic design of the effective symbol vector $\mathbf{d}$ is considered rather than the perturbation vector $\boldsymbol{\omega}$, where the relationship between the two is described in Equation (5.13).

Consider the 4-QAM scheme with $M = 4$. Commencing from the calculation of the error probability of the in-phase component. Similar to what we have shown in Section 5.2.2 and Section 5.2.3, define the error probability or BER encountered at the output of the receiver after the modulo operation for the in-phase component of user k as:

$$P_{e_I,k}(\mathbf{d}) = \text{Prob}\{\text{sgn}(\Re[x_k])\Re[y_k] < 0\}. \tag{5.17}$$

Let us define the signed decision variable $s_R^k = \text{sgn}(\Re[x_k])\Re[\hat{y}_k]$, which has the PDF given by

$$p(s_R^k) = \frac{1}{\sqrt{2\pi}\alpha^{-1}\sigma_n} \exp\left(-\frac{(s_R^k - c_R^k)^2}{2\sigma_n^2\alpha^{-2}}\right), \tag{5.18}$$

with the mean formulated as $c_R^k = \text{sgn}(\Re[x_k])\Re[\mathbf{h}_k\mathbf{d}]$. Note again that the decision areas are periodically extended in the s_R^k-axis. Therefore, the BER of the in-phase component associated with user k is

$$\begin{aligned} P_{e_I,k}(\mathbf{d}) &= \sum_{m=-\infty}^{\infty} \int_{\frac{2m+1}{2}\tau}^{(m+1)\tau} p(s_R^k) ds_R^k \approx \int_{-\infty}^{-3\tau} p(s_R^k) ds_R^k + \int_{-\frac{5\tau}{2}}^{-2\tau} p(s_R^k) ds_R^k + \int_{-\frac{3\tau}{2}}^{-\tau} p(s_R^k) ds_R^k \\ &+ \int_{-\frac{\tau}{2}}^{0} p(s_R^k) ds_R^k + \int_{\frac{\tau}{2}}^{\tau} p(s_R^k) ds_R^k + \int_{\frac{3\tau}{2}}^{2\tau} p(s_R^k) ds_R^k + \int_{\frac{5\tau}{2}}^{3\tau} p(s_R^k) ds_R^k. \end{aligned} \tag{5.19}$$

Similarly to our discussions in Section 5.2.2, the approximation here occurs as we lump the integrations over all the error intervals in the range of $(-\infty, \ -3\tau)$ and $(3\tau, \ +\infty)$ into a single integral over the interval of $(-\infty, \ -3\tau)$. As argued in the context of Section 5.2.2, this approximation is accurate owing to the near symmetry of the PDF shown in Equation (5.18) in the symmetric regions of $(3\tau, \ +\infty)$ and $(-\infty, \ -3\tau)$. We may notice that Equation (5.19) is different from Equation (5.5) although they share a similar expression, since the parameter we consider in Equation (5.19) is the effective symbol vector $\mathbf{d}$ defined in Equation (5.13).

Hence, the average BER of the in-phase component of $\mathbf{y}$ at the receivers is given by

$$P_{e_I,\mathbf{x}}(\mathbf{d}) = \frac{1}{K} \sum_{k=1}^{K} P_{e_I,k}(\mathbf{d}). \tag{5.20}$$

Similarly, he average BEP for the quadrature-phase component of $\mathbf{y}$ at the receivers of the K MSs is given by

$$P_{e_Q,\mathbf{x}}(\mathbf{d}) = \frac{1}{K} \sum_{k=1}^{K} P_{e_Q,k}(\mathbf{d}), \tag{5.21}$$

where $P_{e_Q,k}(\mathbf{d})$ represents the BEP of the quadrature-phase component for the kth user.

The resultant average BEP for 4-QAM signalling then becomes

$$P_{e,\mathbf{x}}(\mathbf{d}) = [P_{e_I,\mathbf{x}}(\mathbf{d}) + P_{e_Q,\mathbf{x}}(\mathbf{d})]/2. \tag{5.22}$$

Hence, the optimal continuous-valued effective symbol vector $\mathbf{d}_{\text{opt}}$ is found by solving the following optimisation problem

$$\mathbf{d}_{\text{opt}} = \arg \min_{\mathbf{d}} P_{e,\mathbf{x}}(\mathbf{d}). \tag{5.23}$$

The above optimization problem turns out to be a challenging non-convex continuous-valued optimization problem, where numerous local minimas may exist, as demostrated below.

Explicitly, as seen in Fig. 5.6, at SNR=$12dB$, even for a simple 1×1 system, there are several local minimas at the complex coordinate.

In order to find either the global minimum or a reasonably 'good' local minimum, we will adopt the continous-valued PSO algorithm introduced in Chapter 3 to solve the optimization problem formulated in Equation (5.23).

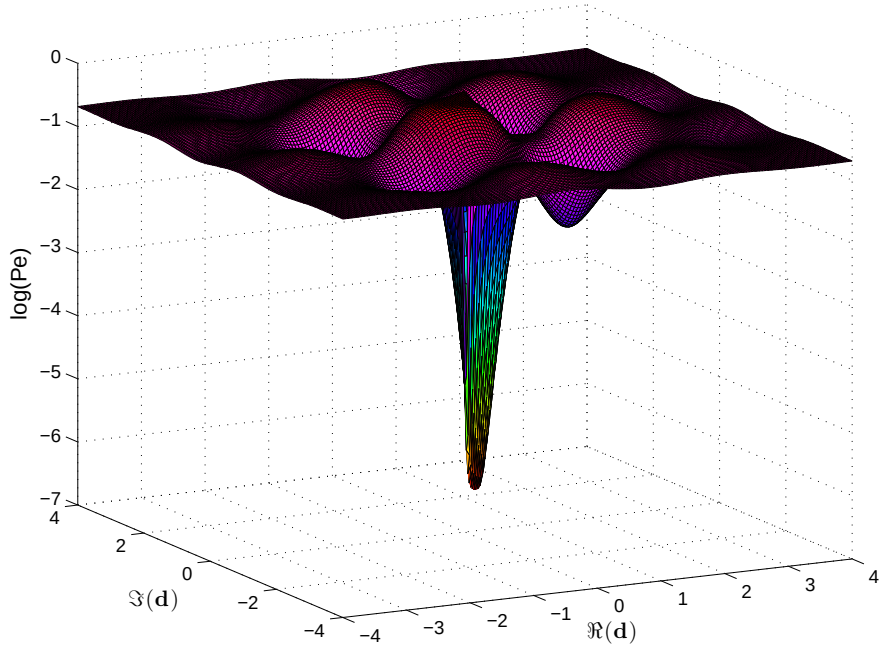

Figure 5.6: BER surface as a function of the effective symbol vector $\mathbf{d}$ for the simplest 4-QAM system with $N = 1$ and $K = 1$, given SNR= 12 dB. The channel coefficient is $\mathbf{H} = [0.7543 + J0.0419]$.

Table 5.1: Computational complexity of the ImMMSE-VP using sphere encoding and our discrete multi-valued PSO approach for QPSK signalling, where N is the number of transmit antennas, K is the number of mobile users, I is the number of iterations, $D_{\mathrm{ImMMSE-VP}}$ denotes the number of extended constellation points visited, and S is the particle size.

Algorithm	Flops
Sphere encoding	$(73 \cdot K + 18 \cdot K \cdot N + 6 \cdot N + 4) D_{\mathrm{ImMMSE-VP}}$
PSO	$(4 + 30 \cdot K \cdot S + (14 \cdot K \cdot N + 30 \cdot K + 6 \cdot N) \cdot S) \cdot I$ $+(14 \cdot K \cdot N + 30 \cdot K + 6 \cdot N) \cdot S$

5.4 Computational Complexity

The computational complexity of our improved MMSE-VP and of the generalized MBER-VP is discussed in this section.

5.4.1 Computational Complexity of the ImMMSE-VP

The complexity of the most substantial contributions determining the overall complexity of finding the ImMMSE-VP solution are summarized in Table 5.1. More explicitly, a detailed key complexity contribution calculation table for our proposed PSO aided ImMMSE-VP scheme per iteration is listed in Table 5.2. All of these contributions depend on the number of users K, on the number of transmit antennas N and on the size of the swarm S.

Table 5.2: Detailed key computational complexity contribution per iteration for the PSO aided ImMMSE-VP design for QPSK signalling, where K is the number of mobile users, N is the number of transmit antennas and S is the particle size. The numbers in () indicate the index of the corresponding block in Fig. 4.1.

Stage	Flops
Update inertia weight (3)	4
Update velocities (3)	$9 \cdot 2 \cdot K \cdot S$
Calculate sigmoid function (3)	$3 \cdot 2 \cdot K \cdot S$
Update positions (3)	$3 \cdot 2 \cdot K \cdot S$
Evaluate fitness (2)	$(14 \cdot K \cdot N + 30 \cdot K + 6 \cdot N) \cdot S$

The computational complexity of the discrete multi-valued PSO aided ImMMSE-VP depends not only on the number of users K, the number of transmit antennas N and the size of the swarm S, but also on the number of iterations the algorithm requires, in order to converge to the optimum point. This will be discussed more in detail in Section 5.5 with the aid of simulation results.

5.4.2 Computational Complexity of the Generalized MBER-VP

Table 5.3: Detailed key computational complexity contributions per iteration for the PSO aided MBER-VP design for QPSK signalling, where K is the number of mobile users, N is the number of transmit antennas and S is the particle size. The numbers in () indicate the index of the corresponding block in Fig. 2.8.

Stage	Flops
Update system parameters (3)	$6 \cdot S$
Update velocities and positions (3)	$23 \cdot N \cdot S$
Evaluate fitness (2)	$(73 \cdot K + 7 \cdot N \cdot K) \cdot S$

The computational complexity of the proposed generalized MBER-VP algorithm designed for QPSK signalling may be evaluated by considering Equation (5.23), yielding a total complexity of:

$$C_{\mathrm{GMBER-VP}} = \big(7 \cdot N + (73 + 7 \cdot N) \cdot K + (23 \cdot N + (73 + 7 \cdot N) \cdot K + 6) I_{\max}\big) \cdot S + C_{\mathrm{ImMMSE-VP}} + 2 \cdot K + 7 \cdot K \cdot N + 5 \cdot S, \quad (5.24)$$

where N is the number of transmit antennas, K is the number of mobile users, $I_{\max}$ is the number of iterations needed to converge to optimal solution, S is the particle size and $C_{\mathrm{ImMMSE-VP}}$ denotes the complexity imposed by obtaining the ImMMSE-VP solution for the system. The detailed key complexity contributions of our proposed PSO aided MBER-VP scheme per iteration are summarized in Table 5.3.

5.5 Simulations and Discussions

In this section, simulation results are provided for characterizing our solution, which are followed by corresponding discussions. In the following simulations, we used a swarm size of $S = 40$ for discrete-valued

Table 5.4: Simulation parameters.

Parameter	Value or Type
System	
Modulation scheme	QPSK
Transmit antennas	2 or 4
Receive end users	4
Channel	flat Rayleigh fading
CSIT knowledge	perfect
Channel realizations	100
PSO	
Swarm size for discrete multi-valued PSO S_{dpso}	40
Swarm size for continuous-valued PSO S_{cpso}	20

PSO and a swarm size of $S = 20$ for continuous-valued PSO. This decision was made based on our experiences with PSO shown in Section 3.7.4 and Section 4.7.6. We would like to point out that the choice of the swarm size may not be the best, but nevertheless, constitutes a reasonable design compromise between the performance attained and the complexity imposed.

5.5.1 Verification of the approximation

First, we considered the effects of the approximation we made in Equation (5.5) and Equation (5.19), when designing the ImMMSE-VP and the generalized MBER-VP schemes. The related system parameters are shown in Table 5.4, where the DL of a multiuser system employing $N = 4$ transmit antennas at the BS to support $K = 4$ 4-QAM MSs was considered. Perfect CSI knowledge was assumed at the BS for transmission over the $(N \times K)$-element flat Rayleigh fading MIMO channel, and the results were obtained by averaging the resultant performances over 100 channel realizations.

First of all, let us consider the effects of different approximations in the context of Equation (5.6), when the ImMMSE-VP algorithm is adopted. Generally speaking, when more integrals are calculated over the error intervals shown in Fig. 5.3, the related approximation would become more accurate. Naturally, the computational complexity would also be increased. However, the overall BER performance of the system may not be substantially improved, when more integrations are calculated over the error intervals. In Fig. 5.7, we characterized four error probability approximations, which are:

Case 1: By observing Fig. 5.3, we approximate the integrals over all the error intervals in $(-\infty,\ -\tau)$ and $(\tau,\ +\infty)$ as the single integral over the interval $(-\infty,\ -\tau)$, which implies the assumption that the probability of encountering errors in the range of $(\tau,\ +\infty)$ is neglected. Furthermore, we consider the shaded areas of $(-\frac{\tau}{2},\ 0)$ and $\frac{\tau}{2},\ \tau$ in Fig. 5.3, yielding:

$$\sum_{t=-\infty}^{\infty} \int_{\frac{2t+1}{2}\tau}^{(t+1)\tau} p(s_R^k) ds_R^k \approx \int_{-\infty}^{-\tau} p(s_R^k) ds_R^k + \int_{-\frac{\tau}{2}}^{0} p(s_R^k) ds_R^k + \int_{\frac{\tau}{2}}^{\tau} p(s_R^k) ds_R^k.$$

Case 2: With reference to Fig. 5.3, we approximate the integrals over all the error intervals in $(-\infty, \ -2\tau)$ and $(2\tau, \ +\infty)$ as the single integration over the interval $(-\infty, \ -2\tau)$:

$$\sum_{t=-\infty}^{\infty} \int_{\frac{2t+1}{2}\tau}^{(t+1)\tau} p(s_R^k) ds_R^k \approx \int_{-\infty}^{-2\tau} p(s_R^k) ds_R^k + \int_{-\frac{3\tau}{2}}^{-\tau} p(s_R^k) ds_R^k + \int_{-\frac{\tau}{2}}^{0} p(s_R^k) ds_R^k + \int_{\frac{\tau}{2}}^{\tau} p(s_R^k) ds_R^k + \int_{\frac{3\tau}{2}}^{2\tau} p(s_R^k) ds_R^k. \quad (5.25)$$

Case 3: This is the approximation we opted for in our proposed design, which considers seven of the shaded areas in Fig. 5.3:

$$\sum_{t=-\infty}^{\infty} \int_{\frac{2t+1}{2}\tau}^{(t+1)\tau} p(s_R^k) ds_R^k \approx \int_{-\infty}^{-3\tau} p(s_R^k) ds_R^k + \int_{-\frac{5\tau}{2}}^{-2\tau} p(s_R^k) ds_R^k + \int_{-\frac{3\tau}{2}}^{-\tau} p(s_R^k) ds_R^k + \int_{-\frac{\tau}{2}}^{0} p(s_R^k) ds_R^k + \int_{\frac{\tau}{2}}^{\tau} p(s_R^k) ds_R^k + \int_{\frac{3\tau}{2}}^{2\tau} p(s_R^k) ds_R^k + \int_{\frac{5\tau}{2}}^{3\tau} p(s_R^k) ds_R^k. \quad (5.26)$$

Case 4: Again, with reference to Fig. 5.3, we approximate the integrals over all the error intervals in $(-\infty, \ -5\tau)$ and $(5\tau, \ +\infty)$ as the single integral over the interval of $(-\infty, \ -5\tau)$, and we consider a

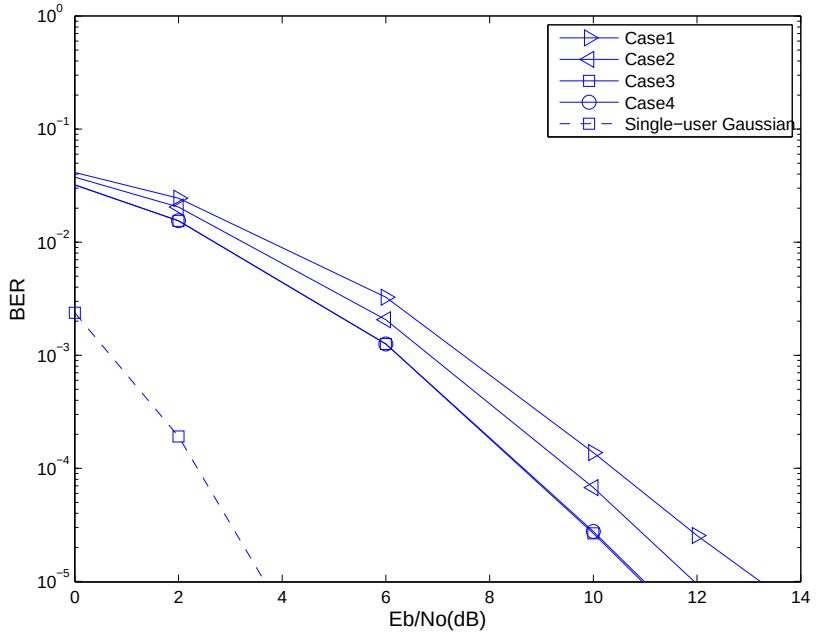

Figure 5.7: BER versus SNR performance of our proposed improved MMSE vector precoding algorithm based on MBER criterion, while different BER approximations are considered. Case 1 refers to the integration considering the interval $(-\tau, \ \tau)$; case 2 refers to the integration considering the interval $(-2\tau, \ 2\tau)$; case 3 refers to the integration considering the interval $(-3\tau, \ 3\tau)$; case 4 refers to the integration considering the interval $(-5\tau, \ 5\tau)$. The modulo operations are employed at the receivers. Transmissions are over flat Rayleigh fading channels using $N = 4$ transmit antennas to support $K = 4$ 4-QAM users. All system parameters are summarized in Table 5.4. The performance of the MBER-MUT recorded in the same scenario was shown in Fig. 3.16.

total of 11 shaded areas in Fig. 5.3, yielding:

$$\begin{aligned}\sum_{t=-\infty}^{\infty}\int_{\frac{2t+1}{2}\tau}^{(t+1)\tau} p(s_R^k)ds_R^k \approx & \int_{-\infty}^{-5\tau} p(s_R^k)ds_R^k + \int_{-\frac{9\tau}{2}}^{-4\tau} p(s_R^k)ds_R^k + \int_{-\frac{7\tau}{2}}^{-3\tau} p(s_R^k)ds_R^k \\ + & \int_{-\frac{5\tau}{2}}^{-2\tau} p(s_R^k)ds_R^k + \int_{-\frac{3\tau}{2}}^{-\tau} p(s_R^k)ds_R^k + \int_{-\frac{\tau}{2}}^{0} p(s_R^k)ds_R^k \\ + & \int_{\frac{\tau}{2}}^{\tau} p(s_R^k)ds_R^k + \int_{\frac{3\tau}{2}}^{2\tau} p(s_R^k)ds_R^k + \int_{\frac{5\tau}{2}}^{3\tau} p(s_R^k)ds_R^k \\ + & \int_{\frac{7\tau}{2}}^{4\tau} p(s_R^k)ds_R^k + \int_{\frac{9\tau}{2}}^{5\tau} p(s_R^k)ds_R^k. \end{aligned} \tag{5.27}$$

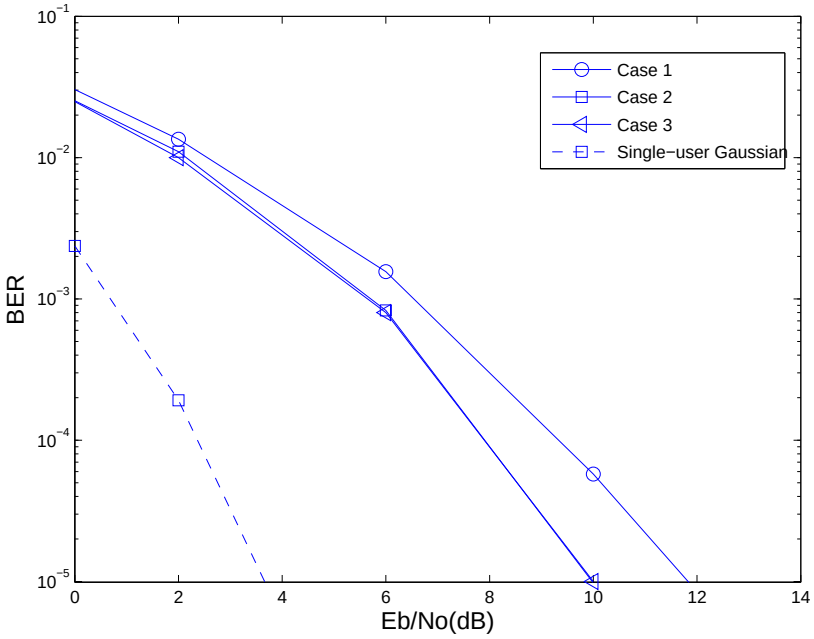

Figure 5.8: BER versus SNR performance of our proposed generalized MBER vector precoding algorithm based on MBER criterion, while different BER approximations are considered. Case 1 refers to the integration considering the interval $(-2\tau,\ 2\tau)$; case 2 refers to the integration considering the interval $(-3\tau,\ 3\tau)$; case 3 refers to the integration considering the interval $(-5\tau,\ 5\tau)$. The modulo operations are employed at the receivers. All system parameters are summarized in Table 5.4. The performance of the MBER-MUT recorded in the same scenario was shown in Fig. 3.16.

The influence of the different approximations of the desired BER is shown in Fig. 5.7. It is clear that Case 3 strikes the best trade-off between the complexity imposed and the BER performance attained.

Let us now consider the generalized MBER-VP algorithm. In Fig. 5.8, three different BER approximations are considered. Case 1 refers to the integration considering the interval $(-2\tau,\ 2\tau)$; Case 2 represents the integration considering the interval $(-3\tau,\ 3\tau)$; Case 3 refers to the integration considering the interval $(-5\tau,\ 5\tau)$.

Observe from Fig. 5.8 that the approximation of Case 1 is insufficiently accurate, while the performance obtained by using the approximations of Case 2 and Case 3 are similar. Since Case 2 benefits from a lower computational complexity, it may be deemed to be the best choice among the three approximations.

5.5.2 Guaranteed generalized MBER-VP performance

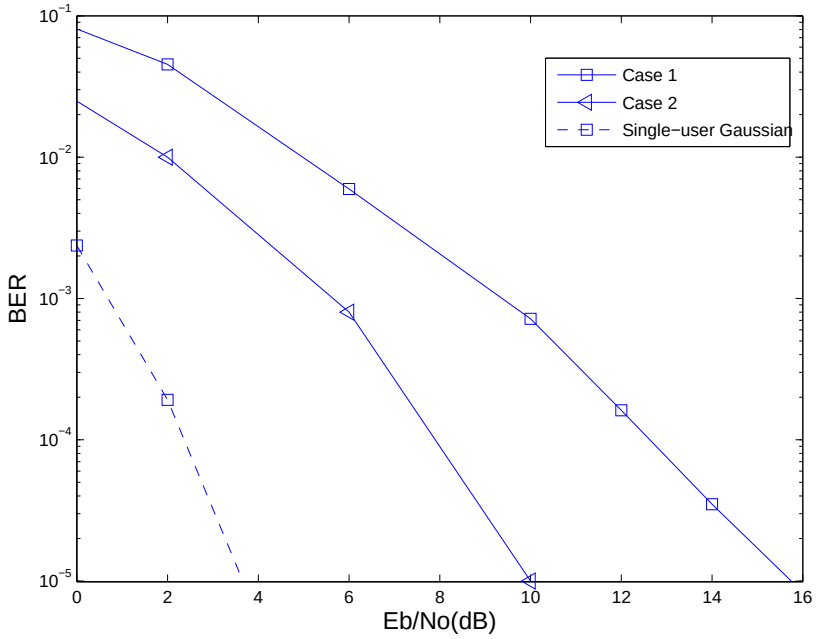

Figure 5.9: Performance comparison of Case 1 (all particles are randomly initialized) and Case 2(one of the particles is initialized to be the solution of the previously proposed improved MMSE VP, while the others are randomly initialized) communicating over flat Rayleigh fading channels using $N = 4$ transmit antennas to support $K = 4$ 4-QAM users. All system parameters are summarized in Table 5.4. The performance of the MBER-MUT recorded in the same scenario was shown in Fig. 3.16.

In this part, let us consider the performance gain of the continous-valued PSO aided generalized MBER-VP when the ImMMSE-VP solution is used as part of the initial swarm. The system parameters are listed in Table 5.4, where the DL of a multiuser system employing $N = 4$ transmit antennas at the BS to support $K = 4$ 4-QAM MSs is considered. Perfect CSI knowledge was assumed at the BS for transmission over an $(N \times K)$-element flat Rayleigh fading MIMO channel and the results were obtained by averaging the resultant performances over 100 channel realizations.

Fig. 5.9 shows the BER performance comparison of two different cases, namely where all particles are randomly initialized in Case 1, while in Case2, one of the particles is initialized to be the previously proposed ImMMSE-VP solution, with the others being randomly initialized. It is clear from Fig. 5.9 that in Case 1 only a relatively low-quality local minimum can be found, while in Case 2, when a good starting point was provided during the initialization stage, a much better local minimum was found, which ensures a better BER performance. This suggests that it is beneficial to use the ImMMSE-VP solution as one of the initialization points, when the generalized MBER-VP is adopted, although naturally this increases the system's computational complexity.

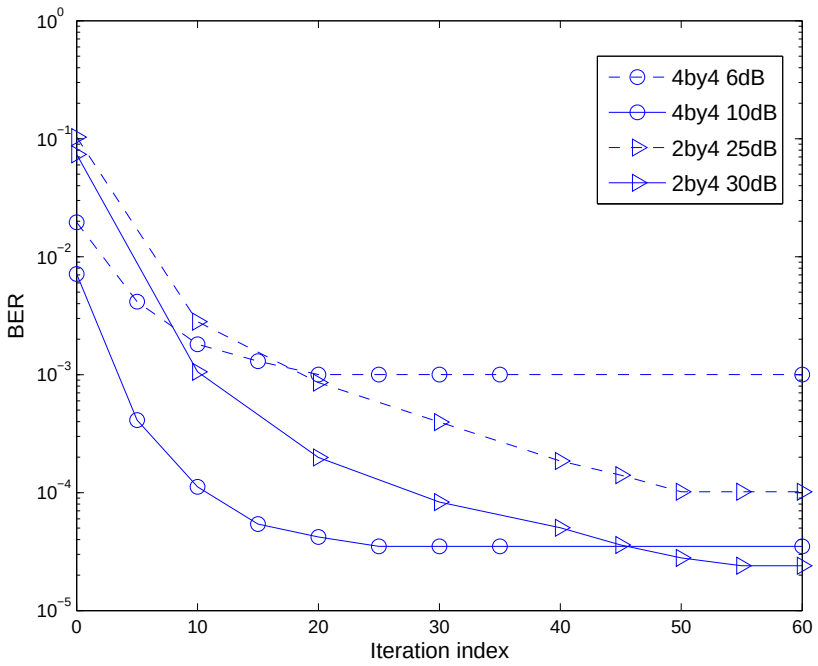

Figure 5.10: Convergence performance of our proposed ImMMSE-VP algorithm based on the MBER criterion, while using the modulo operation at the receivers for communicating over flat Rayleigh fading channels in different scenarios. All system parameters are summarized in Table 5.4.

Table 5.5: Computational complexity of the proposed ImMMSE-VP algorithm in different scenarios, evaluated from Table 5.1.

SNR	6dB (4×4)	10dB (4×4)	25dB (2×4)	30dB (2×4)
Complexity (Flops)	405,200	502,820	520,040	571,260

5.5.3 Convergence and Complexity

The covergence behavior of our proposed discrete multi-valued PSO aided ImMMSE-VP scheme, of the continuous-valued PSO aided generalized MBER-VP algorithm and of the corresponding implementational complexity is considered here. The parameters of the test scenario are listed in Table 5.4. The DL of a multiuser $(N \times K)$-element MIMO system employing N transmit antennas at the BS is considered, when supporting K QPSK users. Perfect CSI knowledge was assumed at the BS for transmission over the $(N \times K)$-element flat Rayleigh fading MIMO channel.

Firstly, we consider the convergence of our discrete multi-valued PSO aided ImMMSE-VP algorithm. The attainable performance can be seen in Fig. 5.10. When the system employs $N = 4$ transmit antennas to support $K = 4$ QPSK mobile users over flat Rayleigh fading channels, while using the swarm size $S = 40$, we can see that the ImMMSE-VP algorithm requires I =20 iteration on average to converge at $Eb/No = 6$dB. The corresponding computational complexity evaluated from Table 5.1 is C =405,200, while at $Eb/No = 10$dB, the algorithm needs I =25 iterations on average to converge. The corresponding computational complexity is C =502,820.

The system was reconfigured to use $N = 2$ transmit antennas to support $K = 4$ QPSK mobile users over flat Rayleigh fading channels, which is a rank deficient scenario. The swarm size was kept constant at $S = 40$. Observe in Fig. 5.10 that the proposed ImMMSE-VP algorithm needs I =50 iterations on average to converge at $Eb/No = 25$dB. The corresponding computational complexity evaluated from Table 5.1 is C =520,040, while at $Eb/No = 30$dB, the algorithm needs I =55 iterations on average to converge. The resultant computational complexity is C =571,260.

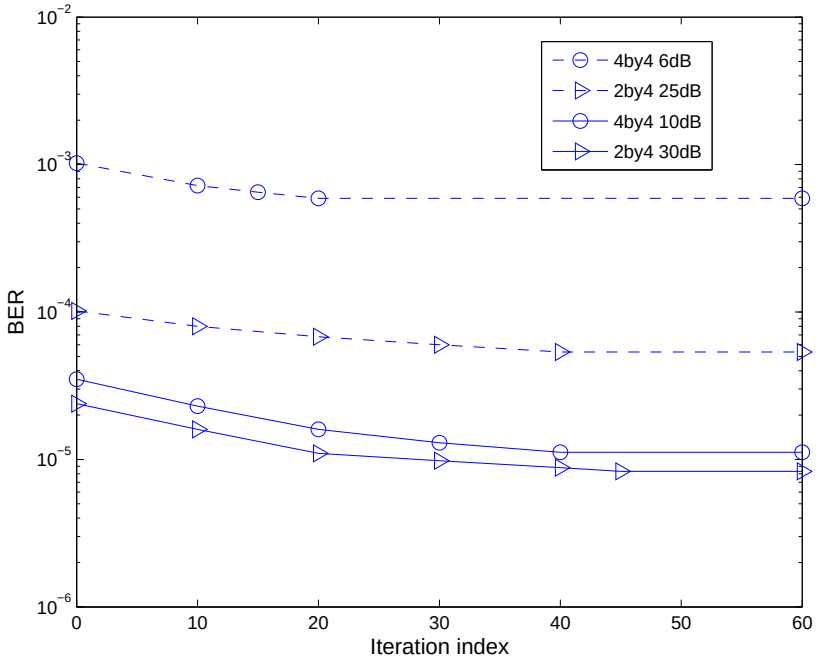

Figure 5.11: Convergence performance of our proposed generalized MBER-VP scheme, while using the modulo operation at the receivers for communicating over flat Rayleigh fading channels in different scenarios. All system parameters are summarized in Table 5.4.

Let us now consider the convergence behavior of the generalized MBER-VP algorithm, which is portrayed in Fig. 5.11. When the system employs $N = 4$ transmit antennas to support $K = 4$ QPSK mobile users over flat Rayleigh fading channels, when using a swarm size of $S = 20$, we can see that the generalized MBER-VP scheme needs I =20 iterations on average to converge at $Eb/No = 6$dB. The corresponding computational complexity evaluated from Table 5.3 is $(C_{\mathrm{ImMMSE-VP}}+209,660)$, while at $Eb/No = 10$dB, the algorithm requires I =40 iterations on average to converge, the corresponding computational complexity is then $(C_{\mathrm{ImMMSE-VP}} + 410,460)$.

Let us now reconfigure the system to operate in a rank-deficient scenario where $N = 2$ transmit antennas are used for supporting $K = 4$ QPSK mobile users for communicating over flat Rayleigh fading channels. As before, we set the swarm size to $S = 20$. Observe in Fig. 5.11 that the proposed generalized MBER-VP algorithm needs I =40 iterations on average to converge at $Eb/No = 25$dB. The corresponding computational complexity evaluated from Table 5.3 is $(C_{\mathrm{ImMMSE-VP}} + 244,760)$. By contrast, at $Eb/No = 30$dB, the algorithm requires I =45 iterations on average to converge, when the associated computational complexity is $(C_{\mathrm{ImMMSE-VP}} + 274,760)$.

Table 5.6: Computational complexity of the proposed generalized MBER-VP algorithm in different scenarios, evaluated from Table 5.3.

SNR	6dB (4×4)	10dB (4×4)
Complexity(Flops)	$C_{\mathrm{ImMMSE-VP}} + 209,660$	$C_{\mathrm{ImMMSE-VP}} + 410,460$
SNR	25dB (2×4)	30dB (2×4)
Complexity(Flops)	$C_{\mathrm{ImMMSE-VP}} + 244,760$	$C_{\mathrm{ImMMSE-VP}} + 274,760$

5.5.4 Overall system performance

The overall BER performance of the proposed algorithms is discussed here.

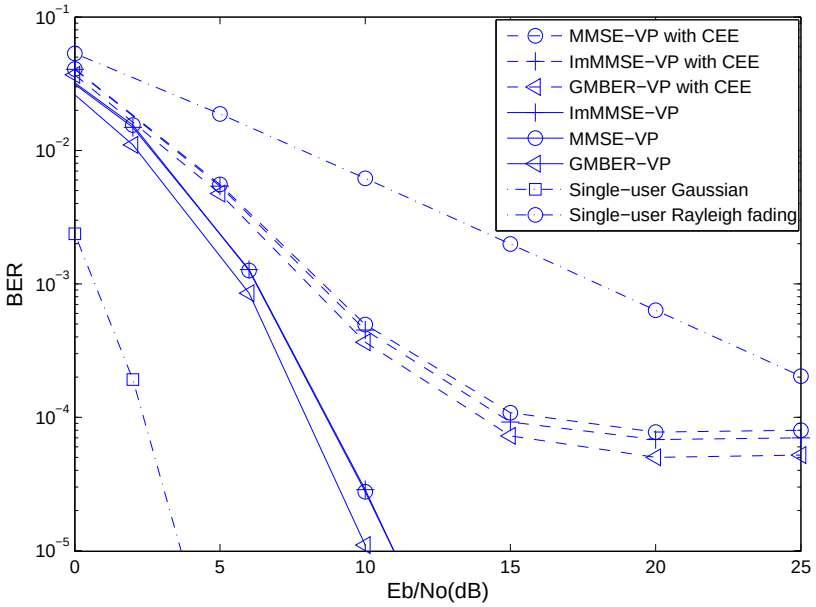

Figure 5.12: BER versus SNR performance of the MMSE-VP of [32] and of our proposed ImMMSE-VP scheme based on the MBER criterion and generalized MBER-VP algorithm, while using the modulo operation at the receivers for communicating over flat Rayleigh fading channels using $N = 4$ transmit antennas to support $K = 4$ 4-QAM users. All system parameters are summarized in Table 5.4. The performance of the MBER-MUT recorded in the same scenario was shown in Fig. 3.16.

5.5.4.1 Full-rank system

The BER performance of the MMSE-VP of [32] and of our proposed ImMMSE-VP algorithm based on the MBER criterion using the discrete perturbation scheme and the continous-valued PSO aided generalized MBER-VP algorithm are compared in Fig. 5.12 for full rank systems, when using the system parameters summarized in Table 5.4.

We considered the case of $N = 4$ and $K = 4$. First the perfect knowledge of the DL CIR matrix was assumed at the BS. It can be seen from Fig. 5.12 that the proposed PSO-aided generalized MBER-VP

scheme achieved an approximately 1 dB SNR gain at the target BER of 10^{-5} over both the MMSE-VP as well as the ImMMSE-VP algorithm. For this full-rank system, the ImMMSE-VP and the MMSE-VP were seen to achieve a virtually identical BER performance, which was also demonstrated in [36]. The robustness of the algorithms against channel estimation errors was investigated next. A complex-valued Gaussian white noise with a variance of 0.01 was added to each channel tap $h_{i,k}$ to model the channel estimation error. The BERs of these three VP designs under this channel estimation error model were also depicted in Fig. 5.12. Observe in the figure that the proposed generalized MBER-VP design was no more sensitive to channel estimation errors than the MMSE-VP and the ImMMSE-VP designs.

5.5.4.2 Rank-deficient system

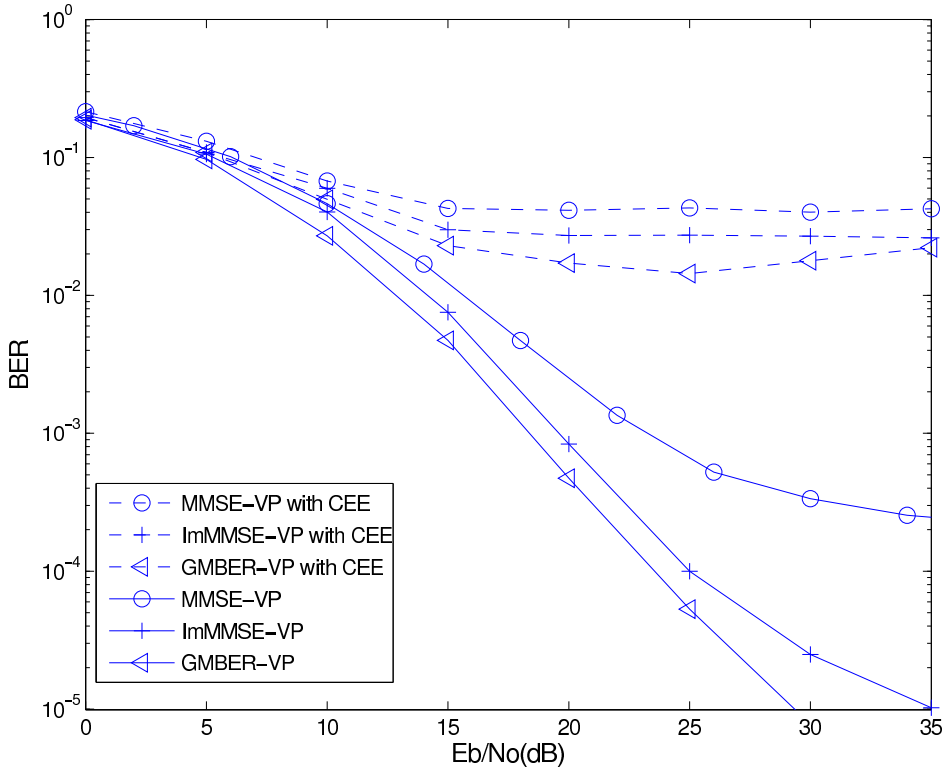

Figure 5.13: Performance comparison of the MMSE VP precoder and our proposed improved MMSE vector precoding algorithm based on MBER criterion for communicating over flat Rayleigh fading channels using $N = 2$ transmit antennas to support $K = 4$ 4-QAM users. All system parameters are summarized in Table 5.4. The performance of the MBER-MUT recorded in the same scenario was shown in Fig. 3.16.

The system was then configured to use $N = 2$ transmit antennas for supporting $K = 4$ 4-QAM users, which was a challenging rank-deficient scenario. The system parameters are summarized in Table 5.4, while the BER performances of the three algorithms can be seen in Fig. 5.13.

As oberved in Fig. 5.13, the MMSE VP scheme encountered an error floor, since it was unable to confidently differentiate the users' information in this demanding scenario. On the other hand, the improved MMSE-VP scheme based on the MBER criterion showed a significantly better performance, but still sufferred from an error floor, as seen in Fig. 5.13. By contrast, the generalized MBER-VP outperformed the other two designs and, as a further benefit, it did not exhibit a visible error floor. The absence of an

error-floor demonstrated its ability to operate successfully in the rank-deficient scenario. Furthermore, the generalized MBER-VP algorithm was seen to be no more sensitive to channel estimation errors than the other two designs.

5.6 Conclusions

In this chapter, we invoked the MBER criterion for designing vector precoding schemes, where transmitted signal is appropriately perturbed at the BS for the sake of directly minimizing the BER at the receiver. The perturbation induced ambiguity has to be removed at the MS's receiver with the aid of appropriate modulo devices. Based on this novel MBER criterion which is prominently featured in the schematic of Fig. 5.2.2, we proposed two different vector precoding algorithms.

Table 5.7: Performance summary of benchmark schemes evaluated in this chapter. The SNR gap refers to the performance SNR gain over other schemes when using the proposed GMBER-VP algorithm.

	GMBER-VP	ImMMSE-VP	MMSE-VP
SNR gap at 10^{-5} (4×4)	benchmark	1 dB	1 dB
Complexity(Flops)/SNR (4×4)	793,230/10dB	502,820/10dB	382,770/10dB
Relative complexity (4×4)	2.07	1.31	1
SNR gap at 10^{-5} (2×4)	benchmark	6 dB	>10 dB
Complexity(Flops)/SNR (2×4)	846,020/30dB	571,260/30dB	433,670/30dB
Relative complexity (2×4)	1.95	1.32	1

In Fig. 5.1 of Section 5.2, we firstly introduced an improved MMSE-VP design based on the MBER criterion. This transmit preprocessing scheme invokes a regularized channel inversion and then superimposes a discrete-valued perturbation vector on the transmitted signal in order to minimize the BER of the system as an improvement of the well-established MMSE-VP scheme. The discrete multi-valued PSO can be adopted to solve the corresponding optimization problem and its computational complexity was discussed in Section 5.4. To further improve the system's BER performance, a generalized MBER-based continuous-valued VP algorithm was proposed in Section 5.3. Given the knowledge of the information symbol vector to be transmitted and the CIR matrix, we consider the generation of the effective symbol vector to be transmitted by directly minimizing the BER of the system. We showed that continous-valued PSO can be used to solve the corresponding optimization problem. The corresponding computational complexity was discussed in 5.4. Simulation results were also provided to show the advantage of these VP schemes relying on the MBER criterion, especially for rank-deficient systems where the number of BS transmit antennas is lower than the number of MSs supported. It was shown in Equation (5.3) of Section 5.2.2 that an appropriate approximation may need to be taken in order to calculate the BEP of the system invoking the proposed algorithms. Hence, we demonstrated the appropriate approximation for both scenarios through simulations, which were shown in Fig. 5.7 and Fig. 5.8. The convergence bahavior of our proposed discrete multi-valued PSO aided ImMMSE-VP scheme, of the continuous-valued PSO aided generalized MBER-VP algorithm and of the corresponding implementational complexity was shown in Fig. 5.10 and Fig. 5.11 of Section 5.5.3. The

overall BER performance of the algorithms in full-rank system was shown in Fig. 5.12, while their performance in rank-deficient system was shown in Fig. 5.13. Both of the algorithms were capable of achieving a better performance than MMSE-VP technique in both scenarios, while a substantial BER performance gain could be attained by the generalized MBER-VP algorithm over other schemes in the challenging rank-deficient scenario. The robustness of these two designs to CIR estimation errors were also investigated in Fig. 5.12 and Fig. 5.13, showing that the proposed algorithms are no more sensitive to channel estimation errors than the MMSE-VP scheme.

The overall BER and computational complexity performances of the MMSE-VP technique, the proposed ImMMSE-VP and generalized MBER-VP scheme were summarized in Table 5.7. It can be observed that in a 4×4 full-rank system, the SNR gain of the generalized MBER-VP scheme over the other two algorithms was 1 dB at the target BER of 10^{-5}, while its computational complexity imposed was around two times of that imposed by using the MMSE-VP technique. Hence, the proposed generalized MBER-VP scheme may not be the best choice in terms of striking a trade-off between the attainable BER performance and the implementation complexity imposed, although it achieved the best BER performance amongst the techniques. On the other hand, when the operating system was a 2×4 rank-deficient one, a substantial SNR gain was achieved by the proposed generalized MBER-VP scheme over the other two algorithms. Again, the imposed complexity by it was around two times of that imposed by using the MMSE-VP technique as seen in Table 5.7. This suggests that the generalized MBER-VP algorithm may be deemed as a good alternative of the MMSE-VP scheme in rank-deficient scenarios. In summary, the proposed generalized MBER-VP algorithm is more suitable to be adopted in the challenging rank-deficient scenarios, in order to beneficially strike a trade-off between the BER performance attained and the complexity imposed.

In the next chapter, we will further extend the MBER vector precoding technique to a MIMO transceiver design.

Chapter 6

Transceiver Design Based On Uniform Channel Decomposition and MBER Vector Perturbation

6.1 Introduction and Relevance to previous Chapters

In Chapter 5, we developed the MBER vector precoder design. In Fig. 5.12, we observed that the proposed generalized MBER-VP can only achieve a marginal SNR gain over the well-established MMSE-VP scheme in a (4×4)-element full-rank system. As argued in Chapter 1, MIMO techniques are capable of offering an increased channel capacity in interference-free scenarios, albeit their achievable performances remain limited by the MUI. Nonetheless, the MUI can be mitigated at the receiver [147] or at the transmitter [32] as well as jointly at the transmitter and receiver [8]. The latter approach leads to a joint MIMO transmitter/receiver structure, which we refer to as a transceiver. In order to further increase the attainable BER performance of a system in both full-rank and rank-deficient scenarios in this chapter, we are interested in invoking the MBER vector precoding technique in our transceiver design.

A nonlinear transceiver design based on the geometric mean decomposition (GMD) was proposed in [6]. The GMD is capable of beneficially diagonalising the MIMO channel matrix leading to identical diagonal elements, hence offering identical MIMO subchannel gains. It is worth mentioning that the GMD approach has been considered for adoption in both the Third-generation Partnership Project's Long Term Evolution Advanced (3GPP LTE-A) and in the WiMAX (802.16m) standards [148]. Later, the uniform channel decomposition (UCD) was proposed in [7] as an improvement of the GMD. The UCD maintains the highest possible capacity at any SNR, and it achieves the maximal attainable diversity gain [7]. The precoder design of [6, 7] constitutes a THP [22], which constitutes a specific implementation of the dirty paper coding principle [31]. This THP design is generally outperformed by the VP algorithm. The solutions proposed in [8] extended the idea of [6] to a GMD MMSE-VP (GMD-MMSE-VP) transceiver design. Since the BER is the ultimate system performance indicator, the schemes designed by minimising the BER criterion are

attractive. It may also expected that a UCD based VP design will outperform a GMD based VP design. Although the authors of [7] proposed a UCD based THP design (UCD-THP), to the best of our knowledge, no UCD aided VP transceiver design was proposed to date in the open literature. Against this background, in this chapter we propose a joint transceiver design by combining the UCD and the MBER based VP, where the precoding and equalization matrices are calculated by the UCD method, while the perturbation vector is chosen directly based on the MBER criterion.

The rest of this chapter is structured as follows. In Section 6.3, the MIMO system model is introduced, while Section 6.4 details the proposed UCD-MBER-VP transceiver design. Simulation results are presented in Section 6.6 to compare our proposed design to several existing benchmark schemes. We conclude our discourse in Section 6.7.

6.2 Uniform Channel Decomposition

In the field of MIMO transceiver design, the singular value decomposition (SVD) [39] constitutes a popular technique since it is capable of decomposing a MIMO channel into multiple different-quality parallel subchannels. When combined with the classic water filling algorithm [6], the channel capacity can be approached [149]. More specifically, the SVD algorithm decomposes the $(N \times K)$-element channel matrix $\mathbf{H}$ as:

$$\mathbf{H} = \mathbf{U}\mathbf{\Lambda}\mathbf{V}^H, \tag{6.1}$$

where $\mathbf{\Lambda}$ is the $(O \times O)$-element diagonal matrix, whose diagonal elements $\{\lambda_o\}_{o=1}^{O}$ are the nonzero singular values of $\mathbf{H}$, $\mathbf{U}$ is an $(N \times O)$-element orthonormal matrix, and $\mathbf{V}^H$ is an $(O \times K)$-element orthonormal matrix.

In the classic SVD aided MIMO systems, the transmitted signal can be expressed as $\mathbf{s} = \mathbf{V}\mathbf{x}$, where the orthonormal precoding matrix $\mathbf{V}$ must not change the transmit power. The equalization matrix employed at the receiver may be expressed as $\mathbf{\Lambda}^{-1}\mathbf{U}^H$, resulting in the received signal $\mathbf{y}$ after equalization in the following form [67]:

$$\begin{aligned} \mathbf{y} &= \mathbf{\Lambda}^{-1}\mathbf{U}^H(\mathbf{H}\mathbf{V}\mathbf{x} + \mathbf{n}) \\ &= \mathbf{x} + \mathbf{n}', \end{aligned} \tag{6.2}$$

where $\mathbf{n}' = \mathbf{\Lambda}^{-1}\mathbf{U}^H\mathbf{n}$ and $\mathbf{R}_{\mathbf{n}'} = E[\mathbf{n}'\mathbf{n}'^H] = \sigma_n^2 diag(\frac{1}{\lambda_1}, \cdots, \frac{1}{\lambda_O})$, which implies that we have O parallel AWGN channels contaminated by uncorrelated noise of power σ_n^2/λ_o^2.

We may observe that the SVD could result in subchannels with vastly different SNRs, imposing further complexity in terms of the subchannel ordering problem, subsequent subchannel specific modulation/demodulation as well as different-rate channel coding/decoding procedures. To overcome this potential problem, Jiang *et al.* proposed the so-called geometric mean decomposition (GMD) technique [6]. The GMD algorithm is capable of beneficially diagonalizing the MIMO channel matrix leading to identical diagonal elements, hence offering identical subchannel gains, as detailed in Section 6.2.1. Later, uniform

Table 6.1: Selected contributions on the development of GMD and UCD techniques

Year	Author(s)	Contributions
2005	[6] Jiang *et al.*	Proposed GMD, characterizing it from a purely mathematical point of view.
2005	[150] Jiang *et al.*	Proposed a joint transceiver design that combines GMD with either a zero-forcing VBLAST decoder or zero-forcing THP.
2005	[7] Jiang *et al.*	Proposed a joint transceiver design that combines UCD with either a MMSE VBLAST decoder or THP.
2006	[151] Lin *et al.*	Extended the single user GMD and UCD MIMO transceiver designs to the multi-user broadcast channel scenario by invoking the Block-Diagonalization method, resulting in the so-called BD-GMD and BD-UCD designs.
2006	[152] Jiang and Varanasi	Analyzed the diversity-multiplexing tradeoff of GMD/UCD combined with optimal antenna selection. Approximated the error probability with the aid of the Gaussian Q-function.
2007	[153] Peh and Liang	Proposed an expanded soft symbol-to-bit demapper scheme specifically designed for the GMD-THP MIMO systemfor the sake of supporting soft decision-aided channel decoding.
2007	[8] Liu *et al.*	Proposed a MIMO transceiver design by combining the GMD and the MMSE-VP techniques.
2009	[154] Chen *et al.*	Proposed a robust UCD scheme, which was capable of improving both the BER and the achievable capacity in the context of imperfect CSI, which was benchmarked against the conventional UCD scheme.
2009	[155] Lee and Lee	Proposed an UCD design. Demonstrated that the proposed scheme had an enhanced diversity order compared to the SVD scheme, which was achieved by exploiting the specific properties of the UCD.
2010	[156] Liu *et al.*	Proposed a MIMO transceiver design based on the amalgam of the BD-GMD and ZF-VP.

channel decomposition (UCD) was proposed also by Jiang *et al.* in [7] as an improvement of GMD. The UCD maintains the highest possible capacity at any signal-to-noise ratio (SNR), and it achieves the maximal attainable diversity gain [7]. The UCD is detailed in Section 6.2.2. First of all, let us briefly consider the development of GMD and UCD techniques, as seen in Table 6.1.

6.2.1 Geometric Mean Decomposition

The mathematical description of GMD was provided in [6], where an $(N \times K)$-element channel matrix having a rank of O was decomposed in the following manner:

$$\mathbf{H} = \mathbf{Q}_g \mathbf{R}_g \mathbf{P}_g^H, \tag{6.3}$$

where $\mathbf{Q}_g$ and $\mathbf{P}_g$ have orthonormal columns, and $\mathbf{R}_g$ is an $(O \times O)$-element real-valued upper-triangular matrix having identical diagonal elements, all of which are equal to the geometric mean of the positive singular values, namely:

$$r_g^{i,i} = \bar{\lambda} = \left(\prod_{\lambda_j > 0} \lambda_j \right)^{1/O}, 1 \leq i \leq O, \tag{6.4}$$

where $\bar{\lambda}$ is the geometric mean of the positive singular values.

The advantage of GMD may be explained as follows. Consider a MIMO system modeled by

$$\mathbf{y} = \mathbf{H}\mathbf{s} + \mathbf{n}, \tag{6.5}$$

where $\mathbf{s}$ is the transmitted signal, $\mathbf{y}$ is the received signal and $\mathbf{n}$ is the noise. We assume that $\mathbf{H}$ is decomposed as $\mathbf{H} = \mathbf{Q}\mathbf{R}\mathbf{P}^H$, where $\mathbf{R}$ is a $(O \times O)$-element upper-triangular matrix, while $\mathbf{P}$ and $\mathbf{Q}$ are matrices having orthonormal columns. The actions of the matrices $\mathbf{P}$ and $\mathbf{Q}$ may be interpreted as those of filters, filtering the transmitted and received signals. Then, we arrive at the equivalent expression:

$$\hat{\mathbf{y}} = \mathbf{R}\mathbf{x} + \mathbf{n}', \tag{6.6}$$

where $\mathbf{s} = \mathbf{P}\mathbf{x}$, $\hat{\mathbf{y}} = \mathbf{Q}^H\mathbf{y}$ and $\mathbf{n}' = \mathbf{Q}^H\mathbf{n}$.

By exploiting Costa's suggestion [31] that the interference known at the transmitter may be completely canceled without consuming any additional transmit power, the system can be converted into O decoupled parallel subchannels, each modeled as:

$$\hat{y}_i = r^{i,i} x_i + n_i', \quad i = 1, \cdots, O. \tag{6.7}$$

Assuming that the variance of the noise imposed on the O subchannels is identical, the subchannels associated with the smallest $r^{i,i}$ yield the highest error rate. This leads to the problem of appropriately choosing $\mathbf{P}$ and $\mathbf{Q}$ in order to maximize the minimum of $r^{i,i}$ [6]:

$$\max_{\mathbf{P},\mathbf{Q}} \min\{r^{i,i} : 1 \leq i \leq O\}, \quad s.t. \quad \mathbf{Q}\mathbf{R}\mathbf{P}^H = \mathbf{H}, \mathbf{Q}^H\mathbf{Q} = \mathbf{I}, \quad \mathbf{P}^H\mathbf{P} = \mathbf{I}, r^{i,j} = 0 \ \ for \ \ i > j. \tag{6.8}$$

It was shown in [6] that the GMD provides the optimal solution to Equation 6.8.

The GMD operations may be based on an initial SVD step, and it may be summarized as follows [6]:

1. Let $\mathbf{H} = \mathbf{U}\mathbf{\Lambda}\mathbf{V}^H$ be the SVD of $\mathbf{H}$. Let us furthermore initialize $\mathbf{Q}_g = \mathbf{U}$, $\mathbf{R}_g = \mathbf{\Lambda}$, $\mathbf{P}_g = \mathbf{V}$ and $o = 1$.

2. If $r_g^{o,o} \geq \bar{\lambda}$, choose $p > o$ so that $r_g^{o,o} \leq \bar{\lambda}$. If $r_g^{o,o} < \bar{\lambda}$, choose $p > o$ so that $r_g^{o,o} \geq \bar{\lambda}$. In $\mathbf{Q}_g$, $\mathbf{R}_g$ and $\mathbf{P}_g$ perform the following exchanges:

$$\begin{aligned} r_g^{o+1,o+1} &\longleftrightarrow r_g^{p,p}, \\ \mathbf{Q}_g^{:,o} &\longleftrightarrow \mathbf{Q}_g^{:,p}, \\ \mathbf{P}_g^{:,o+1} &\longleftrightarrow \mathbf{Q}_g^{:,p}. \end{aligned} \tag{6.9}$$

3. Construct the orthogonal matrices $\mathbf{G}_1$ and $\mathbf{G}_2$ according to Equation (9) of [6]. Replace $\mathbf{R}_g$ by $\mathbf{G}_2^T\mathbf{R}_g\mathbf{G}_1$, replace $\mathbf{Q}_g$ by $\mathbf{Q}_g\mathbf{G}_2$ and replace $\mathbf{P}_g$ by $\mathbf{P}_g\mathbf{G}_1$.

4. If $o = O - 1$, the process stop and $\mathbf{Q}_g\mathbf{R}_g\mathbf{P}_g^H$ is the GMD of $\mathbf{H}$. Otherwise, replace o with $o + 1$ and go to step 2.

It is worth mentioning in closing that the Matlab implementation of this GMD algorithm was posted by the authors of [6] at the following website:
http://www.math.ufl.edu/ hager/papers/gmd.m .

6.2.2 Uniform Channel Decomposition

The GMD algorithm was shown to be asymptotically optimal at high SNRs in terms of both its throughput and BER performance [7]. Hence, it does not have to strike a tradeoffs between the achievable capacity and BER performance. Instead, it attempts to achieve the 'best of both worlds' simultaneously. Nonetheless, it may suffer from considerable capacity loss at low SNRs due to the inherent 'zero-forcing' operations since it does not take the noise into consideration, which results in a reduced capacity at low SNRs [7] where the noise-amplification is more dominant. Against this background, Jiang *et al.* proposed the UCD algorithm in [7] as an improvement of GMD, which decomposes a MIMO channel into multiple identical subchannels under MMSE criteria [154], which is depicted later in this section.

Let us recall the SVD of $\mathbf{H}$ from Equation (6.1). The research in [149] showed that the optimal precoder from an information theoretic point of view is formulated as

$$\mathbf{F}_{svd} = \mathbf{V}\mathbf{\Phi}, \tag{6.10}$$

where $\mathbf{\Phi}$ is a $(O \times O)$-element diagonal matrix whose diagonal elements $\{\phi_o\}_{o=1}^{O}$ are found by the water filling process as [149]

$$\phi_o^2(\mu) = (\mu - \frac{\beta}{\lambda_o^2})^+, \tag{6.11}$$

where β is defined as $\beta = \frac{2\sigma_n^2}{\sigma_x^2}$, μ is chosen so that $\sum_{o=1}^{O} \phi_o^2(\mu) = O$ and $(a)^+ = \max\{0, a\}$.

In contrast to the SVD-based precoder of Equation (6.10), the UCD precoder $\mathbf{F}_{ucd}$ is derived from the SVD precoder of Equation (6.10) as follows:

$$\mathbf{F}_{ucd} = \mathbf{V}\mathbf{\Phi}\mathbf{\Omega}^H, \tag{6.12}$$

where $\mathbf{\Omega}$ is a $(N \times O)$-element semi-unitary matrix, which satisfies $\mathbf{\Omega}^H\mathbf{\Omega} = \mathbf{I}$. Then UCD precoder $\mathbf{F}_{ucd}$ is known for maximizing the channel's throughput [7]. Moreover, a higher grade of flexibility can be achieved by introducing $\mathbf{\Omega}$ in the precoder matrix $\mathbf{F}_{ucd}$ in Equation (6.12) than that of the SVD precoder of $\mathbf{F}_{svd}$ in Equation (6.10). Hence, now the problem lies in beneficially designing the semi-unitary matrix $\mathbf{\Omega}$.

The virtual channel created by introducing the precoder $\mathbf{F}_{svd}$ can be expressed as:

$$\mathbf{G} = \mathbf{H}\mathbf{F}_{svd} = \mathbf{U}\mathbf{\Lambda}\mathbf{\Phi}\mathbf{\Omega}^H = \mathbf{U}\mathbf{\Sigma}\mathbf{\Omega}^H \quad , \tag{6.13}$$

where $\mathbf{\Sigma} = \mathbf{\Lambda}\mathbf{\Phi}$ is a diagonal matrix. Let us also introduce $\mathbf{G}_a$ to denote the augmented matrix

$$\mathbf{G}_a = \begin{bmatrix} \mathbf{U}\mathbf{\Sigma}\mathbf{\Omega}^H \\ \sqrt{\beta}\mathbf{I}_N \end{bmatrix}. \tag{6.14}$$

Then our aim is to find a semi-unitary matrix $\mathbf{\Omega}$ so that the QR decomposition [150] of $\mathbf{G}_a$ yields an upper triangular matrix having identical diagonal elements. The authors of [7] proved the following lemma:

"For any matrix of the form given in (29), we can find a semi-unitary matrix $\mathbf{\Omega}$ such that the QR decomposition of $\mathbf{G}_a$ yields an upper triangular matrix with equal diagonal elements."

Equation (29) in [7] is the matrix $\mathbf{G}_a$, and $\mathbf{\Omega}$ can be obtained by rewriting $\mathbf{G}_a$ of Equation (6.14) as

$$\mathbf{G}_a = \begin{bmatrix} \mathbf{U}\left[\mathbf{\Sigma} \vdots \mathbf{0}_{O\times(N-O)}\right]\mathbf{\Omega}_0^H \\ \sqrt{\beta}\mathbf{I}_N \end{bmatrix} \quad , \tag{6.15}$$

where $\mathbf{\Omega}_0$ is a $(N \times N)$-element unitary matrix whose first O columns form $\mathbf{\Omega}$. Then $\mathbf{G}_a$ can be further rewritten as

$$\mathbf{G}_a = \begin{bmatrix} \mathbf{I}_K & \mathbf{0} \\ \mathbf{0} & \mathbf{\Omega}_0 \end{bmatrix} \begin{bmatrix} \mathbf{U}\left[\mathbf{\Sigma} \vdots \mathbf{0}_{O\times(N-O)}\right] \\ \sqrt{\beta}\mathbf{I}_N \end{bmatrix} \mathbf{\Omega}_0^H \quad . \tag{6.16}$$

We are also able to obtain the following equation by using the GMD:

$$\mathbf{J} = \begin{bmatrix} \mathbf{U}\left[\mathbf{\Sigma} \vdots \mathbf{0}_{O\times(N-O)}\right] \\ \sqrt{\beta}\mathbf{I}_N \end{bmatrix} = \mathbf{Q}_J\mathbf{R}_J\mathbf{P}_J^H, \tag{6.17}$$

where $\mathbf{R}_J$ is a $(N \times N)$-element upper triangular matrix having identical real-valued diagonal elements, $\mathbf{Q}_J$ is a $[(N + K) \times N]$-element semi-unitary matrix, and $\mathbf{P}_J$ is a $(N \times N)$-element unitary matrix. Inserting Equation (6.17) into Equation (6.16), we arrive at

$$\mathbf{G}_a = \begin{bmatrix} \mathbf{I}_K & \mathbf{0} \\ \mathbf{0} & \mathbf{\Omega}_0 \end{bmatrix} \mathbf{Q}_J\mathbf{R}_J\mathbf{P}_J^H\mathbf{\Omega}_0^H. \tag{6.18}$$

Let $\mathbf{\Omega}_0 = \mathbf{P}_J^H$ and

$$\mathbf{Q}_{G_a} = \begin{bmatrix} \mathbf{I}_K & \mathbf{0} \\ \mathbf{0} & \mathbf{\Omega}_0 \end{bmatrix} \mathbf{Q}_J. \tag{6.19}$$

Then Equation (6.18) can be rewritten as $\mathbf{G}_a = \mathbf{Q}_{G_a}\mathbf{R}_J$ which is the QR decomposition of $\mathbf{G}_a$. The semi-unitary matrix $\mathbf{\Omega}$ associated with $\mathbf{G}_a$ consists of the first O columns of $\mathbf{P}_J^H$. Hence, $\mathbf{\Omega}$ is obtained.

6.2.3 Numerical Example

A simple example may be used to show how these algorithms work. Let us consider a 2×2 system operating at $\mathbf{E_b/N_o}$=12 $\mathbf{dB}$ and the channel matrix $\mathbf{H}$ can be described as:

$$\mathbf{H} = \begin{bmatrix} -0.36 + j0.35 & 1.13 + j0.009 \\ -0.06 + j1.80 & -0.11 - j0.86 \end{bmatrix}.$$

When the SVD scheme is considered, according to Equation (6.1), namely

$$\mathbf{H} = \mathbf{U}\mathbf{\Lambda}\mathbf{V}^H.$$

For our specific example, we have:

$$\mathbf{U} = \begin{bmatrix} -0.42 + j0.15 & 0.87 + j0.17 \\ 0.02 + j0.89 & -0.22 + j0.39 \end{bmatrix},$$

$$\mathbf{\Lambda} = \begin{bmatrix} 2.21 + j0.00 & 0.00 + j0.00 \\ 0.00 + j0.00 & 0.82 + j0.00 \end{bmatrix},$$

$$\mathbf{V} = \begin{bmatrix} 0.82 - j0.00 & 0.56 + j0.00 \\ -0.56 + j0.04 & -0.82 - j0.05 \end{bmatrix}.$$

When the GMD algorithm is considered, according to Equation (6.3) of Section 6.2.1, we arrive at:

$$\mathbf{Q}_g = \begin{bmatrix} 0.08 + j0.21 & 0.96 + j0.06 \\ -0.09 + j0.96 & -0.20 - j0.12 \end{bmatrix},$$

$$\mathbf{R}_g = \begin{bmatrix} 1.34 + j0.00 & -1.38 + j0.00 \\ 0.00 + j0.00 & 1.34 + j0.00 \end{bmatrix},$$

$$\mathbf{P}_g = \begin{bmatrix} 0.91 + j0.00 & -0.40 + j0.00 \\ 0.40 - j0.02 & 0.91 - j0.06 \end{bmatrix}.$$

We can see that the diagonal elements of the matrix $\mathbf{R}_g$ have an identical value and this value has the following relationship with the diagonal elements of the matrix $\mathbf{\Lambda}$ according to Equation (6.4):

$$r_g = \bar{\lambda} = (2.21 \times 0.82)^{1/2} = 1.34.$$

Finally, when the UCD technique is considered, our target is that of designing $\mathbf{F}_{ucd}$ of Equation (6.12), yielding:

$$\mathbf{V} = \begin{bmatrix} 0.82 - j0.00 & 0.56 + j0.00 \\ -0.56 + j0.04 & -0.82 - j0.05 \end{bmatrix},$$

$$\mathbf{\Phi} = \begin{bmatrix} 1.00 + j0.00 & -0.00 + j0.00 \\ 0.00 + j0.00 & 0.98 + j0.00 \end{bmatrix},$$

$$\mathbf{\Omega} = \begin{bmatrix} 0.52 + j0.00 & -0.85 + j0.00 \\ -0.85 - j0.00 & 0.52 - j0.00 \end{bmatrix},$$

hence,

$$\mathbf{F}_{ucd} = \begin{bmatrix} 0.91 + j0.00 & -0.41 + j0.00 \\ 0.39 - j0.02 & 0.91 - j0.06 \end{bmatrix}.$$

6.3 System Model

The following system model description is similar to that introduced in Section 2.1.2.1. The difference is that in contrast to Fig. 2.3 a $(K \times K)$-element equalization matrix $\mathbf{Q}^H$ is introduced in the model of Fig. 6.1.

Let us now detail the schematic of the MIMO system depicted in Fig. 6.1, where the BS's DL transmitter equipped with N antennas transmit the K users' data streams to the receiver employing K receive antennas and K modulo devices. Frequency-flat fading MIMO channels are considered. The channel matrix $\mathbf{H}$ of the system is given by

$$\mathbf{H} = [\mathbf{h}_1 \, \mathbf{h}_2 \cdots \mathbf{h}_K],$$

where $\mathbf{h}_k = [h_{1,k} \; h_{2,k} \cdots h_{N,k}]^T$, $1 \leq k \leq K$. The CIR taps $h_{i,k}$ for $1 \leq k \leq K$ and $1 \leq i \leq N$ are independent of each other and obey the complex-valued Gaussian distribution with $E[|h_{i,k}|^2] = 1$. The K-element original information symbol vector is given by $\mathbf{x} = [x_1 \; x_2 \cdots x_K]^T$, where x_k denotes the kth information symbol. It is assumed that $E[\mathbf{x}\mathbf{x}^H] = \sigma_x^2 \mathbf{I}_N$, with $\mathbf{I}_N$ denoting the $(N \times N)$-element identity matrix. The original transmitted symbol vector $\mathbf{x}$ is then perturbed to generate the K-element perturbed vector $\mathbf{u}$, as given by

$$\mathbf{u} = \mathbf{x} + \boldsymbol{\omega},$$

where $\boldsymbol{\omega}$ is a complex-valued perturbation vector. The $(N \times K)$-element precoding matrix $\mathbf{P}$ of Fig. 6.1 is given by

$$\mathbf{P} = [\mathbf{p}_1 \, \mathbf{p}_2 \cdots \mathbf{p}_K],$$

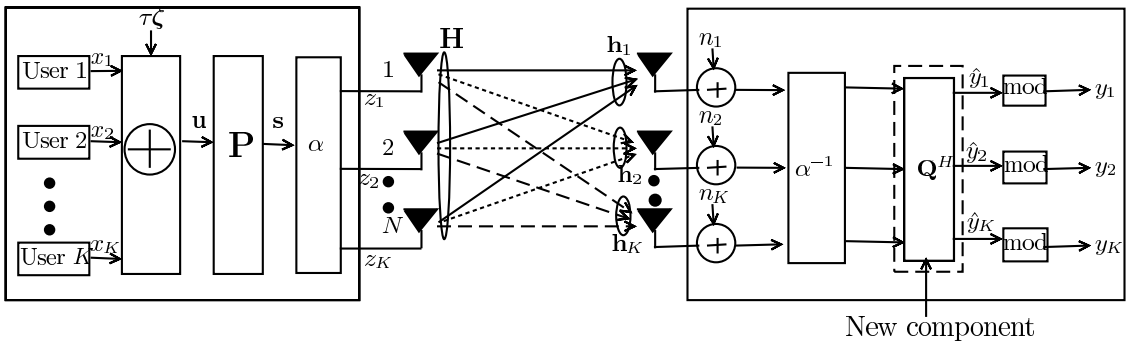

Figure 6.1: Schematic of the DL MIMO system, where the transmitter employing N transmit antennas communicates with the receiver using K receive antennas. Compared to Fig. 2.3, the new component is the $(K \times K)$-element equalisation matrix $\mathbf{Q}^H$.

where $\mathbf{p}_k$, $1 \leq k \leq K$, is the precoder's coefficient vector for the kth user's data stream. Given a fixed total radiated power $\mathrm{E_T}$ at the transmitter, an appropriate scaling factor should be used to fulfill this transmit power constraint, which is defined as

$$\alpha = \sqrt{\mathrm{E_T}/\|\mathbf{Pu}\|^2}.$$

The channel's white noise vector $\mathbf{n}$ is defined by $\mathbf{n} = [n_1\ n_2 \cdots n_K]^T$, where n_k, $1 \leq k \leq K$, is a complex-valued Gaussian random process with zero mean and $E[|n_k|^2] = 2\sigma_n^2 = \mathrm{N_o}$. At the receiver, the reciprocal of the scaling factor, namely α^{-1}, is used to scale the received signal in order to maintain a unity-gain transmission. The received signal vector $\hat{\mathbf{y}} = [\hat{y}_1\ \hat{y}_2 \cdots \hat{y}_K]^T$ before the modulo operation is given by

$$\begin{aligned} \hat{\mathbf{y}} &= \mathbf{Q}^H\mathbf{HPu} + \alpha^{-1}\mathbf{Q}^H\mathbf{n} \\ &= \mathbf{Q}^H\mathbf{HPu} + \hat{\mathbf{n}}, \end{aligned} \tag{6.20}$$

with the $(K \times K)$-element equalisation matrix $\mathbf{Q}$ of Fig. 6.1 defined as $\mathbf{Q} = [\mathbf{q}_1\ \mathbf{q}_2 \cdots \mathbf{q}_K]$, and the effective noise as $\hat{\mathbf{n}} = \alpha^{-1}\mathbf{Q}^H\mathbf{n}$.

The modulo operation of Fig. 6.1 invoked for $\hat{y}_k$, $1 \leq k \leq K$, is described by Equation (2.29), namely:

$$mod_\tau(\hat{y}_k) = \hat{y}_k - \lfloor\frac{\Re[\hat{y}_k] + \tau/2}{\tau}\rfloor\tau - j\lfloor\frac{\Im[\hat{y}_k] + \tau/2}{\tau}\rfloor\tau,$$

where $\Re[\bullet]$ and $\Im[\bullet]$ represents the real and imaginary parts, respectively, $j^2 = -1$, $\lfloor \bullet \rfloor$ denotes the largest integer less than or equal to its argument and τ is a positive number. If the square-shaped M-point Gray coded quadrature amplitude modulation (QAM) constellation of

$$\Big\{\pm\frac{1}{2}, \cdots, \pm\frac{\sqrt{M}-1}{2}\Big\} + j\Big\{\pm\frac{1}{2}, \cdots, \pm\frac{\sqrt{M}-1}{2}\Big\}$$

is used, the modulo operation parameter can be set to $\tau = \sqrt{M}$ [157]. Thus, the received signal vector $\mathbf{y} = [y_1\ y_2 \cdots y_K]^T$ after the modulo operation is given by

$$\mathbf{y} = mod_\tau(\hat{\mathbf{y}}),$$

and y_k, $1 \leq k \leq K$, constitutes sufficient statistics for the receiver to make a hard-decision concerning the transmitted information data symbol x_k, $1 \leq k \leq K$.

6.4 UCD aided MBER VP Transceiver Design

For notational simplicity, in this section, we restrict our discourse to the 4-QAM scheme associated with $M = 4$. Its extension to high-order QAM schemes can be achieved by considering the Minimum Symbol Error Rate (MSER) criterion, in the spirit of the MSER multiuser detection case of [158]. The UCD scheme [7] is used here to design both the transmitter's precoding matrix $\mathbf{P}$ and the receiver's equalisation matrix $\mathbf{Q}$ of Fig. 6.1, while the design of the perturbation vector $\boldsymbol{\omega}$ is based on the MBER criterion, as detailed in Section 5.2.

The design introduced in Section 6.2.2 is actually the UCD-VBLAST scheme [7], which consists of a linear DL precoder at the BS and the MMSE-VBLAST detector at the MS's receiver. We may exploit

the uplink-downlink duality [159] here in order to design the UCD-MBER-VP scheme, which implies the idealized simplifying assumption of having an identical CIR in the UL and DL.

The linear equalisation matrix $\mathbf{Q}$ of Fig. 6.1 can be calculated by using the same technique as that employed for designing the linear precoder of [7] in the reverse channel. Let us denote the SVD [39] of $\mathbf{H}^H$ as $\mathbf{H}^H = \mathbf{U}\mathbf{\Lambda}\mathbf{V}^H$, where $\mathbf{\Lambda}$ is the $(O \times O)$-element diagonal matrix, whose diagonal elements $\{\lambda_o\}_{o=1}^{O}$ are the nonzero singular values of $\mathbf{H}^H$, $\mathbf{U}$ is an $(N \times O)$-element matrix, and $\mathbf{V}^H$ is an $(O \times K)$-element matrix. We calculate the equalisation matrix $\mathbf{Q}$ in the following manner [7]:

$$\mathbf{Q} = \mathbf{V}\mathbf{\Phi}\mathbf{\Omega}^H, \tag{6.21}$$

where the $(O \times O)$-element diagonal matrix $\mathbf{\Phi}$ and the $(K \times O)$-element matrix $\mathbf{\Omega}$ are obtained by following [149]. Explicitly, the diagonal elements $\{\phi_o\}_{o=1}^{O}$ of $\mathbf{\Phi}$ are found by the water filling process formulated as [7]:

$$\phi_o^2(\mu) = (\mu - \frac{\beta}{\lambda_o^2})^+, \tag{6.22}$$

where β is defined as $\beta = \frac{2\sigma_n^2}{\sigma_x^2}$, μ is chosen to satisfy $\sum_{o=1}^{O} \phi_o^2(\mu) = O$ and $(a)^+ = \max\{0, a\}$. Let us now introduce $\mathbf{\Sigma} = \mathbf{\Lambda}\mathbf{\Phi}$. Then $\mathbf{\Omega}$ is obtained with the aid of the GMD [7] in the form of:

$$\begin{bmatrix} \mathbf{U}\begin{bmatrix}\mathbf{\Sigma} \vdots \mathbf{0}_{O\times(K-O)}\end{bmatrix} \\ \sqrt{\beta}\mathbf{I}_K \end{bmatrix} = \mathbf{Q}_J\mathbf{R}_J\mathbf{P}_J^H, \tag{6.23}$$

where $\mathbf{R}_J$ is a $(K \times K)$-element upper triangular matrix having identical real-valued diagonal elements, $\mathbf{Q}_J$ is a $[(N+K) \times K]$-element semi-unitary matrix, and $\mathbf{P}_J$ is a $(K \times K)$-element unitary matrix. The matrix $\mathbf{\Omega}$ simply consists of the first O columns of $\mathbf{P}_J^H$.

The calculation of the precoding matrix $\mathbf{P}$ can be interpreted in two ways. First, according to [7], it may be expressed as

$$\mathbf{P} = \mathbf{Q}_u(\mathbf{R}_J^H)^{-1}, \tag{6.24}$$

where $\mathbf{Q}_u$ consists of the first N rows of $\mathbf{Q}_J$.

The second way is as follows. Given the knowledge of the linear equalisation matrix $\mathbf{Q}$, the effective channel matrix may be expressed as:

$$\begin{aligned} \mathbf{H}_e &= \mathbf{Q}^H\mathbf{H} \\ &= \mathbf{\Omega}\mathbf{\Phi}^H\mathbf{V}^H\mathbf{H} \\ &= \mathbf{\Omega}\mathbf{\Phi}^H\mathbf{V}^H\mathbf{V}\mathbf{\Lambda}^H\mathbf{U}^H \\ &= \mathbf{\Omega}\mathbf{\Phi}^H\mathbf{\Lambda}^H\mathbf{U}^H \\ &= \mathbf{\Omega}\mathbf{\Sigma}^H\mathbf{U}^H \\ &= (\mathbf{U}\mathbf{\Sigma}\mathbf{\Omega}^H)^H. \end{aligned} \tag{6.25}$$

It was shown in [155] that the precoding matrix $\mathbf{P}$ may be chosen to be [155]:

$$\mathbf{P} = \mathbf{H}_e^H(\mathbf{H}_e\mathbf{H}_e^H + \frac{2\sigma_n^2}{\mathrm{E_T}}\mathbf{I})^{-1}, \tag{6.26}$$

noting that the sepcific form of $\mathbf{P}$ in Equation (6.26) is similar to that of the MMSE linear precoder. This was verified by our simulations, demonstrating that the elements of the matrix $\mathbf{P}$ obtained by using the two different methods are identical, which suggests that in this case we have:

$$\begin{aligned} \mathbf{P} &= \mathbf{Q}_u(\mathbf{R}_J^H)^{-1} \\ &= \mathbf{H}_e^H(\mathbf{H}_e\mathbf{H}_e^H + \frac{2\sigma_n^2}{\mathrm{E_T}}\mathbf{I})^{-1}. \end{aligned} \tag{6.27}$$

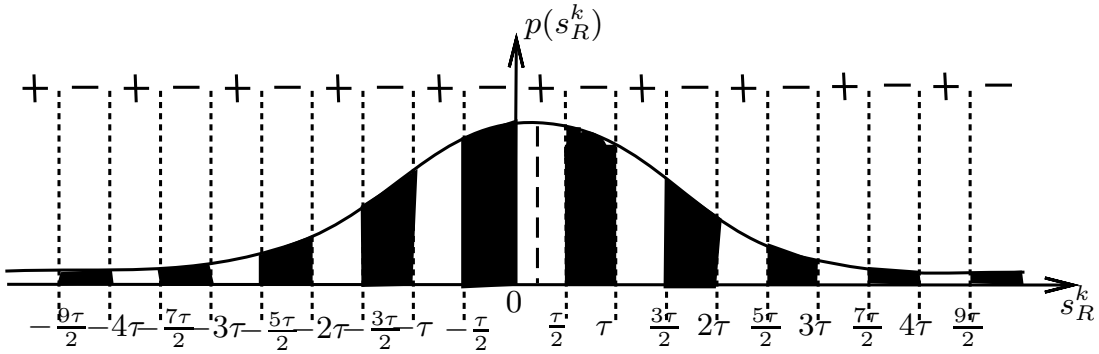

Figure 6.2: Probability density function of the decision variable s_R^k in the proposed UCD-MBER-VP design when the modulo operation of Fig. 2.3, explained with the aid of Fig. 2.4, is employed at the receiver. The shaded areas represent all the erroneous decision regions. This figure is for illustration purpose and its shape is the same to the one shown in Fig. 5.2. However, the meaning of s_R^k here associated with Equation (6.29) is different from that associated with Equation (5.2) in Fig. 5.2.

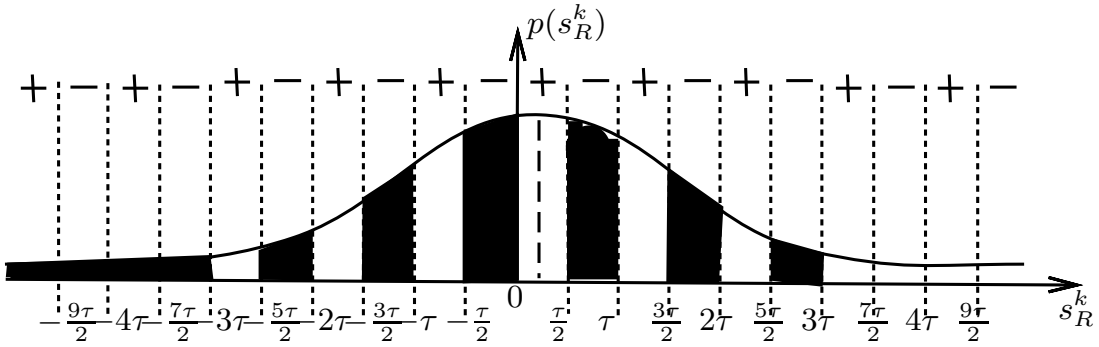

Figure 6.3: Probability density function of the decision variable s_R^k in the proposed UCD-MBER-VP design when the modulo operation of Fig. 2.3 is employed at the receivers, shaded areas represent the approximated erroneous decision regions, which can be contrasted to the exact regions of Fig. 6.2. Again, this figure was repeated here for convenience, its shape is the same as the one seen in Fig. 5.3.

Having designed the precoding and equalisation matrices, $\mathbf{P}$ and $\mathbf{Q}$, we now move on to the design of the algorithm of choosing a specific perturbation vector $\boldsymbol{\omega}$ so that the error probability or BER of the system is minimized.

Similar to the scenario considered in Chapter 5, the BER encountered at the output of the receiver after the modulo operation of Fig. 6.1 for the in-phase component of the kth symbol in our system may be defined as

$$P_{e_I,k}(\boldsymbol{\omega}) = \text{Prob}\{\text{sgn}(\Re[x_k])\Re[y_k] < 0\}. \tag{6.28}$$

In order to evaluate this BER, let us define the signed decision variable $s_R^k = \text{sgn}(\Re[x_k])\Re[\hat{y}_k]$, which has a mean of $c_R^{(k)} = \text{sgn}(\Re[x_k])\Re[\mathbf{q}_k^H \mathbf{h}_k \mathbf{P}(\mathbf{x}+\boldsymbol{\omega})]$ and the PDF given by

$$p(s_R^k) = \frac{1}{\alpha^{-1}\sigma_n\sqrt{2\pi\mathbf{q}_k^H\mathbf{q}_k}} \exp\left(-\frac{(s_R^k - c_R^{(k)})^2}{2\sigma_n^2\alpha^{-2}\mathbf{q}_k^H\mathbf{q}_k}\right). \tag{6.29}$$

Again, the decision areas are periodically extended in the s_R^k-axis, as seen in Fig. 6.2, where the intervals marked by $-$ are the erroneous decision areas, i.e. where we have $\text{sgn}(\Re[x_k])\Re[y_k] < 0$, while the intervals marked by $+$ are the error-free areas, i.e. $\text{sgn}(\Re[x_k])\Re[y_k] > 0$. Hence, the BER of the in-phase component associated with the kth symbol is given by

$$\begin{aligned} P_{e_I,k}(\boldsymbol{\omega}) &= \sum_{t=-\infty}^{\infty} \int_{\frac{2t+1}{2}\tau}^{(t+1)\tau} p(s_R^k) ds_R^k \approx \int_{-\infty}^{-3\tau} p(s_R^k) ds_R^k + \int_{-\frac{5\tau}{2}}^{-2\tau} p(s_R^k) ds_R^k + \int_{-\frac{3\tau}{2}}^{-\tau} p(s_R^k) ds_R^k \\ &+ \int_{-\frac{\tau}{2}}^{0} p(s_R^k) ds_R^k + \int_{\frac{\tau}{2}}^{\tau} p(s_R^k) ds_R^k + \int_{\frac{3\tau}{2}}^{2\tau} p(s_R^k) ds_R^k + \int_{\frac{5\tau}{2}}^{3\tau} p(s_R^k) ds_R^k, \end{aligned} \tag{6.30}$$

where the approximation occurs as we combine the integrations over all the error intervals in $(-\infty,\ -3\tau)$ and $(3\tau,\ +\infty)$ into the single integration over the interval $(-\infty,\ -3\tau)$.

Fig. 6.3 shows this approximation. We demonstrated this through intensive simulations which are shown in Section 6.6. $P_{e_I,k}(\boldsymbol{\omega})$ can therefore be expressed as:

$$\begin{aligned} P_{e_I,k}(\boldsymbol{\omega}) &\approx Q\left(\frac{c_R^{(k)} + 3\tau}{\alpha^{-1}\sigma_n\sqrt{\mathbf{q}_k^H\mathbf{q}_k}}\right) + Q\left(\frac{-\frac{5\tau}{2} - c_R^{(k)}}{\alpha^{-1}\sigma_n\sqrt{\mathbf{q}_k^H\mathbf{q}_k}}\right) - Q\left(\frac{-2\tau - c_R^{(k)}}{\alpha^{-1}\sigma_n\sqrt{\mathbf{q}_k^H\mathbf{q}_k}}\right) \\ &+ Q\left(\frac{-\frac{3\tau}{2} - c_R^{(k)}}{\alpha^{-1}\sigma_n\sqrt{\mathbf{q}_k^H\mathbf{q}_k}}\right) - Q\left(\frac{-\tau - c_R^{(k)}}{\alpha^{-1}\sigma_n\sqrt{\mathbf{q}_k^H\mathbf{q}_k}}\right) + Q\left(\frac{-\frac{\tau}{2} - c_R^{(k)}}{\alpha^{-1}\sigma_n\sqrt{\mathbf{q}_k^H\mathbf{q}_k}}\right) \\ &- Q\left(\frac{-c_R^{(k)}}{\alpha^{-1}\sigma_n\sqrt{\mathbf{q}_k^H\mathbf{q}_k}}\right) + Q\left(\frac{\frac{\tau}{2} - c_R^{(k)}}{\alpha^{-1}\sigma_n\sqrt{\mathbf{q}_k^H\mathbf{q}_k}}\right) - Q\left(\frac{\tau - c_R^{(k)}}{\alpha^{-1}\sigma_n\sqrt{\mathbf{q}_k^H\mathbf{q}_k}}\right) \\ &+ Q\left(\frac{\frac{3\tau}{2} - c_R^{(k)}}{\alpha^{-1}\sigma_n\sqrt{\mathbf{q}_k^H\mathbf{q}_k}}\right) - Q\left(\frac{2\tau - c_R^{(k)}}{\alpha^{-1}\sigma_n\sqrt{\mathbf{q}_k^H\mathbf{q}_k}}\right) + Q\left(\frac{\frac{5\tau}{2} - c_R^{(k)}}{\alpha^{-1}\sigma_n\sqrt{\mathbf{q}_k^H\mathbf{q}_k}}\right) \\ &- Q\left(\frac{3\tau - c_R^{(k)}}{\alpha^{-1}\sigma_n\sqrt{\mathbf{q}_k^H\mathbf{q}_k}}\right). \end{aligned} \tag{6.31}$$

Hence, the average BER for the in-phase component of $\mathbf{y}$ at the receiver is given by

$$P_{e_I,\mathbf{x}}(\boldsymbol{\omega}) = \frac{1}{K}\sum_{k=1}^{K} P_{e_I,k}(\boldsymbol{\omega}). \tag{6.32}$$

Similarly, let $c_I^{(k)} = \text{sgn}(\Im[x_k])\Im[\mathbf{q}_k^H \mathbf{h}_k \mathbf{P}(\mathbf{x}+\boldsymbol{\omega})]$. Then the BER of the quadrature-phase component

for the kth symbol is given by

$$\begin{aligned} P_{e_Q,k}(\boldsymbol{\omega}) \approx\ & Q\left(\frac{c_I^{(k)}+3\tau}{\alpha^{-1}\sigma_n\sqrt{\mathbf{q}_k^H\mathbf{q}_k}}\right)+Q\left(\frac{-\frac{5\tau}{2}-c_I^{(k)}}{\alpha^{-1}\sigma_n\sqrt{\mathbf{q}_k^H\mathbf{q}_k}}\right)-Q\left(\frac{-2\tau-c_I^{(k)}}{\alpha^{-1}\sigma_n\sqrt{\mathbf{q}_k^H\mathbf{q}_k}}\right) \\ &+ Q\left(\frac{-\frac{3\tau}{2}-c_I^{(k)}}{\alpha^{-1}\sigma_n\sqrt{\mathbf{q}_k^H\mathbf{q}_k}}\right)-Q\left(\frac{-\tau-c_I^{(k)}}{\alpha^{-1}\sigma_n\sqrt{\mathbf{q}_k^H\mathbf{q}_k}}\right)+Q\left(\frac{-\frac{\tau}{2}-c_I^{(k)}}{\alpha^{-1}\sigma_n\sqrt{\mathbf{q}_k^H\mathbf{q}_k}}\right) \\ &- Q\left(\frac{-c_I^{(k)}}{\alpha^{-1}\sigma_n\sqrt{\mathbf{q}_k^H\mathbf{q}_k}}\right)+Q\left(\frac{\frac{\tau}{2}-c_I^{(k)}}{\alpha^{-1}\sigma_n\sqrt{\mathbf{q}_k^H\mathbf{q}_k}}\right)-Q\left(\frac{\tau-c_I^{(k)}}{\alpha^{-1}\sigma_n\sqrt{\mathbf{q}_k^H\mathbf{q}_k}}\right) \\ &+ Q\left(\frac{\frac{3\tau}{2}-c_I^{(k)}}{\alpha^{-1}\sigma_n\sqrt{\mathbf{q}_k^H\mathbf{q}_k}}\right)-Q\left(\frac{2\tau-c_I^{(k)}}{\alpha^{-1}\sigma_n\sqrt{\mathbf{q}_k^H\mathbf{q}_k}}\right)+Q\left(\frac{\frac{5\tau}{2}-c_I^{(k)}}{\alpha^{-1}\sigma_n\sqrt{\mathbf{q}_k^H\mathbf{q}_k}}\right) \\ &- Q\left(\frac{3\tau-c_I^{(k)}}{\alpha^{-1}\sigma_n\sqrt{\mathbf{q}_k^H\mathbf{q}_k}}\right). \end{aligned} \tag{6.33}$$

Then the average BER for the quadrature-phase component of $\mathbf{y}$ at the receiver is given by

$$P_{e_Q,\mathbf{x}}(\boldsymbol{\omega}) = \frac{1}{K}\sum_{k=1}^{K} P_{e_Q,k}(\boldsymbol{\omega}). \tag{6.34}$$

Thus, the resultant average BER of 4-QAM signalling becomes

$$P_{e,\mathbf{x}}(\boldsymbol{\omega}) = \left(P_{e_I,\mathbf{x}}(\boldsymbol{\omega}) + P_{e_Q,\mathbf{x}}(\boldsymbol{\omega})\right)/2. \tag{6.35}$$

Hence, the optimal perturbation vector $\boldsymbol{\omega}_{\text{opt}}$ is determined by solving the following optimization problem

$$\boldsymbol{\omega}_{\text{opt}} = \arg\min_{\boldsymbol{\omega}} P_{e,\mathbf{x}}(\boldsymbol{\omega}). \tag{6.36}$$

The perturbation vector $\boldsymbol{\omega}$ can be discrete-valued [32] or continuous-valued [36]. When only the discrete-valued selection is considered, we have

$$\boldsymbol{\omega} = \tau\boldsymbol{\zeta}, \tag{6.37}$$

where $\boldsymbol{\zeta}$ is a complex vector taking values from the set $\{a+jb\}$ with a and b being integers. Then, the optimization problem in Equation (6.36) is reduced to

$$\boldsymbol{\zeta}_{\text{opt}} = \arg\min_{\boldsymbol{\zeta}} P_{e,\mathbf{x}}(\boldsymbol{\zeta}). \tag{6.38}$$

The optimization problem in Equation (6.38) shares similar properties as the one we saw in Equation (5.11) of Section 5.2.3 and can be readily solved using the discrete multi-valued PSO algorithm.

Since the UCD has a comparable computational complexity to the SVD [7], it is plausible that the computational complexity of the UCD-MBER-VP design is dominated by the search of the optimal discrete-valued perturbation vector. It may be deemed to have a similar complexity to the GMD-MMSE-VP design [8], to the MMSE-VP algorithm [32] and the MMSE-MBER-VP algorithm [36], whose computational requirements are also dominated by the search for the optimal discrete-valued perturbation vector. The complexity values were detailed in Table 5.2 and Table 5.3. The UCD-THP design [7] benefits from a lower computational complexity, but it is outperformed by all the other designs in terms of its BER at high SNRs, as we will demonstrate in Section 6.6.

6.5 Computational Complexity

Table 6.2: Detailed key computational complexity contributions per iteration for the discrete multi-valued PSO aided UCD-MBER-VP design using QPSK signalling, where K is the number of mobile users, N is the number of transmit antennas, and S is the number of particles. The numbers in () indicate the index of the corresponding block in Fig. 4.1.

Stage	Flops
Update inertia weight (3)	4
Update velocities (3)	$9 \cdot 2 \cdot K \cdot S$
Calculate sigmoid function (3)	$3 \cdot 2 \cdot K \cdot S$
Update positions (3)	$3 \cdot 2 \cdot K \cdot S$
Evaluate fitness (2)	$(18 \cdot K \cdot N + 9 \cdot K^2 + 71 \cdot K + 6 \cdot N + 4) \cdot S$

The computational complexity of our proposed UCD-MBER-VP algorithm is discussed in this section. Its complexity for QPSK signalling may be evaluated with the aid of considering the actions shown in Fig. 4.1:

$$C_{\mathrm{UCD-MBER-VP}} = ((18 \cdot K \cdot N + 9 \cdot K^2 + 101 \cdot K + 6 \cdot N + 4) \cdot S + 4) \cdot I_{\max} + 8 \cdot K^2 - K,$$

where N is the number of transmit antennas, K is the number of mobile users, $I_{\max}$ is the number of iterations needed to converge to optimal solution and S is the swarm size. More explicitly, the detailed key complexity contribution summary table for our proposed PSO aided scheme per iteration is listed in Table 6.2.

6.6 Simulation Results

Our simulation results are presented in this section, followed by the corresponding discussions.

6.6.1 Verification of the approximation

The effect of the approximation we made in Equation (6.33) in deriving the proposed algorithm is considered here. The related system parameters are shown in Table 6.3, where the DL of a multiuser system employing $N = 3$ transmit antennas at the BS to support $K = 3$ 4-QAM MSs was considered, perfect CSI knowledge was assumed at the BS for transmission over the $(N \times K)$-element flat Rayleigh fading MIMO channel, and the results were obtained by averaging the resultant performances over 500 channel realizations.

As we discussed in Chapter 5, when more integrals are calculated over the error intervals shown in Fig. 6.2, the related approximation would become more accurate. The computational complexity would also be increased. However, the overall BER performance of the system may not be substantially improved when more integrations are calculated over the error intervals. In Fig. 6.4, we characterized four error probability approximations, which are:

Table 6.3: Simulation parameters.

Parameter	Value or Type
System	
Modulation scheme	QPSK
Modulo operation	2
Number of transmit antennas	N
Number of receive end users	K
Channel	flat Rayleigh fading
Channel realizations	500
PSO	
Swarm size for discrete multi-valued PSO S_{dpso}	40

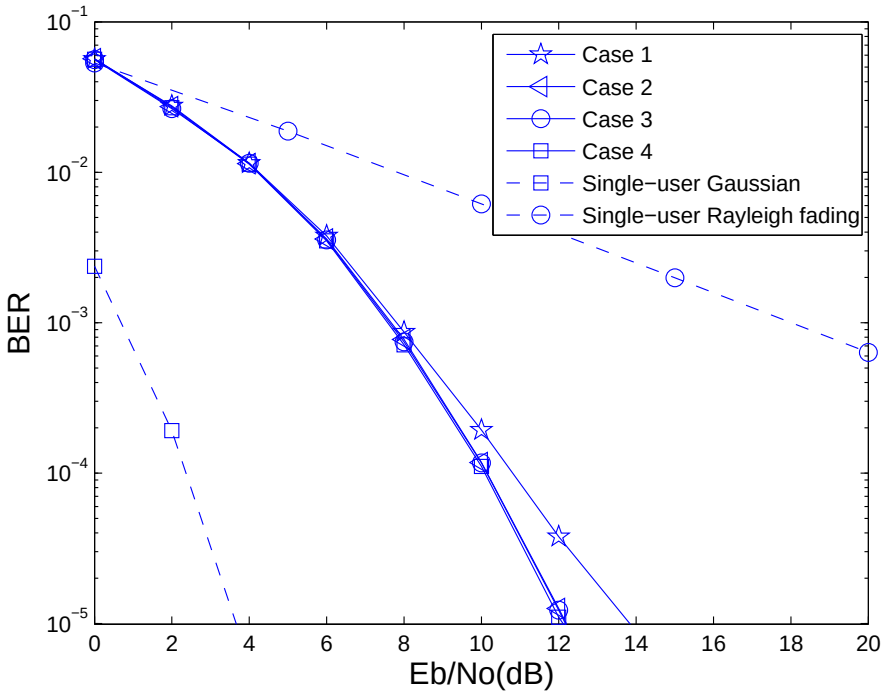

Figure 6.4: The BER performance comparsion of our proposed UCD-MBER-VP design with different error probability approximations for communicating over flat Rayleigh fading channels using $N = 3$ transmit antennas and $K = 3$ receive antennas to support $K = 3$ 4-QAM users. Averaged over 500 channel realisations. All system parameters are summarized in Table 6.3.

Case 1: With reference to Fig. 6.4, we approximate the integrals over all the error intervals in $(-\infty, -2\tau)$ and $(2\tau, +\infty)$ as the single integral over the interval $(-\infty, -2\tau)$:

$$\sum_{t=-\infty}^{\infty} \int_{\frac{2t+1}{2}\tau}^{(t+1)\tau} p(s_R^k) ds_R^k \approx \int_{-\infty}^{-2\tau} p(s_R^k) ds_R^k + \int_{-\frac{3\tau}{2}}^{-\tau} p(s_R^k) ds_R^k + \int_{-\frac{\tau}{2}}^{0} p(s_R^k) ds_R^k + \int_{\frac{\tau}{2}}^{\tau} p(s_R^k) ds_R^k + \int_{\frac{3\tau}{2}}^{2\tau} p(s_R^k) ds_R^k. \tag{6.39}$$

Case 2: This is the approximation we adopted in our proposed design:

$$\begin{aligned}\sum_{t=-\infty}^{\infty}\int_{\frac{2t+1}{2}\tau}^{(t+1)\tau} p(s_R^k)ds_R^k \;\approx\; & \int_{-\infty}^{-3\tau} p(s_R^k)ds_R^k + \int_{-\frac{5\tau}{2}}^{-2\tau} p(s_R^k)ds_R^k + \int_{-\frac{3\tau}{2}}^{-\tau} p(s_R^k)ds_R^k \\ + & \int_{-\frac{\tau}{2}}^{0} p(s_R^k)ds_R^k + \int_{\frac{\tau}{2}}^{\tau} p(s_R^k)ds_R^k + \int_{\frac{3\tau}{2}}^{2\tau} p(s_R^k)ds_R^k \\ + & \int_{\frac{5\tau}{2}}^{3\tau} p(s_R^k)ds_R^k. \end{aligned} \tag{6.40}$$

Case 3: By observing Fig. 6.4, we approximate the integrals over all the error intervals in $(-\infty,\ -4\tau)$ and $(4\tau,\ +\infty)$ as the single integral over the interval $(-\infty,\ -4\tau)$:

$$\begin{aligned}\sum_{t=-\infty}^{\infty}\int_{\frac{2t+1}{2}\tau}^{(t+1)\tau} p(s_R^k)ds_R^k \;\approx\; & \int_{-\infty}^{-4\tau} p(s_R^k)ds_R^k + \int_{-\frac{7\tau}{2}}^{-3\tau} p(s_R^k)ds_R^k + \int_{-\frac{5\tau}{2}}^{-2\tau} p(s_R^k)ds_R^k \\ + & \int_{-\frac{3\tau}{2}}^{-\tau} p(s_R^k)ds_R^k + \int_{-\frac{\tau}{2}}^{0} p(s_R^k)ds_R^k + \int_{\frac{\tau}{2}}^{\tau} p(s_R^k)ds_R^k \\ + & \int_{\frac{3\tau}{2}}^{2\tau} p(s_R^k)ds_R^k + \int_{\frac{5\tau}{2}}^{3\tau} p(s_R^k)ds_R^k + \int_{\frac{7\tau}{2}}^{4\tau} p(s_R^k)ds_R^k. \end{aligned} \tag{6.41}$$

Case 4: Again, with reference to Fig. 6.4, we approximate the integrals over all the error intervals in $(-\infty,\ -5\tau)$ and $(5\tau,\ +\infty)$ as the single integral over the interval $(-\infty,\ -5\tau)$:

$$\begin{aligned}\sum_{t=-\infty}^{\infty}\int_{\frac{2t+1}{2}\tau}^{(t+1)\tau} p(s_R^k)ds_R^k \;\approx\; & \int_{-\infty}^{-5\tau} p(s_R^k)ds_R^k + \int_{-\frac{9\tau}{2}}^{-4\tau} p(s_R^k)ds_R^k + \int_{-\frac{7\tau}{2}}^{-3\tau} p(s_R^k)ds_R^k \\ + & \int_{-\frac{5\tau}{2}}^{-2\tau} p(s_R^k)ds_R^k + \int_{-\frac{3\tau}{2}}^{-\tau} p(s_R^k)ds_R^k + \int_{-\frac{\tau}{2}}^{0} p(s_R^k)ds_R^k \\ + & \int_{\frac{\tau}{2}}^{\tau} p(s_R^k)ds_R^k + \int_{\frac{3\tau}{2}}^{2\tau} p(s_R^k)ds_R^k + \int_{\frac{5\tau}{2}}^{3\tau} p(s_R^k)ds_R^k \\ + & \int_{\frac{7\tau}{2}}^{4\tau} p(s_R^k)ds_R^k + \int_{\frac{9\tau}{2}}^{5\tau} p(s_R^k)ds_R^k. \end{aligned} \tag{6.42}$$

As can be seen in the figure, the approximation of Case 1 is insufficiently accurate, while Case 2, Case 3 and Case 4 showed a similar BER performance, which means the approximations of these three cases are all accurate enough to be used to represent the BER. It is clear then that the approximation of Case 2 when we approximate the integrals over all the error intervals in $(-\infty,\ -3\tau)$ and $(3\tau,\ +\infty)$ as the single integral over the interval $(-\infty,\ -3\tau)$ provides the best trade-off between the BER performance attained and the computational complexity imposed, since less intergrations are calculated compared to Case3 and Case 4. Therefore, the approximation made in Case 2 may be deemed to be the best choice among all the approximations.

6.6.2 Convergence and Complexity

The convergence performance as well as the corresponding computational complexity of the discrete multi-valued PSO aided UCD-MBER-VP scheme is considered here.

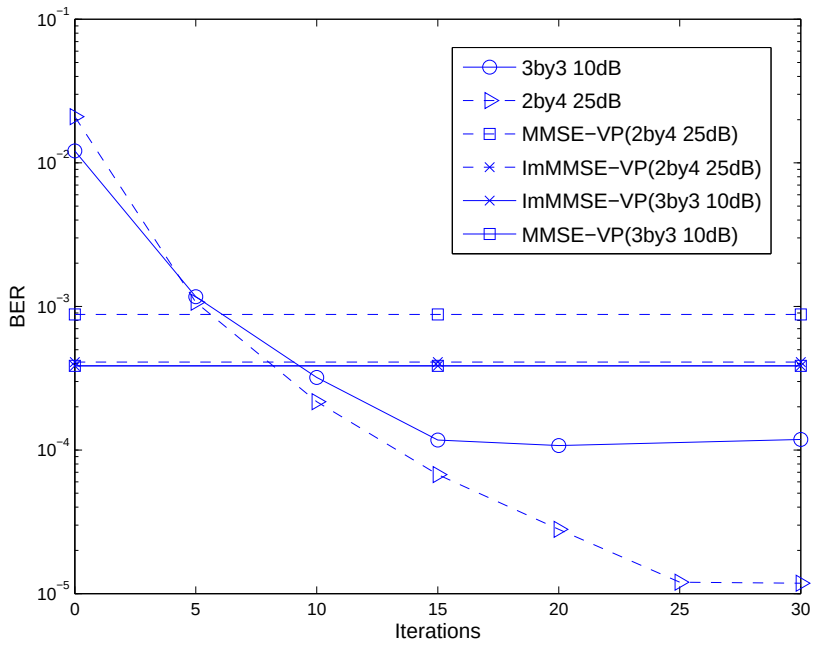

Figure 6.5: Convergence performances of our proposed UCD-MBER-VP algorithm, while using the modulo operation at the receivers for communicating over flat Rayleigh fading channels in different scenarios. The benchmark performances of the MMSE-VP and the ImMMSE-VP schemes of a 3×3 full-rank system at Eb/No=10dB which can be seen from Fig. 6.6 and of a 2×4 rank-deficient system at Eb/No=25dB which can be seen from Fig. 6.3 are also shown in this figure. All system parameters are summarized in Table 6.3.

The system parameters of the test scenario are summarized in Table 6.3. We consider a multiuser $(N \times K)$-element MIMO system employing N transmit antennas at the BS, supporting K QPSK users. Perfect CSI knowledge was assumed at the BS and the receiver end for transmission over the $(N \times K)$-element flat Rayleigh fading MIMO channel. The attainable performance can be seen in Fig. 6.5.

As we can observed from Fig. 6.5, when the system uses $N = 3$ transmit antennas for supporting $K = 3$ users with $K = 3$ receive antennas, our algorithm needs 15 iterations on average to converge while operating at the SNR of $Eb/No = 10$dB, the corresponding computational complexity is 691,404.

When the system is reconfigured to use $N = 2$ transmit and $K = 4$ receive antennas for 4 4-QAM users, which was a rank-deficient scenario, at $Eb/No = 30$dB, the algorithm needs 25 iterations on average to converge with the corresponding computational complexity of 708,224.

6.6.3 Overall system performance

The overall BER performance of the proposed algorithm is discussed here. The corresponding system parameters are summarized in Table 6.3. We considered the MIMO system employing K antennas to receive K 4-QAM users' data streams from N transmit antennas. The square-shaped 4-QAM constellation of $\{\pm\frac{1}{2}\} + j\{\pm\frac{1}{2}\}$ was used and $\tau = 2$ was chosen. The four benchmark algorithms were the MMSE-VP design [32], the ImMMSE-VP scheme [36], the UCD-THP algorithm [7] and the GMD-MMSE-VP design [8]. Only discrete-valued vector perturbation vectors were considered in the related designs. All the

simulation results were averaged over 500 channel realizations.

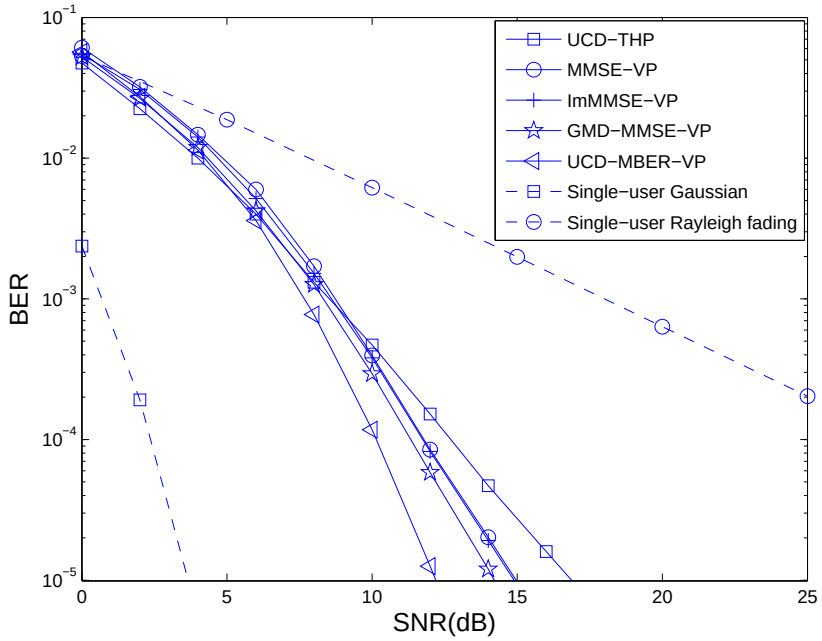

Figure 6.6: BER performance comparsion of the MMSE-VP design [32], the ImMMSE-VP scheme [36], the UCD-THP algorithm [7], the GMD-MMSE-VP design [8] and our proposed UCD-MBER-VP transceiver design for communicating over flat Rayleigh fading channels using $N = 3$ transmit antennas and $K = 3$ receive antennas to support $K = 3$ 4-QAM users, assuming the perfect channel state information. All system parameters are summarized in Table 6.3.

First we considered the case of $N = 3$ and $K = 3$ which is a full-rank system. The system parameters are summarized in Table 6.3. Assuming the availability of perfect channel state information at both the transmitter and receiver, the BER performance of the five designs are compared in Fig. 6.6. It can be seen that, among the four benchmark algorithms, the ImMMSE-VP had a similar BER performance as the MMSE-VP, while the GMD-MMSE-VP design outperformed these two transmission preprocessing designs by 0.8 dB. Although the UCD-THP transceiver design achieved the best performance at low SNR values, its performance degraded significantly at high SNRs and was outperformed by all the other designs. It can also be seen from Fig. 6.6 that the proposed UCD-MBER-VP scheme achieved a 2 dB SNR gain at the target BER of 10^{-5} over the GMD-MMSE-VP.

The robustness of all the five algorithms against the channel estimation error (CEE) was next investigated. A complex-valued Gaussian white noise with a variance 0.01 was added to each channel tap $h_{i,k}$ to represent the CEE at both the transmitter and receiver, and the BERs of the five designs under this CEE were depicted in Fig. 6.7. It can be seen that the performance of the five designs were all degraded. In particular, the UCD-THP scheme was seen to be very sensitive to the CEE and completely broke down. It can also be seen from Fig. 6.7 that the proposed UCD-MBER-VP design was no more sensitive to CEE than the other benchmark designs and it maintained the best BER performance.

The system was then configured to use $N = 2$ transmit antennas and $K = 4$ receive antennas for $K = 4$ 4-QAM users, which was a challenging rank-deficient scenario. The system parameters are summarized in Table 6.3. The BERs of the five algorithms assuming the perfect knowledge of the channel matrix at

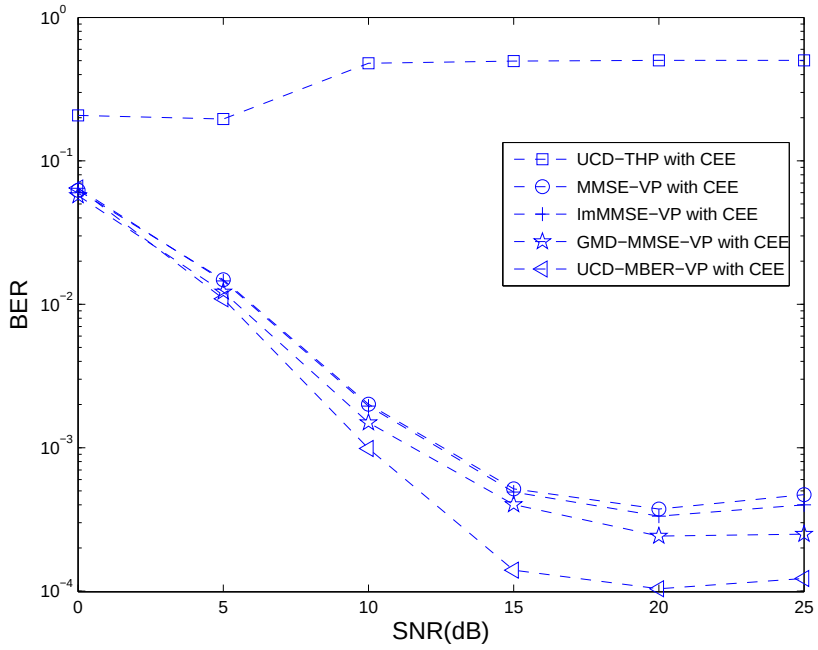

Figure 6.7: BER performance comparsion of the MMSE-VP design [32], the ImMMSE-VP scheme [36], the UCD-THP algorithm [7], the GMD-MMSE-VP design [8] and our proposed UCD-MBER-VP transceiver design for communicating over flat Rayleigh fading channels using $N = 3$ transmit antennas and $K = 3$ receive antennas to support $K = 3$ 4-QAM users, assuming the imperfect channel state information with channel estimation error. All system parameters are summarized in Table 6.3.

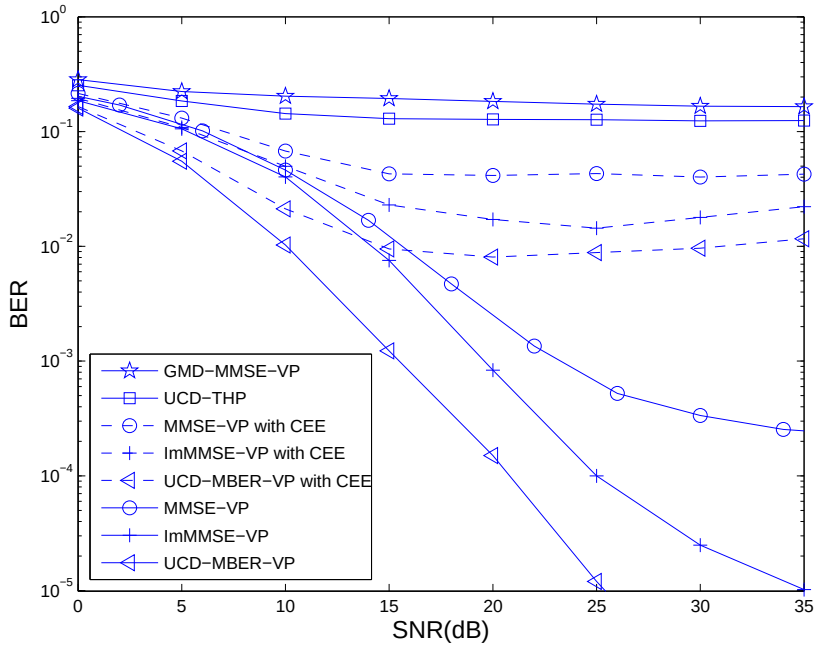

Figure 6.8: BER performance comparsion of the MMSE-VP design [32], the ImMMSE-VP scheme [36], the UCD-THP algorithm [7], the GMD-MMSE-VP design [8] and our proposed UCD-MBER-VP transceiver design for communicating over flat Rayleigh fading channels using $N = 2$ transmit antennas and $K = 4$ receive antennas to support $K = 4$ 4-QAM users, assuming the perfect CSI (solid curves) as well as the imperfect CSI with channel estimation error (dashed curves). All system parameters are summarized in Table 6.3.

both the transmitter and receiver are shown in Fig. 6.8. The two joint transceiver designs, namely the GMD-MMSE-VP and UCD-THP schemes, encountered high error floors which showed that they were unable to differentiate the users' information in this demanding scenario. The MMSE-VP scheme showed a significantly better performance, but still suffered from a visible error floor, as seen in Fig. 6.8. The ImMMSE-VP algorithm considerably outperformed the above three designs and exhibited a much reduced error floor. By contrast, the proposed UCD-MBER-VP transceiver design outperformed the ImMMSE-VP design by about 10 dB at the target BER of 10^{-5} and it did not exhibit an error floor. This showed its capability to operate successfully in the challenging rank-deficient scenario.

The MMSE-VP, the ImMMSE-VP and the UCD-MBER-VP were then tested under the same CEE condition as specified in the previous example, and their BERs obtained under this CEE are also shown in Fig. 6.8. It can be seen that the effect of CEE was more serious in the rank-deficient case. Again the UCD-MBER-VP design achieved the best BER performance and it was no more sensitive to CEE than the other two benchmark schemes.

6.7 Conclusions

In this chapter, we proposed a novel transceiver design exploiting the joint benefits of the UCD algorithm and of the MBER criterion for developing a new vector precoding algorithm, which can be found in Fig. 6.1. The resultant UCD-MBER-VP scheme was shown to be an attractive transceiver design, which is capable of providing a better BER performance when compared to other state of the art algorithms. This was achieved without imposing a significant increase of the computational complexity especially in the rank-deficient scenarios.

Table 6.4: Performance summary of benchmark schemes evaluated in this chapter. The SNR gap refers to the performance SNR gain over other schemes when using the proposed UCD-MBER-VP algorithm..

	UCD-MBER-VP	ImMMSE-VP	MMSE-VP
SNR gap at 10^{-5} (3×3)	benchmark	3 dB	3 dB
Complexity(Flops)/SNR (3×3)	691,404/10dB	333,460/10dB	252,448/10dB
Relative complexity (3×3)	2.73	1.32	1
SNR gap at 10^{-5} (2×4)	benchmark	10 dB	$>$ 10 dB
Complexity(Flops)/SNR (2×4)	708,224/30dB	571,260/30dB	433,670/30dB
Relative complexity (2×4)	1.63	1.31	1

More explicitly, the system model was introduced in Section 6.3, where Fig. 6.1 showed the schematic, based on which we proposed the UCD-MBER-VP design in Section 6.4. The cost function for this technique was also derived in Equation (6.38) of Section 6.4. The computational complexity of the proposed algorithm was investigated in Section 6.5, followed by the correspondng simulation studies in Section 6.6. Similar to what we observed in Chapter 5, the calculation of the BEP in the proposed design may also require an approximation. We demonstrated the appropriate approximation of the BEP in Fig. 6.4. In Fig.

6.5, we discussed the convergence behavior of the proposed algorithm. The overall BER performance of the proposed scheme in full-rank system under the assumption of the knowledge of perfect CIRs at both the transmitter and receiver was investigated in Fig. 6.6, where the number of transmit antennas and receive antennas was $N = K = 3$. The proposed UCD-MBER-VP scheme was shown to be capable of achieving around 3 dB SNR gain over the MMSE-VP technique at the target BER of 10^{-5}. In Fig. 6.3, we investigated the system's performance when the rank-deficient scenario was encountered, where there was $N = 2$ transmit antennas supporting $K = 4$ 4-QAM users. The proposed UCD-MBER-VP algorithm showed a substantial performance over other schemes since it did not exhibit an error floor, which showed its capability to operate successfully in the challenging rank-deficient scenario. The algorithm's performance against CEE was investigated in Fig. 6.7 for full-rank system and in Fig. 6.3 for rank-deficient system. It can be seen that the proposed UCD-MBER-VP design was no more sensitive to CEE than the other benchmark schemes.

The overall BER and computational complexity performances of the MMSE-VP technique, the ImMMSE-VP and the proposed UCD-MBER-VP scheme were summarized in Table 5.7. In a (3×3) full-rank system, the proposed UCD-MBER-VP scheme was capable of achieving an SNR gain of 3 dB over the other two, while imposing a 2.7 times higher computational complexity over the MMSE-VP technique. This demonstrated that the proposed algorithm may not be chosen in implementation when a trade-off between the attainable BER performance and the imposed complexity is required. When the system was operating in a (2×4) rank-deficient scenario, the proposed UCD-MBER-VP algorithm showed a substantial SNR gain over the other schemes, while only imposing 1.6 times higher complexity than the MMSE-VP technique. This demonstrated that the proposed UCD-MBER-VP algorithm would be a good choice to be implemented in rank-deficient scenarios. In summary, similar to the conlusion we made in Chapter 5, the proposed UCD-MBER-VP algorithm would be more beneficial to be adopted in rank-deficient systems.

Chapter 7

Conclusions and Future Work

In this final chapter, we will first provide the overall summary and conclusions of this treatise in Section 7.1, followed by a range of topics concerning potential future research issues in Section 7.2.

7.1 Conclusions

In this treatise, we investigated a range of reduced-complexity PSO assisted MIMO downlink transmission schemes conceived for transmission over Rayleigh fading wireless channels operating in multi-user scenarios. The preliminaries were covered in Chapter 2. Our work is constituted of two major parts. In the first part, we demonstrated the efficiency of using PSO to solve the optimization problems in MUT. We proposed several novel signal transmission algorithms based on the MBER criterion in the second part. In Chapter 3 and Chapter 4, we focused our attention on the computational complexity reduction of the state-of-the-art MUT schemes by using the PSO algorithm. More explicitly, in Section 3.5 we proposed using continuous-valued PSO to reduce the complexity of the linear MBER-MUT algorithms instead of the popular SQP approach [24]. The corresponding schematic can be found in Fig. 7.1(a). Then in Chapter 4 we proposed using discrete multi-valued PSO to reduce the complexity of powerful nonlinear MUT, namely of the vector precoding algorithm. The corresponding schematic can be found in Fig. 7.1(b). In Chapter 5 we focused our attention on the novel MBER criterion combined with the employment of modulo devices at the receiver side. There are literally thousands of papers based on MMSE-optimization in the context of diverse research problems, while MBER-based solutions only emerged during the past few years. Bearing this in mind, we firstly advocated the MBER solution in the context of vector precoding, as discussed in Chapter 5. The schematic for this generalized MBER-VP design can be found in Fig. 7.1(c). We then extended the 'idea' into the MIMO transceiver design, and proposed a novel UCD-MBER-VP transceiver design, as discussed in Chapter 6, where the schematic is shown in Fig. 7.1(d).

Table 7.1 summarizes the overall BER and computational complexity performances of the MMSE-VP technique, the proposed ImMMSE-VP, generalized MBER-VP and UCD-MBER-VP schemes. As we concluded in Table 5.7 and Table 6.4, the proposed generalized MBER-VP and UCD-MBER-VP algorithms

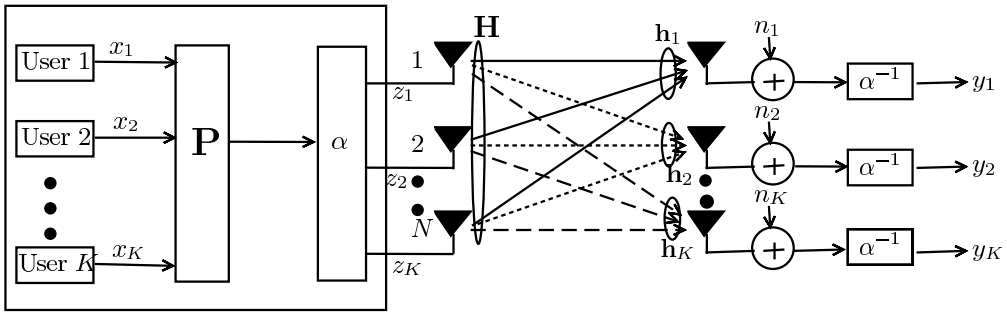

(a)

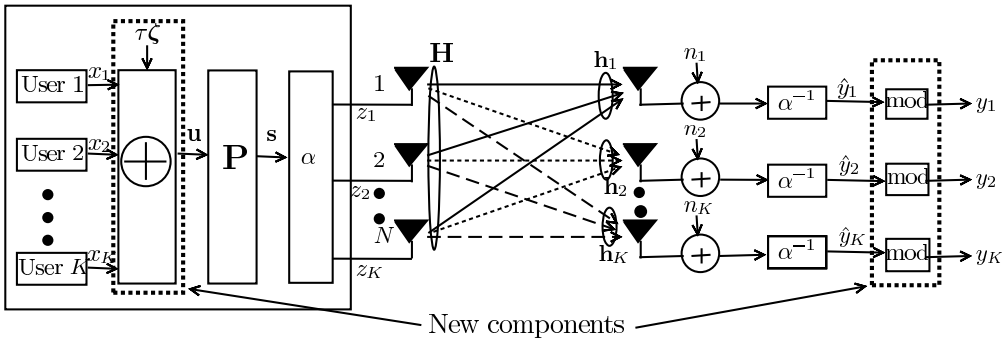

(b)

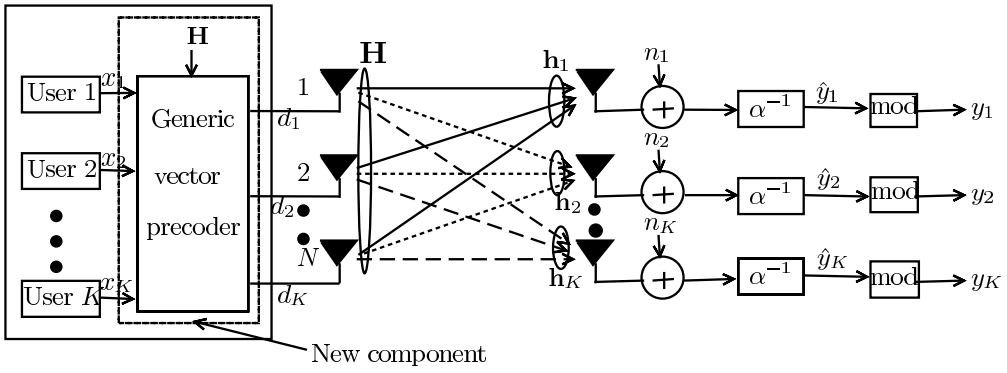

(c)

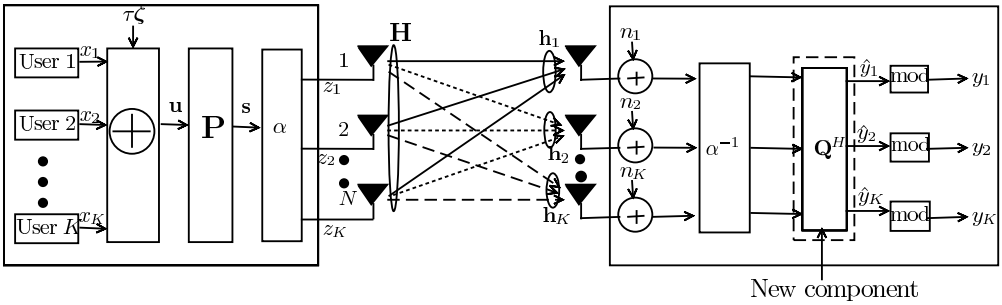

(d)

Figure 7.1: Evolution of the system's achitecture throughout this treatise. (a) is the schematic of linear MUT of Section 3.3. (b) is the schematic of the classic vector precoding-based nonlinear MUT of Section 4.2. (c) is the schematic of the system using the proposed generalized MBER-VP algorithm of Section 5.3.1. (d) is the schematic of the system employing the proposed UCD-MBER-VP transceiver technique of Section 6.3.

Table 7.1: Performance summary of benchmark schemes evaluated in this chapter.

	UCD-MBER-VP	GMBER-VP	ImMMSE-VP	MMSE-VP
SNR gap at 10^{-5} (3×3)	benchmark	N/A	3 dB	3 dB
Complexity(Flops)/SNR (3×3)	691,404/10dB	N/A	333,460/10dB	252,448/10dB
Relative complexity (3×3)	2.73	N/A	1.32	1
SNR gap at 10^{-5} (4×4)	N/A	benchmark	1 dB	1 dB
Complexity(Flops)/SNR (4×4)	N/A	793,230/10dB	502,820/10dB	382,770/10dB
Relative complexity (4×4)	N/A	2.07	1.31	1
SNR gap at 10^{-5} (2×4)	benchmark	4 dB	10 dB	$>$ 10 dB
Complexity(Flops)/SNR (2×4)	708,224/30dB	846,020/30dB	571,260/30dB	433,670/30dB
Relative complexity (2×4)	1.63	1.95	1.31	1

are more beneficial to be implemented in rank-deficient scenarios. More explicitly, the generalized MBER-VP algorithm is suitable for the scenario where the receivers are decentralized, while the UCD-MBER-VP algorithm works for the systems which are capable of adopting joint transceiver schemes.

Let us now briefly revisit all these chapters in order to gain a more detailed insight.

7.1.1 Chapter 2

The preliminary knowledge required for the detailed discussions of this treatise was provided in this chapter. More specifically, in Section 2.1, we offered a rudimentary introduction to MUT covering the family of linear MUT schemes, namely ZF-MUT, MMSE-MUT and MBER-MUT, as well as the nonlinear VP MUT algorithm. The MUD counterparts of the MUT algorithms can be seen in Table 2.15. It has been shown in [57] that several linear MUT schemes may be readily designed from their linear MUD counterparts, including the ZF-MUT and MMSE-MUT provided that the number of antennas at the BS is no less than that of the MSs supported. Generally speaking, nonlinear MUT schemes are capable of achieving a better attainable BER performance than linear MUT algorithms at the expense of higher computational complexity as stated in Section 2.1. In Section 2.2, the PSO algorithm was introduced, where it was splited into two parts, focused on continuous-valued PSO and discrete-valued PSO, respectively. More specifically, the continuous-valued PSO scheme which is more suitable for solving continuous-valued optimization problems, was introduced in Section 2.2.1, while Section 2.2.2 covered the introduction of the discrete-valued PSO algorithm invoked for solving combinatorial optimization problems.

The PSO algorithm is a promising optimization tool and this was demonstrated in Chapter 3-6.

7.1.2 Chapter 3

In this chapter, we demonstrated the efficiency of the continuous-valued PSO algorithm. More explicitly, we focused our attention on the computational complexity reduction of linear MBER-MUTs, namely that

of the symbol-specific MBER-MUT and of the average MBER-MUT. The MUT using the MMSE criterion is popular owing to its representational and conceptional simplicity. However, since the BER is the ultimate system performance indicator, we are more interested in the MBER-MUT design. Unlike the MBER-MUD, the MBER-MUT design encounters a power constrained nonlinear optimization problem. The SQP algorithm [24] may be used to obtain the precoder's coefficients. However, the computational complexity of the SQP based MBER-MUT solution may be excessive for high-rate systems. Hence, as an attractive design alternative, in this chapter, continuous-valued PSO was invoked in order to find the MBER-MUT's precoder matrix $\mathbf{P}$ for reducing its computational complexity.

Two PSO aided MBER-MUTs were designed and characterized in this chapter. The first one may be referred to as the symbol-specific MBER-MUT, while the other one as the average MBER-MUT. Simulation results of Fig. 3.15 demonstrated that both of our designs provided an improvement in comparison to conventional linear MUT schemes at a reduced complexity compared to the state-of-art SQP based MBER-MUT. More explicitly, in the case of the symbol-specific MBER-MUT of Section 3.4.1, for example, in a (4×4)-element MIMO system communicating over flat Rayleigh fading channels at an SNR of $\frac{Eb}{No} = 10$dB when a QPSK modulation scheme was adopted, observe in Fig. 3.14 that our PSO aided MBER-MUT algorithm arrived at the MBER-MUT solution at a twelve times lower complexity than the SQP based MBER-MUT design as seen in Table 3.8. Similarly, from Table 3.8, its computational complexity was nine times lower than that of the SQP based approach when the operating SNR was $\frac{Eb}{No} = 15$ dB. In the case of the average MBER-MUT scheme of Section 3.4.2, for example, in a (4×4)-element MIMO system communicating over flat Rayleigh fading channels at an given SNR of $\frac{Eb}{No} = 10$dB when a QPSK modulation scheme was adopted, our PSO aided MBER-MUT algorithm arrived at the MBER-MUT solution at a seven times lower complexity than the SQP based MBER-MUT design. Similarly, its computational complexity was seen to be five times lower in Fig. 3.14 than that of the SQP based approach, when the operating SNR was $\frac{Eb}{No} = 15$dB. Again, these results were summarized in Table 3.8.

7.1.3 Chapter 4

We demonstrated the efficiency of discrete-valued PSO in this chapter. More explicitly, we proposed discrete multi-valued PSO aided VP designs. As a nonlinear MUT scheme, VP provides an attractive BER performance, which was demonstrated in Fig. 2.5. However, the computational complexity imposed by the optimum shpere-encoder during the search for the optimal perturbation vector may become excessive. Hence it becomes necessary to find a reduced-complexity algorithm, while maintaining a near-optimum BER performance. Against this background, we developed a discrete multi-valued PSO aided MMSE-VP design, which was shown to be capable of approaching optimum sphere-encoder's performance at a significantly reduced computational complexity compared to that imposed by the sphere encoder. The system model was introduced in Section 4.2. Based on the system model, we may have the cost function in Equation (2.59) in Section 4.3. A rudimentary introduction to discrete multi-valued PSO algorithm was then provided in Section 4.4, followed by the description of the proposed discrete multi-valued PSO aided VP technique in Section 4.5. The corresponding computational complexity was discussed in Section 4.6. In Section 4.7, the simulation results were provided.

We focused our attention on the performance of the MMSE-VP in Section 4.7. The simulation results of Section 4.7.7 characterized the attainable performance in the case of employing N=4 transmit antennas at the BS for supporting K=4 QPSK users, while communicating over flat Rayleigh fading MIMO channel. Our approach is capable of finding the optimum perturbation vector at a reduced complexity of about 20% compared to that imposed by sphere encoding at $Eb/No = 6$ dB. Similarly, the complexity compared to that imposed by sphere encoding was about 30% at $Eb/No = 10$ dB, while the total number of nodes in the search space was $5^8 = 390,625$. The results were summarized in Table 4.9. Hence, our approach may be deemed to constitute a low-complexity near-optimum VP algorithm. Moreover, our approach is capable of striking a flexible BER versus complexity trade-off, thanks to its iterative optimization regime.

7.1.4 Chapter 5

In this chapter, we invoked the MBER criterion for designing vector precoding schemes, where transmitted signal is appropriately perturbed at the BS for the sake of directly minimizing the BER at the receiver. The perturbation induced ambiguity has to be removed at the MS's receiver with the aid of appropriate modulo devices. Based on this novel MBER criterion which is prominently featured in the schematic of Fig. 5.2.2, we proposed two different vector precoding algorithms. Namely the.improved MMSE-VP design based on the MBER criterion in Section 5.2 which we referred to as the ImMMSE-VP scheme and the generalized MBER-VP design in Section 5.3. It may be concluded with the aid of Table 5.7 that the proposed generalized MBER-VP design would be suitable to be implemented in rank-deficient scenarios.

More explicitly, in Fig. 5.1 of Section 5.2, we firstly introduced an improved MMSE-VP design based on the MBER criterion. This transmit preprocessing scheme invokes a regularized channel inversion and then superimposes a discrete-valued perturbation vector on the transmitted signal in order to minimize the BER of the system as an improvement of the well-established MMSE-VP scheme. The discrete multi-valued PSO can be adopted to solve the corresponding optimization problem and its computational complexity was discussed in Section 5.4. To further improve the system's BER performance, a generalized MBER-based continuous-valued VP algorithm was proposed in Section 5.3. Given the knowledge of the information symbol vector to be transmitted and the CIR matrix, we consider the generation of the effective symbol vector to be transmitted by directly minimizing the BER of the system. We showed that continuous-valued PSO can be used to solve the corresponding optimization problem. The corresponding computational complexity was discussed in Section 5.4. Simulation results were also provided to quantify the advantage of these VP schemes relying on the MBER criterion, especially for rank-deficient systems, where the number of BS transmit antennas is lower than the number of MSs supported. It was shown in Equation (5.3) of Section 5.2.2 that an appropriate approximation may have to be introduced, in order to calculate the BEP of the system invoking the proposed algorithms. Hence, we invoked the appropriate approximations for both scenarios, which were characterized in Fig. 5.7 and Fig. 5.8. The convergence bahavior of our proposed discrete multi-valued PSO aided ImMMSE-VP scheme, of the continuous-valued PSO aided generalized MBER-VP algorithm and of the corresponding representational complexity was shown in Fig. 5.10 and Fig. 5.11 of Section 5.5.3. The overall BER performance of the algorithms in full-rank system was shown in Fig. 5.12, while their performance in rank-deficient system was shown in Fig. 5.13. Both of the algorithms were

capable of achieving a better performance than MMSE-VP technique in both scenarios, while a substantial BER performance gain could be attained by the generalized MBER-VP algorithm over other schemes in the challenging rank-deficient scenario. The robustness of these two designs to CIR estimation errors were also investigated in Fig. 5.12 and Fig. 5.13, demonstrating that the proposed algorithms are no more sensitive to channel estimation errors than the MMSE-VP scheme.

7.1.5 Chapter 6

In this chapter, we proposed a novel transceiver design exploiting the joint benefits of the UCD algorithm and of the MBER criterion for developing a new vector precoding algorithm, which can be found in Fig. 6.1. The resultant UCD-MBER-VP scheme was shown to be an attractive transceiver design, which is capable of providing a better BER performance when compared to other state of the art algorithms. This was achieved without imposing a significant increase of the computational complexity especially in the rank-deficient scenarios.

More explicitly, the system model was introduced in Section 6.3, where Fig. 6.1 outlined the associated schematic. Based on this scheme, in Section 6.4 we proposed the UCD-MBER-VP design. The cost function for this technique was also derived in Equation (6.38) of Section 6.4. The computational complexity of the proposed algorithm was investigated in Section 6.5, followed by the corresponding simulation studies in Section 6.6. Similar to what we observed in Chapter 5, the calculation of the BEP in the proposed design may also require an approximation. We demonstrated the appropriate approximation of the BEP in Fig. 6.4. In Fig. 6.5, we discussed the convergence behavior of the proposed algorithm. The overall BER performance of the proposed scheme in full-rank system under the assumption of the knowledge of perfect CIRs at both the transmitter and receiver was investigated in Fig. 6.6, where the number of transmit and receive antennas was $N = K = 3$. The proposed UCD-MBER-VP scheme was shown to be capable of achieving an approximately 3 dB SNR gain over the MMSE-VP technique at the target BER of 10^{-5}. In Fig. 6.3, we investigated the system's performance when the rank-deficient scenario was encountered, where there was $N = 2$ transmit antennas supporting $K = 4$ 4-QAM users. The proposed UCD-MBER-VP algorithm showed a substantial performance over other schemes since it did not exhibit an error floor, which showed its capability to operate successfully in the challenging rank-deficient scenario. The algorithm's performance against CEE was investigated in Fig. 6.7 for full-rank system and in Fig. 6.3 for rank-deficient system. It can be seen that the proposed UCD-MBER-VP design was no more sensitive to CEE than the other benchmark schemes.

7.2 Future Work

In this study we demonstrated that PSO constitutes a promising technique in the context of MIMO transceiver designs. Future work ideas may be categorized into two major areas, namely the broader applications of PSO in wireless communications and more sophisticated transceiver designs.

7.2.1 Block-diagonal uniform channel decomposition aided MBER vector perturbation for multiuser MIMO systems

The family of multiuser Block Diagonalisation (BD), Vector precoding (VP), Geometric Mean Decomposition (GMD) or Uniform Channel Decomposition (UCD) based DL solutions constitute attractive techniques for approaching the sum capacity of multiuser MIMO broadcast channels [160, 161]. The authors of [160] proposed a technique, which combines BD and ZF-VP, while an algorithm based on combining BD and GMD (also covers BD combined with UCD) was proposed in [161]. It is a promising idea to further combine BD with both UCD and with our MBER-VP to achieve an improved performance.

7.2.2 Robust transmit preprocessing relying on imperfect channel knowledge

In most of the proposed MUT designs we assumed perfect CSI knowledge at the BS, which is a demanding assumption, since the DL CIR has to be fedback to the transmitter from the receiver. Hence, it is useful to consider a more realistic model. For example, in a TDD system, it may be possible to employ a channel predictor to predict the CIR taps into the future based on their past values. There are a number of papers in the literature considering the robust design of the THP ([162] [163], [164]) for the sake of mitigating the effects of channel estimation errors. However, there is no robust design proposed for vector precoding in the open literature. Hence, it would be beneficial to develop a robust vector precoder, which is robust against imperfect channel knowledge.

7.2.3 Differential vector precoding

Noncoherent differential detection dispensing with channel estimation constitutes a promising technique for the future, when it is excessively complex to estimate the MIMO channels, namely when the number of transmitters and receivers is high. The design of a new differential encoding algorithm capable of reducing the complexity at the receiver is an open problem at the time of writing. Powerful nonlinear multiuser transmission schemes may offer a way out. A differential THP algorithm was proposed in [165]. However, there is no technique in the open literature, which combines differential decoding with vector precoding. Therefore, it would be beneficial to design a new differential scheme by combing these two techniques.

7.2.4 Cooperative transmission schemes for MIMO broadcast channels

Cooperative BS transmissions have the potential of significantly improving the spectral efficiency of multiuser, multicell MIMO systems. It is expected that when powerful precoding schemes are employed at the BSs, the cooperative system becomes capable of improving the attainable performance. Hence, based on the work in [166], [167] and [168], a new design which combines vector precoding with cooperative networks would be a promising research topic.

7.2.5 Jointly optimized downlink multiuser MIMO system

A novel transceiver design was proposed in Chapter 6, which may be further developed. Explicitly, a sophisticated transmitter along with a low complexity receiver or a simple transmitter combined with a sophisticated receiver may be beneficial in specific applications.

7.2.6 Broader applications of particle swarm optimization in wireless communications

PSO has been successfully applied in numerous research fields [101, 102, 107]. Hence, PSO may be employed for solving optimization problems derived from the above-mentioned topics. A few examples are in the field of MUDs [13, 16, 17]. As the search-space is extended, for example owing to using multiple bits/symbol, as in 16QAM, the benefit of PSO may become even more substantial.

Glossary

PSO	Particle Swarm Optimization
SQP	Sequential Quadratic Programming
BER	Bit error ratio, the ratio of the bits received incorrectly
BEP	Bit error probability, similar notation to BER
BPSK	Binary Phase Shift Keying
BS	A common abbreviation for Base Station
MS	A common abbreviation for Mobile Station
CEE	Channel Estimation Error
CSI	Channel State Information
CIR	Channel Impulse Response
CF	Cost Function
DL	Downlink
DF	Decode and Forward
E_b/N_0	Ratio of bit energy to noise power spectral density.
MIMO	Multi-Input Multi-Output
SISO	Single-Input Single-Output
ML	Maximum Likelihood
MSE	Mean Square Error, a criterion used to optimised the coefficients of the equalizer such that the ISI and the noise contained in the received signal is jointly minimised.

MMSE	Minimum Mean Square Error
OFDM	Orthogonal Frequency Division Multiplexing
PSK	Phase Shift Keying
QAM	Quadrature Amplitude Modulation
RS	Relay Station
TDD	Time Division Duplex
FDD	Frequency Division Duplex
CDMA	Code Division Multiple Access
QPSK	Quadrature Phase Shift Keying
SNR	Signal to Noise Ratio, noise energy compared to the signal energy
THP	Tomlison-Harashima precoder
DPC	Dirty Paper Coding
TX	Transmitter
RX	Receiver
ZF	Zero Forcing
MBER	Minimum Bit Error Rate
VP	Vector Precoding or Vector Perturbation
MUT	Multiuser Trasmission
MUD	Multiuser Detection
SVD	Singular Value Decomposition
GMD	Geometric Mean Decomposition
UCD	Uniform Channel Decomposition
UL	Uplink

Bibliography

[1] L. Hanzo, O. Alamri, M. El-hajjar and N. Wu, *Near-Capacity Multi-Functional MIMO Systems: Sphere-Packing, Iterative Detection and Cooperation*. New York, USA: John Wiley and Sons, 2009.

[2] R. Irmer, R. Habendorf, W. Rave and G. Fettweis, "Nonlinear chip-level multiuser transmission for TDD-CDMA with frequency-selective MIMO channels," in *Proceedings of 5th International ITG Conference on Source and Channel Coding*, (Erlangen, Germany), pp. 363–370, January 14-16, 2004.

[3] L.-U. Choi and R. D. Murch, "New transmit schemes and simplified receivers for MIMO wireless communication systems," *IEEE Transactions on Wireless Communications*, vol. 2, pp. 1217–1230, November 2003.

[4] F. Liu, L. Jiang and C. He, "Low complexity MMSE vector precoding using lattice reduction for MIMO systems," in *Proceedings of the IEEE International Conference on Communications*, pp. 2598 – 2603, June 2007.

[5] A. Hjørungnes and S. R. Diniz, "Minimum BER prefilter transform for communications systems with binary signaling and known FIR MIMO channel," *IEEE Signal Processing Letters*, vol. 12, pp. 234–237, March 2005.

[6] Y. Jiang, W. Hager and J. Li, "The geometric mean decomposition," *Linear Algebra and Its Applications*, vol. 396, pp. 373–384, Feburary 2005.

[7] Y. Jiang, J. Li and W. Hager, "Uniform channel decomposition for MIMO communications," *IEEE Transactions on Signal Processing*, vol. 53, pp. 4283–4294, November 2005.

[8] F. Liu, L. Jiang and C. He, "Joint MMSE vector precoding based on GMD method for MIMO systems," *IEICE Transactions on Communications*, vol. E90-B, pp. 2617–2620, September 2007.

[9] L. Xu, S. Chen and L. Hanzo, "EXIT chart analysis aided turbo MUD designs for the rank-deficient multiple antenna assisted OFDM uplink," *IEEE Transactions on Wireless Communications*, vol. 7, pp. 2039–2044, 2008.

[10] R. Zhang and L. Hanzo, "Iterative Multiuser Detection and Channel Decoding for DS-CDMA Using Harmony Search," *IEEE Signal Processing Letters*, vol. 16, pp. 917–920, 2009.

[11] B. Xu, "Particle-swarm-optimization based turbo multiuser detection for STBC MC-CDMA systems," in *Proceedings of the IEEE International Symposium on Personal, Indoor and Mobile Radio Communications*, (Cannes, France), pp. 1 – 5, 15-18 September 2008.

[12] M. Y. Alias, S. Chen and L. Hanzo, "Genetic algorithm assisted minimum bit error rate multiuser detection in multiple antenna aided OFDM," in *Proceedings of the IEEE Vehicular Technology Conference*, vol. 1, pp. 548–552, September 2004.

[13] K. K. Soo, Y. M. Siu, W. S. Chan, L. Yang and R. S. Chen, "Particle-swarm-optimization-based multiuser detector for CDMA communications," *IEEE Transactions on Vehicular Technology*, vol. 56, pp. 3006–3013, September 2007.

[14] Z. Guo, Y. Xiao and M. H. Lee, "Multiuser detection based on particle swarm optimization algorithm over multipath fading channels," *IEICE Transactions on Communications*, vol. E90-B, pp. 421–424, 2007.

[15] Y. Zhao and J. Zheng, "Multiuser detection employing particle swarm optimization in space-time CDMA systems," in *Proceedings of the 2005 International Symposium Communications and Information Technology*, vol. 2, pp. 940–942, Oct. 12-14, 2005.

[16] H. H. El-Mora, A. U. Sheikh and A. Zerguine, "Application of particle swarm optimization algorithm to multiuser detection in CDMA," in *Proceedings of the 16th IEEE International Symposium Personal, Indoor and Mobile Radio Communications*, vol. 4, (Berlin, Germany), pp. 2522–2526, Sept. 11-14, 2005.

[17] Z. Lu and S. Yan, "Multiuser detector based on particle swarm algorithm," in *Proceedings of the 6th IEEE CAS Symposium Emerging Technologies: Frontiers of Mobile and Wireless Communication*, vol. 2, (Shanghai, China), pp. 783–786, May 31 - June 2, 2004.

[18] B. Vojčić and W. Jang, "Transmitter preprocessing in synchronous multiuser communications," *IEEE Transactions on Communications*, vol. 46, pp. 1346–1355, October 1998.

[19] R. Irmer, W. Rave and G. Fettweis, "Minimum BER Transmission for TDD-CDMA in frequency-selective channels," in *Proceedings of IEEE International Symposium On Personal, Indoor And Mobile Radio Communications*, vol. 2, (Beijing, China), pp. 1260–1264, September, 7-10 2003.

[20] R. Irmer, W. Rave and G. Fettweis, "Minimum BER multiuser transmission for spread-spectrum systems in frequency-selective channels," in *Proceedings of the International Workshop on Multi-Carrier Systems and Solutions*, (Oberpfaffenhofen, Germany), September 2003.

[21] R. Irmer, R. Habendorf, W. Rave and G. Fettweis, "Nonlinear multiuser transmission using multiple antennas for TDD-CDMA," in *Proceedings of the International Symposium on Wireless Personal Multimedia Communications*, vol. 3, (Yokosuka, Japan), pp. 251–255, October, 19-22 2003.

[22] M. Tomlinson, "New automatic equaliser employing modulo arithmetic," *Electronics Letters*, vol. 7, pp. 138–139, March 1971.

[23] B. M. Hochwald, C. B. Peel and A. L. Swindlehurst, "A vector-perturbation technique for near-capacity multiantenna multiuser communication - Part II: perturbation," *IEEE Transactions on Communications*, vol. 53, pp. 537–544, March 2005.

[24] R. Irmer, *Multiuser Transmission in Code Division Multiple Access Mobile Communication Systems*. PhD thesis, Technique University Dresden, Dresden, Germany, 2005.

[25] M. Joham, K. Kusume, M. H. Gzara, W. Utschick, and J. A. Nossek, "Transmit Wiener filter for the downlink of TDD DS-CDMA systems," in *Proceedings of the IEEE International Symposium on Spread Spectrum Techniques and Applications*, vol. 1, pp. 9–13, September 2002.

[26] S. Tan, *Minimum Error Rate Beamforming Transceivers*. PhD thesis, School of Electronics and Computer Science, University of Southampton, Southampton, UK, April 2008.

[27] J. Nocedal and S.J. Wright, *Numerical Optimization*. New York: Springer, 1999.

[28] W. Yao S. Chen S. Tan and L. Hanzo, "Minimum bit error rate multiuser transmission designs using particle swarm optimisation," *IEEE Transactions on Wireless Communications*, vol. 8, pp. 5012–5017, October 2009.

[29] R. Eberhart, J. Kennedy, "A new optimizer using particle swarm theory," in *Proceedings of International Symposium on Micro Machine and Human Science*, pp. 39–43, October 1995.

[30] J. Kennedy, R. Eberhart, "Particle swarm optimization," in *Proceedings of the IEEE International Conference on Neural Networks*, vol. 4, pp. 1942–1948, 27 Nov.-1 Dec. 1995.

[31] M. Costa, "Writing on dirty paper," *IEEE Transactions on Information Theory*, vol. 29, pp. 439–441, May 1983.

[32] D. A. Schmidt, M. Joham and W. Utschick, "Minimum mean square error vector precoding," in *Proceedings of the IEEE International Symposium on Personal, Indoor and Mobile Radio Communications*, vol. 1, pp. 107 – 111, September 11-14 2005.

[33] C.-Y. Wei, L. Wang and L. Hanzo, "Iterative irregular sphere detection in high-rate downlink SDMA systems," *IEEE Transactions on Vehicular Technology*, vol. 58, pp. 3855 – 3861, September 2009.

[34] C. Windpassinger, R. F. H. Fischer, and J. B. Huber, "Lattice-reduction-aided broadcast precoding," *IEEE Transactions on Communications*, vol. 52, pp. 2057–2060, December 2004.

[35] A. Callard, A. Khandani, and A. Saleh, "Vector precoding with MMSE for the fast fading and quasi-static multi-User broadcast channel," in *Proceedings of Annual Conference on Information Sciences and Systems*, pp. 1002 – 1007, March 2006.

[36] W. Yao, S. Chen and L. Hanzo, "Improved MMSE vector precoding based on the MBER criterion," in *Proceedings of the IEEE VTC 2009 Spring*, (Barcelona, Spain), April 26-29, 2009.

[37] W. Yao, S. Chen and L. Hanzo, "Minimum bit error rate based generalised vector precoding design for multiuser transmission," *'accepted in' IEEE Transactions on Vehicular Technology*.

[38] W. Yao, S. Chen and L. Hanzo, "A transceiver design based on uniform channel decomposition and MBER vector perturbation," *IEEE Transactions on Vehicular Technology*, vol. 59, pp. 3153 – 3159, July 2010.

[39] G. H. Golub and C. F. Van Loan, *Matrix Computations*. Baltimore, MD, USA: Johns Hopkins University Press, 1983.

[40] W. Yao S. Chen S. Tan and L. Hanzo, "Particle Swarm Optimisation Aided Minimum Bit Error Rate Multiuser Transmission," in *Proceedings of the IEEE International Conference on Communications*, (Dresden, Germany), pp. 1–5, June 2009.

[41] W. Yao S. Chen and L. Hanzo, "Particle swarm optimisation aided multiuser transmission schemes for MIMO communication," in *Proceedings of 3rd International Conference of Bio-Inspired Systems and Signal Processing*, (Valencia, Spain), pp. 53–60, January 2010.

[42] M. Y. Alias, S. Chen and L. Hanzo, "Multiple-antenna-aided OFDM employing genetic-algorithm-assisted minimum bit error rate multiuser detection," *IEEE Transactions on Vehicular Technology*, vol. 54, pp. 1713 – 1721, September 2005.

[43] M. Y. Alias, A. K. Samingan, S. Chen and L. Hanzo, "Multiple antenna aided OFDM employing minimum bit error rate multiuser detection," *IET Electronics Letters*, vol. 39, pp. 1769 – 1770, November 2003.

[44] A. Wolfgang,N. N. Ahmad, S. Chen and L. Hanzo, "Genetic algorithm assisted minimum bit error rate beamforming," in *Proceedings of the IEEE Vehicular Technology Conference*, vol. 1, pp. 142–146, May 2004.

[45] W. Yao S. Chen and L. Hanzo, "Generalised Vector Precoding Design Based on the MBER Criterion for Multiuser Transmission," in *Proceedings of IEEE Vehicular Technology Conference*, (Ottawa, Canada), pp. 1–5, September 2010.

[46] D. Gerlach and A. Paulraj, "Adaptive transmitting antenna arrays with feedback," *IEEE Signal Processing Letters*, vol. 1, pp. 150–152, October 1994.

[47] R. Esmailzadeh, E. Sourour, and M. Nakagawa, "Prerake diversity combining in time-division duplex CDMA mobile communications," *IEEE Transactions on Vehicular Technology*, vol. 48, pp. 795–801, May 1999.

[48] L.-U. Choi and R. D. Murch, "Transmit-preprocessing technique with simplified receivers for the downlink of MISO TDD-CDMA systems," *IEEE Transactions on Vehicular Technology*, vol. 53, pp. 285–295, March 2004.

[49] M. Joham, W. Utschick, and J. A. Nossek, "Linear transmit processing in MIMO communications systems," *IEEE Transactions on Signal Processing*, vol. 53, pp. 2700–2712, August 2005.

[50] T. M. Cover and J. A. Thomas, *Elements of Information Theory*. New York: John Wiley Sons, 1991.

[51] R. Esmailzadeh, M. Nakagawa, and E. A. Sourour, "Time-division duplex CDMA communications," *IEEE Transactions on Personal Communications*, vol. 4, pp. 51–56, April 1997.

[52] M. Haardt, A. Klein, R. Koehn, S. Oestreich, M. Purat, V. Sommer, and T. Ulrich, "The TDCDMA based UTRA TDD mode," *IEEE Journal on Selected Areas Communications*, vol. 18, pp. 1375–1385, August 2000.

[53] G. V. Tsoulos and M. A. Beach, "Calibration and linearity issues for an adaptive antenna system," in *Proceedings of the IEEE Vehicular Technology Conference*, vol. 3, pp. 1597–1600, May 1997.

[54] W. Keusgen, C. M. Walke, and B. Rembold, "A system model considering the influence of front-end imperfections on the reciprocity of up and downlink system impulse responses," in *Proceedings of the Aluminium Surface Science and Technology*, pp. 243–248, September 2001.

[55] K. Nishimori, K. Cho, Y. Takatori, and T. Hori, "Automatic calibration method using transmitting signals of an adaptive array for TDD systems," *IEEE Transactions on Vehicular Technology*, vol. 50, pp. 1636–1640, November 2001.

[56] J. G. Proakis, *Digital Communications*. New York: McGraw-Hill, 1995.

[57] L.-L. Yang, "Design Linear Multiuser Transmitters from Linear Multiuser Receivers," in *Proceedings of IEEE International Conference on Communications*, pp. 5258 – 5263, 24-28 June 2007.

[58] B. R. Vojčić and W. M. Jang, "Transmitter precoding in synchronous multiuser communications," *IEEE Transactions on Communications*, vol. 46, pp. 1346–1355, October 1998.

[59] H. R. Karimi, M. Sandell and J. Salz, "Comparison between transmitter and receiver array processing to achieve interference nulling and diversity," in *Proceedings of IEEE International Symposium Personal, Indoor and Mobile Radio Communications*, vol. 3, pp. 997–1001, September 1999.

[60] A. N. Barreto and G. Fettweis, "Capacity increase in the downlink of spead spectrum system through joint signal processing," in *Proceedings of IEEE International Conference on Communications*, vol. 4, pp. 1142–1146, June 2001.

[61] R. Habendorf and G. Fettweis, "Nonlinear optimization for the multiuser downlink," in *Proceedings of European Wireless Conference*, (Paris, France), p. 1, April 01-04 2007.

[62] F. Richter, A. Fischer, R. Habendorf and G. Fettweis, "Transmitter-based minimization of error rates in the downlink of wireless systems," in *Proceedings of the IEEE Global Communications Conference*, (New Orleans, USA), p. 1, 30. November - 04. December 2008.

[63] I.H. Azzam and R.S. Adve, "Linear precoding for multiuser MIMO systems with multiple base stations," in *Proceedings of the IEEE International Conference on Communications*, (Dresden, Germany), pp. 1–5, June 2009.

[64] C. Masouros and E. Alsusa, "Dynamic linear precoding for the exploitation of known interference in MIMO broadcast systems," *IEEE Transactions on Wireless Communications*, vol. 8, pp. 1396 – 1404, March 2009.

[65] J. Ryu and W. Choi, "A simple linear multiuser precoding technique in cellular relay networks," *IEEE Communications Letters*, vol. 14, pp. 12 – 14, January 2010.

[66] E. Y. Kim and J. Chun, "Optimum vector perturbation minimizing total MSE in multiuser MIMO downlink," in *Proceedings of the IEEE International Conference on Communications*, pp. 4242 – 4247, June 2006.

[67] C. Windpassinger, *Detection and precoding for multiple input multiple output channels*. PhD thesis, University of Erlangen-Nuremberg, Erlangen, Germany, June 2004.

[68] C. Yuen and B. M. Hochwald, "How to gain 1.5 dB in vector precoding," in *Proceedings of the IEEE Global Communications Conference*, (San Francisco, USA), pp. 1–5, 27 November - 01 December 2006.

[69] R. Habendorf, I. Riedel and G. Fettweis, "Reduced complexity vector precoding for the multiuser downlink," in *Proceedings of the IEEE Global Communications Conference*, (San Francisco, USA), pp. 1–5, 27 November - 01 December 2006.

[70] R. Habendorf and G. Fettweis, "Vector precoding with bounded complexity," in *Proceedings of the SPAWC 2007*, (Helsinki, Finland), pp. 1–5, June 17-20, 2007.

[71] W. S. Chua, C. Yuen and F. Chin, "A continuous vector-perturbation for multi-antenna multi-user communication," in *Proceedings of the IEEE Vehicular Technology Conference*, pp. 1806 – 1810, April, 2007.

[72] D. J. Ryan, I. B. Collings, I. V. L. Clarkson and R. W. Heath, "A lattice-theoretic analysis of vector perturbation for multi-user MIMO systems," in *Proceedings of the IEEE International Conference on Communications*, (Beijing, China), pp. 3340 – 3344, May 2008.

[73] U. P. Rico, E. Alsusa and C. Masouros, "A fast least-squares solution-seeker algorithm for vector-perturbation," in *Proceedings of the GLOBECOM 2008*, (New Orleans, Louisiana), pp. 1–5, Nov. 30 - Dec. 4, 2008.

[74] R. R. Muller, D. Guo and A. L. Moustakas, "Vector precoding for wireless MIMO systems and its replica analysis," *IEEE Journal on Selected Areas in Communications*, vol. 26, pp. 530–540, April 2008.

[75] D. J. Ryan, I. B. Collings, I. V. L. Clarkson and R. W. Heath, "Performance of vector perturbation multiuser MIMO systems with limited feedback," *IEEE Transactions on Communications*, vol. 57, pp. 2633–2644, September 2009.

[76] P. Lu and H. Yang, "Vector perturbation precoding for MIMO broadcast channel with quantized channel feedback," in *Proceedings of the IEEE Global Communications Conference*, (Honolulu, USA), pp. 1–5, 30 November - 04 December 2009.

[77] H. Han, S. Park and I. Lee, "Improved vector perturbation with modulo loss reduction for multiuser downlink systems," in *Proceedings of the IEEE International Conference on Communications*, (Dresden, Germany), pp. 1 – 5, 14-18 June 2009.

[78] R. de Miguel and R. R. Muller, "On convex vector precoding for multiuser MIMO broadcast channels," *IEEE Transactions on Signal Processing*, vol. 57, pp. 4497–4508, November 2009.

[79] A. Razi, D. J. Ryan, I. B. Collings and J. Yuan, "Sum rates, rate allocation, and user scheduling for multi-user MIMO vector perturbation precoding," *IEEE Transactions on Wireless Communications*, vol. 9, pp. 356–365, January 2010.

[80] R. de Miguel, V. Gardasevic, R. R. Muller and F. F. Knudsen, "On overloaded vector precoding for single-user MIMO channels," *IEEE Transactions on Wireless Communications*, vol. 9, pp. 745–753, February 2010.

[81] H. Liu and J. Li, "A particle swarm optimization-based multiuser detection for receive-diversity-aided STBC systems," *IEEE Signal Processing Letters*, vol. 15, pp. 29–32, 2008.

[82] X. Huang, Y. Zhang, J. Xu and Y. Wang, "Fast decoding of convolutional codes based on particle swarm optimization," in *Proceedings of the International Conference on Natural Computation*, (Jinan, China), pp. 619 – 623, 18-20 October 2008.

[83] Y.-Q. Hei, X.-H. Li, K.-C. Yi and W.-T. Li, "Multi-user MIMO broadcast system grouping strategy based on particle swarm optimization," in *Proceedings of the International Conference on Advanced Information Networking and Applications*, (Bradford, UK), pp. 212 – 216, 26-29 May 2009.

[84] J. Gao, J. Wang and B. Wang, "Improved particle swarm optimization for PAPR reduction of OFDM systems," in *Proceedings of the International Conference on Networking, Sensing and Control*, (Chicago, USA), pp. 621 – 624, 10-12 April 2010.

[85] C. W. Reynolds, "Flocks,herds and schools: a distributed behavioral model," in *Computer Graphics*, vol. 21, pp. 25–34, 1987.

[86] E.O. Wilson, *Sociobiology: The new synthesis*. Cambridge, MA: Belknap Press, 1975.

[87] L. Xu, S. Tan, S. Chen and L. Hanzo, "Iterative minimum bit error rate multiuser detection in multiple antenna aided OFDM," in *Proceedings of the IEEE Wireless Communications and Networking Conference*, (Las Vegas, USA), pp. 1603 – 1607, 3-6 April 2006.

[88] C. M. Bishop, *Neutral Networks for Pattern Recognition*. Oxford University Press, 1995.

[89] J. E. Dennis and R. B. Schnabel, *Numerical Methods for Unconstrained Optimization and Nonlinear Equations*. Prentice-Hall, 1983.

[90] R. G. Maunder and L. Hanzo, "Genetic algorithm aided design of near-capacity irregular variable length codes," in *Proceedings of the IEEE Wireless Communications and Networking Conference*, (Las Vegas, USA), pp. 1256 – 1260, March 31 - April 3 2008.

[91] H. R. Palally, S. Chen, W. Yao and L.-L. Yang, "Particle swarm optimisation aided semi-blind joint maximum likelihood channel estimation and data detection for MIMO systems," in *Proceedings of the IEEE Workshop on Statistical Signal Processing*, (Cardiff, Wales, UK), pp. 309–312, 31 August - 3 September 2009.

[92] J. Kennedy, "The particle swarm: social adaptation of knowledge," in *Proceedings of the IEEE International Conference on Evolutionary Computation*, (Indianapolis, USA), pp. 303 – 308, 13-16 April 1997.

[93] J. Salerno, "Using the particle swarm optimization technique to train a recurrent neural model," in *Proceedings of the IEEE International Conference on Tools with Artificial Intelligence*, (Newport Beach, USA), pp. 45 – 49, 3-8 November 1997.

[94] Y. Shi and R. Eberhart, "A modified particle swarm optimizer," in *Proceedings of the IEEE International Conference on Evolutionary Computation*, (Anchorage, USA), pp. 69 – 73, 4-9 May 1998.

[95] Z. He, C. Wei, L. Yang, X. Gao, S. Yao, R. Eberhart and Y. Shi, "Extracting rules from fuzzy neural network by particle swarm optimisation," in *Proceedings of the IEEE International Conference on Evolutionary Computation*, (Anchorage, USA), pp. 74 – 77, 4-9 May 1998.

[96] Y. Shi and R. Eberhart, "Empirical study of particle swarm optimization," in *Proceedings of the Congress on Evolutionary Computation*, (Washington, USA), 6-9 July 1999.

[97] M. Clerc, "The swarm and the queen: towards a deterministic and adaptive particle swarm optimization," in *Proceedings of the Congress on Evolutionary Computation*, (Washington, USA), 6-9 July 1999.

[98] R. Eberhart and Y. Shi, "Comparing inertia weights and constriction factors in particle swarm optimization," in *Proceedings of the IEEE International Conference on Evolutionary Computation*, (Anchorage, USA), pp. 84 – 88, 16-19 July 2000.

[99] R. Eberhart and Y. Shi, "Particle swarm optimization: developments, applications and resources," in *Proceedings of the Congress on Evolutionary Computation*, (Seoul, Korea), pp. 81 – 86, 27-30 May 2001.

[100] Y. Shi and R. Eberhart, "Fuzzy adaptive particle swarm optimization," in *Proceedings of the Congress on Evolutionary Computation*, (Seoul, Korea), pp. 101 – 106, 27-30 May 2001.

[101] C. A. Coello Coello and M. S. Lechuga, "MOPSO: a proposal for multiple objective particle swarm optimization," in *Proceedings of the Congress on Evolutionary Computation*, (Honolulu, USA), pp. 1051 – 1056, 12-17 May 2002.

[102] T. Krink, J. S. Vesterstrom and J. Riget, "Particle swarm optimisation with spatial particle extension," in *Proceedings of the Congress on Evolutionary Computation*, (Honolulu, USA), pp. 1474 – 1479, 12-17 May 2002.

[103] S. Janson and M. Middendorf, "A hierarchical particle swarm optimizer," in *Proceedings of the Congress on Evolutionary Computation*, pp. 1474 – 1479, 8-12 December 2003.

[104] A. Stacey, M. Jancic and I. Grundy, "Particle swarm optimization with mutation," in *Proceedings of the Congress on Evolutionary Computation*, pp. 1474 – 1479, 8-12 December 2003.

[105] K. E. Parsopoulos and M. N. Vrahatis, "On the computation of all global minimizers through particle swarm optimization," *IEEE Transactions on Evolutionary Computation*, vol. 8, pp. 211–224, June 2004.

[106] F. van den Bergh and A. P. Engelbrecht, "A Cooperative approach to particle swarm optimization," *IEEE Transactions on Evolutionary Computation*, vol. 8, pp. 225–239, June 2004.

[107] A. Ratnaweera, S. K. Halgamuge and H. C. Watson, "Self-organizing hierarchical particle swarm optimizer with time-varying acceleration coefficients," *IEEE Transactions on Evolutionary Computation*, vol. 8, pp. 240–255, June 2004.

[108] C. Yang and D. Simon, "A new particle swarm optimization technique," in *Proceedings of the International Conference on Systems Engineering*, pp. 164–169, 16 - 18 August, 2005.

[109] M. Breaban and H. Luchian, "PSO under an adaptive scheme," in *Proceedings of the Congress on Evolutionary Computation*, pp. 1212 – 1217, 2-5 September 2005.

[110] T. Hendtlass, "WoSP: a multi-optima particle swarm algorithm," in *Proceedings of the Congress on Evolutionary Computation*, pp. 727 – 734, 2-5 September 2005.

[111] Y. Yang, F. Zhao, Y. Yao and A. Zhu, "A PSO and simulated annealing hybrid algorithm to task allocation problem for holonic manufacturing system," in *Proceedings of World Congress on Intelligent Control and Automation*, (Dalian, China), pp. 6767 – 6771, 2006.

[112] M. P. Vecchi and S. C. Kirkpatrick, "Global wiring by simulated annealing," *IEEE Transactions on Computer-Aided Design of Integrated Circuits and Systems*, vol. 2, pp. 215–222, October 1983.

[113] Y. Maeda and T. Kuratani, "Simultaneous perturbation particle swarm optimization," in *Proceedings of the Congress on Evolutionary Computation*, (Vancouver, Canada), pp. 672 – 676, 2006.

[114] S. D. Hill and M. C. Fu, "Simulation optimization via simultaneous perturbation stochastic approximation," in *Proceedings of the Winter Simulation Conference*, (Lake Buena Vista, USA), pp. 1461–1464, December 1994.

[115] Z. Pei, S. Tian and H. Huang, "A novel method for solving nonlinear bilevel programming based on hybrid particle swarm optimization," in *Proceedings of the International Conference on Signal Processing*, (Beijing, China), 16-20 November 2006.

[116] Q. Kang, L. Wang and Q. Wu, "A novel self-organizing particle swarm optimization based on gravitation field model," in *Proceedings of American Control Conference*, (New York, USA), pp. 528 – 533, 9-13 July 2007.

[117] B. Xie, S. Chen and F. Liu, "Biclustering of gene expression data using PSO-GA hybrid," in *Proceedings of the International Conference on Bioinformatics and Biomedical Engineering*, (Wuhan, China), pp. 302 – 305, 6-8 July 2007.

[118] K. Bryan, P. Cunningham and N. Bolshakova, "Application of simulated annealing to the biclustering of gene expression data," *IEEE Transactions on Information Technology in Biomedicine*, vol. 10, pp. 519 – 525, July 2006.

[119] S.-Y. Ho, H.-S. Lin, W.-H. Liauh and S.-J. Ho, "OPSO: orthogonal particle swarm optimization and its application to task assignment problems," *IEEE Transactions on Systems, Man and Cybernetics*, vol. 38, pp. 288–298, March 2008.

[120] H. Fang, L. Chen and W. Wang, "A novel PSO algorithm for global optimization of multi-dimensional function," in *Proceedings of the Chinese Control and Decision Conference*, (Yantai, China), pp. 956 – 960, 2-4 July 2008.

[121] C.-H. Chen, Y.-C. Liu, C.-J. Lin and C.-T. Lin, "A hybrid of cooperative particle swarm optimization and cultural algorithm for neural fuzzy networks," in *Proceedings of the IEEE International Conference on Fuzzy Systems*, (Hong Kong, China), pp. 238 – 245, 1-6 June 2008.

[122] M. Sternberg and R. G. Reynolds, "Using cultural algorithms to support re-engineering of rule-based expert systems in dynamic performance environments: a case study in fraud detection," *IEEE Transactions on Evolutionary Computation*, vol. 1, pp. 225 – 243, November 1997.

[123] Z. Wu, Z. Ni, C. Zhang and L. Gu, "A novel PSO for multi-stage portfolio planning," in *Proceedings of the International Conference on Artificial Intelligence and Computational Intelligence*, (Shanghai, China), pp. 71 – 77, 7-8 November 2009.

[124] J. Tang and X. Zhao, "Particle swarm optimization with adaptive mutation," in *Proceedings of the International Conference on Information Engineering*, (Taiyuan, China), pp. 234 – 237, 10-11 July 2009.

[125] L. Hao and L. Hu, "Hybrid particle swarm optimization for continuous problems," in *Proceedings of the International Colloquium on Computing, Communication, Control, and Management*, (Sanya, China), pp. 217 – 220, 8-9 August 2009.

[126] X. Bai and Y.-X. Ding, "Particle swarm optimization based on an improved learning strategy," in *Proceedings of the International Workshop on Education Technology and Computer Science*, (Wuhan, China), pp. 395 – 398, 6-7 March 2010.

[127] L. Liu, S. Yang, and D. Wang, "Particle wwarm optimization with composite particles in dynamic environments," *IEEE Transactions on Systems, Man and Cybernetics*, vol. 38, pp. 1–15, April 2010.

[128] S. M. Guru, S. K. Halgamuge and S. Fernando, "Particle swarm optimisers for cluster formation in wireless sensor networks," in *Proceedings of International Conference on Intelligent Sensors, Sensor Networks and Information Processing*, (Melbourne, Australia), pp. 319–324, December 5-8, 2005.

[129] J. Kennedy and R. C. Eberhart, "A discrete binary version of the particle swarm algorithm," in *Proceedings of the IEEE International Conference on Systems, Man, and Cybernetics*, vol. 5, pp. 4104–4108, October, 1997.

[130] W. Pang, K.-P. Wang, C.-G. Zhou and L.-J. Dong, "Fuzzy discrete particle swarm optimization for solving traveling salesman problem," in *Proceedings of the International Conference on Computer and Information Technology*, pp. 796 – 800, 14-16 September 2004.

[131] F. Afshinmanesh, A. Marandi and A. Rahimi-Kian, "A novel binary particle swarm optimization method using artificial immune system," in *Proceedings of the International Conference on Computer as a Tool*, pp. 217 – 220, 21-24 November 2005.

[132] C.-L. Huang and C.-H. Tung, "Using mutation to improve discrete particle swarm optimization for single machine total weighted tardiness problem," in *Proceedings of the World Automation Congress*, (Budapest, Hungry), pp. 1 – 6, 24-26 July 2006.

[133] B. Jafarpour, M. R. Meybodi and S. Shiry, "A hybrid method for optimization (discrete PSO + CLA)," in *Proceedings of the International Conference on Intelligent and Advanced Systems*, (Kuala Lumpur, Malaysia), pp. 55 – 60, 25-28 November 2007.

[134] F. Seredynski and A. Y. Zomaya, "Sequential and parallel cellular automata-based scheduling algorithms," *IEEE Transactions on Parallel and Distributed Systems*, vol. 13, pp. 1009 – 1023, October 2002.

[135] K. Veeramachaneni, L. Osadciw and G. Kamath, "Probabilistically driven particle swarms for optimization of multi valued discrete problems: design and analysis," in *Proceedings of the IEEE Swarm Intelligence Symposium*, pp. 141–149, April, 2007.

[136] X. Li, H. Xu and Z. Cheng, "One improved discrete particle swarm optimization based on quantum evolution concept," in *Proceedings of the International Conference on Intelligent Computation Technology and Automation*, (Hunan, China), pp. 96 – 100, 20-22 October 2008.

[137] X. You, D. Shuai and S. Liu, " Research and implementation of quantum evolution algorithm based on immune theory," in *Proceedings of The Sixth World Congress on Intelligent Control and Automation*, (Dalian, China), pp. 3410 – 3414, October 2006.

[138] Y. Xu, Q. Wang and J. Hu, "One improved discrete particle swarm optimization based on quantum evolution concept," in *Proceedings of the IEEE International Conference on Web Intelligence and Intelligent Agent Technology*, (Sydney, Australia), pp. 79 – 82, 9-12 December 2008.

[139] H. Song, R. B. Diolata and Y. H. Joo, "A novel multi-level quantization scheme for discrete particle swarm optimization," in *Proceedings of the IEEE International Conference on Fuzzy Systems*, (Jeju Island, Korea), pp. 1834 – 1838, 20-24 August 2009.

[140] W.-N. Chen, J. Zhang, H.S.H. Chung, W.-L. Zhong, W.-G. Wu and Y.-h. Shi, "A novel set-based particle swarm optimization method for discrete optimization problems," *IEEE Transactions on Evolutionary Computation*, vol. 14, pp. 278–300, April 2010.

[141] R. Irmer, R. Habendorf, W. Rave and G. Fettweis, "Overloaded TDD-CDMA Cells with Multiuser Transmission," in *Proceedings of the ITG/IEEE Workshop on Smart Antennas*, (Munich, Germany), pp. 235–242, March 2004.

[142] S. Chen, A. Livingstone and L. Hanzo, "Minimum bit-error rate design for space-time equalization-based multiuser detection," *IEEE Transactions on Communications*, vol. 54, pp. 824–832, May 2006.

[143] S. Chen and L.-L. Yang, "Downlink MBER beamforming transmitter based on uplink MBER beamforming receiver for TDD-SDMA systems," in *Proceedings of the IEEE Workshop on Statistical Signal Processing*, (Cardiff, Wales, UK), pp. 433–436, 31 August - 3 September 2009.

[144] L. Babai, "On Lovasz's lattice reduction and the nearest lattice point problem," *Combinatorica*, vol. 6, pp. 1–13, January 1986.

[145] H. Yao and G. W. Wornell, "Lattice-reduction-aided detectors for MIMO communication systems," in *Proceedings of the IEEE Globecom*, pp. 424–428, November 2002.

[146] C. Windpassinger and R. F. H. Fischer, "Low-complexity near-maximum-likelihood detection and precoding for MIMO systems," in *Proceedings of the IEEE Informatioin Theory Workshop*, pp. 345–348, March 2004.

[147] S. Chen, W. Yao and L. Hanzo, "Semi-blind adaptive spatial equalization for MIMO systems with high-order QAM signalling," *IEEE Transactions on Wireless Communications*, vol. 7, pp. 4486–4491, Nov. 2008.

[148] , "GMD beamforming for LTE-Advanced SU/MU-MIMO," in *3GPP TG RAN WG1 Meeting 58*, (Miyazaki, Japan), pp. R1–093799, October 2009.

[149] I. E. Telatar, "Capacity of multi-antenna Gaussian channels," *European Transactions on Teleommunications*, vol. 10, pp. 585–595, Nov./Dec. 1999.

[150] Y. Jiang, J. Li and W. Hager, "Joint transceiver design for MIMO communications using geometric mean decomposition," *IEEE Transactions on Signal Processing*, vol. 53, pp. 3791–3803, October 2005.

[151] S. Lin, W. W. L. Ho and Y.-C. Liang, "MIMO broadcast communications using block-diagonal uniform channel decomposition (BD-UCD)," in *Proceedings of the IEEE International Symposium on Personal, Indoor and Mobile Radio Communications*, (Helsinki, Finland), pp. 1 – 5, 11-14 September 2006.

[152] Y. Jiang and M. K. Varanasi, "Diversity-multiplexing tradeoff of GMD/UCD with antenna selection," in *Proceedings of the Fortieth Asilomar Conference on Signals, Systems and Computers*, (USA), pp. 1625 – 1629, 29 October - 1 November 2006.

[153] E. C. Y. Peh and Y.-C. Liang, "Expanded soft demapper for LDPC coded GMD-THP MIMO system," in *Proceedings of the IEEE Radio and Wireless Symposium*, (Long Beach, USA), pp. 519 – 522, 9 - 11 January 2007.

[154] R. Chen, J. Li, W. Liu, L. Chen and C. Li, "Robust uniform channel decomposition for MIMO communications," in *Proceedings of the IEEE International Symposium on Personal, Indoor and Mobile Radio Communications*, (Tokyo, Japan), pp. 1307 – 1311, 13 - 16 September 2009.

[155] K.-J. Lee and I. Lee, "Transceiver design based on blockwise uniform channel decomposition for coded MIMO systems," *IEEE Transactions on Wireless Communications*, vol. 8, pp. 4241 – 4251, August 2009.

[156] F. Liu, L. Jiang and C. He, "Advanced joint transceiver design for block-diagonal geometric-mean-decomposition-based multiuser MIMO systems," *IEEE Transactions on Vehicular Technology*, vol. 59, pp. 692 – 703, Feburary 2010.

[157] F. Liu, L. Jiang and C. He, "Low complexity MMSE vector precoding using lattice reduction for MIMO Systems," in *Proceedings of the ICC 2007*, (Glasgow, UK), pp. 2598–2603, June 24-28, 2007.

[158] M. Abuthinien, S. Chen and L. Hanzo, "Semi-blind joint maximum likelihood channel estimation and data detection for MIMO systems," *IEEE Signal Processing Letters*, vol. 15, pp. 202 – 205, 2006.

[159] P. Viswanath and D. Tse, "Sum capacity of the vector Gaussian broadcast channel and uplink-downlink duality," *IEEE Transactions on Information Theory*, vol. 49, pp. 1073 – 1096, May 2003.

[160] C. Chan-Byoung, S. Shim and R. Heath, "Block diagonalized vector perturbation for multiuser MIMO systems," *IEEE Transactions on Wireless Communications*, vol. 7, pp. 4051 – 4057, November 2008.

[161] S. W. Lin, W. W. L. Ho and Y. C. Liang, "Block diagonal geometric mean decomposition (BD-GMD) for MIMO broadcast channels," *IEEE Transactions on Wireless Communications*, vol. 7, pp. 2778 – 2789, July 2008.

[162] P. Ubaidulla and A. Chockalingam, "Robust THP transceiver designs for multiuser MIMO downlink," in *Proceedings of the WCNC 2009*, (Budapest, Hungary), pp. 1–6, April 5-8, 2009.

[163] H. K. Bizaki and A. Falahati, "Tomlinson-Harashima precoding with imperfect channel state information," *IET Communications*, vol. 2, pp. 151 – 158, January 2008.

[164] F. A. Dietrich, P. Breun and M. Utschick, "Robust Tomlinson-Harashima precoding for the wireless broadcast channel," *IEEE Transactions on Signal Processing*, vol. 55, pp. 631 – 644, Febuary 2007.

[165] S. Fukushi, K. Ishibashi and R. Kohno, "Tomlinson-Harashima Precoded MIMO system with differential detection," in *Proceedings of the PIMRC 2007*, (Athens, Greece), pp. 1–5, September 3-7, 2007.

[166] H. Y. Zhang, N. B. Mehta, A. F. Molisch, J. Zhang and H. Y. Dai, "Asynchronous interference mitigation in cooperative base station systems," *IEEE Transactions on Wireless Communications*, vol. 7, pp. 155 – 165, January 2008.

[167] Z. Zhou, L. Wu, W. Hardjawana and B. Vucetic, "Cooperative transmission scheme in MIMO relay broadcast channels," in *Proceedings of the PIMRC2008*, (Cannes, France), pp. 1–5, September 15-18, 2008.

[168] K. Nishimori, K. Riichi, Y. Takatori, A. Ohta and S. Kubota, "Cooperative interference cancellation for multiuser transmission," in *Proceedings of the EuCAP 2007*, (Edinburgh, UK), pp. 1–5, November 11-16, 2007.

Author Index

D

E

F

G

H

I

J

K

L

M

N

O

P

R

S

T

U

V

W

X

Y

Z